Evaluation of the Impact of Mechanical Vibration on the Adult Skeleton

Lucy Clare Harris
Academic Unit of Bone Metabolism
Department of Human Metabolism
University of Sheffield
Thesis submitted for the degree of Doctor of Philosophy

Summary

The potential for exercise to maintain or enhance bone strength during ageing is of increasing interest. Preliminary evidence suggests that whole body vibration (WBV) can enhance muscle strength and maintain bone density in postmenopausal women, and may provide low impact anabolic exercise suitable for use in patients with weakened skeletons.

The main aim of this thesis is to evaluate the impact of WBV on the adult human skeleton, putting the impact of WBV in the context of other habitual locomotor activities in order to analyse which WBV settings may hold most osteogenic potential. The potential for a unilateral model of WBV using the Galileo 900 was also assessed.

To investigate these aims, transmission of WBV delivered by the Galileo 900, Powerplate Pro 5 and Juvent 1000 platforms was assessed using a motion capture system. Strain at the tibia was recorded using a bone surface bonded strain gauge.

The results presented here suggest that WBV is transmitted to the hip and spine on all platforms, however attenuation of the WBV stimulus is observed above the anterior superior iliac spine. The greatest attenuation is observed with the Galileo 900 which has a side alternating motion as opposed to the vertical motion of the Powerplate Pro 5 and Juvent 1000. The greatest accelerations transmitted to the hip and spine are generated by the Powerplate Pro 5, with the Galileo 900 delivering lower accelerations for similar input frequency and amplitudes and the Juvent 1000 delivering 10 fold lower accelerations.

The unilateral loading model of WBV appears to be possible as, when a single leg is placed on the platform, transmission of WBV to the contralateral leg is far less than to the leg on the platform. This is also reflected in the strain and strain rates observed when the strain gauged leg is placed on the platform as opposed to off the platform during WBV.

Strains and strain rates generated during WBV on the Powerplate Pro 5 and Juvent 1000 are comparable to those generated whilst walking, however on the Galileo 900, strains equivalent to those generated whilst performing high impact activities such as jumping are observed. Strain rates of much greater magnitude than those observed during habitual locomotor activities are also generated on the Galileo 900.

Acknowledgements

Firstly I would like to thank my supervisors, Prof Eugene McCloskey and Prof Tim Skerry, for their support, guidance and teaching throughout my PhD. You have helped me grow and develop as a researcher and it has been a privilege and pleasure to work with you. Thank you to Dr Lang Yang and Prof Mark Wilkinson from the Academic Unit of Bone Metabolism at the University of Sheffield. Lang you have helped me demystify the language of computers and provided me with mentoring in the unfamiliar area of medical engineering. Mark, without your efforts to practice and develop the technique of applying a strain gauge to the tibia, this project would not have been possible.

Thank you to Dr Chris Monk, Dr Jill Van Der Meulen, Emma Pratt and Mark Reeves from medical engineering and the gait laboratory at the Northern General Hospital. Thank you Jill for letting us fiddle with the Vicon system and take over the gait lab. Thank you Emma for answering my questions on motion capture and data processing. Mark, thank you for providing an ever enthusiastic ear and offering support and opinion when I felt like I had no idea what I was doing! From the Clinical Research Facility at the Northern General hospital, I would like to thank the research nurses, especially Julie Walker, for her efforts in coordinating the study. From the Engineering Department at the University of Sheffield, I thank Chris Grigson, Prof Keith Wardon and Ramon Fuentes for their help with technical equipment, data processing and analysis.

Along with those providing academic support, I would like to thank my friends for keeping me going to the end. Amy Evans, Fatma Gossiel and Becky Bright, thank you for listening to my ramblings, picking me up when required and providing the much needed coffee breaks to get me through the writing. Rachel Harrison, thank you for being my comrade in WBV research!

I would also like to express my gratitude to my family. Thank you to my parents for teaching me to persevere and my dad for his never fading support and encouragement. Finally to Wil, for being my rock and absolutely amazing best friend. I am truly lucky to have you and would not have finished this without your dedication and support.

Table of Contents

List of Figures

List of Tables

List of Equations

List of Abbreviations

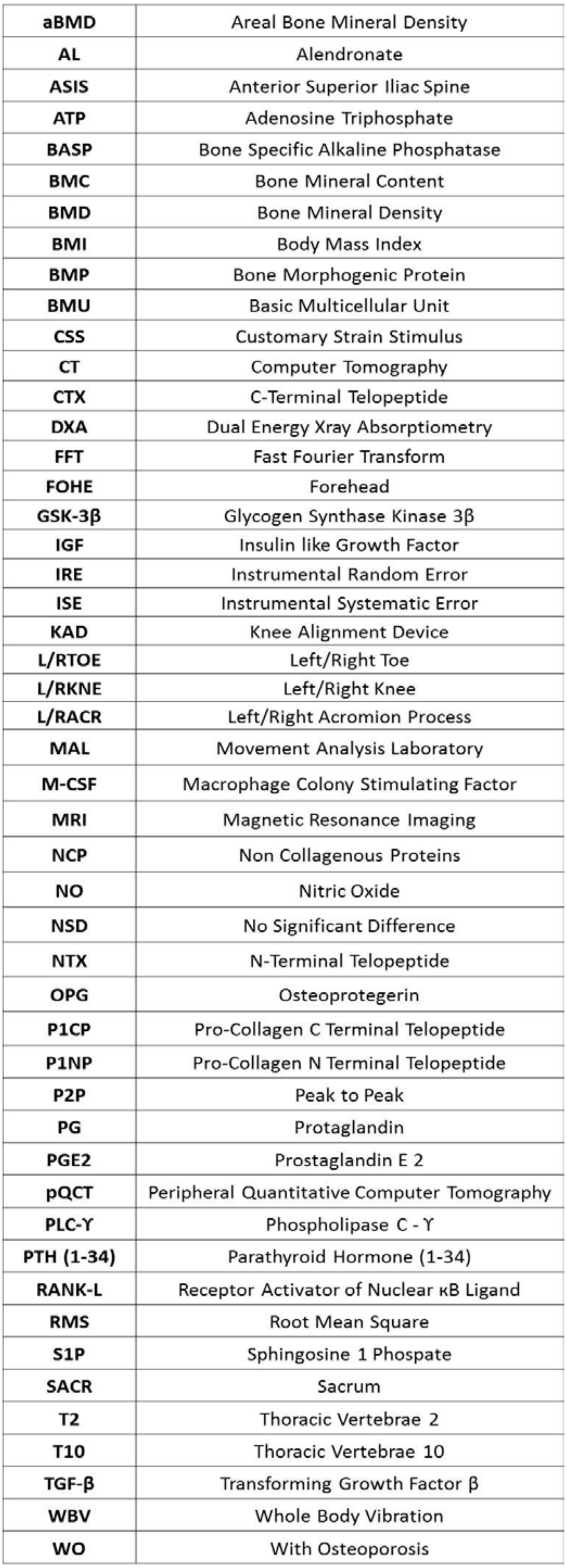

aBMD	Areal Bone Mineral Density
AL	Alendronate
ASIS	Anterior Superior Iliac Spine
ATP	Adenosine Triphosphate
BASP	Bone Specific Alkaline Phosphatase
BMC	Bone Mineral Content
BMD	Bone Mineral Density
BMI	Body Mass Index
BMP	Bone Morphogenic Protein
BMU	Basic Multicellular Unit
CSS	Customary Strain Stimulus
CT	Computer Tomography
CTX	C-Terminal Telopeptide
DXA	Dual Energy Xray Absorptiometry
FFT	Fast Fourier Transform
FOHE	Forehead
GSK-3β	Glycogen Synthase Kinase 3β
IGF	Insulin like Growth Factor
IRE	Instrumental Random Error
ISE	Instrumental Systematic Error
KAD	Knee Alignment Device
L/RTOE	Left/Right Toe
L/RKNE	Left/Right Knee
L/RACR	Left/Right Acromion Process
MAL	Movement Analysis Laboratory
M-CSF	Macrophage Colony Stimulating Factor
MRI	Magnetic Resonance Imaging
NCP	Non Collagenous Proteins
NO	Nitric Oxide
NSD	No Significant Difference
NTX	N-Terminal Telopeptide
OPG	Osteoprotegerin
P1CP	Pro-Collagen C Terminal Telopeptide
P1NP	Pro-Collagen N Terminal Telopeptide
P2P	Peak to Peak
PG	Protaglandin
PGE2	Prostaglandin E 2
pQCT	Peripheral Quantitative Computer Tomography
PLC-ϒ	Phospholipase C - ϒ
PTH (1-34)	Parathyroid Hormone (1-34)
RANK-L	Receptor Activator of Nuclear κB Ligand
RMS	Root Mean Square
S1P	Sphingosine 1 Phospate
SACR	Sacrum
T2	Thoracic Vertebrae 2
T10	Thoracic Vertebrae 10
TGF-β	Transforming Growth Factor β
WBV	Whole Body Vibration
WO	With Osteoporosis

1 Chapter One: Introduction

1.1 Bone Structure and architecture

The human skeleton is composed of bones with a multitude of functions, from supporting the body to stand and protecting internal organs, to enabling the sense of hearing. Successfully delivering such a diverse range of functions is achieved through the inhomogeneous, anisotropic structure of bone.

At a microscopic level, bone is primarily composed of collagen, mineralised by Calcium phosphate, along with other less well defined non-collagenous proteins (NCPs), water and multiple cell types[2]. The specific composition of different bone types gives them their unique characteristics, for instance bones of the inner ear are highly mineralised, producing the stiff structure required for the sensitive transmission of sound waves [3, 4]. If such a stiff bone was found in the spine, vertebral fracture incidence would be extremely high, however this is a perfect example of the adaptable nature of bone to function as, in vertebra, the bone is much more porous, allowing the strains experienced at the spine to be dissipated leaving little damage and protecting the spinal cord.

At the macroscopic level, bone is composed of two types, cortical bone on the outside and trabecular (or cancellous) bone on the inside (Figure 1).

Cortical bone is made up of osteons, structures composed of concentric rings of cartilaginous lamellae[5, 6]. At the centre of the osteon is the haversian canal which contains blood vessels and nerves innervating the bone.

Trabecular bone is found within the medullary cavity and is surrounded by bone marrow[5]. In contrast to the tightly packed and organised structure of cortical bone, trabecular bone is composed of irregular lamellae forming strut like trabeculae, resulting in a much more porous structure. Whilst appearing to be in random alignment, the direction in which the trabecular rods form reflects the strength characteristics of bone, with trabeculae aligning not in random but along the direction of frequent loading of the bone [5].

Along the length of a long bone, bone composition varies. At the epiphysis there is a great volume of trabecular bone whereas in the diaphysis the predominant bone type is cortical [7] (Figure 1). Cortical thickness and, to a lesser extent, spacing and thickness of trabeculae effect bone strength [8]. By varying these parameters, again the bone can adapt to function, forming a strong structure in the direction of frequent loading [9, 10].

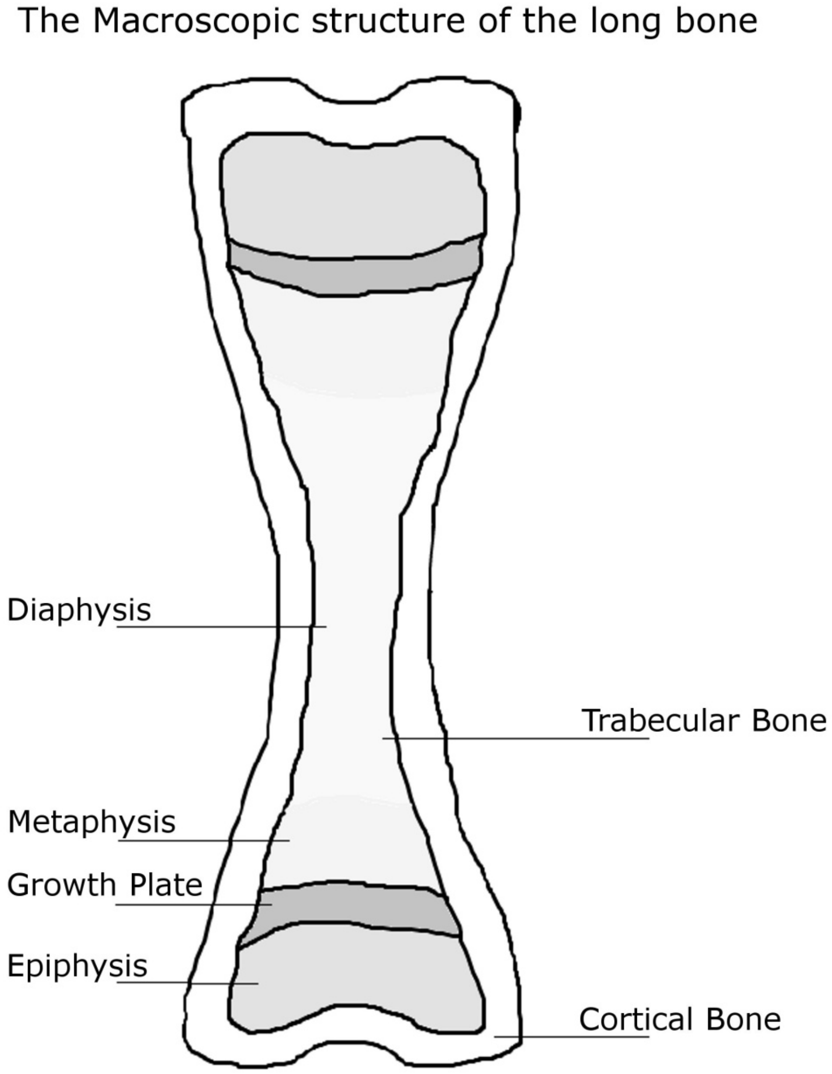

Figure 1: The macroscopic structure of the long bone.

This figure shows the macroscopic structure of a long bone. Around the outside of the bone is solid cortical bone, in the centre of the bone is the struts of trabecular bone. The epiphysis is the end section of the bone that forms joints with other bones and is rich in trabecular bone. The diaphysis is the mid section of the bone which is mainly composed of cortical bone. The metaphysis is the slightly wider midesction of the bone which undergoes growth during childhood. The growth plate is responsible for the lengthening of the bone during growth. Once growth ends, both the metaphysis and growth plate become ossified, forming solid bone and the epiphyseal line.

1.2 Adaptions in bone geometry and composition

Bone is a metabolically active tissue composed of mature osteocytes as well as osteoblasts and osteoclasts which are employed in the growth and maintenance of the skeleton. Osteoclasts are responsible for resorption of bone, and osteoblasts for bone formation (Figure 2). Resorption and formation are the processes underlying bone modelling and remodelling, the two main mechanisms which allow the adaption of bone architecture and structure to create bones of suitable strength to meet mechanical demand.

Bone modelling results in the selective activation of osteoclasts or osteoblasts (but never both together) and subsequent bone resorption or formation at the endosteal or periosteal surface of bone. This results in a net gain or loss of bone material, allowing adaption of bone size and shape during growth[11].

In a long bone, growth occurs in the metaphysis with apposition at the endosteal surface resulting in an increase in bone length and apposition at the periosteal surface resulting in an increase in bone width [12].

Alongside modelling, bone remodelling repairs and renews bone tissue, ensuring the skeleton remains strong and fit for function. Whilst modelling is minimal after bone growth ceases, bone remodelling continues throughout life.

Unlike bone modelling, bone remodelling relies on a coupling of bone resorption to bone formation such that bone is resorbed and then replaced in succession (Figure 2) [11]. To achieve this, the multitude of cells involved in bone remodelling move along the bone together in a specific order as a 'basic multicellular unit'(BMU). The leading edge of the BMU contains osteoclasts which resorb the bone. Following in behind the osteoclasts are mononuclear cells which fill the resorption cavity during the transition from the resorption to formation stage of remodelling (Figure 2). Finally osteoblasts follow these two cell types, depositing osteoid into the resorption cavity before maturing into osteoclasts as the osteoid is mineralised, restoring the bone to a quiescent state (Figure 2) [11].

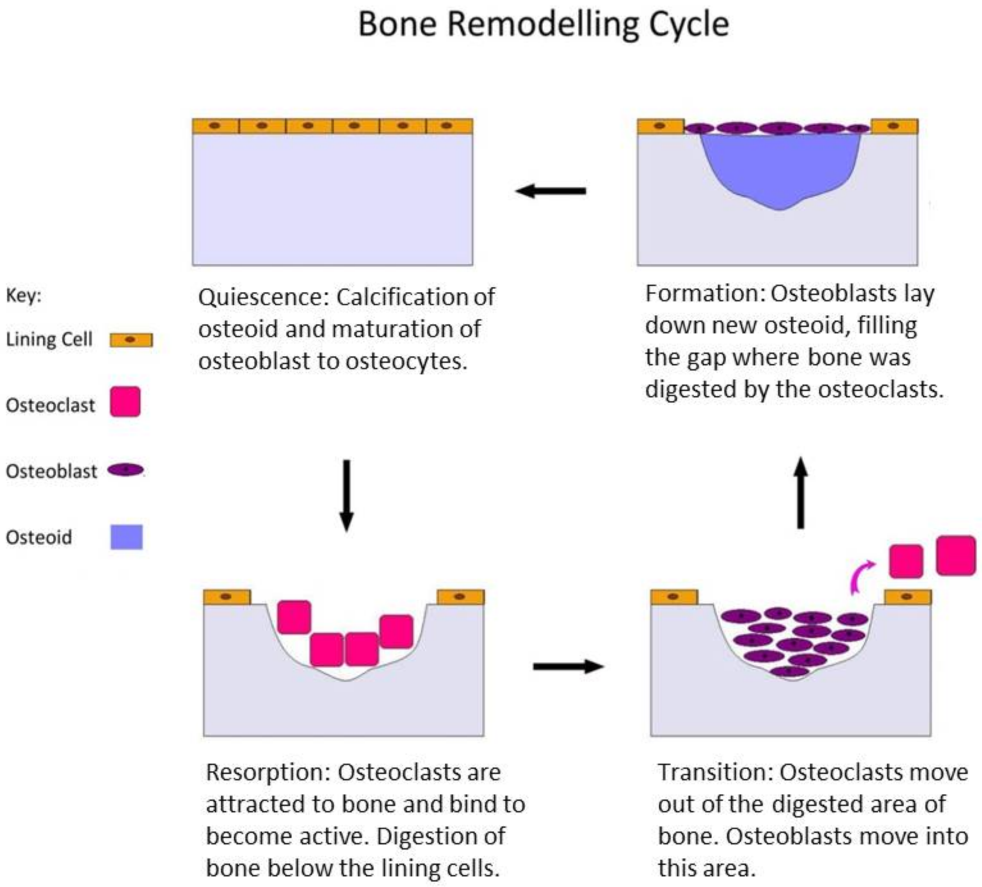

Figure 2: Bone Remodelling Cycle.
Bone is constantly undergoing remodelling. This occurs in four steps; firstly resorption is triggered by signals from osteocytes. The lining cells retract and the underlying membrane is removed. Osteoclasts are recruited to this area of exposed bone where they are activated and digest the underlying bone. Next is a transition stage where the maximum depth of digested bone is reached, osteoclasts are removed from the gap they have formed and the osteoblasts are recruited to fill this gap. Finally there is the formation stage where the osteoblasts mature into osteocytes ready for the cycle to begin again. Normally there is a balance maintained through feedback resulting in the amount of resorption being equal to that of formation, however in conditions such as osteoporosis osteocytes are activated more than osteoblasts, the balance is lost and resorption occurs to a greater extent than formation.

Tight control of the bone remodelling cycle results in equal amounts of bone resorption and formation in the healthy skeleton. This level of control is achieved through cross-talk between the cells in the BMU, through release of factors from within the bone matrix, cell-cell contact and secreted molecules.

The most well characterised interaction between the cells of the BMU is that which controls osteoclastogenesis in osteoclast precursor cells.

The initiation of BMU activity requires differentiation of osteoclasts from osteoclast precursor cells, a process that is reliant upon expression of macrophage colony stimulating factor (M-CSF) and the membrane bound receptor activator of nuclear factor κB ligand (RANK-L) [13-15]. Whilst M-CSF expression is constitutive, RANK-L requires up-regulation in order to induce the further differentiation of osteoclast precursors.

Through the RANK signalling pathway, NF- κB is released from Iκ-B and translocates to the nucleus of the pre-osteoclast resulting in phospholipase C ϒ (PLC-ϒ) signalling being up-regulated through the co-stimulation of immunoglobulin like receptors on the cells surface[11]. Together, these two signalling cascades result in the transcription of genes essential to osteoclastogenesis.

It has been proposed that targeted bone remodelling due to micro damage to the skeleton is triggered by osteocyte apoptosis which in turn triggers osteoclastogenesis through the release of M-CSF and RANK-L [16, 17].
In addition to mechanical damage, osteoblasts and bone marrow stromal cells respond to factors which promote bone resorption such as Vitamin D_3 (1α, 25-dihydrocyvitamin D_3), by up-regulating RANK-L expression, providing the stimulus for osteoclast differentiation and up-regulation of bone resorption [18].

Conversely, through the stimulation of the canonical wnt-signalling pathway, RANK-L is down-regulated and osteoprotegerin (OPG), a decoy RANK-L receptor, is up-regulated. OPG binds to RANK-L, preventing the binding of RANK to RANK-L and subsequently preventing osteoclast differentiation, down-regulating bone resorption [19].

Communication between osteoblasts and osteoclasts is proposed to be a two way mechanism, with osteoclasts having been shown to influence osteoblast differentiation and bone formation both positively and negatively. Sphingosine 1-phosphate (S1P) is secreted by osteoclasts and positively regulates osteoblast survival and migration, Ephrin signalling by direct cell-cell contact also enhances osteoblast differentiation whilst simultaneously inhibiting osteoclast differentiation and bone morphogenetic proteins (BMPs), insulin like growth factors (IGFs) and transforming growth factor beta (TGFβ) released from the resorbed bone matrix may also play a role in promoting bone formation[11]. On the other hand, osteoclasts can inhibit osteoblast differentiation through the action of Semaphorin 4D which leads to suppression of IGF-1.

Whilst osteoblasts have an established critical role in osteoclastogenesis, osteoclasts can only influence bone formation, being non-essential in the differentiation of osteoblasts and resulting bone formation[11].

The major control of osteoblast differentiation comes via the canonical wnt-signalling cascade, predominantly under the control of sclerostin which is secreted by osteocytes [20]. Sclerostin is an antagonist of the wnt-signalling pathway and as such inhibits osteoblast differentiation, however in the presence of bone formation promoting factors sclerostin down-regulation allows osteoblast differentiation and bone formation[21, 22].

This complex network of signalling provides an example of the cross talk between cells in the BMU, however the full details of the signalling underlying coupled remodelling are still under investigation.

Whilst under normal conditions, bone remodelling is a balanced process with net bone resorption equal to new bone formation, in conditions such as osteoporosis this balance is lost. Bone resorption outweighs bone formation and as a result, bone material is lost.

1.3 The effect of Hormones on the Remodelling Cycle

Differing sex hormones in the man and woman result in different skeletal development through their action on bone.

At different times in life the remodelling rate of bone differs. During adolescence bone turnover rate is at its highest with around 26% of peak bone mass being laid down during this time [23]. However, after peak bone mass is achieved in the thirties, bone mass reduces for the remainder of life.

In women, oestrogen causes fluctuations in bone remodelling, with 33% of a females peak bone mass being obtained in the first 4 years after menarche and the introduction of oestrogen secretion. At menarche there is a dramatic decrease in bone turnover which does not occur in men, thus in men, peak bone mass is obtained later and is higher than that in women [24].

Menstrual dysfunction at this time, as is prevalent in young athletes, can significantly affect the bone mass, resulting in a lower peak bone mass being achieved [25].

Throughout the adult life of a woman, oestrogen protects the skeleton from loss of mass by down-regulating bone turnover. One mechanism by which oestrogen achieves this is by inhibiting osteoclast function, preventing osteoclastogenesis whilst simultaneously enhancing osteoclast apoptosis [26-28].

After peak bone mass is reached at around the age of 35, bone loss is steady with a reported rate of 0.3% per year in both men and women.

The menopause is accompanied by a sudden increase in bone turnover in response to the loss of oestrogen signalling [29, 30]. Given the osteoclastic inhibition by oestrogen, this bone turnover is imbalanced, favouring resorption and resulting in an increase in the rate of bone loss [31].

1.4 Osteoporosis

The rapid rate of bone loss immediately after the menopause makes postmenopausal women particularly susceptible to developing osteopenia or osteoporosis, conditions which result in increased risk of ‘low energy fracture’, especially in the hip or vertebra, as well as increased mortality and morbidity [32].

The gold standard in osteoporosis diagnosis and fracture risk assessment is measurement of bone mineral density (BMD) by dual energy xray absorptiometry (DXA). Diagnosis of osteoporosis is made based on T-Score, a measure of how many standard deviations below the mean BMD for a young adult a patient’s BMD is. Fracture risk has been shown to almost double for every 1 standard deviation decrease in BMD below the young adult mean, making BMD by DXA a strong tool in identifying those at risk of future fracture[33]. However, short term changes in BMD measured by DXA are small and not dramatically different to the measurement error for DXA, making it less useful in the immediate monitoring of treatment outcomes and assessment of new therapeutics [34].

1.5 Measuring Bone Turnover

As osteoporosis is a disease with an imbalance in bone remodelling, it follows that measuring bone turnover presents an alternative option for the monitoring of patients with osteoporosis.

Markers of bone turnover allow the process of remodelling to be measured and the resorption/formation balance to be assessed. This has proven invaluable in the development of therapeutics for osteoporosis and other bone disease. Whereas expected changes of only a few percent in BMD measured by DXA result in low signal to noise ratio, markers of bone turnover show dramatic changes within the first few months of treatment [34]. This provides a good signal to noise ratio and an early indicator of changes in the skeleton in response to interventions.

Molecules released during bone resorption or formation as well as those mediating the remodelling process have been identified and validated as bone resorption and formation markers.

1.5.1 Markers of Bone Resorption

The most well used markers of bone resorption are by-products of the bone degradation process. As bone is broken down by osteoclasts, collagen degradation results in the release of C- terminal telopeptides (CTX) and N-terminal telopeptides (NTX). As such, measurement of serum and urinary CTX and NTX reflect the resorption rate of bone[34].

Alongside collagenous bone resorption markers, mediators of osteoclastogenesis and osteoclast number are also indicative of resorption, however the validation of their use in clinical study is still in development. These markers may give additional information on top of the measure of resorption activity measured with CTX and NTX, for instance markers of osteoclastogenesis such as RANK-L and OPG may be useful in characterising the mechanism of action of a drug [34].

1.5.2 Markers of Bone Formation

Three different stages of bone formation can be assessed using bone formation markers. Firstly, pro-collagen N & C terminal pro-peptides (P1NP/P1CP) are cleaved from pro-collagen as it forms collagen and act as a marker of collegen synthesis during the proliferative phase of bone formation. After the proliferative phase of formation, matrix maturation ensues, preparing the newly laid bone for mineralisation. During this period, bone specific alkaline phosphatase (BASP) is expressed in osteoblasts and is thought to mark competence for cell mineralisation. Therefore BASP provides a measure relating to bone matrix synthesis. Finally, osteocalcin which stimulates the absorption of hydroxyapatite into the bone matrix, is a measure of bone mineralisation[34].

1.6 Current Pharmaceutical Therapeutics for Osteoporosis

Pharmaceutical therapies for osteoporosis aim to redress the imbalance between bone resorption and formation that is characteristic of the condition. They achieve this in one of two ways, anti-catabolic therapies act by preventing bone resorption, whereas anabolic therapy acts by promoting bone formation.

1.1.1. Anti-Catabolic Therapy

The current treatment for osteoporosis is pharmaceutically based, with the most common prescription being bisphosphonates, an anti-catabolic class of drugs. From the analysis of bone turnover markers, bisphosphonates have been shown to reduce both bone resorption and formation markers, reflecting reduced bone turnover. With Alendronate therapy, the reduction in the bone resorption marker NTX is greater than the reduction in bone formation markers, indicative of the increase in bone density observed with bisphosphonate therapy in osteoporosis sufferers, which leads to reduced mortality and improved quality of life [35-37]. However this is not without its drawbacks as bone turnover serves a purpose in maintaining good quality bone. Long term use of catabolic therapies, whilst reducing the risk of osteoporotic fracture, has been suggested to increase risk of atypical sub trochanteric fracture due to build-up of micro damage causing a stress like fracture [38, 39]. Another perspective suggests that these fractures are osteoporotic fractures which would have occurred irrespective of bisphosphonate therapy. This reflects the presentation of the fractures which mirror those seen as typical osteoporotic fracture in all but location. Therefore the real risk for fracture may be the osteoporosis rather than the bisphosphonate used to treat the osteoporosis[40].

Even if bisphosphonate use does not increase of atypical fracture, there is still room for improvement in the 48% reduction in vertebral and 21% reduction in non-vertebral fracture risk in osteoporotic women on bisphosphonate treatment [41].

The ideal therapy would increase BMD due to an increase in bone formation, leaving a natural level of bone turnover and repair to micro damage in place.

1.1.2. Anabolic Therapy

This ideal is coming closer to being realised, with a more recent development in the treatment of osteoporosis being the use of parathyroid hormone (1-34) (PTH (1-34)), which increases BMD by increasing bone formation. Whereas bone turnover is suppressed with bisphosphonate use, bone turnover with a heavy weighting towards formation has been shown with teriparatide use.

A study into the effects of different doses of recombinant PTH (1-34) found the optimal dose to be 20µg once a day, though the study was cut short due to concerns about increased risk of osteosarcoma found in rats treated with the same form of PTH (1-34)[42]. Given that human trials of PTH(1-34) have showed no link between PTH(1-34) administration and osteosarcoma, it has been licensed for use under the name Teriparatide, with constraints in place to ensure the duration of treatment does not influence osteosarcoma risk [42].

Teriparatide acts in an anabolic manner, increasing bone turnover with a weighting towards increased bone formation for at least the first six months of use, resulting in an initial increase in bone density[43]. Whereas bone turnover markers reflect suppression in turnover with bisphosphonate use, bone formation markers show a dramatic increase, with a concurrent small increase in bone resorption markers with teriparatide therapy, confirming the opposing mechanisms of the two types of drug [44].

By cyclically administering Teriparatide, the initial formation response is capitalised upon, making Teriparatide a useful therapy for osteoporosis. Continuing investigation into the optimal mode of delivery, consequence of treatment duration and the effect of Teriparatide on patients with secondary osteoporosis is still required. It has been reported that prior exposure to bisphosphonates (as is the case in most osteoporotic patients) may reduce the potency of Teriparatide and as such, the development of new therapeutics still holds potential for greater efficacy than current drug treatments for osteoporosis [45, 46].

1.6.1 Drug Development

Alongside Bisphosphonates and Teriparatide therapy, understanding of the components of the remodelling cycle has led to the identification of potential new therapeutic targets. Odanacatib inhibits cathepsin K, a proteinase that plays a key role in the degradation of collagen during bone resorption. Denosumab is a monoclonal antibody that inhibits the action of RANK-L and in turn osteoclastogenesis. As such, both Odanacatib and Denosumab exploit different aspects of bone resorption with the end result of inhibition of bone resorption. Both compounds are currently being investigated in clinical trials, however until more is known about potential side effects, the effect of these anti-resorptive therapies on bone formation and their influence on fracture risk they are not implemented in clinical practice. As it stands, bisphosphonate therapy is still the most widely used osteoporosis treatment, with Teriparatide reserved for use in patients who cannot take bisphosphonates or have additional fractures whilst on bisphosphonate treatment [47]. The need for drug holidays when using bisphosphonates, the reduced response to Teriparatide after or with bisphosphonate use and the regulations on duration of use of Teriparatide means treating osteoporosis using pharmaceuticals is not simple and alternatives or additions to pharmaceuticals are being considered.

1.2. The Mechanostat

Along with oestrogen, the other major influence on bone remodelling and structure is mechanical load. Harold Frost was first to propose the theory of the mechanostat, a hypothesis that describes mechanically induced bone adaption in term of thresholds[48]. The upper strain threshold of the mechanostat lies above a level of strain exerted by a typical mechanical load. If a strain exceeds this threshold then bone modelling ensues, altering the bone surface shape and resulting in strengthening of bone. The lower strain threshold lies below that of a typical mechanical load and if strain does not exceed this threshold, for instance during disuse with bed rest, then bone remodelling by BMUs is activated. This results in conservation or removal of bone, with removal resulting in more porous, less strong bones reflecting the load experienced during disuse [48-50].

In order to achieve this level of control a stimulus must be detected and transduced to an effector which delivers the response to it.

The mechanical stimulus responsible for changes in bone architecture has been heavily debated since Frost’s initial hypothesis. It has become apparent that, whilst the magnitude of the strain experienced is important, it is far from the only aspect of a mechanical load that has the potential to stimulate changes in bone architecture. The frequency of mechanical load (and thus strain rate), number of cycles of loading, duration of loading and rest between cycles of loading have all been suggested to effect the osteogenic potential of a particular mechanical load [51-56]. This led to the coining of the term ‘Customary Strain Stimulus’ (CSS) to incorporate all of the above variables[57]. To account for the factors which influence the CSS (genetics, pharmaceuticals, biochemicals, age, sex and site), Skerry suggests that the mechanostat should be thought of as an integration of all of the relevant factors, which explain the response of an individual section of bone to a CSS in a particular person[57]. The impact of each individual aspect of the CSS on bone architecture is still under investigation and the optimum osteogenic mechanical stimulus is yet to be defined.

At the other end of the process, the effector mechanism is very well defined. This is the action of osteoclasts and osteoblasts in the processes of bone modelling and remodelling, as already described (Figure 2).

Finally there is the sensory detection and transduction of the stimulus which, although not thoroughly understood, is indicated to be driven by the action of osteocytes. Osteocytes are formed when osteoblasts mature into mineralised bone tissue and reside in the lacunae of osteons before ultimately undergoing apoptosis[58]. In contrast to the apoptosis of osteocytes in response to bone micro damage [16, 17], when the bone experiences strain above the mechanostat threshold for bone formation, the number of osteocytes is enhanced through the active suppression of osteocyte apoptosis [59-61]. Influx of ca^{2+} into the osteocyte and mobilisation of intracellular calcium stores in response to mechanical loading triggers multiple signalling cascades resulting in the release of adenosine triphosphate (ATP), Nitric Oxide (NO) and Prostaglandins (PGs) [62, 63]. Together, these transduction molecules act to decrease bone resorption and increase bone formation. ATP has been shown to be necessary for the release of Prostaglandin E2 (PGE_2) [64] which, along with NO, results in the inhibition of osteoclast activity at the bone surface[65-67].

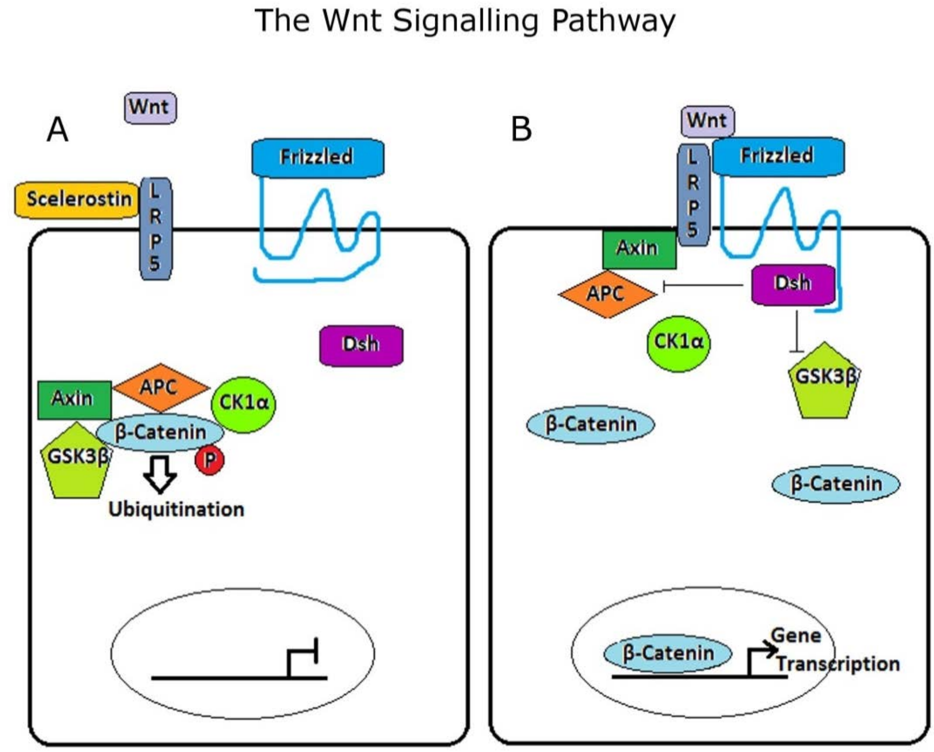

Figure 3: Sclerostin in the Wnt Signalling Pathway.

This figure shows the mechanism by which sclerostin effects bone modelling via the canonical Wnt signalling pathway. In the presence of sclerostin (A) LRP5 is prevented from binding to frizzled to form the Wnt receptor. In the absence of Wnt signalling a destruction complex is formed by GSK-3β, CK1α, Axin and APC which binds to β-catenin. This causes phosphorylation and ubiquitination of β-catenin, leading to its degradation. In the absence of sclerostin (B), LRP5 or LRP6 binds to Frizzled forming the receptor for wnt. Wnt binding to its receptor activated Dishevelled (Dsh) which inhibits the destruction complex. B-catenin is released from the complex and is free to move into the nucleus where it binds to transcriptions factors and up regulates transcription of genes associated with osteoblast differentiation.

Mechanical stimulation is also directly linked to anabolic activity. Osteocyte secretion of sclerostin is reduced in response to mechanical loading which, through the action of the Wnt/ β-Catenin signalling pathway, results in up regulation of osteoblast activity

[68]. In the presence of sclerostin, the wnt co-receptor LRP5/6 is unable to bind the wnt receptor frizzled [69] (Figure 3). This results in no signal transduction by the Wnt/ β-Catenin pathway, β-Catenin remains bound to the glycogen synthase kinase 3β (GSK-3β) complex, does not enter the nucleus and therefore does not cause gene transcription and up-regulation of osteoblast differentiation. On the other hand, when sclerostin is inhibited, wnt binds to its receptor complex, allowing signal transduction resulting in β-Catenin entering the nucleus and transcription of genes involved in the up-regulating osteoblast differentiation (Figure 3)[69]. The greater number of osteoblasts ultimately leads to increased levels of bone formation.

The opposite is observed if the lower mechanostat strain threshold is not reached, with an increase in Osteocyte apoptosis level resulting in a loss of the factors secreted by osteocytes and the up-regulation of osteoclast activity [59]. The complete mechanism of osteoclast up-regulation by osteocytes is not yet clear, however it is more than likely to include the lifting of inhibited sclerostin secretion experienced during mechanical loading and perhaps even up-regulation of sclerostin[70].

The missing link between transduction of the stimulus and effector action of modelling is the detection of the stimulus. One hypothesis for the sensory action of the osteocyte involves interstitial fluid flow through the lacunae and canaliculi. It is thought that this fluid flow imparts strain on the osteocyte which, in response, releases the factors described above that transduce the strain stimulus in order for effector activation[71, 72]. Given that the mechanical influence on bone not only relies on strain magnitude, but also strain rate, fluid flow may provide a good explanation of the sensory mechanism employed by osteocytes. Changes in strain rate would easily translate into changes in the rate of fluid flow, thus providing a change in stimulus to the osteocyte.

The theory of fluid flow as a sensory pathway also supports another hypothesis, that in the absence of mechanical loading and therefore fluid flow, sufficient nutrients cannot be delivered to osteocytes through the interstitial fluid resulting in the observed osteocyte apoptosis with disuse[23].

In addition to fluid flow, direct deformation of the osteocyte and the surrounding extracellular matrix may also play a role in mechanosensation, with strain measurements at the cellular level equating to approximately 3.95 times that detected at the macroscopic level and thus potentially providing a greater gradient of cellular deformation and initiation of micro damage at the cellular level[73]. Whether the proposed micro damage acts to induce osteocyte apoptosis or to relieve local strain, signalling for bone remodelling, is still a point of contention.

1.6.2 The Mechanostat in action – Tennis as a unilateral loading model

Despite an incomplete understanding of the process of mechotransduction, evidence for the action of the mechanostat is well documented.

Tennis players provide a good self-controlled model of the effect of unilateral loading on bone density and studies on players support the theory that the CSS (rather than purely strain magnitude) is responsible for adaption of bone geometry, as a complex skeletal response is observed in the dominant arm of tennis players. The unilateral nature of tennis removes environmental and genetic confounders, allowing the sole analysis of the influence of mechanical loading on bone strength.

Studies using DXA as a means of evaluating BMD in the playing arm of male professional tennis players revealed that, as proposed by the CSS, the increased magnitude of stain as well as the duration and number of playing sessions had an influence on BMD (Table 1). Compared to the non – dominant arm, the dominant playing arm of professional tennis players had a significantly greater BMD ($P<0.05$) [74]. This was also observed in young tennis players and a dependency on hours of tennis practice was observed in young male tennis players [75, 76]. Those that practiced 3.1 hrs /wk on average had a lower inter-arm asymmetry in BMD than those practicing in excess of 10hrs/wk [76].

In young female tennis players, the described inter-arm asymmetry in BMD is apparent from tanner stage III, the period of rapid growth and bone accrual prior to menarche [75, 77]. Two mechanisms of response have been observed during this period. Prior to puberty, bone responds to loading through periosteal apposition, conferring an increased resistance to bending, whereas after puberty, loading results in endosteal contraction which has far less bearing on bone strength [78, 79].

An increase of BMD in response to mechanical loading is suggestive of an increase in skeletal strength; therefore the above is promising evidence that exercise has potential as an effective therapy for people with osteopenia or osteoporosis. However, as the mechanostat depends upon hormone levels for its responsiveness, it is not surprising to find that the time of life when the mechanical loading occurs is another important factor influencing the potency of the effect of loading upon bone.

Adaption to mechanical stimulus continues up to peak bone mass, however in recreational postmenopausal tennis players who started playing tennis after peak bone mass was achieved, no significant difference in BMD was observed between the dominant playing arm and the non-dominant arm (Table 1) [80]. This is not to say that the mechanostat was inactive in these players as bone mineral content (BMC) was significantly greater in the dominant arm of the players, suggesting adaption of geometry to some degree (Table 1) [80].

This greater BMC in the dominant arm was also present in the professional tennis players and young male tennis players, again appearing dependent on training hours in the latter (Table 1) [74, 76]. As BMC increased to a greater degree than BMD in the dominant arms, this suggests that bone adaption occurred via alterations in bone geometry, as with increased bone size, a greater bone mineral content would not necessarily result in a change in BMD.

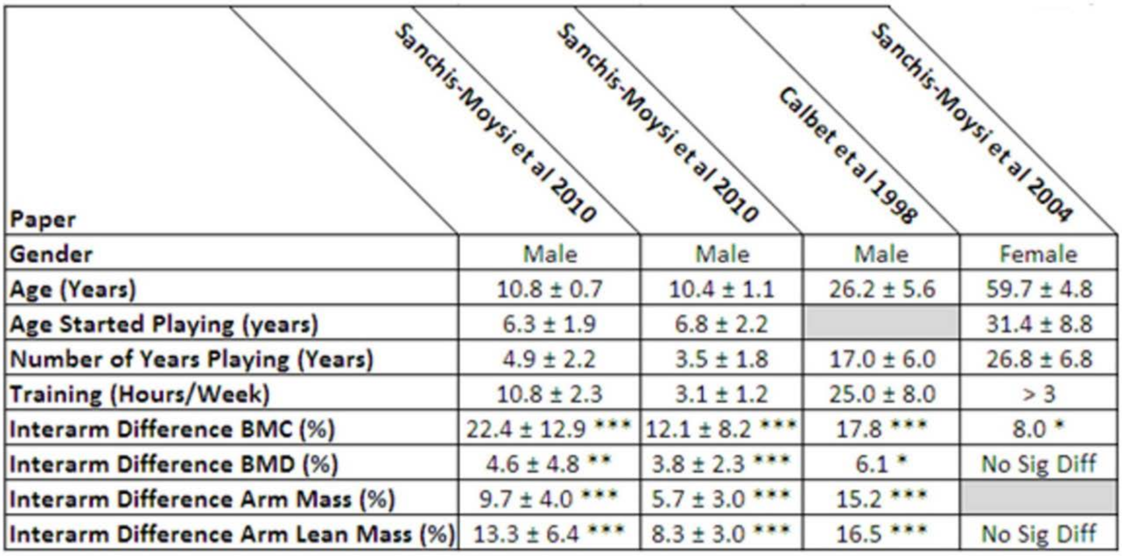

Paper	Sanchis-Moysi et al 2010	Sanchis-Moysi et al 2010	Calbet et al 1998	Sanchis-Moysi et al 2004
Gender	Male	Male	Male	Female
Age (Years)	10.8 ± 0.7	10.4 ± 1.1	26.2 ± 5.6	59.7 ± 4.8
Age Started Playing (years)	6.3 ± 1.9	6.8 ± 2.2		31.4 ± 8.8
Number of Years Playing (Years)	4.9 ± 2.2	3.5 ± 1.8	17.0 ± 6.0	26.8 ± 6.8
Training (Hours/Week)	10.8 ± 2.3	3.1 ± 1.2	25.0 ± 8.0	> 3
Interarm Difference BMC (%)	22.4 ± 12.9 ***	12.1 ± 8.2 ***	17.8 ***	8.0 *
Interarm Difference BMD (%)	4.6 ± 4.8 **	3.8 ± 2.3 ***	6.1 *	No Sig Diff
Interarm Difference Arm Mass (%)	9.7 ± 4.0 ***	5.7 ± 3.0 ***	15.2 ***	
Interarm Difference Arm Lean Mass (%)	13.3 ± 6.4 ***	8.3 ± 3.0 ***	16.5 ***	No Sig Diff

Table 1: A comparison of studies defining the influence of tennis playing on bone parameter as a unilateral model of mechanical loading.

All bone parameters (BMC, BMD, Arm Mass, and Lean Mass) have been determined using DXA and data is presented using percentage increase/decrease in the dominant vs. non dominant arm. Whilst significant increases in bone parameters were observed in younger tennis player, postmenopausal players (mean age 59.7) show little benefit is to be gained from playing recreational tennis at this age. (*-P<0.05, ** - P<0.01, *** - P<0.001).

The calculation of bone geometries using DXA scans, although possible, result in estimations[81]. However other technologies, such as magnetic resonance imaging (MRI) and peripheral quantitative computed tomography (pQCT), allow the simultaneous assessment of volumetric BMD (vBMD), BMC and bone geometry. Using pQCT it is also possible to discriminate between the type of bone (cortical or trabecular) and assess the influence of mechanical loading on each [9].

A combined study of MRI and DXA data from both male and female tennis players allowed the calculation of vBMD in the arms of tennis players at the end of adolescence (Table 2)[82]. As expected if the changes described previously are due to changes in geometry, vBMD showed no significant difference between the dominant playing arm and non-dominant arm. However BMC was still significantly greater in the dominant arm and correlated with the observed asymmetry in bone geometry from the MRI scan. 75% of the BMC asymmetry can be accounted for by asymmetry in total bone volume, confirming that the bone responds to mechanical loading by altering its geometry, not by increasing BMD [82].

The adaption of bone size in response to mechanical loading is further supported by pQCT studies which show an increased BMC but no increase in vBMD in the dominant arm of young tennis players (Table 2) [7, 9]. The cross sectional area of the humerus and radius is larger in the dominant arm of tennis players than the non-dominant arm, however the type of bone affected by the mechanical loading appeared to be site specific. At the humeral shaft and distal humerus the cortical area and cortical wall thickness have been shown to be greater in the dominant arm than the non-dominant arm. In the proximal humerus and radial shaft the total bone area, cortical bone area and marrow cavity sizes are significantly greater in the dominant arm, however the change in cortical wall thickness is little if anything [7, 9]. This ties in with the idea of multiple mechanostats, each regulating a specific site of bone, dependent upon the type of strain typically experienced at each site [57].

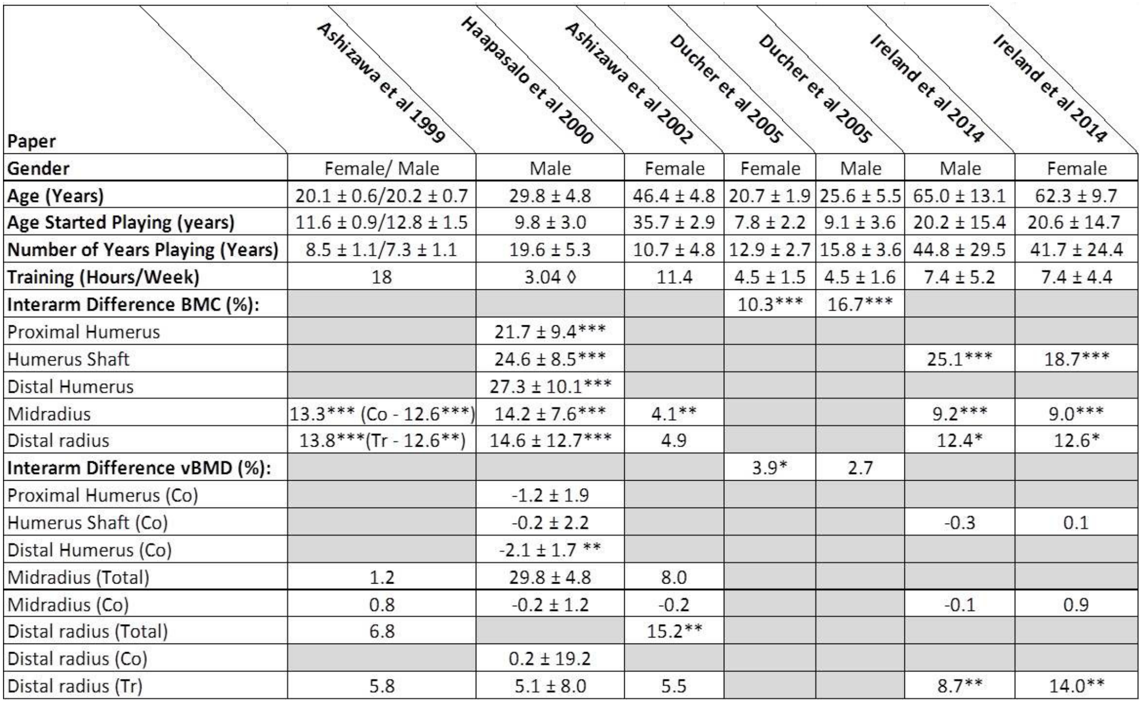

Paper	Ashizawa et al 1999	Haapasalo et al 2000	Ashizawa et al 2002	Ducher et al 2005	Ducher et al 2005	Ireland et al 2014	Ireland et al 2014
Gender	Female/ Male	Male	Female	Female	Male	Male	Female
Age (Years)	20.1 ± 0.6/20.2 ± 0.7	29.8 ± 4.8	46.4 ± 4.8	20.7 ± 1.9	25.6 ± 5.5	65.0 ± 13.1	62.3 ± 9.7
Age Started Playing (years)	11.6 ± 0.9/12.8 ± 1.5	9.8 ± 3.0	35.7 ± 2.9	7.8 ± 2.2	9.1 ± 3.6	20.2 ± 15.4	20.6 ± 14.7
Number of Years Playing (Years)	8.5 ± 1.1/7.3 ± 1.1	19.6 ± 5.3	10.7 ± 4.8	12.9 ± 2.7	15.8 ± 3.6	44.8 ± 29.5	41.7 ± 24.4
Training (Hours/Week)	18	3.04 ◊	11.4	4.5 ± 1.5	4.5 ± 1.6	7.4 ± 5.2	7.4 ± 4.4
Interarm Difference BMC (%):				10.3***	16.7***		
Proximal Humerus		21.7 ± 9.4***					
Humerus Shaft		24.6 ± 8.5***				25.1***	18.7***
Distal Humerus		27.3 ± 10.1***					
Midradius	13.3*** (Co - 12.6***)	14.2 ± 7.6***	4.1**			9.2***	9.0***
Distal radius	13.8***(Tr - 12.6**)	14.6 ± 12.7***	4.9			12.4*	12.6*
Interarm Difference vBMD (%):				3.9*	2.7		
Proximal Humerus (Co)		-1.2 ± 1.9					
Humerus Shaft (Co)		-0.2 ± 2.2				-0.3	0.1
Distal Humerus (Co)		-2.1 ± 1.7 **					
Midradius (Total)	1.2	29.8 ± 4.8	8.0				
Midradius (Co)	0.8	-0.2 ± 1.2	-0.2			-0.1	0.9
Distal radius (Total)	6.8		15.2**				
Distal radius (Co)		0.2 ± 19.2					
Distal radius (Tr)	5.8	5.1 ± 8.0	5.5			8.7**	14.0**

Table 2: A comparison of studies defining the influence of tennis playing on bone parameters as a unilateral model of mechanical loading.

All bone parameters (BMC, vBMD) were determined using pQCT or pQCT and MRI and are presented as % inter-arm difference. Significant improvements in BMC are observed at all sites measured apart from the distal radius (predominantly trabecular bone) in mature players. BMD is significantly influenced at very few sites, in contrast to the data recorded by DXA. (*P<0.05, **P<0.01, ***P<0.001.)

The site specific mechanostat theory is also well supported when we consider the mid-radius, an area rich in cortical bone. Mechanical loading results in increased cortical thickness and cortical drift, as endosteal bone resorption occurs and new periosteal bone is laid down [7]. This results in the cortical bone at the mid-radius being further from the neutral axis, which results in a bone section resistant to bending without a dramatic increase in BMD.

Although DXA is the gold standard in osteoporosis diagnosis, the data presented here suggests that the two dimensional areal BMD is not a sufficient measure when studying the effects of mechanical loading on bone. The fact that the bone grows in size in response to mechanical loading skews the BMD measurement, the greater BMD observed in the dominant arm is due to the greater BMC, not greater vBMD [7, 9].

One thing that is consistent irrespective of scan type is that the response of bone to mechanical loading is dependent on age. At all sites studied the general trend is that during growth, the BMC of the dominant arm increases in response to playing tennis and the bone geometry changes as shown above[7, 9, 74, 76, 80, 82]. In contrast, after peak bone mass is achieved the increase in BMC is no longer observed and at certain sites in the dominant arm there is even a decrease in BMC compared to the non-dominant arm[83]. This shows the adaptive response in bone size due to mechanical loading is attenuated with age.

This is not to say that exercise does not affect mature bone, in contrast to the changes in skeletal architecture seen in young growing bone, mechanical loading in mature bone results in site specific increased trabecular bone density at the distal radius, an area made primarily of trabecular bone, and increased cross sectional area in the diaphysis (Table 2)[83, 84]. It is possible that the increase in trabecular vBMD improves bone strength in the absence of the geometric changes seen in younger bones. With the decrease in BMC observed at the mid-radius it has been proposed that a type of bone mass shift occurs as part of the adaptive mechanism of mature bone, with bone mass from areas experiencing lower strains shifting to areas experiencing the highest strain[85].

It has also been observed that, after peak bone mass is achieved; endosteal bone loss outpaces new periosteal bone apposition, resulting in an absence of cortical drift and thinner cortical bone. In the dominant arm, these changes were not observed therefore it is possible that mechanical loading helps prevent age-related changes in skeletal architecture through endocortical apposition or retention [83, 84].

In female tennis players who started playing after the age of 30, BMC at the distal radius was greater (although not significantly so) in the dominant arm and combined with the greater trabecular vBMD in this area this suggests bone still adapts to strengthen itself in the areas under the highest mechanical load, albeit via a different mechanism to that observed in the growing skeleton[83].

Whilst loading is clearly beneficial to bone, accelerated bone loss after stopping participation in sport removes any benefits in BMD experienced whilst regularly exercising [86, 87]. This is well documented in a young population [86, 88], however, fragility fracture risk appears to be reduced in ex-athletes, especially if a small amount of exercise is maintained [88]. It is possible that the skeletal geometry adaption caused by exercise during bone growth is maintained throughout life and results in fewer fragility fractures later in life, making exercise a useful preventative measure for osteoporosis.

In summary, the current observations suggest that prior to reaching peak bone mass, bone responds to mechanical loading by adapting its geometry via directed modelling, resulting in a skeleton with good strength to weight ratio. With age, this response appears to become attenuated and a new adaptive mechanism which leads to the apposition of trabecular bone in response to mechanical loading is observed. Mechanical loading may also contribute to a resistance to age related cortical thinning at specific loaded sites.

Although physical activity appears to be a promising method of maintaining strong bones and reducing fracture risk in elderly people, finding a safe way of delivering the exercise to a population susceptible to fragility fracture is a challenge. Even walking, a low intensity exercise with peak strains only reaching -544 με (compression) and +437 με (tension) in the tibia[89], has been shown to result in fragility fractures at the hip if the ‘prescribed dose’ is too great [90].

1.6.3 The Mechanostat in action -Unloading the skeleton

In contrast to the effects of loading the skeleton observed in tennis players, unloading the skeleton results in marked bone loss and disuse osteoporosis[91]. During space flight, loading of weight bearing regions of the skeleton is reduced due to the loss of the effect of the earth’s gravity. This results in an uncoupling of bone resorption and formation, increased bone resorption and ultimately a decrease in BMD in astronauts [92-94]

1.6.3.1 Bed Rest as a model of unloading

In trying to tackle the bone loss experienced by astronauts, a method for simulating the effects of space travel on earth has been developed.

Changes in BMD and bone turnover markers during head-down tilt bed rest have been shown to be similar to those observed in space flight[95]. This makes bed rest an affordable, controllable model to examine the effects of different interventions on disuse osteoporosis, whether the osteoporosis is caused by space travel or other situations in which normal weight bearing activities are attenuated.

1.7 Vibration Therapy as a form of anabolic exercise

Rubin and colleagues showed whole body vibration (WBV) to have a positive influence on bone formation rates in the proximal tibia of rats and to be more successful than normal weight bearing in preventing the bone loss associated with disuse of the limb [96]. It was also shown that the magnitude of the strain induced by the vibration did not have to be as large as suggested by studies of physical activities. During physical activity strains in the tibia are generally three figures or more, with peaks as high as 2000 με [89]. It has been suggested that the magnitude of the strain engendered by an activity is a key determinant of the response of the skeleton to that activity. For instance, running is more osteogenic than walking, reflecting the larger strains generated by running. However walking is of more benefit to bone than cycling which, due to the non-impact nature of the sport, produces lower strain on the skeleton [97]. Male masters cyclists have been shown to have lower BMD than their more sedentary counterparts, who conversely do more hours of weight bearing exercise per week. This provides additional evidence to support the notion that higher magnitude strains have a greater influence over bone remodelling than low magnitude strains [98].

However, if WBV has a protective or anabolic effect on bone, there must be an alternative stimulus to the magnitude of the strain involved, as strain magnitudes in single figures have been reported to be of benefit to the skeleton when delivered via WBV. Twenty minutes of exposure to WBV at 30Hz frequency and 0.3g acceleration, five times per week produced significant benefit to bone in terms of both the number and size of trabeculae in the tibia of sheep [99]. Strain gauges attached to the tibia of the sheep recorded strains of less than 5με in response to this vibrational loading, far smaller than those found in high impact, osteogenic physical activities.

Given the small strains required with WBV to generate positive effects on bone, this type of skeletal loading has been considered as a potential intervention for both disuse and postmenopausal osteoporosis.

1.7.1 Preventing disuse osteoporosis

Using head down tilt bed rest as a model to generate disuse osteoporosis in otherwise healthy volunteers, the ability of whole body vibration to protect bone from the loss observed due to unloading has been investigated. Whilst the effects of short duration (14 days) unloading on the musculoskeletal system were not counteracted by WBV intervention, WBV has been shown to have a protective effect on bone during bed rest of 56 and 60 days [49, 100-104].

The discrepancy in findings between the short duration and longer duration bed-rest studies could in part be due to the small sample size of the short duration study. Given the short duration of the study, imaging could not be implemented as a measure of changes in bone structure and composition, as has been in the longer duration studies. Therefore a comparison between studies is reliant on early changes in biochemical markers of bone turnover being indicative of the changes seen using imaging in the longer duration studies. Additionally, the WBV intervention delivered in the short duration study required participants on both the control and intervention arm to weight bear for brief periods of time, making WBV not the sole mechanical stimulus delivered to the body during the intervention. This could lead to greater bone retention and associated changes in biochemical markers of bone turnover in the control arm of the study, perhaps rendering potential differences between control and intervention arms of the study smaller and less likely to be significant[49, 101, 102].

In contrast, the larger, longer duration studies delivered WBV interventions whilst participants remained supine [49, 102-104]. The intervention differed to the short duration study in that WBV was combined with resistive exercises. It could therefore be argued that the resistive exercises were the determining factor in the protective effect of the WBV intervention. However, whilst at distal sites there is little difference in the protective effect of resistive exercises or resistive exercises in combination with WBV, at the tibial diaphysis and proximal femur, resistive exercise with WBV was shown to have benefits above that of resistive exercise alone[104]. This suggests that WBV plays its own part in protecting the skeleton from disuse osteoporosis.

1.7.2 Preventing postmenopausal osteoporosis

WBV has also been investigated as a preventative measure or potential therapy for postmenopausal osteoporosis.

Low magnitude, high frequency stimuli have been studied in humans, both young and old, with BMD measurements tending to concentrate on the hip and spine, skeletal locations most susceptible to fragility fracture. The greatest influence of low magnitude WBV appeared to be in subjects with low BMD when the stimulus was consistent, low magnitude and high frequency, in contrast to studies of other physical activity (Table 3) [1, 105, 106]. Having said that, a study using higher magnitude vibration, yet a similar frequency to the aforementioned studies, also indicated an improvement in bone characteristics at the hip and lumbar spine[107] and there are indications that higher magnitude vibration prevents postmenopausal bone loss [108].

Varying the direction of the applied stimuli appeared to reduce the impact of WBV [109, 110], although studies that took this approach were not always in populations with low BMD, making it difficult to make comparisons and a definitive conclusion as to the cause of the lesser response. It is possible that activities other than standing result in less transmission of the stimulus to the hip and lumber spine and therefore a less marked response, as in one study which used knee extensor exercises there was an observed significant influence on hip BMD, however no influence at the lumbar spine[110].

The direction of vibration is an important aspect of research as it may be possible to specifically optimize WBV to target specific regions of the body. The use of side alternating vibration resulted in maintenance of cortical bone in postmenopausal women and, even at low frequencies, positively influenced hip BMD[108, 111]. Accelerations delivered to the lumbar spine (L3) using a side alternating platform have been shown to be greater in the lateral (side to side) direction than the vertical direction [111]. If also true at the hip, this could contribute to the observed enhancement in BMD increase at the femoral neck which is orientated in the lateral direction. The response of the femoral neck to side alternating vibration was greater than that of vertical vibration in postmenopausal women without osteoporosis (Table 3) and therefore this type of WBV may prove more effective for treatment of osteoporosis at the hip.

1.8 Vibration Therapy – Development as a Treatment for Osteoporosis

The current evidence shows the potential for WBV to provide a form of low impact physical activity that improves the bone quality in osteoporosis sufferers. The effect of WBV on BMD is also potentially greater than that currently observed (Table 3), as these are the values obtained from intent to treat analysis. If compliance is analysed, the response in the highest quartile of compliance is much greater than that reported in intent to treat analysis [1, 105]. By improving compliance, WBV could prove a very useful tool in the treatment of osteoporosis. With the increasing evidence that WBV is of benefit to osteoporosis sufferers the compliance rate may increase, especially if research into tolerability of the different frequency and amplitudes is conducted. Improving the experience of WBV treatment using audio-visual entertainment or an exercise class setting may also improve compliance.

Before WBV can be developed as a treatment for osteoporosis, there is still a lot to be understood in order to determine the optimum ‘dose’ of WBV. Currently there are few papers on the subject, each using different parameters and each with varying success (Table 3). It appears that almost unnoticeable displacement of the vibrating platform at high frequency is beneficial in preventing postmenopausal bone loss [1, 105], yet so is higher magnitude vibration [107, 108], suggesting frequency of vibration, and therefore the strain rate, is a key variable in determining skeletal response to this type of activity. The frequency of vibration within studies has not been varied greatly and comparison of different directions of vibration, i.e. vertical or side alternating has not been extensively researched in low BMD populations.

Whilst reducing fracture risk at the hip and lumbar spine is of great benefit, non-vertebral fracture risk, at sites other than the hip, is least benefitted by current treatment. Investigation of the effects of WBV on non-vertebral fracture should also be undertaken.

Paper	Rubin [103]	Gilsanz [104]	Ward [105]	Ruan [106]	Russo [107]	Torvinen [108]	Verscheuren [109]	Gusi [110]	Iwamoto [168]
Gender	Female	Female	Male and Female	Female	Female	Male and Female	Female	Female	Female
Age	PM	15-20yrs	4-19yrs	PM (WO)	PM	19-38yrs	PM	PM	PM (WO)
Vibration Type	Vertical	Vertical	Vertical	Vertical	Side Alternating	Vertical	Vertical	Side Alternating	Side Alternating (+AL)
Position on the platform	Standing	Standing	Standing	Standing	Standing	Multi-directional	Knee Extensor Exercise	Standing	Standing
Training: mins/day days/week	2x10m/d, 7d/w	10m/d, 7d/w	10m/d, 5d/w	10m/d, 5d/w	1-2m/d, 2d/w	2-4m/d, 3-5d/w	max 30m/d, 3d/w	6x1m/d, 3d/w	4m/d, 1d/w
Duration of Study (months)	12	12	6	6	6	8	6	8	12
Type of Control	Placebo Platform	No Activity	Placebo Platform	No Activity	No Activity	No Activity	RES/No Activity	Walking 1h/d, 3d/w	Alendronate
Frequency of Vibration (Hz)	30	30	90	30	28	25-45	35-40	12.6	20
Acceleration of Vibration (g)	0.2	0.3	0.3		0.1-10	2-8	2.3-5.1		
Displacement of Vibraiton (cm)	0.0055	<0.0050		0.5	Varied by feet separation	0.2		3	0.07-0.42
Scan Type	DXA	CT and DXA	QCT	DXA	pQCT	pQCT and DXA	DXA	DXA	DXA
Change in BMD (WBV vs Control) (%):									
Hip	(+)2.17 ◊	(+)2.00 ◊		(+)4.9*		NSD	(+)1.51*/ (+)1.53 **	(+)4.3**	
Femoral Neck									
Lumbar Spine	(+)1.50 ◊	(+)2.30* ◊	(+)4.70Δ	(+)6.20*		NSD	NSD	NSD	NSD
Tibia			(+)17.70 Δ						
Radius						NSD			
Trabecular BMD			SD at Tibia		NSD				
Cortical BMD			NSD		Maintained vs Lost				
Musculoskeletal Improvements				Less chronic back pain	Muscle Power and Velocity	Vertical Jump Height	Muscular Strength	Balance	Less chronic back pain

Table 3: A comparison of WBV studies using both DXA and pQCT.

Data is reported as percentage difference between WBV groups and controls. Whether a study reports WBV to be beneficial to bone depends upon many variables shown within this table. People with low BMD before treatment appear to benefit from WBV [[1]] whereas subjects with normal BMD show little response [108].

The type of WBV also influences the response of bone to this type of mechanical loading with side alternating WBV having a greater influence at the hip than the lumbar spine. By altering the frequency and amplitude of the WBV the response of bone is altered dramatically, with low amplitude high frequency stimuli appearing to be most osteogenic. Compliance with this type of exercise regimen varies greatly and at 85% compliance much greater benefit of WBV is observed [103,104] (*$P<0.05$, **$P<0.01$, ***$P<0.001$, ◊ - Response increases with compliance, Δ-Compliance has no influence, PM – Postmenopausal, WO-With Osteoporosis, NSD-No significant difference, AL – with alendronate).

2 Chapter Two: Aims and Objectives

2.1 Rational for the Methodology

To date, studies into the impact of Whole Body Vibration (WBV) on the skeleton have used an array of stimuli of differing frequency, amplitude, mode (vertical or side alternating), duration and repetition. Whilst this approach has formed a case for the potential use of WBV as an intervention for osteoporosis patients, currently there are many small amounts of research into a large number of different WBV stimuli.

If WBV is to be implemented as an osteoporosis treatment, an optimal 'dose' of WBV needs to be determined. In order for this to be developed, more needs to be known about the impact of the differing settings and modes of vibration used in the current research.

Given the apparent association between strain magnitude and the osteogenic potential of an activity, measurement of the strain induced during WBV is a feasible way to assess the impact of different WBV stimuli [89, 97, 112]. Previous work quantifying the strain induced by different physical activities has focused on the strain at the tibia, an area of bone with relatively easy access making application of strain gauges to the bones surface minimally invasive.

Whilst strain measurements will be made at the tibia, in keeping with previous reports of in vivo strain, the sites of interest in terms of osteoporotic fracture are the hip and lumbar spine [32]. Therefore a means of assessing the impact of the different WBV stimuli at these sites is also required. As applying strain gauges at these locations would greatly increase the invasiveness of the surgery performed, motion capture markers are used to gain a measure of the WBV stimuli at these locations. The motion capture markers are skin mounted and so, whilst there is potential for skin movement to introduce error into the measurements, this approach allows a comprehensive assessment of the WBV stimulus throughout the body [113]. Previous use of motion capture during whole body vibration has produced clear waves of movement corresponding to the input whole body vibration signal [114] and whilst the absolute displacement value may be subject dependent [113], normalised transmission data may serve as a more informative comparison measure. Alternative techniques for the assessment of the WBV stimuli such as strain gauge measurements or bone pin mounted motion capture markers are more invasive and so, whilst these techniques avoid the assumptions associated with data collection from skin makers, compromises in the number of data collection sites must be made. With the planned techniques, the data recorded at the tibia both at the bone surface and on the skin may be used to assess the influence of soft tissue artefact at the tibia during whole body vibration.

2.2 Aims and Objectives

The overall aim of this study is to better characterise the impact of WBV on the human skeleton and to put WBV stimuli into the context of other habitual locomotor activities which are known to be osteogenic or non-osteogenic. With knowledge on the similarities and difference between WBV and other habitual locomotor activities, it is hoped this work will form a basis for informed choice of WBV stimuli in future investigations into WBV as an intervention for osteoporosis.

In order to achieve this objective, we aim to:

- Investigate the transmission of an array of WBV stimuli to locations throughout the body and assess the influence of the frequency and amplitude of the input stimulus on the transmission
- Assess the transmission of differing WBV stimuli to the hip and lumbar spine
- Determine whether a unilateral loading model of WBV can be established
- Compare the strain and strain rate induced at the tibia by the different WBV stimuli and during osteogenic and non-osteogenic activities

3 Chapter Three: Materials and Methods

3.1 Study Population

Six participants aged between 18 and 51 years at the consent visit, were recruited to the study. Participants were ambulatory, generally healthy (as assessed by medical history and physical examination) and were physically willing and able to undergo all study procedures. All participants had a BMI less than 30 and a BMD measured by DXA between +/- 2.5 SD of the young normal range. The characteristics of the six participants included in the study are detailed in Table 4.

Participant	Age	Height (m)	Weight (kg)	BMI (kg/m^2)	T-Score	
					Spine	Hip
1	22	1.87	76	21.7	-1.3	-0.4
2	22	1.73	72.1	24.2	-0.9	0.6
3	51	1.83	96.8	28.9	-0.3	0.3
4	28	1.77	69.2	22.1	-1.3	-0.3
5	18	1.83	71.2	21.4	-1.2	-0.5
6	33	1.84	76.1	22.5	-0.2	0.5

Table 4: Summary of Participant Characteristics.

Participants were excluded from the study if they met any of the exclusion criteria (Table 5).

3.2 Measuring Human Movement

In a clinical setting, qualitative observational assessment of movements by trained practitioners is sometimes sufficient for diagnosis and treatment of movement disorders; however this depends on subjectivity and the human eye is not always capable of identifying subtle differences in gait associated with disorders [115]. To overcome this shortcoming, advances in technology have allowed quantitative measures of human movement to be developed.

Inclusion Criteria	Exclusion Criteria
Aged 18-50 years	Previous diagnosis of osteoporosis
Generally Healthy	History of fracture of the spine, hip, leg or foot
Ambulatory	History of bone or joint disorders affecting the shoulders, spine, pelvis, legs or feet
BMD (by DXA) at the lumbar spine and hip within ± 2 SD of the young normal range	Use of the following medications within the last 2 years: Bisphosphonates, Fluoride (execpt use for oral hygeine), Strontium, Terparatide, Other bone agents), Steroids
BMI < 30	Ongoing conditions or diseases known to cause secondary osteoporosis
	Malabsorption syndromes
	Known disorders of calcium metabolism
	Known history of thyroid disease
	Osteomalacia
	Paget's disease
	Diabetes
	History of cancer within the previous 5 years
	Epilepsy
	Ongoing conditions or use of medications that may impair vision or balance
	Alcohol abuse or illicit drug use
	Pegnancy or currently trying to conceive (women only)
	Inability to give informed consent
	Known hypersensitivity to penicillin or cephalosporins
	Known hypersensitivity to the local anaesthetic lignocaine

Table 5: Inclusion and Exclusion criteria

3.2.1 Techniques for Motion Analysis

Quantitative techniques, which aim to accurately measure aspects of motion without impeding normal human movement, have the potential to help diagnose neuromuscular and skeletal disorders, as well as shaping and monitoring treatment[115].

The complete assessment of movement includes two different types of measure. Kinematic measures define the position, orientation, velocity and acceleration of movement whilst kinetic measures define the forces causing a movement and generated as a reaction to movement [116]. By combining kinematic and kinetic data, detailed analysis of human movement is attainable.

The measurement of kinematics over extended periods of time has been achieved using accelerometers, devices designed to measure the acceleration of a body as a result of a change in force placed upon it. Different activities have specific patterns of kinematics allowing data from accelerometers to provide detailed information on the type and amount of physical activity undertaken [117]. Given the small size and relatively low power required for function, accelerometers have been useful for analysing typical activity levels of individuals over multiple days, weeks and months [118].

Accelerometers, positioned at specific landmarks throughout the body or attached to a bite bar, have also been used to investigate the transmission of vibration experienced when driving a vehicle and using a wheel chair [119-122].This technique has also been applied to assess the transmission of whole body vibration delivered by specially designed vibration platforms [123-125].

Accelerometers are limited to measuring kinematic data and without additional recordings to determine the forces causing the resultant acceleration, kinetic information is not obtained rendering analysis of the movement incomplete. In previous studies, occupational whole body vibration transmission was analysed at set hip flexion angles, monitored using light emitting diodes [119]. However, whilst standing on whole body vibration platforms, the ankle, the knee and hip joint are all influenced by the vibration. Given the higher frequency vibrations delivered by WBV platforms, predefining a set joint angle to maintain at multiple joints would be difficult for the participants and could potentially lead to conclusions based on unnatural positions which would bear little relevance to whole body vibration in a clinical setting.

Thus, in this instance it is of more use to measure changing joint angles throughout a period of whole body vibration. To achieve this, the most widely used quantitative approach is motion capture, a technique based on video recording and reconstruction of reflective markers positioned on the skin. Infra-red light reflected from markers positioned at anatomical landmarks is detected by cameras and mathematical algorithms allow reconstruction and assessment of kinematic data at these positions, a procedure which unlike accelerometry requires no wire attachments which may impede motion.

3.2.2 The Principle of Motion Capture

The Vicon motion capture system is designed to reconstruct 3-dimensional images from videos recorded on specialised cameras. MX-F40 cameras are positioned around the gait laboratory such that their field of views overlap, creating a 3-dimensional capture volume in which at least two cameras can record images in any distinct area.

Reflective markers positioned on the object to be reconstructed readily reflect the infra-red light emitted by the MX-F40 cameras, back onto the camera’s detector.

Reconstruction of the original object in 3-dimensions relies on similar principles to those used by the eyes and brain to see the world in 3-dimensions.

If a single camera is used to detect the reflected light, the image can only be reproduced in 2-dimensions. The 2-dimensional reconstruction relies on the colinearity condition being met. The colinearity condition relates the object of study to its corresponding image and requires any point on an image to be linked, via a straight line, which passes through the camera’s focal point, to the corresponding point on the original object (Figure 4) [126].

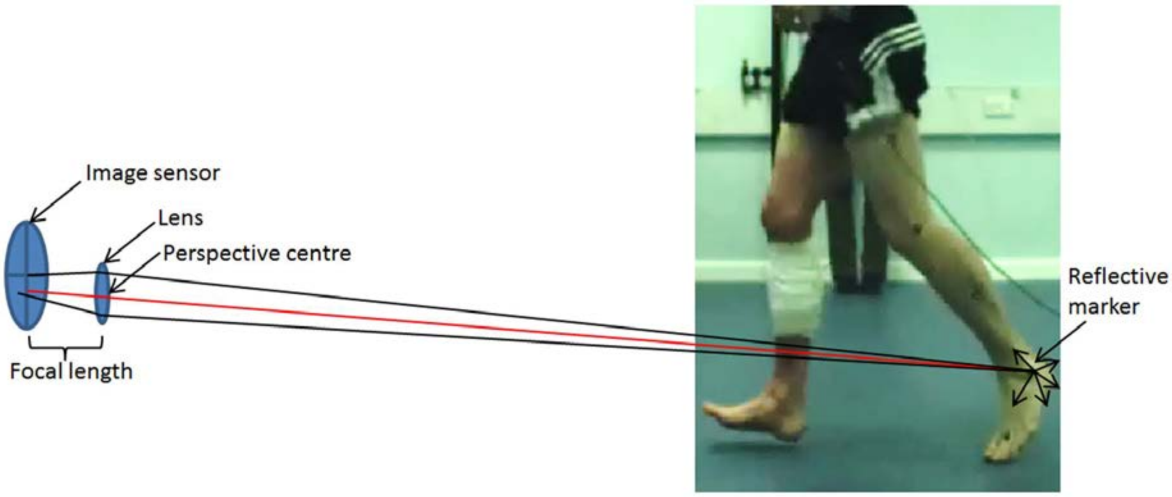

Figure 4: The colinearity condition.

Light rays that are reflected off the marker placed at the ankle pass through the camera lens and are projected onto the image sensor. For the majority of the light rays hitting the lens, diffraction causes the bending of the wave of light towards the image sensor. However, for any rays passing through the perspective centre, diffraction does not occur and the projection of the light ray onto the image sensor forms a straight line between the image sensor, lens and reflective marker.

This allows detection of a marker in a certain direction; however the distance from the detection plate to the marker is still unknown.

To resolve this distance a second camera must also detect a reflection from the same marker at the same time. The marker can then be 3-dimensionally reconstructed according to the coplanarity condition. The coplanarity condition allows multiple images to be related to each other and requires that the point on the object, the focal points of the cameras and the corresponding points on an image all lie in the same plane(Figure 5) [126].

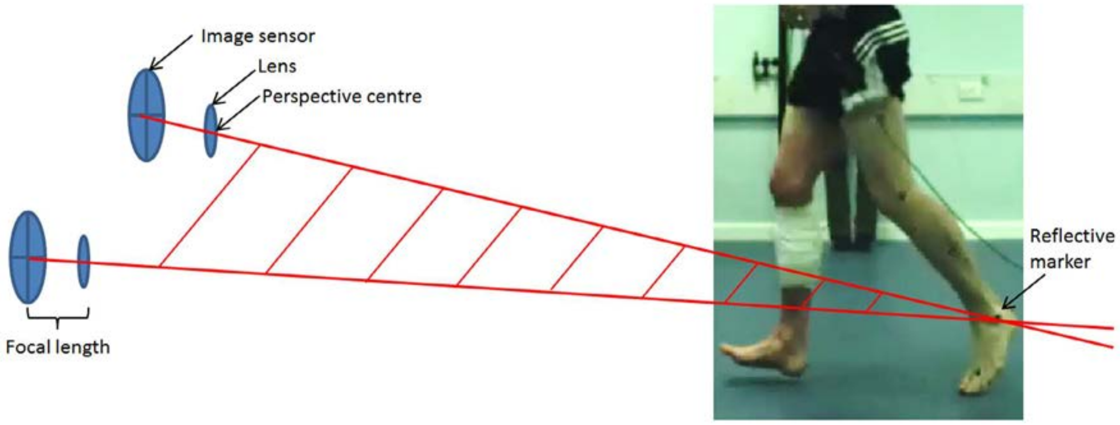

Figure 5: The coplanarity condition.

Light reflected from the ankle marker passes through the perspective centre and is projected onto the image sensor of two cameras (fulfilling the colinearity condition). If the projected images and perspective centres of both cameras, along with the reflective marker, lie in the same plane then the coplanarity condition is fulfilled. This enables the three dimensional position of the reflective marker to be calculated based on the intersection point of the two rays of reflected light.

Assuming the two cameras share a common plane and the reflected light obeys the colinearity condition, the two beams of reflected light will intersect at the markers position. By projecting the reflected light back to the intersection, the distance between the object and image projected on to the cameras image sensor can be resolved and a 3-dimensional image reconstructed.

3.2.3 Calibration of the Motion Capture System

Before the capture of any 3-dimensional images, the cameras need to know their exact position relative to a given 'origin' (external orientation) and their orientation (pose) relative to each other (internal orientation). In Vicon Nexus, this is achieved by a two stage calibration procedure called Dynacal. The result of the Dynacal process is calibration of the internal and external orientations of the cameras within the system.

Calibration of the internal orientation of the cameras allows correction for distortion and determination of the distance between image and object during 3-dimensional reconstruction. The external orientation establishes where in the capture volume a given camera is relative to the defined origin.

3.2.3.1 Dynamic Calibration

The initial step in the Dynacal calibration procedure determines the relative pose of the cameras. A wand with reflective markers of specific separation is waved whilst being carried throughout the capture volume until each camera has captured thousands of images of the wand[127]. The 3-dimensional position of the reflective markers is stored as pairs of 2-dimensional images across multiple cameras. The cameras with the best distribution of overlapping marker recordings are chosen as a ‘seed’ for calibration and their relative pose is determined. The calibration procedure continues by including uncalibrated cameras with recordings that overlap with the calibrated cameras. Once the relative pose of all of the cameras in the set-up is established, the 3-dimensional co-ordinates of the wand markers are determined and the length of the wand calculated. The calculated length of the wand is compared to the true length of the wand (a value stored in the user-set.cro file within Vicon Nexus). The dynamic camera calibration is adjusted until the length of the wand is correct, ensuring accuracy of the internal orientation of the cameras.

3.2.3.2 Static Calibration

The second step in the Dynacal calibration determines the origin and direction of the axes within the capture volume. An L-shaped object with reflective markers is placed within the capture volume and a brief recording made.

The L-shaped calibration object has four reflective markers attached, three form a straight line and one is offset. Two of the three markers forming the straight line are significantly closer together, making all four markers uniquely identifiable from the specified spacing in the user-set.cro file[127].

The recording of the calibration object is reconstructed using the camera parameters established in the dynamic phase of calibration. A line of best fit is plotted through the three markers forming a straight line, defining the first of the three axes. A second line perpendicular to the first and passing through the fourth marker defines the second axis and the third axis is defined as that which is in the same plane as, but perpendicular to the second axis.

3.2.3.3 Knee Alignment Device Calibration

Once the cameras within the Vicon Nexus system can accurately determine the 3D position of the reflective markers with reference to a capture volume origin, recordings of human movement can be performed. However, an additional calibration procedure to define the plane of flexion of the knee can be performed using a knee alignment device (KAD) [128, 129]. Static KAD calibration creates a virtual marker at the knee joint centre from which the axis of flexion is determined. By comparing the transverse alignment of this axis with the transverse alignment of the thigh and tibia markers, thigh and shank rotations correcting for misalignment of thigh and tibia markers are calculated and applied to all recordings made for the subject. This means that application of thigh and tibia markers, a difficult procedure to achieve accurately, can be corrected using the calculated rotations. This ensures accurate alignment of the knee and ankle flexion axes during motion capture recordings.

During the KAD calibration it is assumed that the ankle and knee flexion axes are parallel, however, if this is not the case, values for tibial torsion can be entered manually to the Vicon nexus system to correct the alignment of the axes [129].

3.2.4 Considerations for a clean reconstruction

Assuming that a good calibration procedure has been performed, as outlined in section 3.2.3, marker reconstruction from the motion capture data recorded should result in very few missing bits of data. However, in some cases, for instance as the arm of the participant obscures a motion capture marker such that fewer than two cameras can see it at a given moment, data is incomplete resulting in gaps in the data.

3.2.5 Gap Filling

During post processing of the motion capture data these gaps can be filled using two different approaches depending upon the length of the gap. In clinical gait analysis within Sheffield Teaching Hospitals, gaps of up to 10 frames are filled using a spline fill, gaps of 10-40 frames are filled using pattern fill and great consideration is given to filling gaps of more than 40 frames [130] (Chapter 10.2.1).

As data is collected with a sampling rate of 100Hz, this equates to gaps of 0.1seconds being filled using spline fill, gaps of 0.1-0.4s being filled using pattern fill and gaps greater than 0.4s generally being considered as unacceptable for filling, with subsequent system recalibration required. The same time periods will be applied with respect to gap filling technique in this study, however the sampling rate of recordings will be 300Hz, therefore this will equate to gaps up to 30 frames being filled using spline fill, 30-120 being filled using pattern fill and anything above 120 frames being excluded from analysis.

Filling gaps using spline fill results in a trajectory interpolation based on the marker positions for the marker with the missing data recorded at either end of the gap. Using pattern fill results in a trajectory copied from another marker and therefore makes the assumption that the second marker follows follow a similar trajectory to the trajectory of the marker with the missing bit of data.

3.2.6 Motion Capture - Study Protocol

The Vicon motion capture system used for this study comprised 8 MX-F40 cameras positioned around the gait laboratory at the Northern General Hospital covering a capture volume of 77m^3 (Chapter 10.3.1). Calibration of the system required 3000 data points to be captured by each camera during dynamic calibration. Data acquisition was made using Vicon Nexus software recording at a rate of 300Hz with a minimum of three cameras required to start a trajectory and two to continue a trajectory. Reflective markers were positioned on 21 anatomical landmarks throughout the body (Figure 6).

In the analyses markers are referred to as either in the lower limb (Anterior superior iliac spine, thigh, knee, tibia, ankle, heel, and toe) or in the torso (Sacrum, T10, T2, manubrium, acromion, and Forehead).

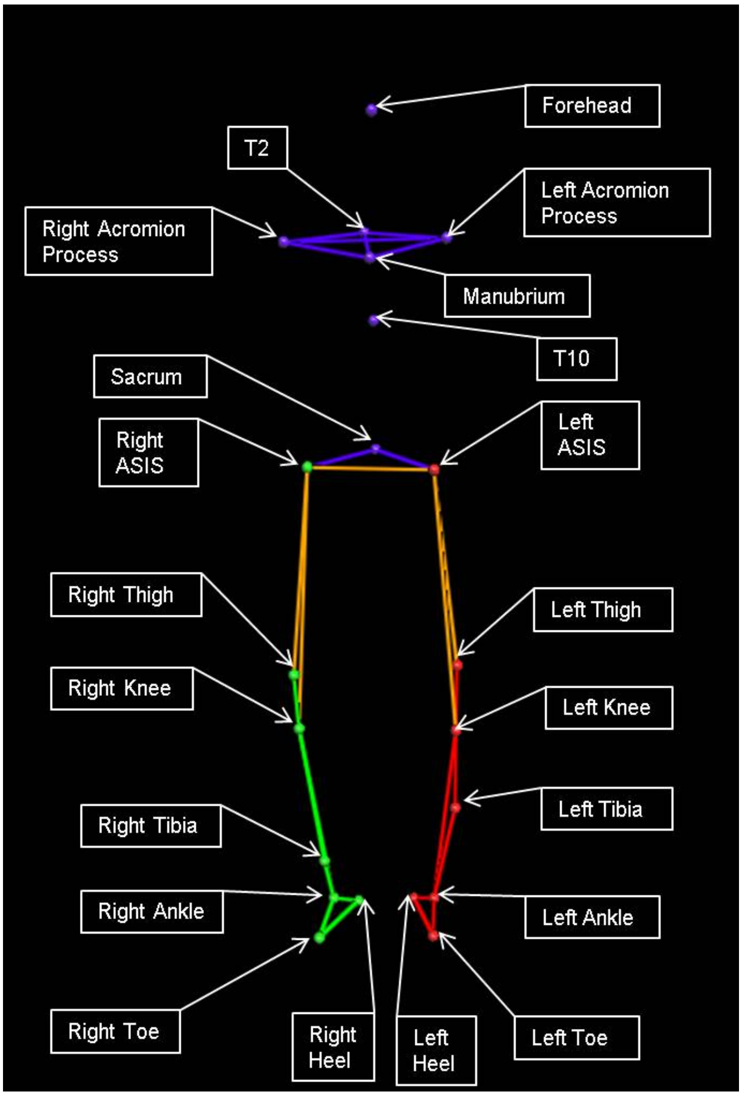

Figure 6: Reflective marker locations.

Positions of the 21 reflective motion capture markers placed at anatomical landmarks throughout the body. ASIS = Anterior Superior Iliac Spine. T2 and T10 refer to the second and tenth thoracic vertebrae respectively.

3.3 Strain Measurements

3.3.1 Stress and Strain

Strain (ε) is defined as the change in length of a material in response to a stress (σ) experienced by the material. Stress is defined as the force per unit area experienced by a material.

The stiffness of a material can be characterised as a material's resistance to deformation, and is defined mathematically in Equation 1, which brings the stress/strain relationship together, introducing the stiffness (Young's Modulus, E) of a material [131].

Multiple characteristics of bone tissue, from the composition of the collagen and relative quantity of minerals within the bone to the geometrical shape of the bone, collectively determine its strength and stiffness [132].

The stiffness of a material influences the stress / strain relationship and therefore how much deformation will occur when a stress is applied.

Equation 1: Stress, Strain and Young's Modulus

$$\varepsilon = \frac{\Delta L}{L} \quad \sigma = \frac{F}{A} \quad E = \frac{\sigma}{\varepsilon}$$

(L=length, F=Force, A=Area, E=Young's Modulus, σ=Stress, ε=Strain)

The strain at a point in a section of material can be compressive, tensile or shear. A Tensile strain describes a strain whereby a materials length has increased due to tensile forces being applied to it. Conversely a compressive strain describes a strain whereby the materials length has shortened due to the compressive forces placed upon it. Shear strain describes the deformation of a material resulting in a change in angle between two planes which were previously perpendicular [131].

Equation 2: Compressive and Tensile Strain

$$\varepsilon_C = \frac{L - L_o}{L_o} = -\frac{\Delta L}{L}$$

$$\varepsilon_T = \frac{L - L_o}{L_o} = \frac{\Delta L}{L}$$

(ε_c = compressive strain, ε_T= tensile strain, L=final length, L_o = original length)

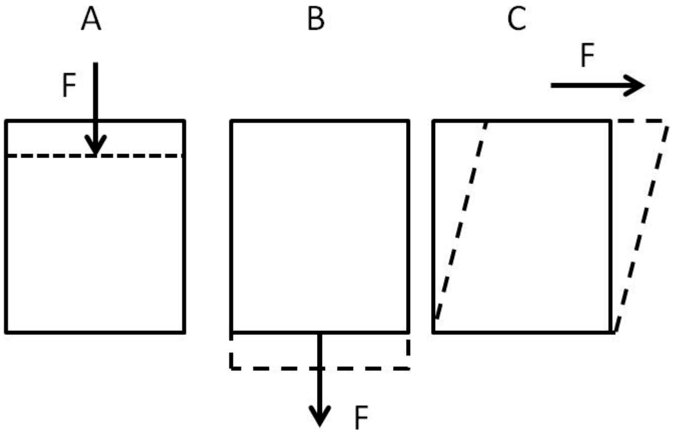

Figure 7: Examples of strain conditions.

Solid line indicates the initial state, dashed line indicates final state, F= Force. A) Compression – the length of the material is reduced due to the force acting upon it. B) Tension – the length of the material is increased due to the force acting upon it. C) Shear – the angle between the two planes is changed from perpendicular.

The strain measured at a particular point on a material is dependent on the direction in which it is measured relative to the forces acting at that point. The principal strains are the strains normal to the forces acting on the point of measurement when the shear forces acting at this point are equal to zero [131]. They represent the maximum compressive and tensile strains acting on that point due to a given force.

3.3.2 Strain Transformation

To determine strains in directions that are not normal to the forces experienced at the point of measurement, a strain transformation is required. This relates the measured strain to the principal strain (Figure 8). For instance, if the forces acting on the point of measurement were normal to the direction of measurement then the principal compressive and tensile strains would be measured (Figure 8: A). However, if the same forces were acting n a point of measurement at 45 degrees from the direction of measurement, then the measured strain would be shear (Figure 8: B). The strain transformation is not limited to normal and 45 degree strains, but relates strain measured in any direction relative to the principal strains acting at the point of measurement.

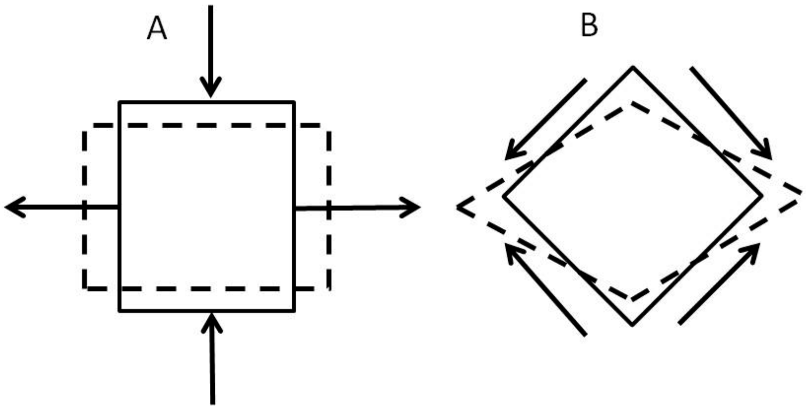

Figure 8: Strain Transformation.

When the strain is measured normal to the direction of the forces acting on the point of measurement, compressive and tensile forces are measured (A). As there is no component of shear strain and these strains are normal to the forces at the point of measurement, they are defined as principal strains. However, if forces acting in the same direction were applied to the material orientated 45 degrees from normal then the measured strains would be shear (B). The strain transformation relates the strain recorded in any direction at a point on a material to the principal strains at that point.

3.3.3 Mohr’s Circle

The strain transformation can be represented in Mohr’s circle, a visual representation of all the possible strain measurements at a given point on a material (Figure 9). The horizontal axis on which the circle is plotted represents compressive and tensile strain whilst the vertical axis represents positive and negative shear strain.
The principal strains are represented by the extremes of Mohr’s circle along the horizontal axis (Figure 9: ε_1 & ε_2). The maximum shear strain is represented as the radius of Mohr’s circle at point A (Figure 9: A). For an arbitrary measurement angle θ between 0 and 45 degrees from normal, the strain can be determined from a point on the circumference of the circle. By measuring twice the angle of measurement from normal around the circle (Figure 9: 2θ) the strain can be read from the circumference of the circle.

The principal strains can be determined from strain measurements made using rosette strain gauges, which measure strain in three different directions (Chapter 3.3.4). Mohr’s circle can be plotted using these measurements. Starting with a horizontal axis, three lines are drawn intercepting the axis at the magnitude of the measured compressive or tensile strains at each strain gauge element (Figure 9: ε_a, ε_b, ε_c). A point along the line in the middle of the three is defined to represent the origin of the rosette strain gauge (Figure 9: O). The configuration of the strain gauge is drawn around this point, with the vertical axis acting as a starting point for measurement of the angles between the element of the rosette strain gauge which recorded ε_c and the other two elements (Figure 9: α, β). Two lines at these angles and extended to intercept the lines ε_a and ε_b (Figure 9: C, D). By drawing a circle incorporating the origin (O) of the strain gauge and the two intercepts (C & D), Mohr’s circle is established and the principal strains can be determined.

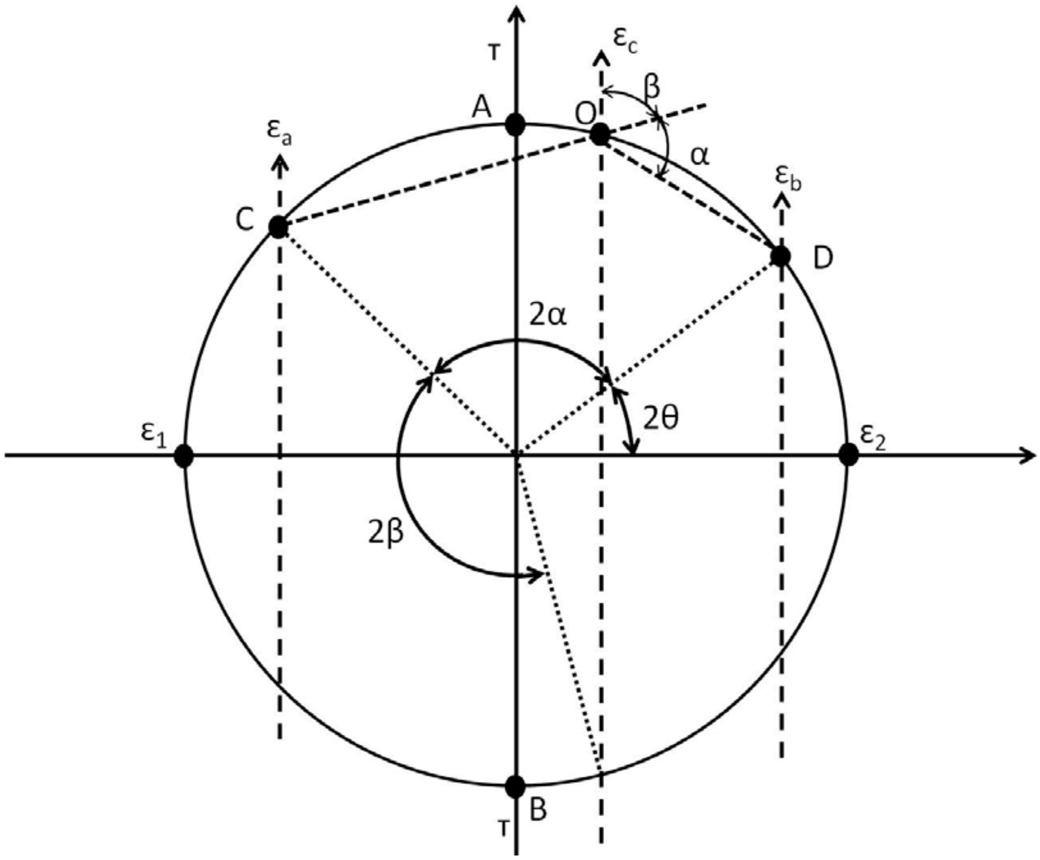

Figure 9: Mohr's Circle.
Principal strains are found at the extremes of the horizontal axis of the circle ($\varepsilon_1, \varepsilon_2$). The maximum shear strain can be found at the extremes of the vertical axis of the circle (A, B). The strain in direction θ degrees from normal can be found from the circumference of the circle 2θ from the horizontal axis. Mohr's circle can be drawn based on strains recorded using a rosette strain gauge (ε_a, ε_b, ε_c). Based on the angle between the three elements within the strain gauge (α, β), Mohr's circle can be defined. Mohr's circle is drawn with a circumference that intercepts a defined origin (O) and the points at which lines extending from the origin at the angles between the elements intercepts the lines representing the strain at the other two elements (C,D).

The association between the strain gauge measurements and the principal strains can also be represented mathematically allowing computation of the principal strains directly from strain gauge recordings (Equation 3).

Equation 3: Principal Strain Equation

$$\boldsymbol{\varepsilon_1}, \boldsymbol{\varepsilon_2} = \frac{\boldsymbol{\varepsilon_a}+\boldsymbol{\varepsilon_c}}{\mathbf{2}} \pm \frac{\mathbf{1}}{\sqrt{2}}\sqrt{(\boldsymbol{\varepsilon_a}-\boldsymbol{\varepsilon_b})^2+(\boldsymbol{\varepsilon_b}-\boldsymbol{\varepsilon_c})^2}$$

$\varepsilon_1, \varepsilon_2$ = Principal Strains, ε_a, ε_b, ε_c = Strains recorded using a rosette strain gauge

3.3.4 The Strain Gauge

In order to determine the Principal strains acting on a structure the strain must be recorded on the surface of the structure. The most commonly used instrument for making strain recordings is a strain gauge, a device which relays a change in length as a change in resistance and thus allows calculation of strain.

3.3.4.1 Single Element Gauge

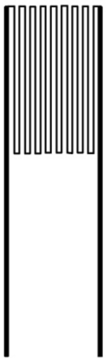

Figure 10: A single strain gauge element comprised of wire formed into a grid.

Each element of a strain gauge is comprised of a basic unit made of wire formed into a grid (Figure 10). The gridded section of the strain gauge is bonded directly onto the surface of the material of interest and therefore, any deformation of the material surface to which it is bonded are transmitted into deformations of the wire.

A strain gauge is an electrical device and therefore Ohm's Law applies to the strain gauge wire. Ohm's Law states that the voltage travelling down a wire is dependent upon the current in the wire and resistance of the wire (Equation 4).

Equation 4: Ohm's Law

$$V=IR$$

V=Voltage, I=Current, R=resistance

As the surface of the material and subsequently the strain gauge wire is deformed due to stress placed upon it, the length and cross sectional area of the strain gauge wire is changed. Under tension the wire becomes elongated and the cross sectional area is reduced whilst under compression the opposite is true. As the cross sectional area and length of the wire is altered, so is the resistance of the wire (Equation 5), resulting in a change of output voltage from the strain gauge.

Equation 5: Resistance

$$\mathbf{R} = \boldsymbol{\rho}.\frac{\mathbf{l}}{\mathbf{A}}$$

R= resistance, ρ= resistivity, l=length, A=cross sectional area

3.3.4.2 Rosette Strain Gauge

The rosette strain gauge is made up of 3 strain gauge elements (Figure 10), each of which detects strain.

Orientation of the individual strain gauge elements with respect to each other can vary, with planar gauge elements on the same plane or stacked gauge elements stacked one on top of the other. Delta strain gauge elements record strain in directions separated by 60 degrees, however the elements in the rectangular rosette strain gauge used in this study are aligned 45 degrees from each other (Figure 11), delivering information on the strain experienced in 3 different planes of a material[133].

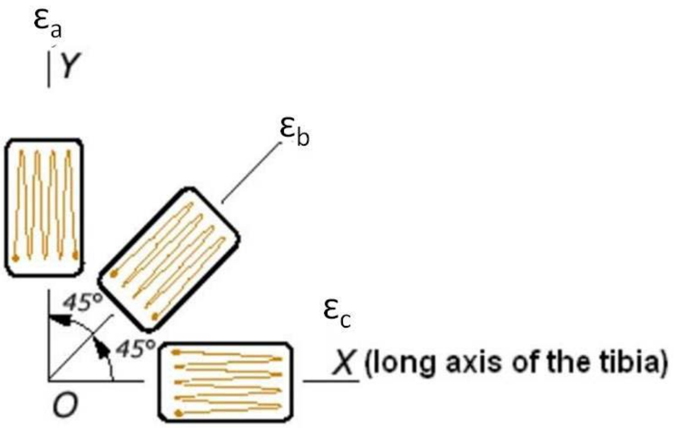

Figure 11: The Rectangular Rosette Strain.

This strain gauge is made up of three elements, Ea, Eb and Ec, each of which records strain in a plane 45 degree to the previous element. The element Ea will be aligned with the long axis of the tibia in this study.

From the three planes of strain, principal strain can be calculated (Equation 3).

3.3.5 Strain Gauge Attachment

In order to achieve good strain measurements in vivo and calculate principal strain, the rosette strain gauge needs to be attached securely and directly to the bone. This has been approached in two different ways in previous in vivo strain recordings, each with their limitations. The initial in vivo recordings in both animals and humans used glue to bond the strain gauge directly to the surface of the bone, requiring the periosteum to be retracted to expose the cortex [89, 134-136]. The validity of recordings was established in animal studies, however concerns were raised over the integrity of the bond between the gauge and the bone[135, 137]. If the bond was weakened then underestimation of the strain at the bones surface may occur.

To overcome the concerns over the integrity of the strain gauge bonding using glue, strain gauged bone staples were developed. Standard bone staples were adapted to have strain gauges applied to the surface and were then implanted into the cortex of the bone [97, 138-145]. Whilst removing the problems associated with bonding in vivo, more reports of strain gauge failure were made using this technique[138]. When a strain gauge failed, one or more wires snapped, resulting in strain in less than three directions being recorded. This made interpreting the data impossible as the principal strain could not be calculated and each individual strain gauge element only reflected the strain in a single direction, with no reference as to how this related to the principal strain. In addition, although bone staples are less invasive (not requiring retraction of the periosteum), punctures into the cortex of the bone are made, potentially introducing weaknesses into the bone under study.

Exposing study volunteers to any level of risk must be weighed up against the potential population benefit of the research conducted. Both methods for strain gauge attachment involve invasive procedures, however in this study, the original method of directly bonding the strain gauge to the surface of the bone was used. This technique was chosen as the potential risk to participants was lower given the less invasive nature of the procedure. The potential for complete data collection was also suggested to be higher given fewer previous reports of strain gauge failure using this technique.

3.3.6 Strain Measurement - Study Protocol

3.3.6.1 Strain Gauges

Strain was measured using an FRA 2-11 stacked rectangular rosette strain gauge (TML, Tokyo Sokki Kenkyujo Co., Ltd.) (or in the case of participant 6, a C2A-06-062LR-120 planar rectangular rosette strain gauge (Vishay – precision group, Basingstoke, UK). The gauge was bonded directly to the anteromedial aspect of the tibia, at the midpoint between the medial aspect of the tibial plateau and the lower border of the medial malleolus.

3.3.6.2 Strain Gauge Application

The strain gauges were applied in the theatre of Professor Mark Wilkinson, within the Sheffield Teaching Hospitals NHS Foundation Trust.

The chance of infection was reduced by administration of a 750mg dose of the antibiotic cefuroxime to the participant prior to surgery. The skin surrounding the application site was cleansed and sterilised using iodine or chlorhexidine. Local anaesthetic (marcaine with adrenaline) was administered to the skin and soft tissues surrounding the site of application.

Two small incisions, approximately 1-1.5cm long, were made through the skin. The first incision was directly over the site of attachment of the strain gauge and extended down to the periosteal surface. The second incision was approximately 2-3cm superolateral to the first. Through the first incision, a small area of the periosteum (~1cm^2) was incised and reflected using a scalpel. Surgical alcohol and surgical hydrogen peroxide were used to 'degrease' the site of application.

The strain gauge was passed through the second incision so that the strain gauge wires tunnelled through from one incision to the other at the site of application. This ensured good fixation of the device and minimised the risk of detachment due to pull on the wires.

The back of the strain gauge was flooded with cyanoacrylate adhesive (surgical superglue) and was applied to the bone surface using firm pressure from a finger. The adhesive can also bond surgical gloves, and for this reason a finger from a sterile glove was placed between the gauge and the gloved finger that applied the pressure, to ensure that the pressure could be removed without detaching the gauge from the bone surface.

After carefully removing the pressure, the gauge was inspected to ensure that all edges were secured to the bone. If the edges were not secure, the gauge was removed and the process repeated with a new gauge. Before the wound was closed, the gauge function was checked by measuring its resistance using an ohm meter and ensuring that the resistance didn't deviate from the manufacturer's specifications.

A thin coat of cyanoacrylate adhesive was applied to the whole upper surface of the strain gauge to provide protection against body fluid.

The wound was temporarily close and covered using an opsite dressing to minimise infection risk. At the end of the experiment, the gauge was removed from the bone surface by sharp dissection using a scalpel or adhesive removal reagent. The wound was closed using sutures. The patient was reviewed approximately 2 weeks post operatively for a wound inspection and removal of sutures.

3.3.6.3 Data Collection

The Strain gauge was attached, via a Wheatstone bridge, to a DLK 900 DataLINK system (Biometrics Ltd, Oxford, UK). Strain data was recorded using DataLog software (Biometrics Ltd., Oxford, UK).

3.4 Statistical and Analytical Techniques

3.4.1 Fourier Transform

Data recorded in the time domain can be represented in the frequency domain by performing a Fourier transformation (Equation 6). The Fourier transform (f(ω)) represents a signal in terms of its constituent sine and cosine waves, allowing analysis of the relative contribution of different frequency components to the overall signal.

Equation 6: Fourier Transform Function:

$$\boldsymbol{a)\ f(\omega) = \int_{-\infty}^{\infty} f(t)e^{-i\omega t}}$$

$$\boldsymbol{b) f(\omega) = \int_{-\infty}^{\infty} f(t)cos(\omega t)\delta\, t + \int_{-\infty}^{\infty} f(t)isin(\omega t)\delta\, t}$$

ω=Angular frequency, *f*=Frequency, t=Time, δt=Change in time

The frequency components that can be analysed are limited by the Nyquist theorem which states that the maximum frequency that can be analysed is equal to half the sampling frequency (Fs/2). If frequencies greater than Fs/2 are analysed then aliasing can occur, where high frequency components are erroneously represented as low frequency components of a signal.

For each frequency analysed, the signal in the time domain (f(t)) is multiplied by both a cosine and a sine wave at that frequency. In Figure 12, the blue line represents a signal comprised of a sine wave with frequency 6Hz and amplitude of 0.7mm and a cosine wave of frequency 4Hz and amplitude of 0.4mm. The FFT calculates the frequency of the signal's components and their amplitudes.

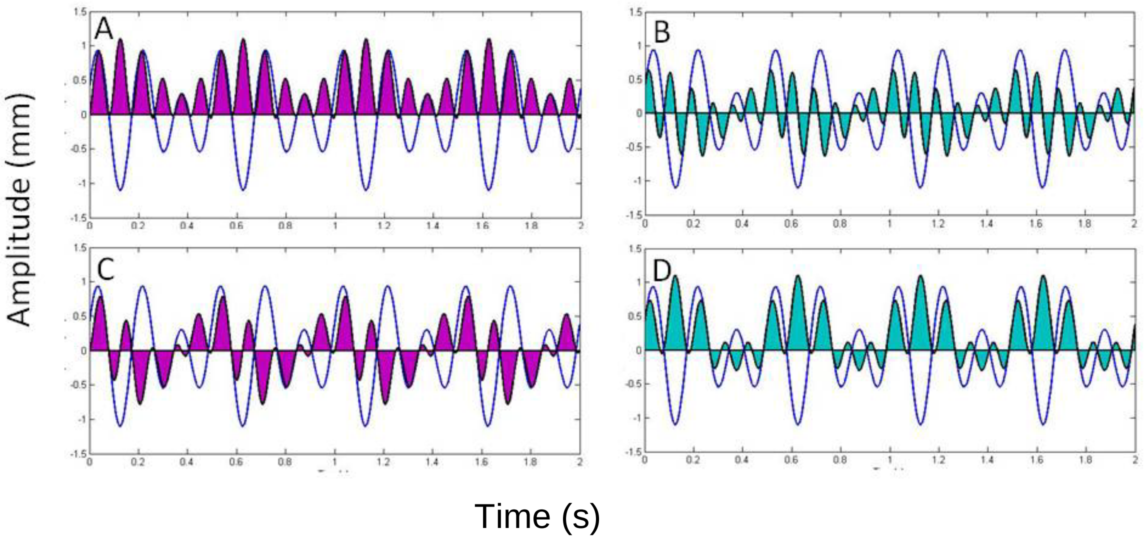

Figure 12: The workings of a Fourier transform.

The blue line represents a signal comprised of a sine wave with frequency 6Hz and amplitude of 0.7mm and a cosine wave of frequency 4Hz and amplitude of 0.4mm. The shaded area represents the signal multiplied by A) a 6Hz sine wave, B) a 6Hz cosine wave, C) a 4Hz sine wave and D) a 4Hz cosine wave. The sum of the shaded area in A and D, the signal multiplied by its constituent sine and cosine waves, is a positive value. The sum of the shaded area in B and C, the signal multiplied by non-constituent sine and cosine waves, is equal to zero.

In this case the signal has a frequency component at 6Hz and another frequency component at 4Hz. The shaded areas in Figure 12 represents part of the Fourier transform function solved for A) a 6Hz sine wave, B) a 6Hz cosine wave, C) a 4Hz sine wave and D) a 4Hz cosine wave.

When the Fourier transform function is solved for the components of the signal A & D, the sum of the shaded area is positive. This is because these are frequencies that are constituent parts of a signal. The sum of the shaded area is zero for B and C, as they are not components of the original signal. The sum of the shaded area for other frequencies (i.e. 2Hz, 3Hz, 5Hz etc.) is also zero, as they are not components of the original signal (not shown).

The Fourier transform can be a lengthy process for large data sets as the number of mathematical operations involved in the transform is proportional to the length of the data (N) squared[146]. To avoid such long calculations, Cooley and Turkey developed an algorithm which they called the fast Fourier transform (FFT) [147]. The FFT is an algorithm used to perform a discrete Fourier transform (DFT) in fewer mathematical operations than directly evaluating the DFT. For N of length equal to a factor of two (e.g 2048), the number of mathematical operations in a fast Fourier transform is approximately $N\log_2 N$. For length 2048, which is relatively short by some digital signal standards, this would result in 22528 fast Fourier transform operations as opposed to 4,194,304 direct Fourier transform operations, reducing the number of operations by 2 orders of magnitude.

3.4.1.1 Spectral Leakage

The FFT relies on the assumption that there are a complete number of repeated cycles within the signal. If the signal starts or ends part way through the cycle of a sine wave, that part of the signal does not fit exactly to one of the frequency lines on the spectrum, introducing error into the FFT spectrum. The result is a flatter and broader frequency peak around the frequency of the incomplete cycle which could ultimately obscure adjacent frequency components [148].

3.4.1.2 Windowing

All time domain data can be said to have had a square or uniform windowing function applied to it such that the signal is unaltered. By applying a windowing function which tapers at the extremes, the problem of spectral leakage can be reduced. When applied to the time domain data, the windowing function reduces the magnitude of the signal at the start and end of the time series[149]. This subsequently reduces the input of the partial cycles to the frequency spectrum compared to the full cycle frequency components as the partial cycles occur at the extremes of the time data. By applying the windowing function in sections which move along the time series data, the frequency spectrum incorporating all of the full cycles can be established with minimal influence of the partial cycles.

3.4.2 Fourier Transform – Study Protocol

A fast Fourier transform with a Hanning window was performed in Matlab R2007b using an in house program (Chapter 10.1.1). The sampling frequency used was 300Hz and the number of points in each FFT was 1024, giving a resolution of 0.3Hz which is ample for the detection of frequencies separated by 5Hz.

3.4.3 Statistical Analysis

Statistical analysis was performed using IBM SPSS 20. Details of the statistical tests performed are within the methods sections of the individual results sections. Results were considered significant if $P<0.05$.

4 Chapter Four: Method Development and Validation

4.1 Motion Capture

Motion capture is typically used in the assessment of habitual locomotor activities, aiding in the choice and monitoring of treatment for neural and musculoskeletal disorders[150]. Whilst accurate measures of marker displacement are required for gait analysis, the assessment of pathological gait using motion capture systems involves the identification of relatively large stages of gait such as 'stance phase' and 'swing phase', and their relative contribution to the gait cycle of an individual[151]. Additional gait analysis measures are based on kinematic calculations which rely not only on the accuracy of recorded marker movement, but also on marker positioning and computational assumptions within the kinematic calculations[150].

Marker placement is important for the accurate calculation of kinematics. It is difficult to replicate marker placement precisely, with small variations possible. Given the size of movements assessed in clinical gait analysis and variation in marker placement which could feasibly exceed the limit of movement detection, the ability of current technology to detect movement in the range of 0.1mm, is ample for accurate clinical gait assessments [152].

In the current study, marker movements as a result of whole body vibration transmission are a direct outcome measure. Peak to peak (P2P) displacements of less than 1mm are expected and therefore the ability of the specific Vicon motion capture system used to detect movements in the range of 1mm and below needs to be assessed.

4.1.1 Background

Along with the resolution of the cameras within a motion capture system, the ability of a motion capture system to accurately determine small movements is dictated by two sources of error.

4.1.1.1 Instrumental Systematic Error

Instrumental systematic error (ISE) is associated with poor camera calibration and inadequate calibration models. It can cause marker reconstruction errors which ultimately affect the determined pose of body segments[153]. As the pose of body segments is critical in the calculation of kinematics from motion capture data it is the kinematic data that is predominantly effected by ISE.

The Vicon camera calibration in this study was performed by a clinical scientist with a speciality in gait analysis, using the method specified by Vicon.

Even with sufficient camera calibration, the accuracy of the system at a given point depends on the position of that point with respect to the camera and the focus of the calibration[153]. To reduce the effect of ISE further, all recordings using the vibration platforms were performed as close to the central focus point of the calibrated area as possible.

Having taken the above steps, the ISE within the system should be minimal.

4.1.1.2 Instrumental Random Error

The second source of error in motion capture systems is instrumental random error (IRE). This type of error can be caused by a variety of things including electrical noise within the system, partially obscured markers and phantom signals[153]. The result of much of the IRE is gaps within recorded data which require filling using interpolative methods (Chapter 3.2.5). This in itself is another potential source of error as the greater the use of interpolation, the less the directly recorded data has a bearing on the outcome measures.

4.1.1.3 Assessment of the accuracy of displacements

In this analysis I aim to assess the impact of the ISE and IRE within the Vicon Nexus system used in this study on the ability of the system to accurately detect small displacements of the skin mounted markers. I aim to determine the threshold of accurate movement detection using the Vicon Nexus system used for this study.

In order to achieve this, I will establish the change in distance between two markers for which there should be no change in distance. Any difference in the distance between the two markers will be assumed to be due to errors within the system and any measurements of movement smaller than this value will be deemed undetectable using the current system.

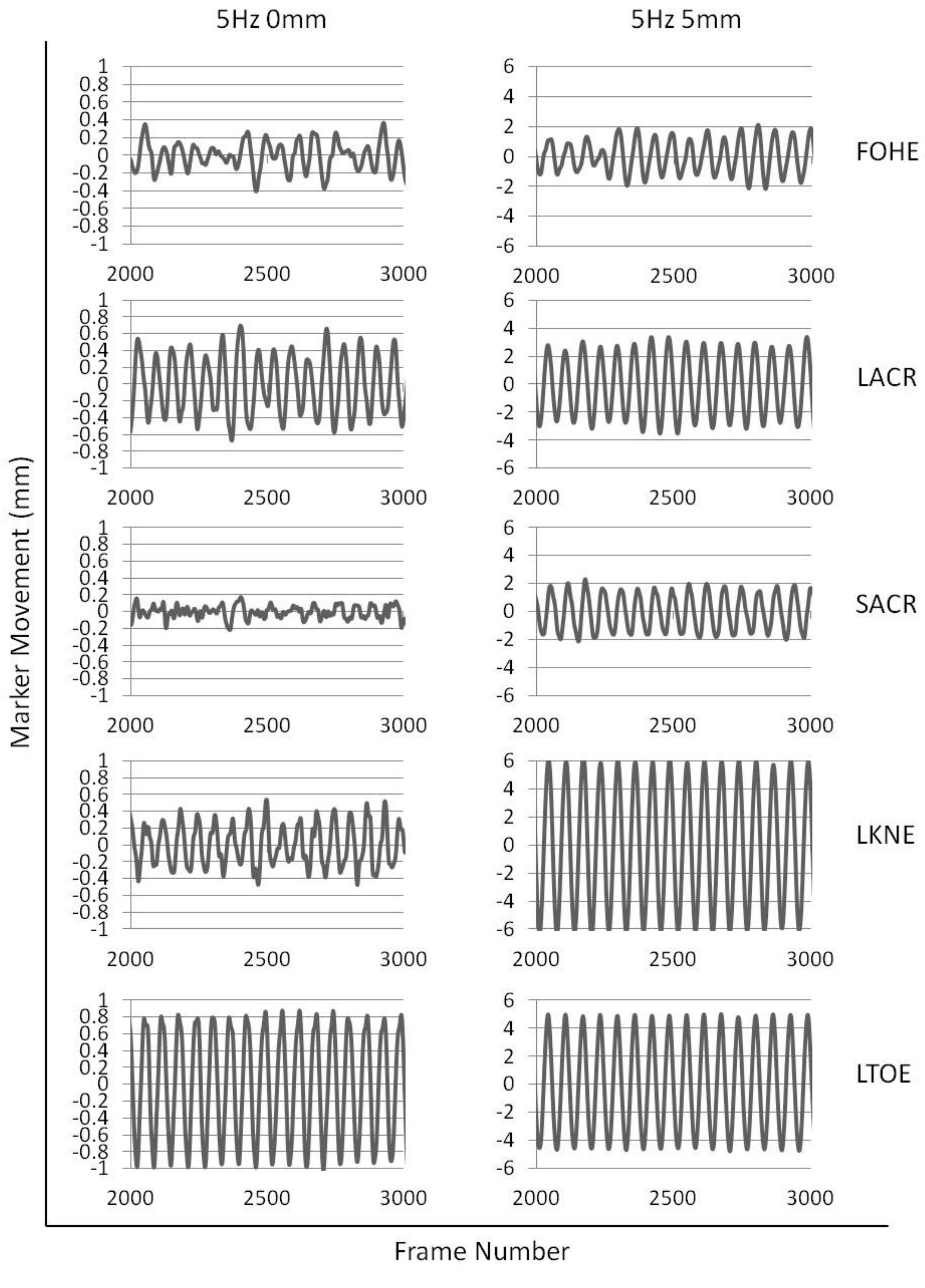

Figure 13: Graphs showing movements recorded using the Vicon nexus system.

Movements were recorded at the left toe (LTOE), left knee (LKNE), sacrum (SACR), left acromion process (LACR) and forehead (FOHE). Recordings were made at 5Hz frequency and 0mm amplitude (left) and 5Hz frequency 5mm amplitude (right) whole body vibration on the Galileo 900. At both 5Hz 0mm and 5Hz 5mm a signal is visible at each marker, however at the sacrum and forehead the signal is more clearly sinusoidal in the 5Hz5mm recording. The amount of movement detected due to noise within the Vicon nexus system needs to be determined in order to set a threshold below which detected movements are more likely due to instrumental random error than caused by propagation of the whole body vibration.

4.1.2 Methods

Motion Capture data was collected using 8 MX-F40 cameras positioned around the gait laboratory at the Northern General Hospital covering a capture volume of 77m^3. Data acquisition was made using Vicon Nexus software recording at 300Hz with a minimum of three cameras required to start a trajectory and two to continue a trajectory. Reflective markers were placed on the Galileo 900 whole body vibration platform at positions resulting in 1, 2, 4 and 5mm amplitudes on both the left and right side of the platform (Figure 14).

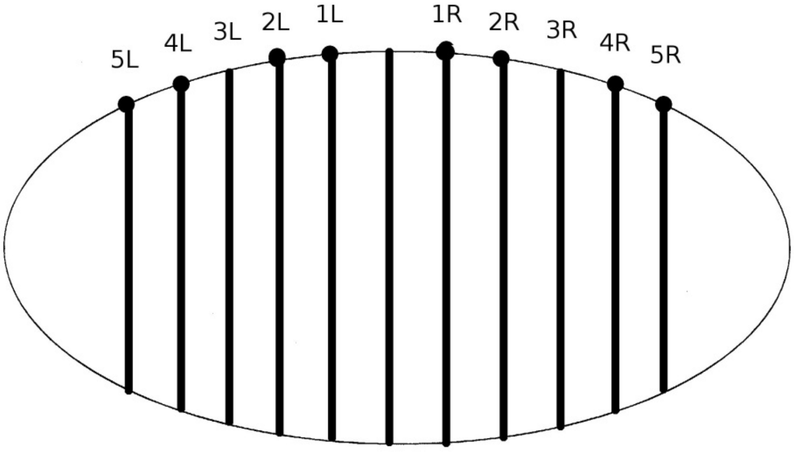

Figure 14: Foot positions on the Galileo 900 platform.
The lines on the footplate represent foot positions of which result in movement of the platform of different amplitudes. 1L/R=1mm amplitude left/right foot position, 2L/R=2mm amplitude left/right foot position, 3L/R= 3mm amplitude left/right foot position, 4L/R= 4mm amplitude left/right foot position, 5L/R = 5mm amplitude left/right foot position. Reflective markers from which measurements were made were placed on 1L/R, 2L/R, 4L/R and 5L/R.

Recordings were made at 5, 10, 15, 20, 25 and 30Hz. Recordings were repeated five times for each frequency except 20Hz for which four recordings were made.

Equation 7*:* Calculation of the distance between two markers.

$$\textbf{Distance between markers} = \sqrt{(\mathbf{x1} - \mathbf{x2})^2 + (\mathbf{y1} - \mathbf{y2})^2 + (\mathbf{z1} - \mathbf{z2})^2}$$

(X, Y and Z refer to positional coordinates of a marker in the X, Y and Z plane with 1 and 2 referring to two different markers, marker 1 and marker 2.)

The distance between two markers when the platform was stationary and when the platform was moving at 5, 10, 15, 20, 25 and 30Hz was calculated using Equation 7. The distance between markers on corresponding amplitude positions on the left and right were calculated (Table 6).

Marker Pair	Markers in Pair
1	1mm left and right markers
2	2mm left and right markers
3	4mm left and right markers
4	5mm left and right markers

Table 6: Marker Pairings.
Table defining the marker pairings used in the analysis of the change in distance between markers.

The maximum change in the distance between markers was determined (Figure 15) for each recording and the average of this across the five recordings for each frequency was reported. Standard deviation and the greatest change in the distance between markers for each marker set was also reported.

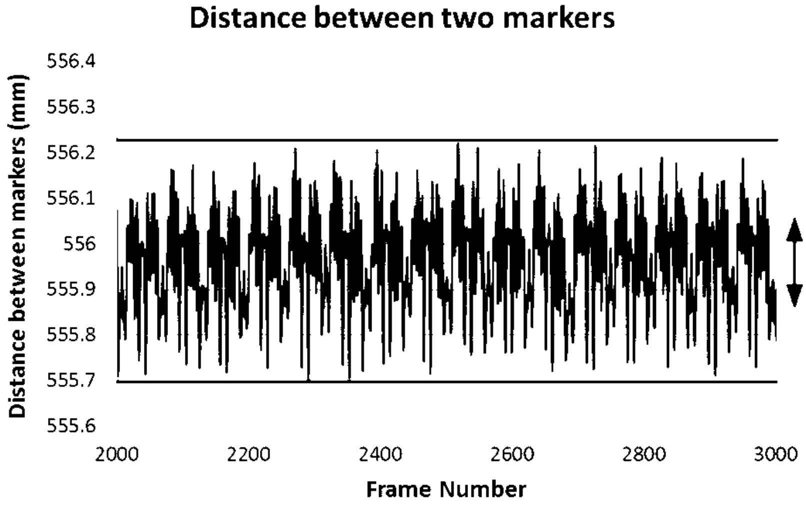

Figure 15: Variation in the distance between two markers placed on the Galileo 900 platform.

Measurement of the maximum change in distance between the markers was taken as the difference between the two bold horizontal lines indicated on the graph.

Measurement of the maximum change in distance between the markers was taken as the difference between the two bold horizontal lines indicated in Figure 15.

4.1.3 Results

	Marker Pair 1	Marker Pair 2	Marker Pair 3	Marker Pair 4
Average Distance between Markers (mm)	0.07	0.07	0.07	0.07
Maximum Distance Between Markers (mm)	0.10	0.09	0.09	0.10
Standard Deviation	0.01	0.01	0.01	0.01

Table 7: The change in distance between markers when the Galileo 900 is stationary. Marker pair 1: markers on 1mm left and right positions. Marker pair 2: markers on 2mm left and right positions. Marker pair 3: markers on 4mm left and right positions. Marker pair 4: markers on 5mm left and right positions. The average greatest change in distance between the markers, standard deviation of the average greatest change and maximum change in distance between the markers across all recordings are reported here.

	Marker Pair 1	Marker Pair 2	Marker Pair 3	Marker Pair 4
Average Distance Between Markers (mm)	0.50	0.45	0.53	0.50
Maximum Distance Between Markers (mm)	0.55	0.55	0.6	0.50
Standard Deviation	0.02	0.05	0.03	0.01

Table 8: The change in distance between markers during Galileo 900 movement.

Marker pair 1: markers on 1mm left and right positions. Marker pair 2: markers on 2mm left and right positions. Marker pair 3: markers on 4mm left and right positions. Marker pair 4: markers on 5mm left and right positions. Recordings of each pairing were made at 5, 10, 15, 20, 25 and 30Hz. The average greatest change in distance between the markers, standard deviation of the average greatest change and maximum change in distance between the markers across all recordings are reported here.

When the Galileo 900 was in motion, the average of the greatest change in distance between two markers ranged between 0.45mm and 0.53mm with standard deviations for each pair of markers not exceeding 0.05mm (Table 8). Of this change in distance between markers, 0.07mm is was also present when the platform was stationary. The maximum change in distance between markers ranged from 0.5mm to 0.6mm (of which 0.09-0.1mm was also observed when the platform was stationary). The threshold used for accurate marker movement detection using this system is movements greater than 0.6mm.

When a fast Fourier transform (FFT) of the change in distance between markers was run, the average FFT peak at the input frequency ranged from 0.036mm to 0.062mm with a maximum standard deviation of 0.02mm (Table 9). The maximum value of a FFT peak had a range from 0.055mm to 0.094mm. The threshold used for FFT peaks as a result of sinusoidal whole body vibration (WBV) transmission is 0.09mm.

	Marker Pair 1	Marker Pair 2	Marker Pair 3	Marker Pair 4
Average FFT Peak (mm)	0.042	0.062	0.036	0.037
Maximum FFT Peak (mm)	0.067	0.094	0.055	0.057
Standard Deviation	0.01	0.02	0.01	0.01

Table 9: Fast Fourier transforms (FFT) of the change in distance between pairs of markers.

Marker pair 1: markers on 1mm left and right positions. Marker pair 2: markers on 2mm left and right positions. Marker pair 3: markers on 4mm left and right positions. Marker pair 4: markers on 5mm left and right positions. Recordings of each pairing were made at 5, 10, 15, 20, 25 and 30Hz and a fast Fourier transform of the change in distance between the markers was run. The average FFT peak at the input frequency, standard deviation and the maximum FFT peak are reported here.

4.1.4 **Discussion**

The change in distance between markers observed when the Galileo 900 is stationary suggests that there is inherent electrical noise in the system, translating to a measurable level of movement between markers when none would be expected. When the platform is in motion, this change in distance between markers is around 5 times greater and shows a repeatable trajectory, suggesting either that the motion capture markers move relative to each other in a repetitive pattern (i.e at one or more resonances). The thresholds determined in this analysis are based on the maximum change in distance observed between markers, which is during motion, as this accounts for the worst case of signal to noise ratio. Above this threshold, the signal of interest should be greater than the random noise within the motion capture system, making it possible to confidently report peak to peak displacements and FFT peaks as a result of the transmission of WBV through the body.

Previous methods used to assess the ability of motion capture systems to detect small movements have used similar principles. Part of the movement analysis laboratory (MAL) test [154] involves determining the coordinates of fixed markers during movement of a metal rod within the capture volume and Ehara et al based their assessment of marker displacement accuracy on the variation in distance between two fixed markers [155, 156].

In this analysis of marker movement, the Galileo 900 whole body vibration plate was used in place of a metal bar. Markers were positioned at fixed points and movements were relevant to those being recorded both in position within the capture volume and in speed. The markers should not have moved relative to each other during the recordings and therefore using the change in distance between markers of differing separation provided a thorough assessment of the error within the system. Whilst the differences observed could be due to movement of the head of the marker with respect to the base, this in itself would be an undesirable measurement of movement and therefore may indicate not only the limit of detectable movement, but the magnitude of an overestimation of movements recorded during whole body vibration.

In previously reported transmission of whole body vibration measured using a motion capture system, peak to peak displacements reported ranged from 0.2-3.68mm[114, 157]. The majority of reported peak to peak displacements were above the threshold determined here [157], suggesting our system is capable of detecting the majority of transmitted WBV signals throughout the body. The use of a higher sampling frequency is a possible reason for the increased sensitivity of the system used to report the peak to peak displacements below the threshold established in this study. The capture volume used for the recordings may also have been smaller with distance from the camera to the markers also reduced, which would allow for increased sensitivity to small movements[158].

Therefore, it is still possible that at markers where sinusoidal movement was not detected using our system, there is transmission that is indistinguishable from noise in context of peak to peak displacement.

Using a FFT may allow us to discriminate between WBV signal and noise in the recordings to a greater degree than through measurement of peak to peak displacement. The FFT relies on the detection of sinusoidal wave forms (Chapter3.4.1) as demonstrated by the threshold of FFT peak (Table 9) being much smaller than that of the peak to peak displacement (Table 8). This suggests there is only a very small sinusoidal component within this signal and reaffirms the assumption that changes in distance between markers is primarily random.

The FFT may allow us to determine whether transmission of a sinusoidal signal has reached a given marker whose peak to peak displacement is below the threshold. However the exact peak to peak displacement or amplitude of the transmitted signal cannot be determined from the FFT as its magnitude is specific to an individual frequency. In the time domain, signal components at several frequencies may converge resulting in an amplitude that differs from the FFT magnitude.

4.2 Strain Gauge Recordings

4.2.1 Background

Tibial strain measurements using rosette strain gauges bonded directly onto the surface of the tibia have been made previously in the analysis of human locomotion [89, 134, 135]. Absolute values of strain have been reported in all instances, with principal compressive strains of 30-1300με and principal tensile strains of 30-750με reported [89, 134, 135]. The absolute strain values recorded are dependent upon the defined zero of the strain gauge. At the human tibia, muscles involved in flexion of the toes, plantar and dorsi flexion at the ankle, knee stabilisation, flexion and extension and hip extension all insert upon on the tibia, exerting forces on the bone during these movements[159]. Defining a leg position that represents true zero, whereby no force is exerted upon the tibia through muscle contraction or weight, is therefore impossible to achieve. In previous work, zero has been determined using non weight bearing during which there is minimal contraction of the major muscles inserting on the tibia. In two instances participants were required to lift the leg with the strain gauge off the floor and hold it in a static position whilst the strain gauge was zeroed [89, 135].In the third study, participants were required to sit on the edge of a seat with their legs hanging freely and not touching the floor[134]. Although the strains recorded in each of the studies were similar in magnitude [89, 134, 135], the variation in zero technique may have influenced the absolute values of strain recorded. Thus, in this analysis I aim to describe any differences in strain magnitude achieved using the two different zero techniques previously reported as well as two additional techniques. I will also assess the reproducibility of zero positions and the maintenance of the zero point over time.

4.2.2 Methods

The strain gauge setup used for these tests consisted of an FRA-2-11 rosette strain gauge attached to the DataLINK DLK900 amplifier with data recorded using DataLog software (Biometrics Ltd, Oxford UK). Recordings were made at a sampling frequency of 500Hz and strain output was exported to excel files in engineering units from which principal strains were calculated (**Equation 8**).

Equation 8: Principal Strain Calculation. $\varepsilon_{P,Q}$ = compressive and tensile principal strain, ε1=strain recorded from strain gauge channel 1, ε_2=strain recorded from strain gauge channel 2, ε_3=strain recorded from strain gauge channel 3:

$$\varepsilon_{P,Q} = \frac{\varepsilon_1 + \varepsilon_3}{2} \pm \frac{1}{\sqrt{2}}\sqrt{(\varepsilon_1 - \varepsilon_2) + (\varepsilon_2 - \varepsilon_3)}$$

Prior to use, the strain gauge setup was tested for accuracy using a fixed resistor test. The test was undertaken using a Vishay strain indicator and the resistance detected by the strain gauge setup was compared to a known input resistance. The resistance used was equivalent to a strain of 4080με.

The Penko LCS-3 load cell simulator was used to test the accuracy of the strain gauge setup by assessing the ability of the system to measure a load of known quantity.

After the initial setup tests, a single FRA-2-11 rosette strain gauge was bonded directly to the anteromedial surface of the right tibia at the midpoint between the medial aspect of the tibial plateau and the lower border of the medial malleolus of a healthy male adult.

Strain data was collected for a single participant whilst the system was zeroed in four different ways. The system was zeroed whilst the participant: 1) stood with the right leg flexed at the knee, 2) stood with the right leg flexed at the hip and the thigh supported, 3) lay supine with the leg supported by the bed, 4) sat on the edge of a chair with legs hanging freely. Recordings of the strain gauge being zeroed, the participant rising onto their tip toes, going into squat position and returning to the original zero position were made for zero whilst knee flexed (1) and hip flexed (2). The strain in the tip toes and squat position were recorded after zero whilst supine (3) and tip toes, squat and original zero position recorded after zeroing whilst sitting (4).

4.2.3 Results

Test (vs 4080µε)	Measured strain (µε)
1	4060
2	4030
3	4030

Table 10: Results from a fixed resister test.

The fixed resistance used simulated a strain of 4080µε. Measured strain varied between 4030µε and 4060µε.

The strain gauge setup recorded strain within 50µε of that expected from the resister used during the fixed resister test (Table 10) and load cell simulation showed agreement to be better than 1% between the load cell input and the strain gauge system output.

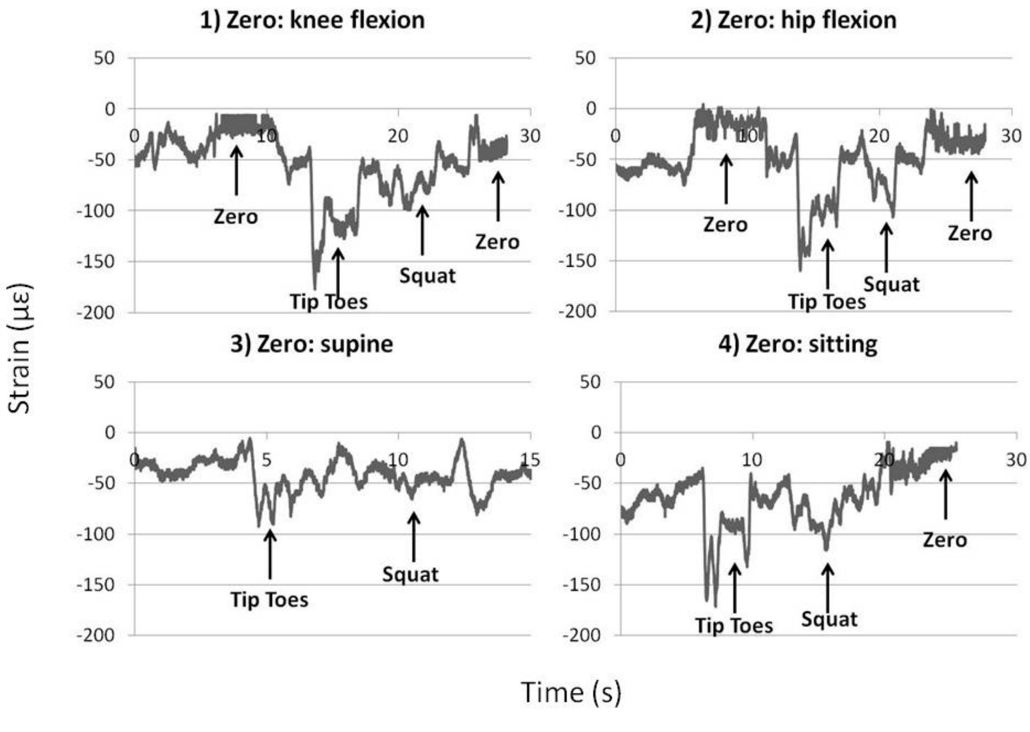

Figure 16: The influence of zero technique on the principal strain recorded at the tibia.

Principal compressive strains recorded at the anteromedial aspect of the tibia whilst 1)strain gauge zeroed with knee in flexion, raising onto tip toes, going into squat position, returning to zero position 2) strain gauge zeroed with hip in flexion, raising onto tip toes, going into squat position, returning to zero position 3) raising onto tip toes and going into squat position after strain gauge zeroed whilst supine 4) raising onto tip toes, going into squat position and returning to zero position after strain gauge zeroed whilst sitting.

The time point at which the strain gauge is zeroed with 1)the knee in flexion and 2) the hip in flexion can be clearly seen as the principal compressive strain magnitude reaches zero (Figure 16 – zero). Small fluctuations in the zeroed strain value can be observed.

When the participant rises onto their tip toes, the maximum principal compressive strain reached lies between approximately -160με and -180με in all cases except that when the strain gauge was zeroed with the participant supine (Figure 16– 1), 2), 4) – tip toes). In this instance, the maximum principal compressive strain obtained when the participant went onto their tip toes was approximately -100με (Figure 16 – 3) – tip toes). A similar trend was seen when the participant adopted a squat position with peak compressive principal strains between approximately -100με and -120με (Figure 16 -1), 2), 4) – Squat) in all cases except zero when supine in which a peak of approximately -60με was observed (Figure 16 – 3) – Squat).

When the initial zero position was adopted post movement, the compressive principal strain magnitude returned to value close to zero, with a little fluctuation in the exact value achieved (Figure 16 – zero position).

Although data presented here is for compressive principal strain, a similar trend was seen in tensile principal strain.

4.2.4 **Discussion**

The strain gauge setup used in this project was in good agreement with a load cell simulator and could accurately and reproducibly measure a fixed resistance (Table 10). This indicated that the setup is capable of accurately and reproducibly recording strain.

When measuring strain at the tibia whilst the strain gauge is zeroed, fluctuations around zero are apparent (Figure 16). These fluctuations lie below the level of variability in the fixed resister test and therefore could be due to variation within the recording system. The fluctuation in strain lies well below the magnitude of the strain induced by the movements measured in this study (Figure 16) and in previous work [89, 134, 135]. This makes it possible to identify the strain due to a given movement although, as previously stated by Lanyon et al [135] care should be taken when interpreting principal strains around zero.

Achieving a zero point using any of the zero techniques in this analysis rendered similar strain magnitudes when the participant went onto their tip toes or into a squat position (Figure 16). In the case of zero with knee flexion (Figure 16 – (1)), hip flexion(Figure 16– (2)) or whilst sitting (Figure 16-(4)), variations in the strain magnitudes observed during movement could be due to variation in the height achieved when on tip toes or the depth of the squat. When zero was defined as in a supine position with the lower leg supported on a bed (Figure 16 – (3)), the strain magnitudes tended to be lower than those observed with the other three techniques. A possible explanation for this could be the force exerted on the lower leg by the bed. This force would exert a strain on the tibia and as such, zero may be obtained under a higher state of load. This would result in a lower strain magnitude as the initial baseline strain defined as zero would be higher than in the other cases.

This analysis suggests that the strain gauge set up is capable of recording accurate measurements and that defining zero in any position where the lower limb is non weight bearing and unsupported will render similar outcomes. This makes comparison to previously reported absolute strain magnitudes possible. Any differences between the strain magnitudes observed across individuals will be likely to be due to variations in bone geometry[160] or the exact positioning of the strain gauge on the tibia.

4.3 Butterworth Filter Design

4.3.1 Background

Elements of unwanted background noise can have substantial bearing on the interpretation of recorded digital signals. To discriminate between background noise and characteristics of the true signal is not always clean cut, however if something is known about the frequency band within which a signal is expected to lie, filtering can result in removal of noise from the recorded signal.

Moving average filters have previously been used in a de-trending algorithm to remove movements due to postural sway from motion capture data recorded during WBV [157, 161] (Chapter 10.2.2). When applied to a signal, the moving average filter produces a good smoothing result, removing random noise from the signal. In the detrending algorithm, this smoothed signal is subtracted from the original signal leaving the ‘random noise’, in this case the WBV signal.

Whilst previously used, subtraction of the moving average from the current data set after applying a low pass filter with 100Hz cut-off did not remove the noise within the data set sufficiently for use with the in house program use to detect peak to peak displacements accurately.

Whilst moving average filters produce good time domain results, they are not frequency specific, leaving components of high frequency displacement in the signal and making use of the in house program (Chapter 10.1.2) reliant on manual input, whilst potentially filtering out elements of the desired signal [162].

A more direct approach is the application of a band pass filter about the input frequency [163]. Whilst potentially omitting a greater range of frequencies, the omitted and retained frequencies are defined with this technique.

The starting point for most filter designs is a low pass filter, in which elements of the signal below a defined frequency are retained, whilst elements of the signal above the defined frequency are filtered out[162]. A high pass filter has the opposite effect on the signal, with frequency components above a defined frequency being retained. The low and high pass filters each work around a single defined cut-off frequency, whereas by cascading a low and high pass filter, a band pass filter can be attained with two cut-off frequencies. This allows unwanted noise at both low and high frequencies to be filtered out, leaving a specific band of frequency components in the remaining signal.

The ideal band pass filter would filter out all of the frequency components of a signal outside of the pass band (Figure 17: A). However, this ideal band pass filter cannot be realised, the step from stop to pass band will not occur instantaneously, ripple may be introduced in the pass band and the stop band attenuation will be finite(Figure 17: B) [164].

Practically, choice of filter is often a trade-off between the performance of the filter in the time domain and the frequency domain. As we aim to measure peak to peak displacement in the time domain for a signal composed of specific frequencies, a filter which has minimal effect on the amplitude of the signal yet is capable of being specific to certain frequencies is desirable.

The Chebyshev response of a filter describes the ability of a filter to increase the roll off rate at the cut off frequency at the expense of additional ripple in the pass band. The Butterworth filter describes a filter which provides the best compromise between attenuation in the time domain and phase shift in the frequency domain[164]. It is maximally flat (no ripple in the pass or stop band) therefore, as the intention is to take measurements of peak to peak displacement, the Butterworth filter presents the best option of filter to maintain accurate peak to peak displacements whilst removing unwanted frequency components and minimally altering the phase of the frequency component of the signal.

By defining the cut-off frequencies to incorporate the input frequency of the WBV signal and the first harmonic above the input frequency, the aim of this analysis is design suitable filters for the motion capture data collected. The ideal filter would cut off perfectly at a specified frequency. The filters will be made up of cascading 4th order sections. The greater the number of sections, the greater the order and roll off and the closer the filter is to having an ideal cut off. However, by increasing the order and the steepness of the cut off, greater ripple is seen in the pass band, potentially greatly altering the input signal. Therefore, a compromise will be met with filters that have the greatest roll off possible whilst keeping pass band ripple maximally flat.

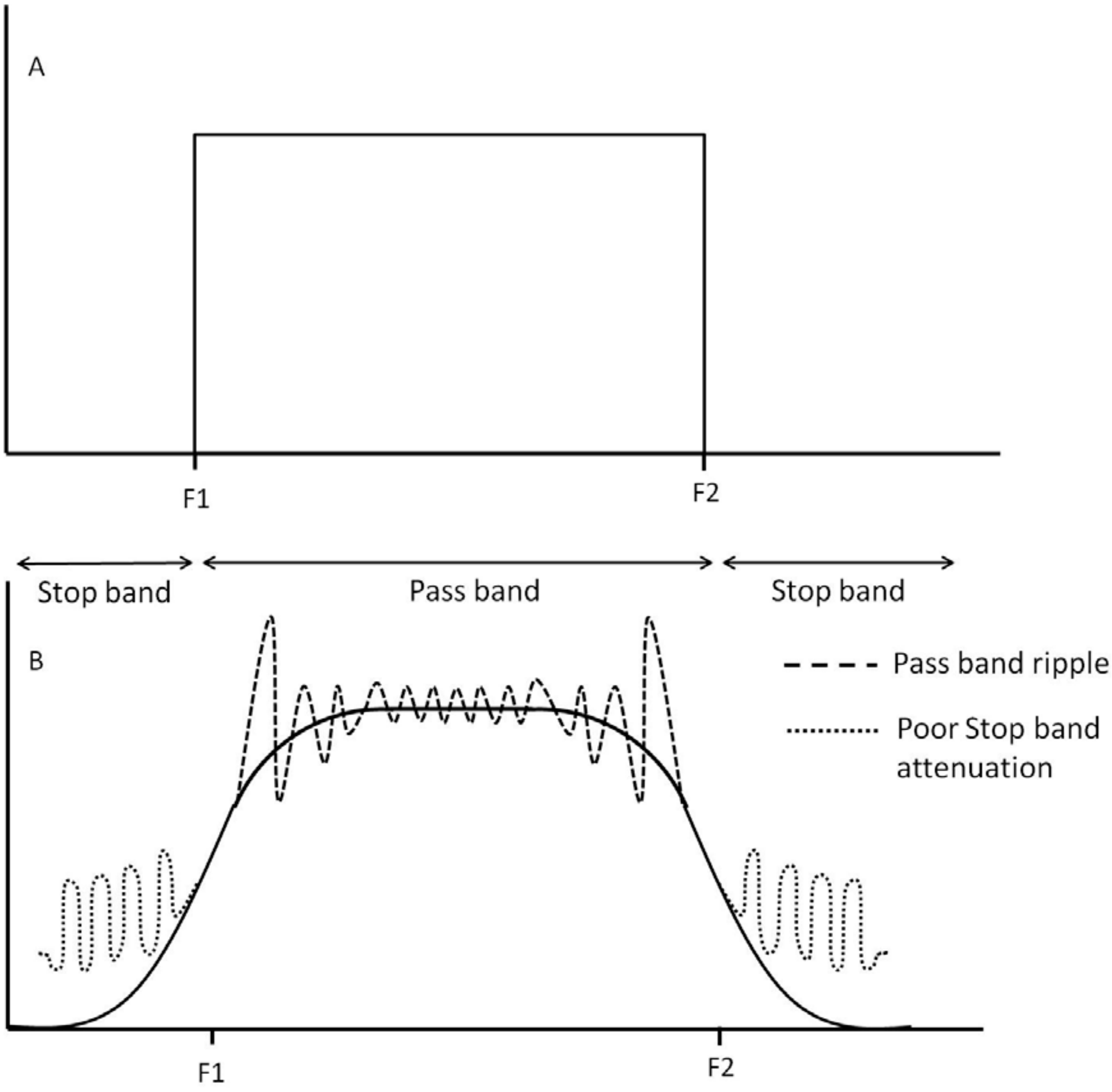

Figure 17: Designing a bandpass filter.

A: the ideal filter response. B: an attainable frequency response. F1= Low frequency cut off. F2 = high frequency cut off. Trade-offs are made between the frequency domain in terms of the steepness of the step response at the cut of frequencies and the time domain in terms of ripple in the pass band and poor stop band attenuation.

4.3.2 Methods

Motion Capture data was collected for a single participant using 8 MX-F40 cameras positioned around the gait laboratory at the Northern General Hospital. Data acquisition was made using Vicon Nexus software recording at 300Hz with a minimum of three cameras required to start a trajectory and two to continue a trajectory.

Reflective markers were placed at 21 anatomical landmarks throughout the body (Chapter 3.2.6).

Motion capture data was recorded whilst the participant stood on the Galileo 900 WBV platform. Their feet were positioned so that the input signal had amplitudes of 0, 1, 3 and 5mm and the frequency was increased from 5Hz to 30Hz in 5Hz increments resulting in 24 measurements.
Fast Fourier transforms (FFTs) of unfiltered motion capture data were performed using the in house Matlab program (Chapter 10.1.1) for each of the 24 trials. The magnitude of the FFT peak at the input frequency was determined and that at the first, second and third harmonics if present was also recorded.

Band pass Butterworth filters were designed (Table 11) with the specification that all frequencies with a FFT magnitude within 10 fold of that at the input frequency were not attenuated.

Filter	Frequency Cut Off 1 (Hz)	Frequency Cut Off 2 (Hz)
30Hz	18	80
25Hz	15	70
20Hz	11	60
15Hz	8	48
10Hz	4.5	35
5Hz	2.2	25

Table 11: Specifications of the Butterworth filters for each input frequency.

Individual filters were designed for each input frequency and applied to a chirp,(Figure 18), a signal which increases in frequency relative to the time along the x-axis such that at 1 second the frequency is 1Hz, at 2 seconds the frequency is 2Hz etc. This was achieved using an in house Matlab program (Chapter 10.1.3).

The filtered chirp was used to determine the frequency response of the individual filters and establish that the design specifications were met. Any attenuation of the amplitude of the chirp was a result of the filter and corresponded to a frequency dependent upon what time the attenuation occurred.

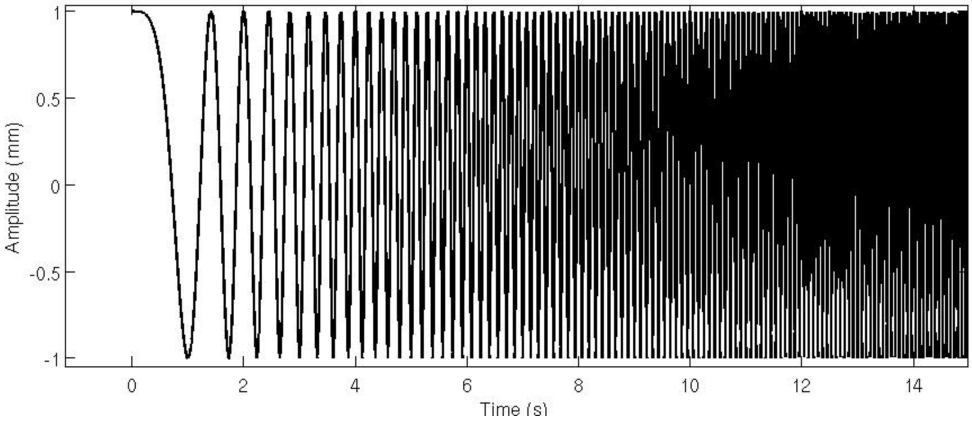

Figure 18: Example of an unfiltered Chirp.

For every second along the x axis, the frequency of the sine wave increases by one Hz. This results in a sine wave of peak to peak displacement of 1mm and frequency of 1Hz at 1seconds, 2Hz at 2seconds, 3Hz and 3seconds etc.

4.3.3 <u>Results</u>

Figure 19: The contribution of the first three harmonics to the overall signal.

Blue represents the input frequency, red represents the first harmonic, green the second harmonic and purple the third harmonic. By the second harmonic, the contribution to the overall signal is tenfold lower than that of the input frequency for all frequencies and amplitudes. Given the small contribution of the second harmonic and above to the overall signal, filters were designed to include the input frequency and first harmonic.

The FFT magnitude at the frequency of the input signal is much greater than that at any other frequency (Figure 19). There is a component of the signal at the frequency of the first harmonic and in some cases, second and third harmonics however by the second harmonic, the magnitude of the FFT peak is at least ten fold lower than that at the input frequency.

The Butterworth filters to be applied to the motion capture data at each different frequency have cut offs below and above the input frequency (Table 11).

When each filter is applied to a chirp (Figure 20) the input frequency and first harmonic are not attenuated. The amplitude of the signal is attenuated to 50% by the cut off frequencies. Frequency cut off one has a greater roll off than frequency cut off two, with roll off beginning approximately 2Hz above frequency cut off one and 10-25Hz below frequency cut off two. There is no substantial pass band ripple in any of the filters.

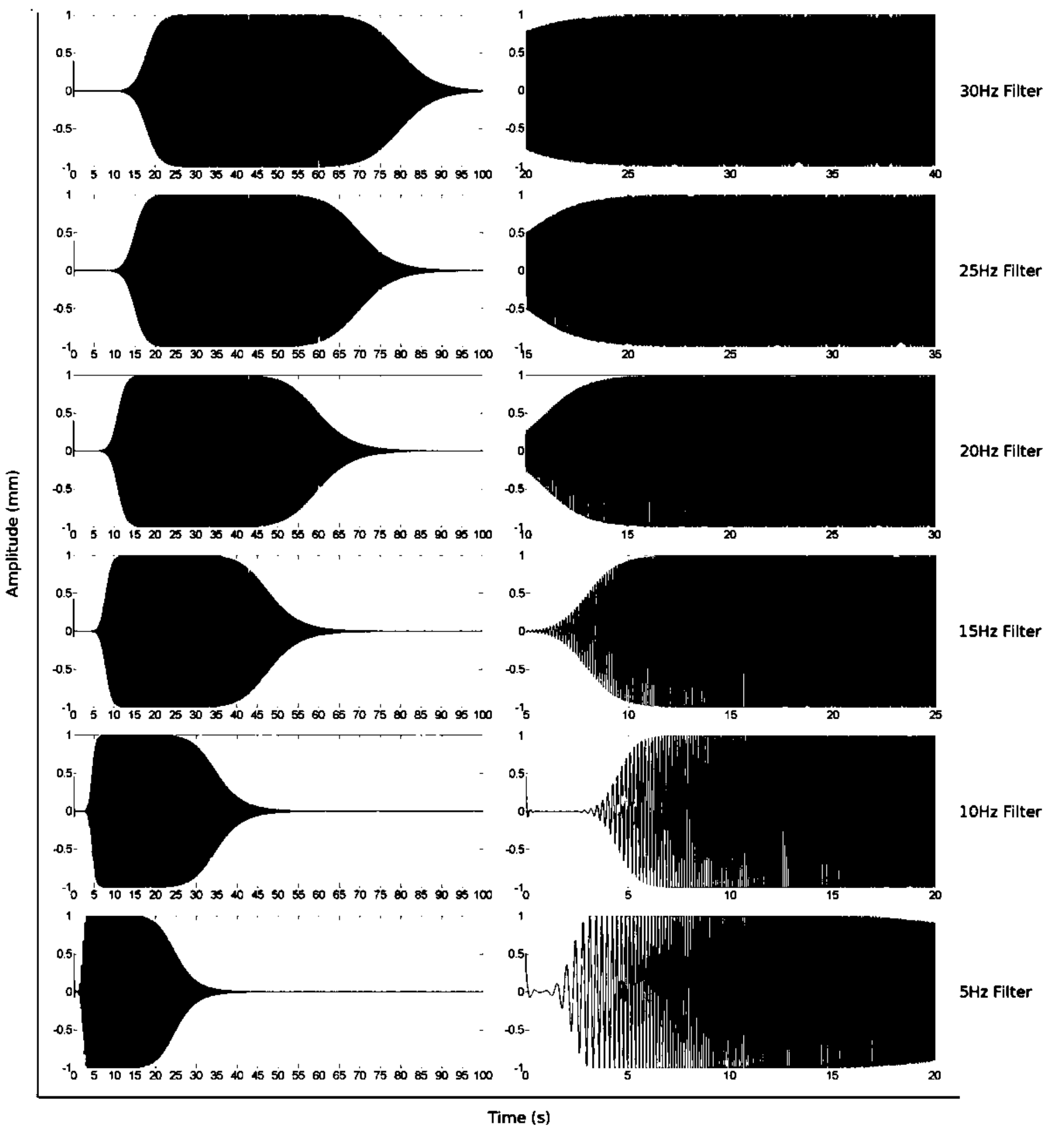

Figure 20: Filtered Chirps.

Chirp signals filtered with the Butterworth filters specified in Table 9. Attenuation of the amplitude of the signals indicates the frequency response of each filter. The left column shows the frequency response between 0 and 100Hz. The right column shows the frequency response at the input frequency and first harmonic in more detail. For each filter, the amplitude at the input frequency and first harmonic are not attenuated.

4.3.4 Discussion

Motion capture data contains inherent errors stemming from high frequency noise within the motion capture system [153]. In some instances, the noise within the system is large enough to obscure true signals within recordings, making measurements of small movements difficult. In this particular project, the frequency of the signal of interest is known due to the input stimulus being a vibration at a predefined frequency. This allows specific digital filters to be designed in order to overcome this problem by removing signals at frequencies other than the input frequency.

When specifying the cut offs of the digital filters to be used, it is important to take into account the possibility of the transmission of vibration at harmonic frequencies. From the FFT of a subset of the raw data, transmission of the WBV can be seen at the input frequency and first harmonic in all instances (Figure 19). By the second harmonic, the magnitude of the FFT is ten-fold lower than that at the input frequency (Figure 19).

Designing filters is a balancing act between omitting enough of the undesired noise and not removing significant portions of the signal of interest. Given the ten-fold or greater decrease in the FFT magnitude by the second harmonic, the signal at these frequencies and above is unlikely to greatly influence outcome measures of peak to peak displacement or root mean squared acceleration. Therefore, filters were designed with cut offs that maintained the frequency components at the input frequency and first harmonic, but decreased the magnitude of the signal components below and above these frequencies. Each filter was centred on the input frequency, as in previous whole body vibration study [163]

The filter design used implements the filters in a number of cascading sections. By increasing the number of sections, the filter order is increased and therefore the roll off of the filter is increased allowing a more tightly banded filter to be designed [164]. However, by increasing the order of the filter, the ripple in the pass band is increased and above a certain point results in great augmentation of the signal around the lower cut off frequency. Therefore, the filters designed all have two sections as this proved a good compromise with a reasonable roll off rate but no significant ripple in the pass band.

Analysis of the performance of each filter using chirps demonstrated the ability of each filter to successfully remove unwanted high and low frequency noise whilst leaving signal components at the input frequency and first harmonic unaffected (Figure 20). Therefore it can be concluded that the use of the proposed filters will allow accurate measurements to be made without the loss or augmentation of significant portions of the signal.

5 Chapter Five: Transmission of Whole Body Vibration in Healthy Adults

5.1 Whole body vibration: impact on the skeleton

Multiple studies into the effect of whole body vibration (WBV) on the skeleton have shown maintenance or increases in bone density after WBV interventions [1, 105-111].

The skeletal areas of most interest when considering WBV as an intervention for osteopenia or osteoporosis are the femoral neck and lumbar spine. These are common sites of osteoporotic fracture and associated morbidity [32] and reported outcomes of WBV studies have generally focused on changes in areal bone mineral density (aBMD) at these sites.

5.1.1 Whole Body Vibration: a mechanical stimulus

The effects of mechanical stimuli on bone are local, as demonstrated by the differences in geometry and density between the dominant and non-dominant playing arms of tennis players[9, 74-77]. In order for whole body vibration (WBV) to cause a change in bone mineral density (BMD) at a specific site, a mechanical stimulus as a result of the WBV input must reach the site.

Occupational studies of whole body vibration have demonstrated transmission of whole body vibration to the head when participants are in a seated position. The frequency and magnitude of the WBV as well as the posture of the participants have all been shown to influence the transmission of vibration in an occupational setting [119, 165].

In this study, we aimed to determine the vertical transmission of WBV of different frequencies and amplitudes, delivered by fitness and medical WBV platforms, throughout the human body when in an standing position. We measured the magnitude of stimulus, if any, that reached the level of the hip (as inferred by recordings made at the anterior superior iliac spine) and spine (recordings at Sacrum, T2 and T10). We also aimed to examine how the transmission was influenced by the frequency and the amplitude of the input WBV in this setting.

5.2 Methods

5.2.1 Participant Population

Data was collected from six healthy volunteers who met the inclusion and exclusion criteria of the study (Chapter 3.1). The participants were aged between 18 and 51 years at the consent visit, were ambulatory, generally healthy (as assessed by medical history and physical examination) and were physically willing and able to undergo all study procedures. All participants had a BMI less than 30 and a BMD measured by DXA between +/- 2.5 SD of the young normal range. The characteristics of the six participants included in the study are detailed in Chapter 3.1, Table 4.

5.2.2 Measurement of Transmission

Motion capture data was recorded using a Vicon Nexus system with reflective markers positioned on 21 anatomical landmarks (Chapter 3.2.6: Figure 6) as described in Chapter 3.2.6.

5.2.3 Whole Body Vibration

Transmission of WBV delivered by three different platforms was analysed. The Galileo 900 platform delivered reciprocal WBV at amplitudes of 0-5mm in 5mm increments and frequencies of 5-30Hz at increments of 5Hz. To achieve the different amplitudes the participant changed the spacing of their feet on the platform (Chapter 4.1.2: Figure 14).

The Powerplate Pro 5 platform delivered vertical WBV at amplitudes defined by the manufacturer as ‘Low’ and ‘High’ and frequencies of 25Hz and 30Hz. Both the amplitude and frequency were changed using the electronic platform settings.

The Juvent 1000 platform delivered vertical WBV at amplitudes 10 fold lower than either the Galileo 900 or Powerplate Pro 5 at a frequency between 32Hz and 37Hz. The outcome was an acceleration of 0.3g.

All participants underwent WBV on the Galileo, Powerplate and Juvent platforms as described above (for the order, see appendix **S 1**). For each frequency and amplitude, a single one minute period of WBV was delivered to each participant, during which a 20 second recording was made. A rest of up to three minutes between WBV settings was given. This gave a total WBV testing time of up to 3 hours for each participant.

Recordings were made with participants maintaining a bilateral stance with knees slightly bent. Knee angle was at the discretion of the participant and the stance adopted was directed to be ‘comfortable’ for the participant.

5.2.4 Data processing

5.2.4.1 Peak to Peak Displacement

Raw trajectories were exported to an excel spreadsheet (Microsoft 2010). Data for each marker was then filtered in MATLAB 2007b using a bandpass filter, with cut-offs dependent upon frequency (Chapter 4.3:Table 11) as defined in chapter 4.3.

Filtered data was cropped to encompass only a period of recording at which the WBV was at a consistent frequency and amplitude.

The cropped data files were imported into Matlab 2007b and the maximum and minimum points of each vibration cycle were determined using the Tibial_Marker Matlab program (Chapter 10.1.2).

Peak to peak displacements for each vibration cycle were determined using the minimum and maximum points (Equation 9).

Equation 9: The Peak to Peak Displacement of a given vibration cycle:

$$P2P\ Displacement = Maximum\ point\ \ of\ trajectory - minimum\ point\ of\ trajectory$$

5.2.4.2 Acceleration

Accelerations were calculated as the second derivative of the marker position data (Equation 10).

Equation 10: Calculating Acceleration

$$First\ Derivative\ (velocity, m/s) = \frac{\Delta d}{t}$$

$$Second\ Derivative\ (acceleration, m/s^2) = \frac{\Delta v}{t}$$

(t=time in seconds, d=distance moved by the marker between data capture points, v=velocity)

Root-mean-square (RMS) acceleration was calculated as the square root of the mean of the squared acceleration values in g.

Expected RMS acceleration was calculated from the expected frequency and amplitude of input using Equation 11 and Equation 12.

Equation 11: Acceleration from Displacement and Frequency

$$A = X(2\pi f)^2$$

(A=acceleration, X=displacement, f=frequency)

Equation 12: RMS Acceleration from Peak Acceleration

$$RMS\ Acceleration = \frac{Peak\ Acceleration}{\sqrt{2}}$$

5.2.4.3 Transmission

To determine the transmission of the WBV, the input signal was defined from the toe markers as these were in closest contact with the platform. For the Galileo 900 platform, the input signal was taken as the mean of the peak to peak (P2P) displacements recorded at the right and left toe. P2P displacement was used in this case as a clear sinusoidal signal was observed and displacement was the primary output of the motion capture system from the trajectories of each marker. For the Powerplate Pro 5 and Juvent 1000 platforms, the input signal had a lower signal to noise ratio, making the technique for determining P2P displacement more reliant on manual adjustments. To reduce the influence of the individual observer interpretation, the input was taken as the mean of the Fast Fourier Transform (FFT) peak at the right and left toe as the FFT peak could be determined without manual adjustment. To validate this approach, transmission for the Galileo 900 was reported firstly using P2P displacement and then using the FFT peak. Correlation between the two trends was assessed to determine consistency between the techniques.

Transmission was calculated as the percentage of the input signal recorded at a given landmark (Equation 13). To ensure the transmission percentage calculated using both P2P displacement and FFT peak were comparable, the two different measurements were compared using the data for the Galileo 900 platform.

Equation 13: Calculation of the transmission of whole body vibration to a given landmark

$$\text{Transmission Percentage} = \left(\frac{\text{P2P Displacement or FFT peak (landmark x)}}{\text{Input}}\right)\text{x100}$$

(P2P=Peak to Peak, FFT= Fast Fourier Transform)

5.2.5 Statistical Analysis

Comparison of the transmission percentage calculated using the P2P displacement and and the FFT peak was conducted using a Pearson correlation. Contralateral differences in peak to peak displacement and transmission of WBV were analysed using an independent T-Test. The influence of amplitude and frequency on the transmission of WBV was assessed using a two-way ANOVA with a Dunnett's T3 post hoc test. Significance was assumed at P< 0.05 or below.

All statistical tests were performed in IBM SPSS version 20.

5.3 Results

5.3.1 Manufacturer Specified Whole Body Vibration Settings

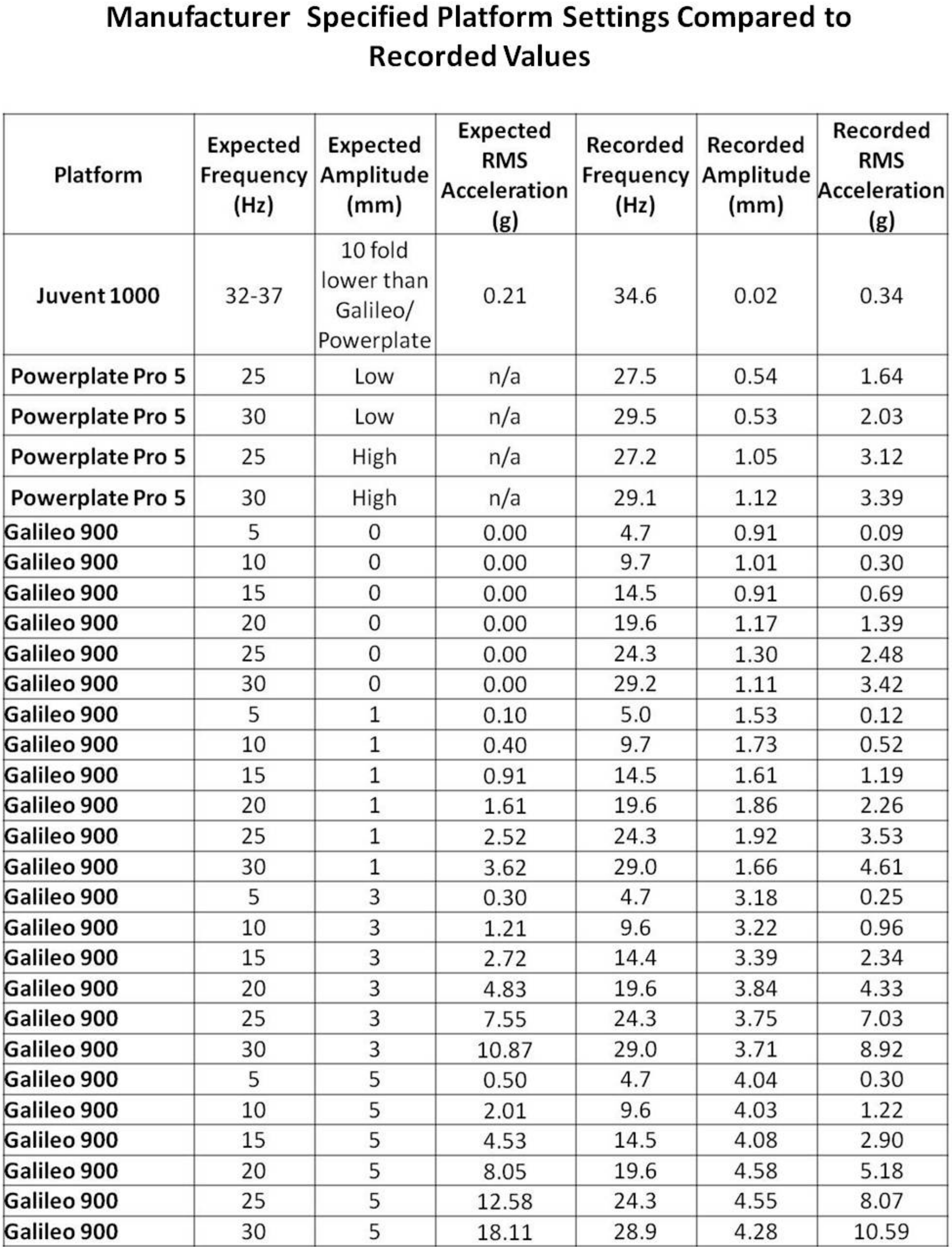

Manufacturer Specified Platform Settings Compared to Recorded Values

Platform	Expected Frequency (Hz)	Expected Amplitude (mm)	Expected RMS Acceleration (g)	Recorded Frequency (Hz)	Recorded Amplitude (mm)	Recorded RMS Acceleration (g)
Juvent 1000	32-37	10 fold lower than Galileo/ Powerplate	0.21	34.6	0.02	0.34
Powerplate Pro 5	25	Low	n/a	27.5	0.54	1.64
Powerplate Pro 5	30	Low	n/a	29.5	0.53	2.03
Powerplate Pro 5	25	High	n/a	27.2	1.05	3.12
Powerplate Pro 5	30	High	n/a	29.1	1.12	3.39
Galileo 900	5	0	0.00	4.7	0.91	0.09
Galileo 900	10	0	0.00	9.7	1.01	0.30
Galileo 900	15	0	0.00	14.5	0.91	0.69
Galileo 900	20	0	0.00	19.6	1.17	1.39
Galileo 900	25	0	0.00	24.3	1.30	2.48
Galileo 900	30	0	0.00	29.2	1.11	3.42
Galileo 900	5	1	0.10	5.0	1.53	0.12
Galileo 900	10	1	0.40	9.7	1.73	0.52
Galileo 900	15	1	0.91	14.5	1.61	1.19
Galileo 900	20	1	1.61	19.6	1.86	2.26
Galileo 900	25	1	2.52	24.3	1.92	3.53
Galileo 900	30	1	3.62	29.0	1.66	4.61
Galileo 900	5	3	0.30	4.7	3.18	0.25
Galileo 900	10	3	1.21	9.6	3.22	0.96
Galileo 900	15	3	2.72	14.4	3.39	2.34
Galileo 900	20	3	4.83	19.6	3.84	4.33
Galileo 900	25	3	7.55	24.3	3.75	7.03
Galileo 900	30	3	10.87	29.0	3.71	8.92
Galileo 900	5	5	0.50	4.7	4.04	0.30
Galileo 900	10	5	2.01	9.6	4.03	1.22
Galileo 900	15	5	4.53	14.5	4.08	2.90
Galileo 900	20	5	8.05	19.6	4.58	5.18
Galileo 900	25	5	12.58	24.3	4.55	8.07
Galileo 900	30	5	18.11	28.9	4.28	10.59

Table 12: Manufacturer specified (expected) settings vs recorded measures at the toe.

The Juvent 1000 frequency is within the specified range of 32-37Hz. The amplitude is 10-fold lower than those of the Powerplate Pro 5 or Galileo 900 and the RMS acceleration is 0.34g. The Powerplate frequency is within 1Hz at 30Hz however is 2.5Hz greater than the specified 25Hz. ‘Low’ yields amplitude of ~ 0.5mm and ‘High’ amplitude of ~1.1mm. Expected accelerations for Galileo 900 platform were calculated from the specified frequency and amplitude. All Galileo 900 frequencies are within 1Hz of expected. Amplitudes are 0.18mm to 1.3mm greater than expected for 0mm, 1mm and 3mm expected amplitudes and 0.42mm to 0.97mm lower than the 5mm expected amplitude. Expected accelerations are greater than those calculated due to the differences in recorded vs expected amplitudes and frequencies.

The Juvent 1000 platform delivers synchronous whole body vibration (WBV) at a frequency of 34.6Hz and amplitude of 0.02mm resulting in root mean square (RMS) accelerations of 0.34g, comparable to the expected frequency range of 32-37Hz and peak acceleration of 0.3g stated by the manufacturer (Table 12).

The measured frequencies of the Powerplate Pro 5 platform are closer in magnitude than expected from the manufacturer's designated 25 and 30Hz. Regardless of the amplitude (Low or High), the 25Hz setting delivered a frequency in the range of 27.2-27.5Hz while the 30Hz setting delivers synchronous WBV at frequencies of 29.1-29.5Hz (Table 12). At both 25Hz and 30Hz slightly higher frequencies are observed at 'Low' amplitude than 'High' amplitude.

The amplitude of the synchronous WBV Powerplate Pro 5 is specified as 'Low' or 'High' by the manufacturer. 'Low' produced an amplitude of 0.54mm at 27.5Hz and 0.53mm at 29.5Hz. 'High' produced an amplitude of 1.05mm at 27.2Hz and 1.12mm at 29.1Hz (Table 12). The Powerplate therefore produced RMS accelerations of 1.64g at 25Hz 'Low' setting, 2.03g at 30Hz 'Low' setting, 3.12g at 25Hz 'High' setting and 3.39g at 30Hz 'High' setting (Table 12).

The Galileo 900 platform delivers side alternating WBV with manufacturer specified settings of 5Hz-30Hz and amplitudes of 0mm-5mm. All recorded frequencies are within approximately 1Hz of the expected value and this was independent of the amplitude measured (Table 12).

Differences between expected and recorded amplitude are observed for the Galileo 900 platform. The recorded amplitude increases with frequency from 5-25Hz for expected amplitude 0mm and 1mm and from 5-20Hz at expected amplitudes of 3mm and 5mm. Recorded amplitudes are greater than expected at expected amplitudes of 0-3mm, however are lower than expected for an expected amplitude of 5mm. In all cases, the discrepancy between expected and recorded amplitude for the Galileo 900 platform is less at 5Hz-15Hz expected frequency than at 20Hz-30Hz expected frequency (Table 12).

As expected, the RMS accelerations recorded for the Galileo 900 platform increase with both increasing input frequency and amplitude (Table 12). The recorded RMS accelerations are different to those expected due to the discrepancies in expected and recorded frequencies and amplitudes. Recorded amplitudes are greater than expected at 0mm and 1mm settings but less than expected at the 5mm setting, whilst recorded frequencies are lower than expected in all cases. As the accelerations at 0mm and 1mm expected amplitudes are greater than expected and at 5mm expected amplitude are lower than expected, the discrepancy in the acceleration between recorded and expected is primarily influenced by the discrepancy in amplitude (Table 12).

The Galileo 900 platform delivers a range of accelerations from low magnitude accelerations (e.g. 0.12g at 5Hz 1mm input) to high magnitude accelerations (e.g 10.59g at 30Hz 5mm input) (Table 12).

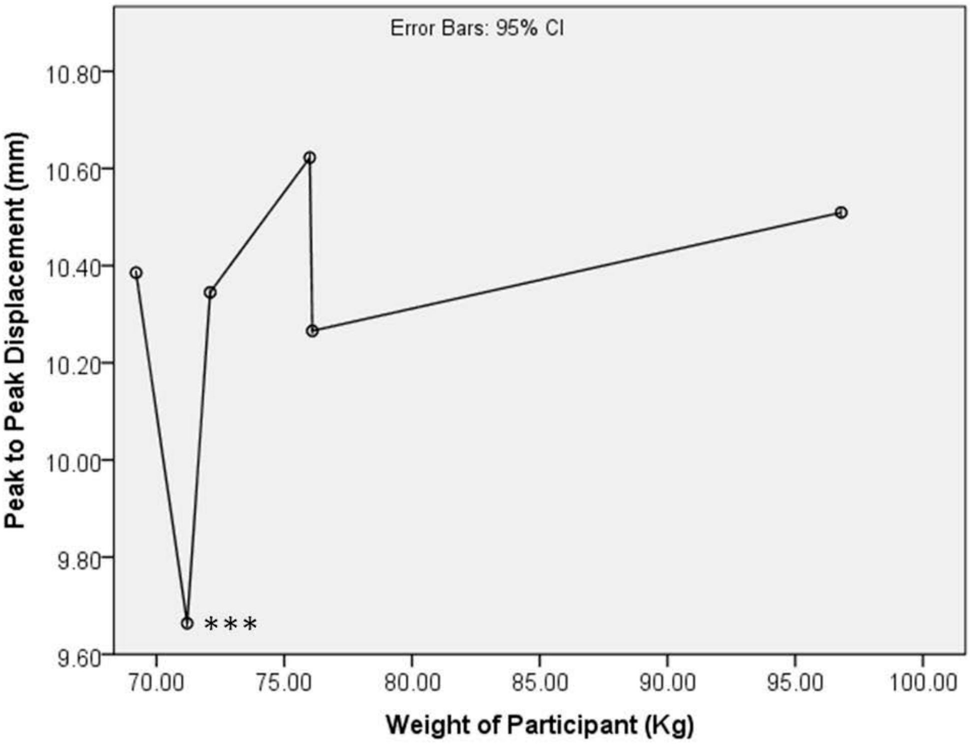

Figure 21: Effect of weight on the motion at the surface of the Galileo 900. The difference in the peak to peak displacements recorded at the surface of the Galileo 900 platform were compared between participants of differing weight using a two way annova with Dunnett's T3 post hoc test. Peak to peak displacement is presented as the mean with 95% confidence interval. There was no clear relationship between weight and the peak to peak displacement at the surface of the platform. However a significant difference between the peak to peak displacement at the surface of the platform for the participant weighing 72.1kg and all other participants was observed. Significance level is ***P<0.001.

When assessing the manufacturer specified settings, there was no participant stood on any of the platforms. When loaded with different weights, the platforms may have performed differently dependent upon the load. To determine whether the weight of the participants resulted in differences in input vibration, the input stimulus was compared between participants of differing weight (Figure 21). For the Galileo 900, peak to peak displacement was used as a measure of the input stimulus. No relationship between weight and the peak to peak displacement was observed. However for the participant weighing 72.1kg, the peak to peak displacement at the surface of the platform was significantly lower than that recorded for all other participants. In the case of the Powerplate Pro 5, no significant difference between the FFT peak at the platform was seen between participants of different weights (Figure 22).

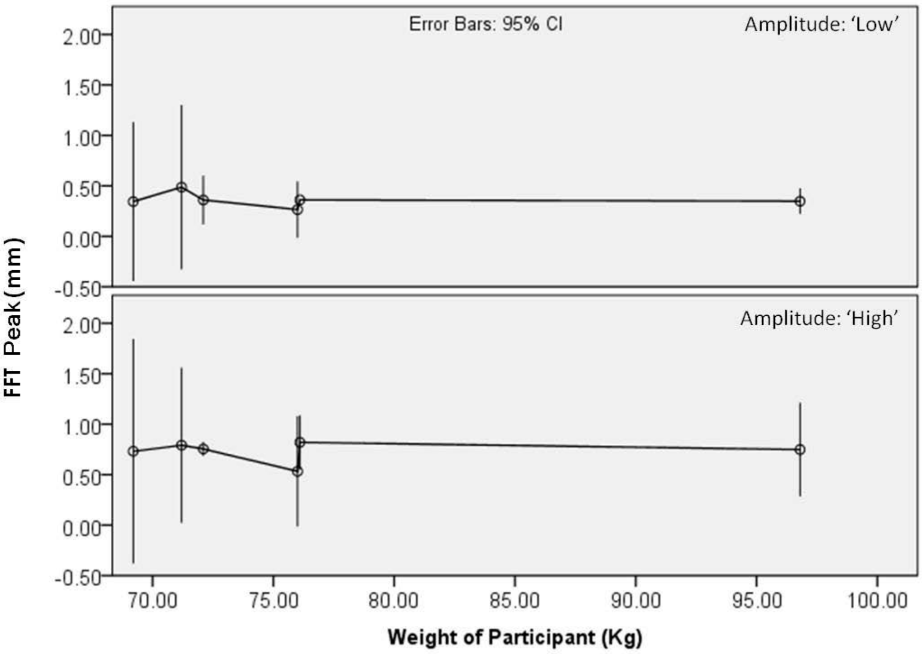

Figure 22: Effect of weight on the motion at the surface of the Powerplate Pro 5.

The difference in the FFT Peaks recorded at the surface of the Powerplate Pro 5 platform were compared between participants of differing weight using a two way annova with Dunnett's T3 post hoc test. FFT peak is presented as the mean with 95% confidence interval. There was no significant difference between the FFT Peaks at the surface of the platform for any of the participants

5.3.2 Accelerations at Anatomical Landmarks Generated by Whole Body Vibration of Different Frequencies and Amplitudes

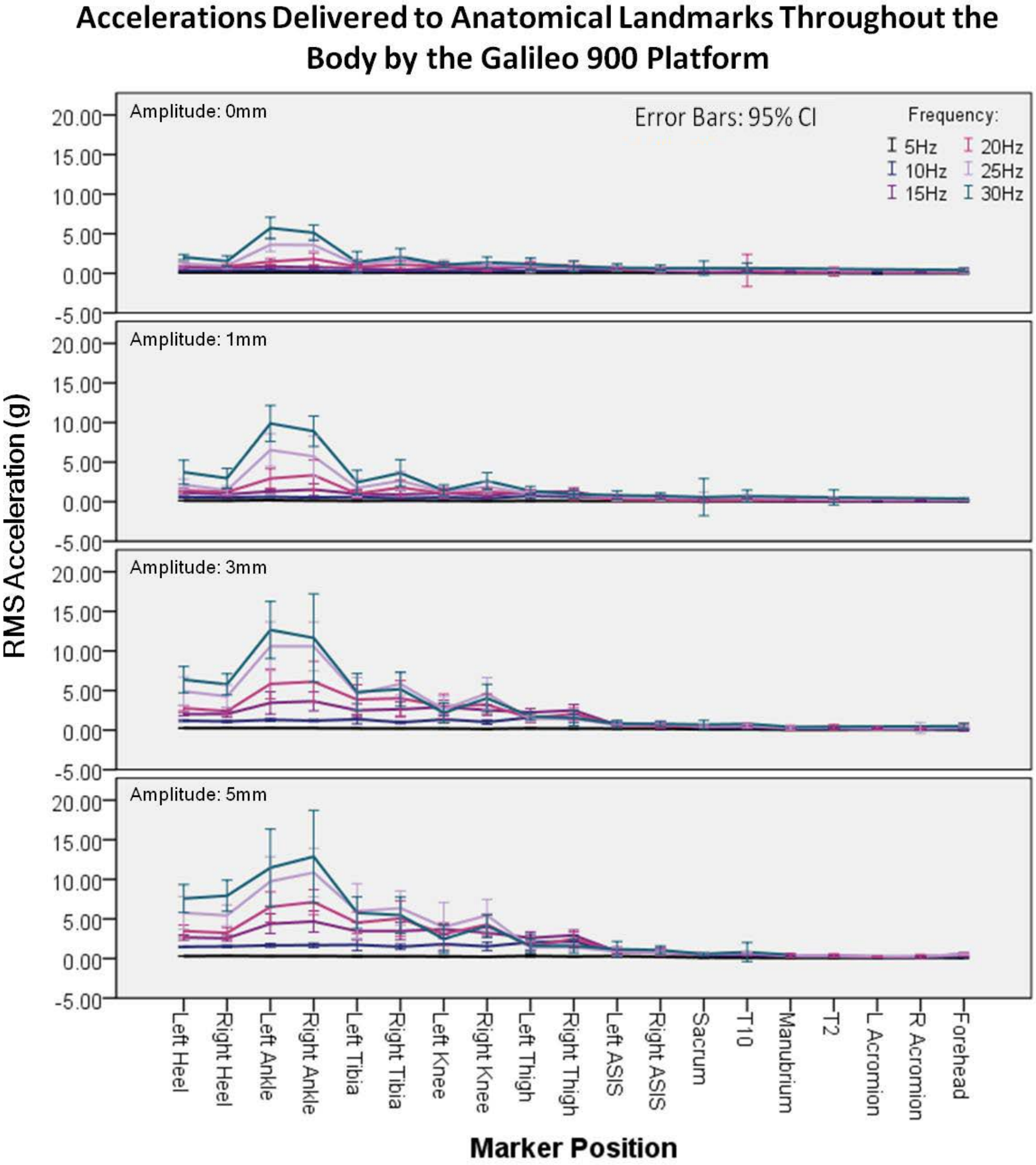

Figure 23: Accelerations delivered by the Galileo 900 platform at frequencies between 5Hz and 30Hz and amplitudes between 0mm and 5mm.

Accelerations were calculated from displacements of the markers recorded using the Vicon Nexus motion capture system. The magnitude of the acceleration increases from the heel to the ankle before decreasing up to the forehead. Maximum root mean squared (RMS) acceleration ranges from 0.1g at the heel and ankle 5Hz0mm to 12.87g at the ankle 30Hz5mm.The smallest acceleration detected is 0.03g in the torso at 5Hz0mm. ASIS= Anterior Superior Iliac Spine, T10=10th Thoracic Vertebrae, T2= 2nd Thoracic Vertebrae, L&R Acromion= Left and Right Acromion Process respectively. Error bars: 95% confidence intervals.

As expected the RMS acceleration increases with increasing amplitude and/or frequency (Figure 26). As input amplitude increases, so does the RMS acceleration for a given frequency (Figure 26, Figure 23). As input frequency increases, the RMS acceleration for a given input amplitude also increases (Figure 26, Figure 23). In all cases, the greatest RMS acceleration observed for a given frequency is at the ankle at an input amplitude of 5mm (Figure 23 Amplitude: 5mm). The relationship between amplitude, frequency and acceleration is described further in terms of transmission (Chapter 0).

In the lower limb, RMS accelerations delivered by the Galileo 900 platform increase from the heel to the ankle before decreasing from the ankle to the ASIS at most frequencies and amplitudes (Figure 23).

For the lowest frequency (5Hz), the greatest RMS is 0.32g, observed at the right heel at 5Hz 5mm (Figure 23 Amplitude: 5mm). This acceleration is not dissimilar to the input RMS acceleration of 0.3g (Table 12) and the difference between the heel and ankle that is observed at higher frequencies is not observed at 5Hz 5mm, with a RMS acceleration of 0.3g being observed at the ankle (Figure 23 Amplitude:5mm).

The greatest RMS acceleration for a given amplitude increases from 5Hz to 30Hz, with the greatest RMS acceleration of 12.87g observed at the right ankle at 30Hz5mm (Figure 23 Amplitude: 5mm). This is slightly greater than the RMS acceleration of 10.59g at input (Table 12).

In the torso, great attenuation of the WBV signal is observed. For the 5Hz 5mm input, the input RMS acceleration of 0.3g decreases to values between 0.07g and 0.11g in the torso (Figure 23 Amplitude:5mm). The smallest RMS acceleration observed at 5Hz is 0.03g in the torso at 5Hz 0mm (Figure 23 Amplitude: 0mm).

At higher frequencies, greater RMS accelerations are observed in the torso. The smallest RMS acceleration observed at 30Hz is 0.38g at the forehead at 30Hz1mm, similar to that of the input at 5Hz0mm (Figure 23 Amplitude:0mm, Figure 23 Amplitude: 1mm).

At the anterior superior iliac spine (ASIS) and spine (Sacrum, T10,T2), the greatest RMS accelerations generated are at 30Hz5mm, where 1.17g and 1.07g were recorded at the left and right ASIS respectively, 0.57g was recorded at the sacrum and 0.81g was recorded at the 10th thoracic vertebrae (T10) (Figure 23 Amplitude: 5mm). The smallest RMS accelerations delivered to the ASIS and spine are at 5Hz0mm where RMS accelerations equal to or less than 0.08g are observed at the ASIS, sacrum, T10 and T2 (Figure 23 Amplitude: 0mm).

As with the Galileo 900 platform, the Powerplate Pro 5 platform generates greater RMS accelerations for a given frequency as input amplitude increases and also for a given amplitude as input frequency increases (Figure 24).

Again, the greatest RMS accelerations generated by the Powerplate Pro 5 are observed at the ankle, with values exceeding the accelerations at the heel. In the case of 25Hz and 30Hz 'High', the RMS accelerations of 4.07g and 6.38g respectively at the ankle are slightly higher than those seen during WBV on the Galileo 900 at similar input frequencies and amplitudes (Table 12 Galileo 900: 25Hz0mm & 30Hz0mm), for which 3.61g at 25Hz0mm and 5.72g at 30Hz0mm are generated at the ankle (Figure 23 Amplitude:0mm).

At the level of the ASIS the RMS accelerations are attenuated compared to those at the ankle, however in the case of 25Hz and 30Hz High, are still greater than those delivered by the Galileo 900 at similar amplitude and frequency.

For the 'Low' amplitude inputs, accelerations at the ASIS and spine are lower than those at the 'High' amplitude inputs and, with the exception of T2, the RMS accelerations observed at 25Hz 'High' are the greatest generated at these sites by the Powerplate Pro 5.

Whilst RMS accelerations are attenuated in the torso, the attenuation occurs to a lesser extent than that observed for the Galileo 900.

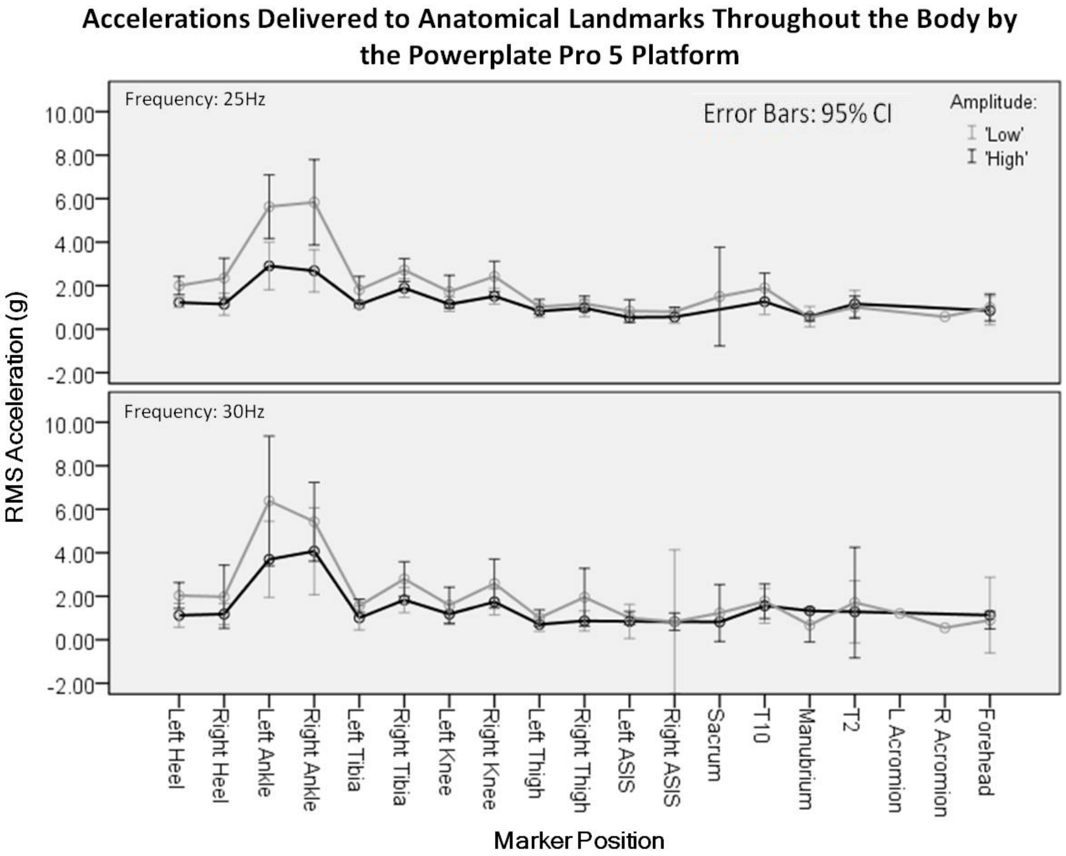

Figure 24: Accelerations delivered by the Powerplate Pro 5 platform at frequencies of 25Hz and 30Hz and amplitude settings of 'Low' and 'High'.

Accelerations were calculated from displacements of the markers recorded using the Vicon Nexus motion capture system. The accelerations are reported as means with error bars showing the 95% confidence interval. The magnitude of the acceleration increases from the heel to the ankle before decreasing up to the forehead with a slight discrepancy between the markers on the left and right leg. Maximum root mean squared (rms) acceleration ranges from 2.9g at the ankle at 25Hz 'Low' to 6.4g at the ankle at 30Hz 'High'.The smallest acceleration detected is 0.5g in the torso at 25Hz 'High' and the ASIS at 25Hz 'Low'. ASIS= Anterior Superior Iliac Spine, T10=10th Thoracic Vertebrae, T2= 2nd Thoracic Vertebrae, L&R Acroimion= Left and Right Acromion Process respectively. Error bars: 95% confidence intervals.

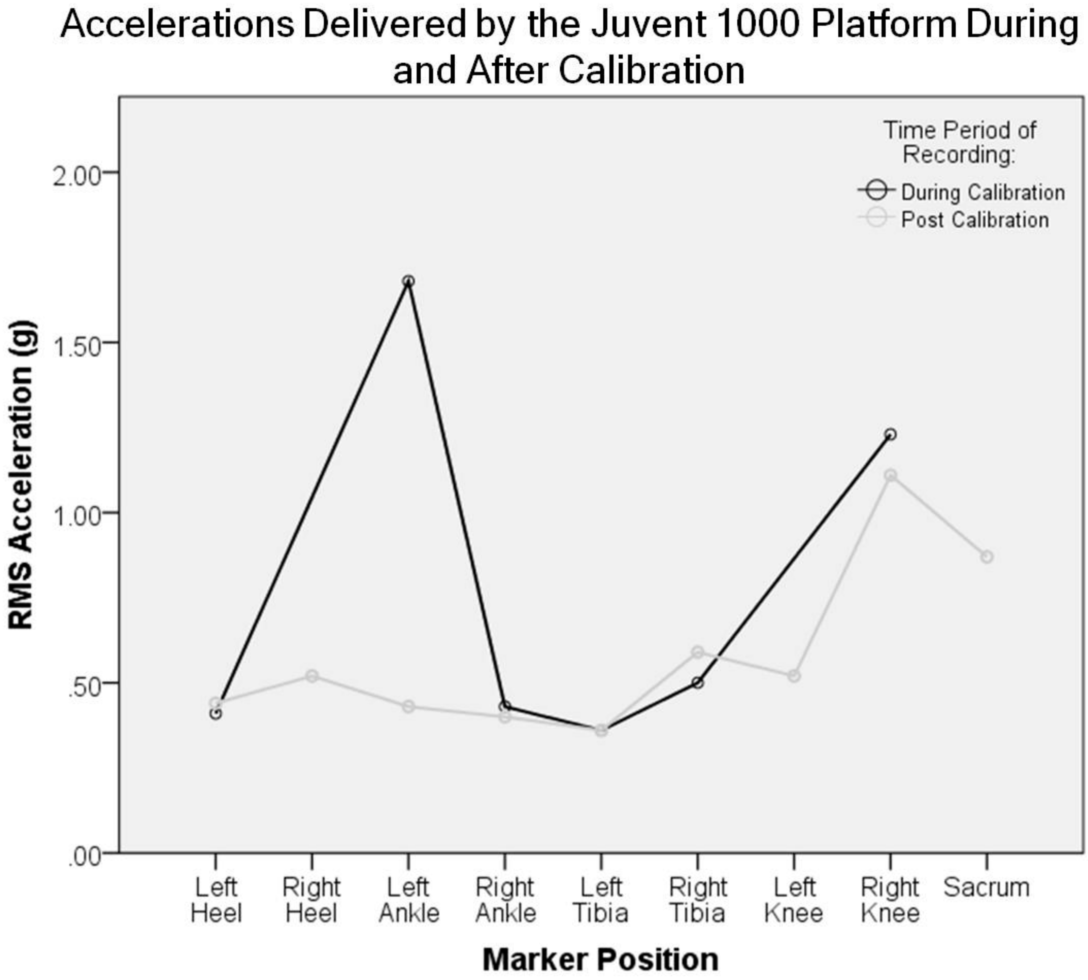

Figure 25: Juvent 1000 during and after calibration.

Root mean square (RMS) accelerations delivered by the Juvent 1000 platform at frequencies between 32-37Hz and acceleration in the order of 0.3g, during and after calibration of the platform. Accelerations were calculated from displacements of the markers recorded using the Vicon Nexus motion capture system. The trend of RMS accelerations generated by the Juvent 1000 platform differs only slightly between the period during and the period after calibration of the platform. The greatest difference is at the left ankle, where the RMS acceleration during calibration is greater. At the left knee and sacrum, there is a RMS acceleration during calibration but not after calibration. ASIS= Anterior Superior Iliac Spine, T10=10th Thoracic Vertebrae, T2= 2nd Thoracic Vertebrae, L&R Acroimion= Left and Right Acromion Process respectively.

During calibration, the Juvent 1000 generates RMS accelerations comparable to those generated by the platform after calibration (Figure 25). The greatest difference in RMS acceleration observed between the calibration period of the Juvent 1000 and the period after calibration is seen at the left ankle where, during calibration, a RMS acceleration 1.25g greater than after calibration is generated (Figure 25). At the left knee and the sacrum, RMS acceleration generated by the Juvent 1000 is seen during but not after calibration (Figure 25).

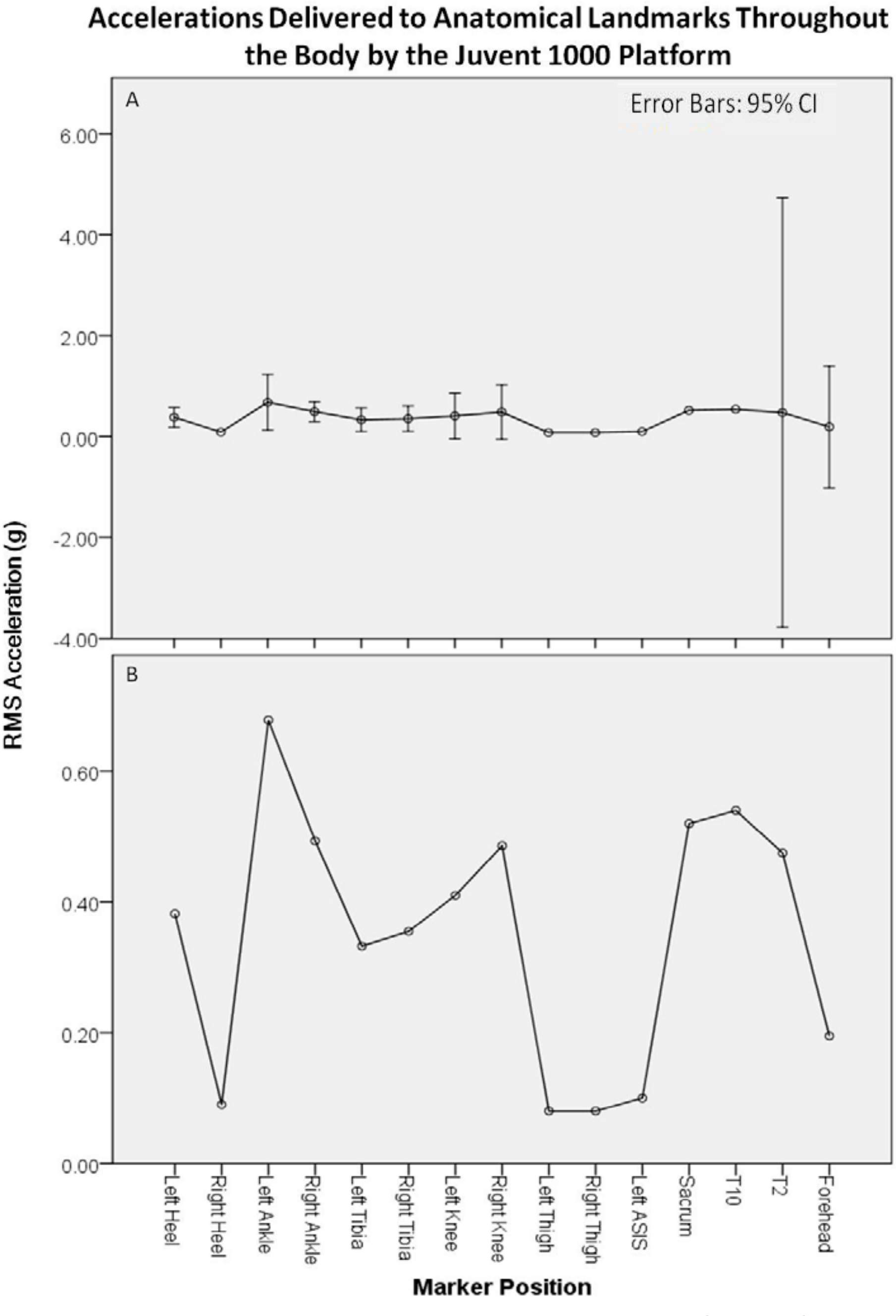

Figure 26: Accelerations delivered by the Juvent 1000 platform at frequencies between 32-37Hz and acceleration in the order of 0.3g.

A) Root-Mean-Square (RMS) accelerations with 95% confidence intervals. B) RMS accelerations. Accelerations were calculated from displacements of the markers recorded using the Vicon Nexus motion capture system. The magnitude of accelerations increase from the heel to the ankle and the tibia to the knee, before decreasing to the ASIS. Greater accelerations are seen at the sacrum compared to the ASIS and there is a decrease in accelerations from the sacrum to the forehead. Accelerations range from 0.08g at the thigh to 0.72g at the sacrum. ASIS= Anterior Superior Iliac Spine, T10=10th Thoracic Vertebrae, T2= 2nd Thoracic Vertebrae, L&R Acromion= Left and Right Acromion Process respectively. Error bars: 95% confidence

The confidence intervals associated with the RMS acceleration generated at the right heel, right knee, thighs, left ASIS, sacrum, T2 and forehead by the Juvent 1000 all cross zero. At the right heel, right knee, sacrum and T2 the confidence intervals are also large (Figure 26: A).

The greatest RMS acceleration generated by the Juvent 1000 platform is observed at the ankle, with magnitudes of 0.68g and 0.49g at the left and right ankle respectively (Figure 26: B). This is greater than the input acceleration of 0.34g (Table 12: Juvent 1000). In the lower leg, the RMS acceleration is greater at the ankle and knee than the heel, tibia and thigh, with a smaller RMS acceleration at the thigh than at the tibia and smaller RMS acceleration at the tibia than at the heel (Figure 26). At the sacrum, the RMS acceleration is greater than that at the ASIS with a magnitude of 0.61g, similar to that at the ankle (Figure 26: B).

The 0.1g RMS acceleration at the ASIS is lower than at input, however at the sacrum, T10 and T2, the RMS accelerations of 0.61g, 0.54g and 0.47g respectively are greater than at input and similar to those observed at the ankle and knee (Figure 26: B).

Compared to the Powerplate Pro 5, the RMS accelerations at the ASIS and spine generated by the Juvent 1000 are much smaller, with values around half of those generated by the Powerplate Pro 5 (Figure 24, Figure 26 B). Compared with the Galileo 900 at input frequencies of 5Hz and 10Hz at all input amplitudes and 15Hz when the input amplitude is 0mm, 1mm or 3mm, the RMS acceleration generated at the ASIS and spine by the Juvent 1000 is greater by up to a factor of 10. At Galileo 900 input settings of 15Hz5mm and above, RMS accelerations generated at the ASIS and spine by the Juvent 1000 are similar in magnitude (Figure 23, Figure 26 B). For the Galileo 900 settings which result in RMS accelerations at the ASIS and spine of similar magnitude to the Juvent 1000, the RMS accelerations at input, the heel and the ankle are much greater than those generated at the same location by the Juvent 1000 (Figure 23, Figure 26 B). Galileo 900 settings of 5Hz 5mm and 10Hz 0mm produce RMS accelerations comparable to those generated by the Juvent 1000 at input, the heel and the ankle. For these settings, the RMS accelerations at the ASIS are greater that those generated by the Juvent 1000, with magnitudes at 5Hz5mm of 0.29g and 0.2g and at 10Hz0mm of

0.41g and 0.23g at the left and right ASIS respectively (Figure 23, Figure 26 B). Above the ASIS, accelerations generated by the Galileo 900 at 5Hz5mm and 10Hz0mm are smaller than those generated by the Juvent 1000, with RMS acceleration ranging between 0.07g and 0.13g (Figure 23, Figure 26 B).

5.3.3 Contralateral Differences in Whole Body Vibration Transmission

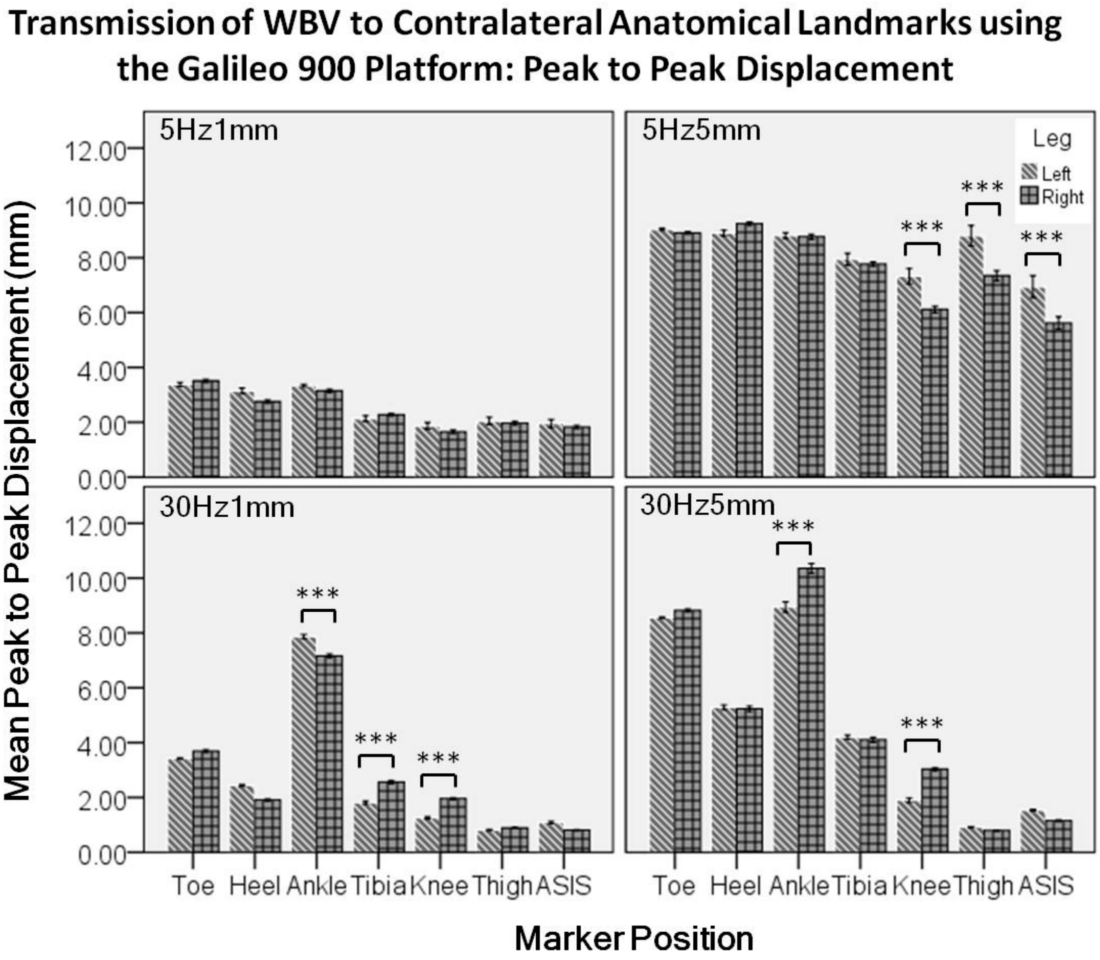

Figure 27: Contralateral differences in peak to peak (P2P) displacements generated by the Galileo 900 platform.

There are small but significant differences between the P2P displacements observed on the right and left sides of the body at 5Hz5mm, 30Hz1mm and 30Hz5mm. ASIS = Anterior Superior Iliac Spine. Side to side differences were assessed using an independent T-test, *P<0.05, ** P<0.01, ***P<0.001.

The peak to peak (P2P) displacement delivered to the left and right leg of participants when stood on the Galileo 900 platform was significantly different at several sites at 30Hz frequency 1mm amplitude, 5Hz frequency 5mm amplitude and 30Hz frequency 5mm amplitude WBV settings (Figure 27). The P2P displacement at the left and right knee is significantly different in all three cases, as is the P2P displacement at the left and right ankle at a frequency of 30Hz (Figure 27).

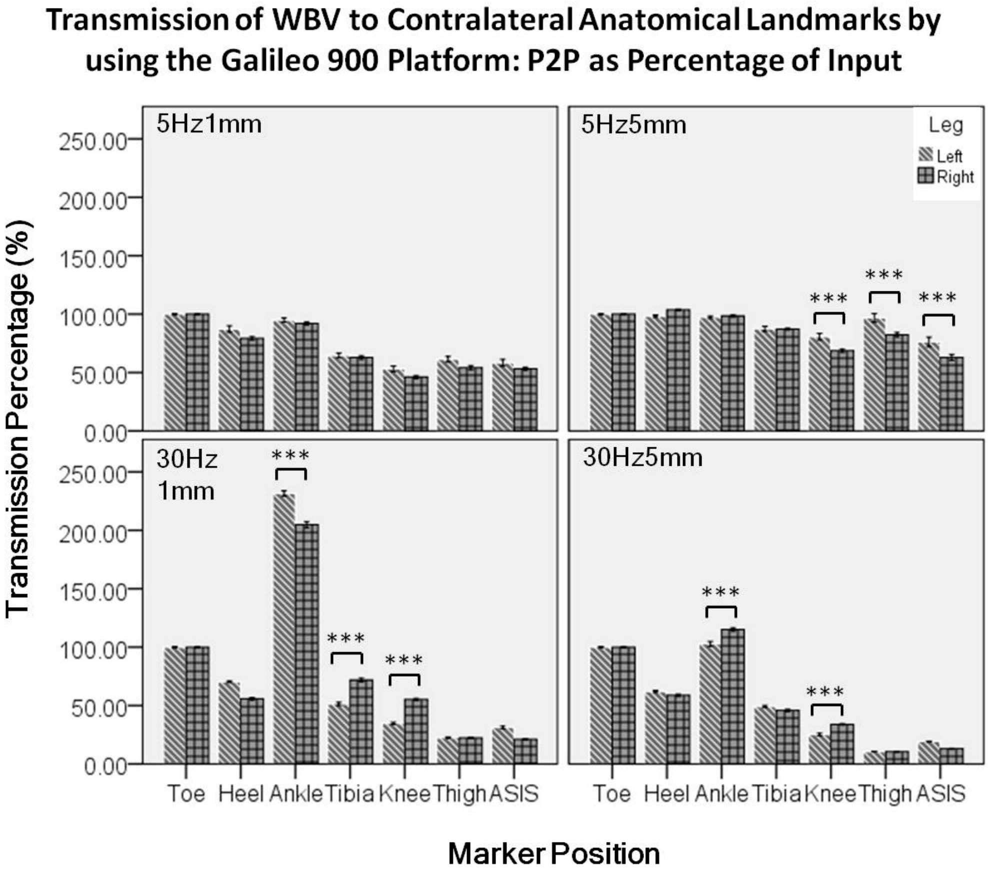

Figure 28: Contralateral differences in peak to peak (P2P) displacements generated by the Galileo 900 platform.

Transmission percentage is the P2P displacement taken as a percentage of the input. Mean transmission percentage with 95% confidence intervals are presented. There are small but significant differences between the transmission percentage observed on the right and left sides of the body at 5Hz5mm, 30Hz1mm and 30Hz5mm. ASIS = Anterior Superior Iliac Spine. Side to side differences were assessed using an independent T-test, * $P<0.05$, ** $P<0.01$, ***$P<0.001$.

When the P2P displacement generated by the Galileo 900 platform was represented as a percentage of the input stimulus (taken as the mean P2P displacement at the toe), the contralateral differences with a significant difference between the left and right heel, knee and anterior superior iliac spine at all WBV settings. The toe markers no longer showed a difference at any WBV setting' with: 'remained at the sites seen when P2P displacement was plotted (Figure 28).

Percentage transmission, calculated from FFT magnitude as a percentage of the input, show fewer significant side to side differences for the Powerplate Pro 5 recordings, with a significant difference observed at the tibia at 25Hz 'Low' and 'High', the knee at 25Hz 'High' and the ASIS at 30Hz 'Low' (Figure 29). No significant side to side differences in percentage transmission were observed for the Juvent 1000 platform (Figure 30).

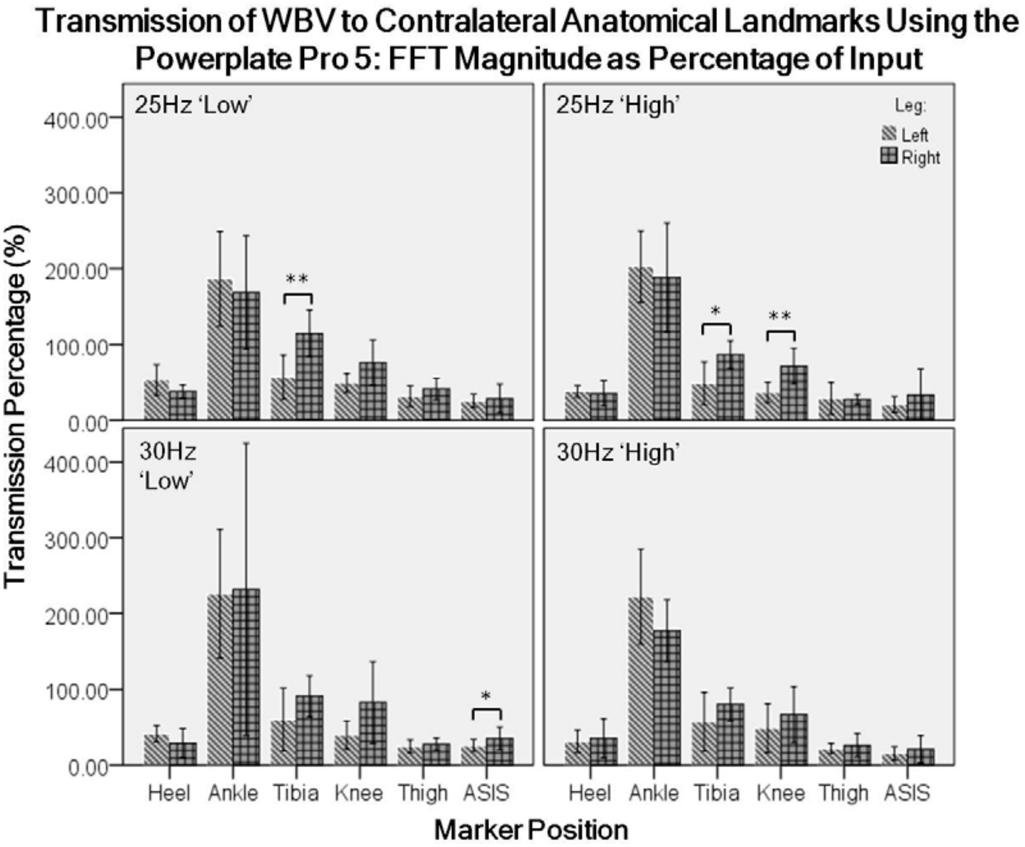

Figure 29: Contralateral differences in whole body vibration transmission on the Powerplate Pro 5 platform.

A fast Fourier transform of displacements measured using a Vicon motion capture system was performed and the magnitude at each marker represented as a percentage of that at input. Mean transmission percentage with 95% confidence intervals are presented. Markers were positioned bilaterally at anatomical landmark, ASIS = Anterior Superior Iliac Spine Side to side differences were assessed using an independent T-test, * P<0.05, ** P<0.01, ***P<0.001. Side to side differences were observed at the Tibia at 25Hz Low and 25Hz High, the knee at 25Hz High and the ASIS at 30Hz Low.

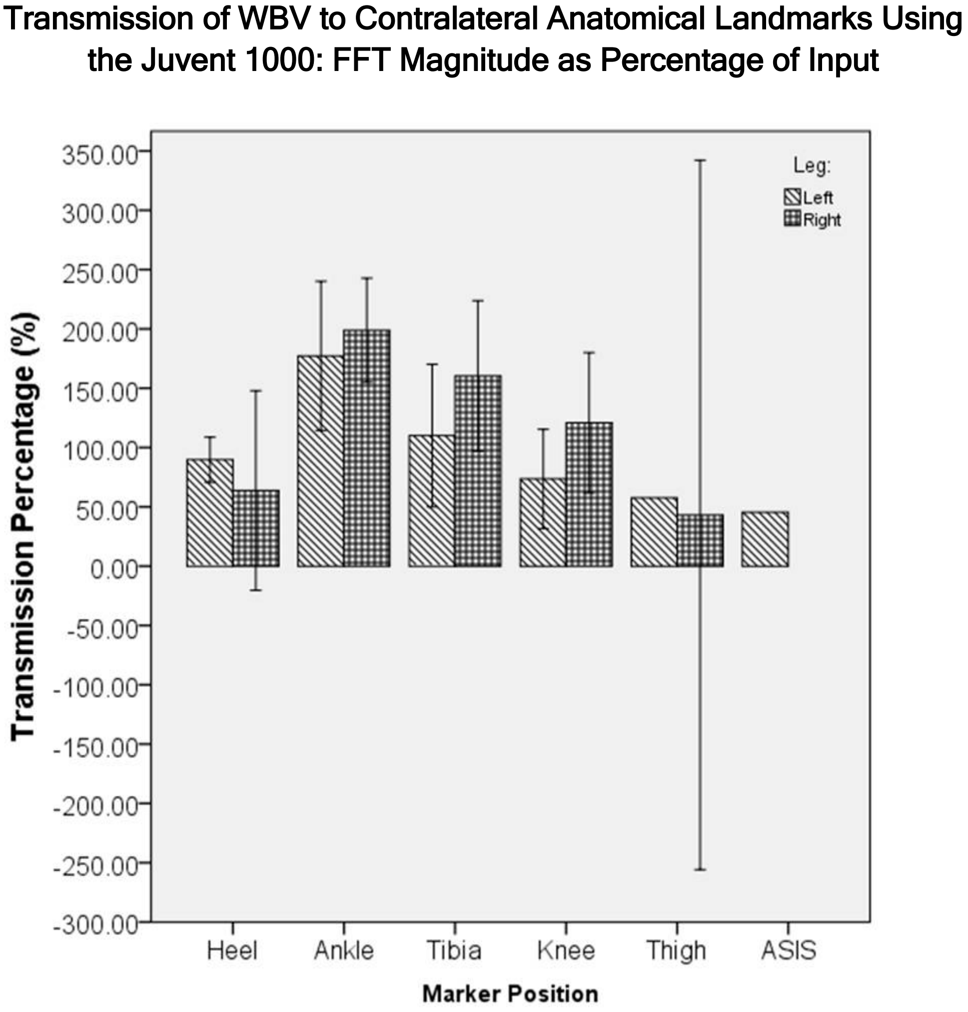

Figure 30: Contralateral differences in whole body vibration transmission on the Juvent 1000 platform.

A fast Fourier transform (FFT) of the displacements measured using a Vicon motion capture system was performed and the magnitude at each marker represented as a percentage of that at input. Mean transmission percentage with 95% confidence intervals are presented. Markers were positioned bilaterally at anatomical landmarks. ASIS = Anterior Superior Iliac Spine. Side to side differences were assessed using an independent T-test, no significant difference was found.

5.3.4 Transmission of Whole Body Vibration: Galileo 900 Platform

5.3.4.1 Transmission of Whole Body Vibration at Anatomical Landmarks Compared to Input

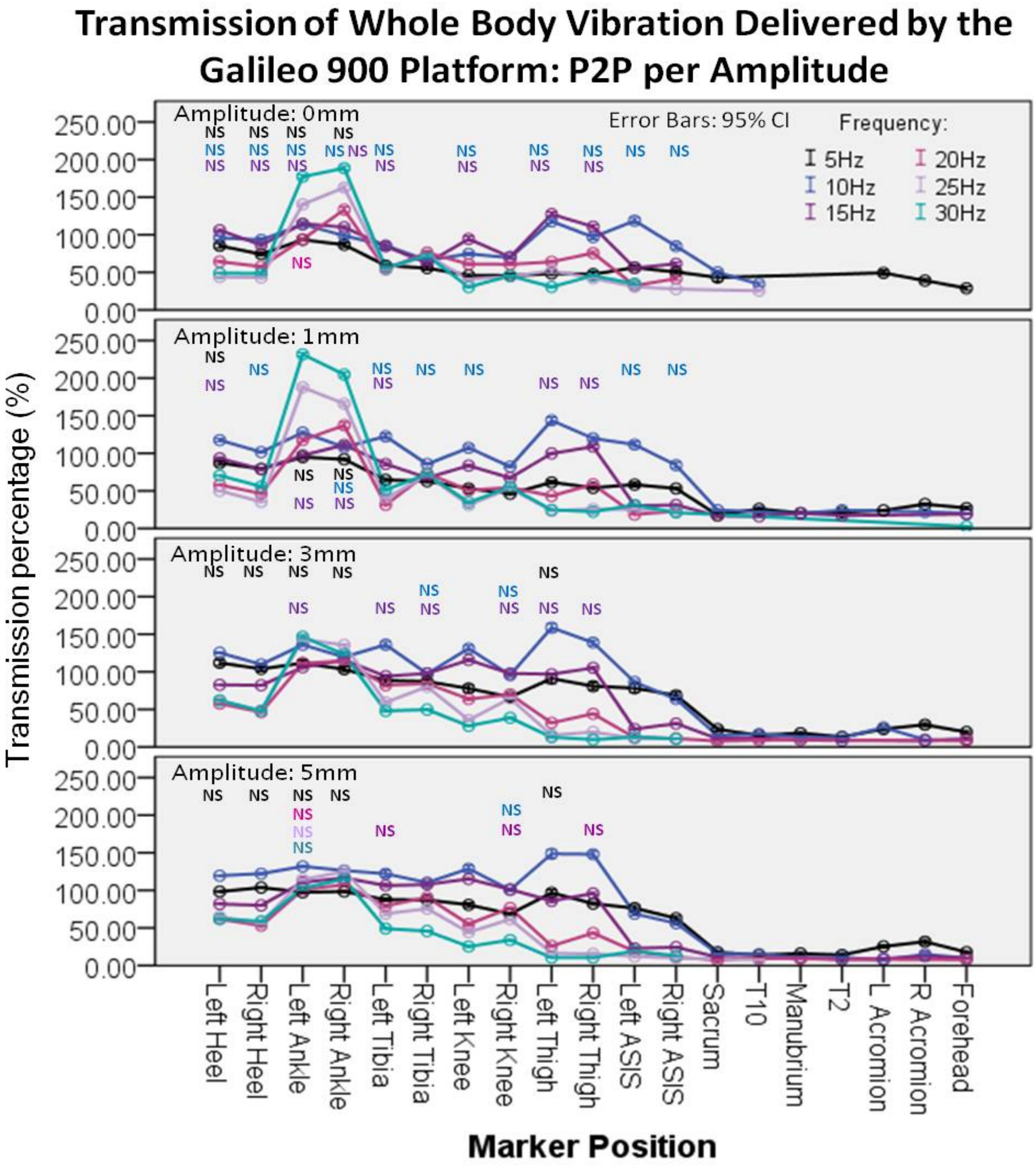

Figure 31: The effect of frequency on the transmission of whole body vibration (WBV) delivered by the Galileo 900 platform compared to input.

The Galileo delivered side alternating WBV at frequencies of 5-30Hz and amplitudes of 0-5mm. Percentage of WBV transmitted to anatomical landmarks was calculated from peak to peak displacements measured using a Vicon motion capture system. Mean transmission percentage with 95% confidence intervals are presented. Transmission decreases from input to forehead, with deviations in this trend at the ankle and thigh. The exact trend of the transmission of vibration from input to forehead appears to show amplitude dependence. L & R refer to the left and right respectively. ASIS = anterior superior iliac spine. Differences between vibration transmission at input and at each anatomical landmark were assessed using a one-way ANOVA with Dunnett's T3 post-hoc test. All outcomes significant at $p<0.001$ unless indicated. NS=Not Significant, *$p<0.05$, ** The transmission of WBV delivered using the Galileo 900 platform is significantly attenuated above the anterior superior iliac spine (ASIS) at all frequencies and amplitudes investigated (Figure 31 &Figure 32).

In the lower limb, transmission increases from the heel to the ankle, before generally decreasing from the ankle to the ASIS, with a significant decrease compared to input at most anatomical landmarks studied. At the ankle, there is greater transmission than at the heel or tibia and the transmission at the ankle is also significantly different to the input at frequencies above 15Hz at all amplitudes ($P<0.001$ with the exception of the left ankle at 20Hz0mm and at 20,25 and 30Hz 5mm which show no significant difference (Figure 31)). At the higher frequencies of 20-30Hz, there is a significant increase in transmission compared to input; whereas at lower frequencies there is either no significant difference compared to input or the observed difference in is a decrease..

At the thigh, there is greater transmission than at the knee or ASIS and the transmission is significantly different to the input at the majority of amplitudes and frequencies studied ($P<0.001$ with the exception of the left thigh at 10&15Hz 0mm, 15Hz 1mm, 5&15Hz 3mm, 5Hz 5mm and the right thigh at 10&15Hz0mm, 15Hz1mm, 15Hz3mm and 15Hz5mm where there is no significant difference (Figure 31)). In this instance, the transmission is significantly greater than at input for the lower frequencies between 5-15Hz, whereas at higher frequencies the transmission is significantly lower than at input.

The amplitude of the input appears to have less bearing on the attenuation pattern of the WBV signal (Figure 32)). At frequencies up to 20Hz, attenuation shows a similar pattern for all amplitude inputs. At 25 and 30Hz, 0mm and 1mm amplitude inputs show greater transmission at the ankle than 3mm and 5mm amplitude inputs, however all amplitudes can be show to result in greater transmission at the ankle than at input (Figure 32).

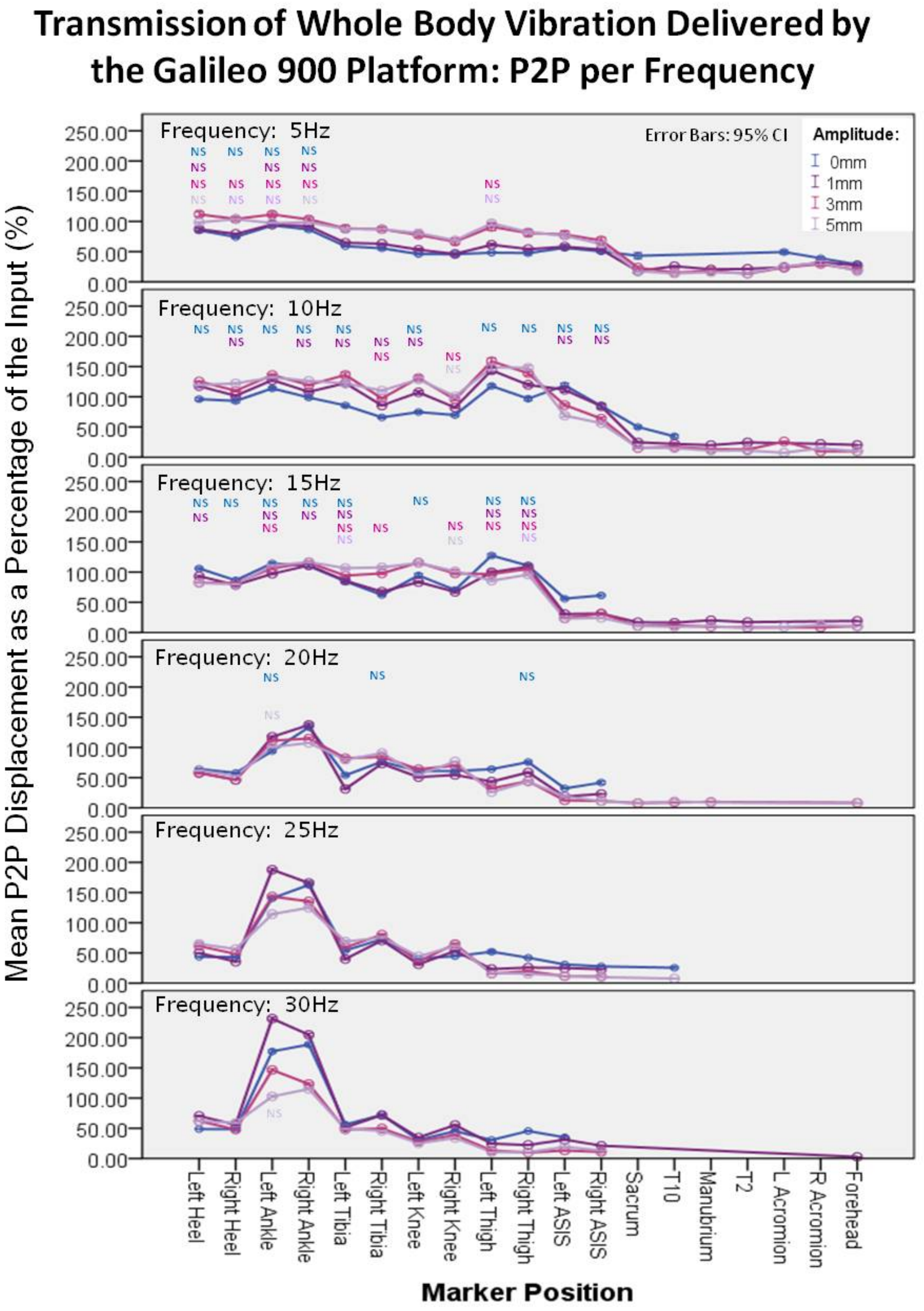

Figure 32: The effect of amplitude on the transmission of whole body vibration (WBV) delivered by the Galileo 900 platform compared to input.

The Galileo delivered WBV at frequencies of 5-30Hz and amplitudes of 0-5mm. Percentage of WBV transmitted to anatomical landmarks was calculated from peak to peak displacements measured using a Vicon motion capture system. Mean transmission percentage with 95% confidence intervals are presented. Transmission decreases from input to forehead, with deviations in this trend at the ankle and thigh. The exact trend of the transmission of vibration from input to forehead appears to show frequency dependence. L & R refer to the left and right respectively. ASIS = anterior superior iliac spine. Differences between vibration transmission at input and at each anatomical landmark were assessed using a one-way ANOVA with Dunnett's T3 post-hoc test. All outcomes significant at p<0.001 unless indicated. NS=Not Significant, *p<0.05, ** p<0.01.

5.3.5 Using the Fast Fourier Transform to Determine the Transmission of Whole Body Vibration

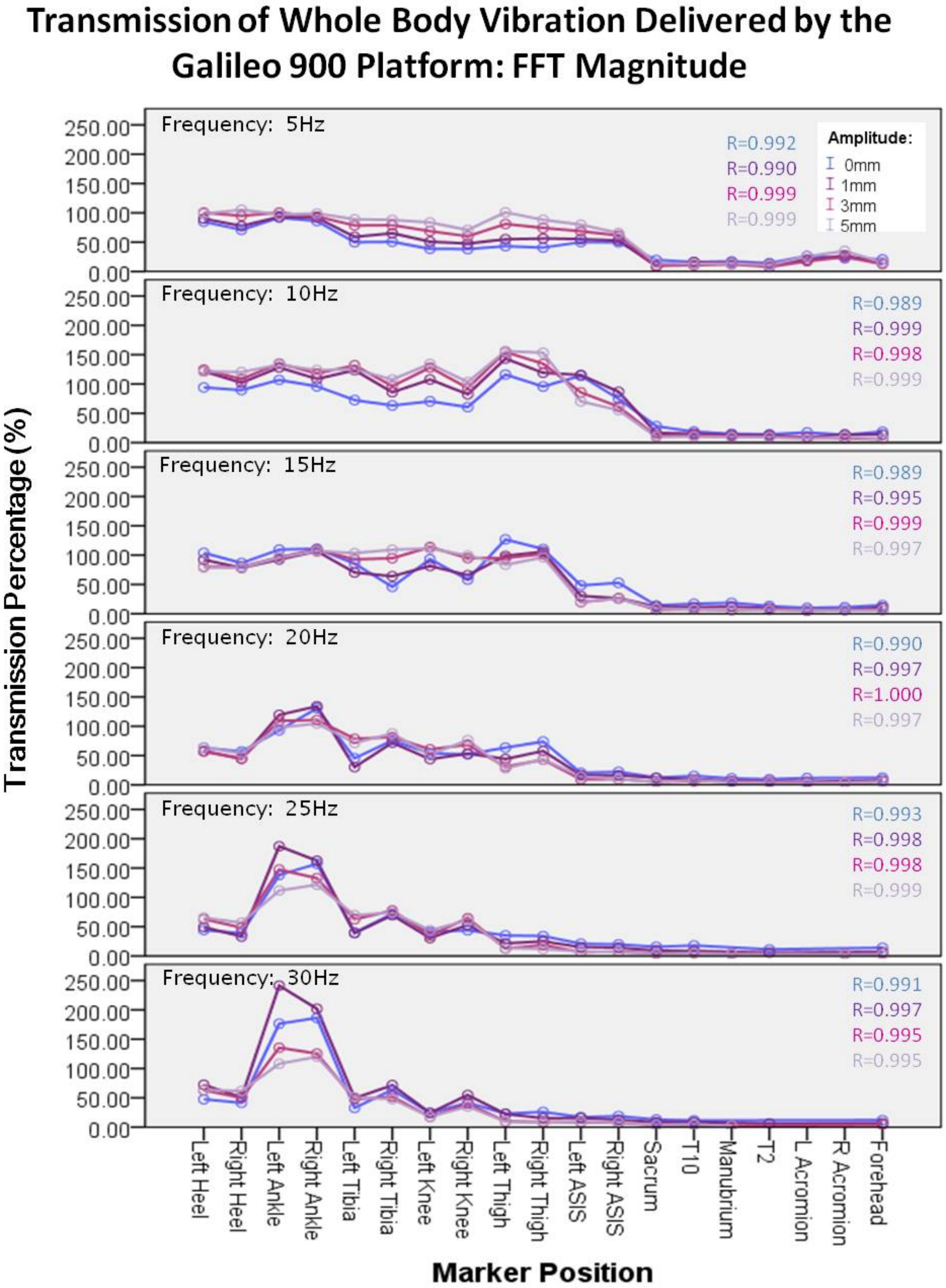

Figure 33: Transmission of whole body vibration (WBV) delivered by the Galileo 900 platform at frequencies of 5-30Hz and amplitudes of 0-5mm.

A fast Fourier transform (FFT) of the displacements measured using a Vicon motion capture system was performed and the magnitude at the input frequency was recorded for each marker. Mean transmission percentage with 95% confidence intervals are presented. The transmission based on FFT magnitude closely is strongly positively correlated with the transmission based on peak to peak displacement. Pearson's correlation to compare transmission based on FFT magnitude and transmission based on peak to peak displacement was performed. There were significant R values between 0.989 and 1.000 in all cases ($P<0.001$). L & R refer to the left and right respectively. ASIS = anterior superior iliac spine.

The trend observed when transmission is assessed using the FFT magnitude at the input frequency (Figure 33) closely matches the trend seen when transmission is assessed based on peak to peak displacements (Figure 31, Figure 32, Figure 33). The two trends are significantly positively correlated with R values ranging between 0.989 and 1.000 (P<0.001) in all cases (Figure 33).

5.3.5.1 Frequency Dependency of Whole Body Vibration Transmission

When observing the trend of WBV transmission with the inputs grouped by frequency, it appears that the transmission percentage at a given marker is dependent on the input frequency. At the ankle, transmission percentage increases as frequency increases whereas at markers above the ankle an inverse relationship between frequency and transmission percentage is observed (Figure 34).

At a 0mm input amplitude, the transmission of the vibration to the knee, thigh and ASIS shows clear frequency dependence, with an increase in transmission from 5Hz to 15Hz input frequency (5Hz-10Hz at the ASIS) and a decrease from 15Hz to 30Hz input frequency (10Hz-30Hz at the ASIS) (P< 0.001 as shown in Figure 34 with the right knee showing no significant trend) (Figure 34 Amplitude: 0mm).

At 1mm, 3mm and 5mm input amplitudes, the trend is generally the same, however the initial increase in transmission is only between input frequencies of 5Hz and 10Hz and there is a significant decrease in transmission from 10Hz to 30Hz (Figure 34 Amplitude: 1mm, 3mm, 5mm).

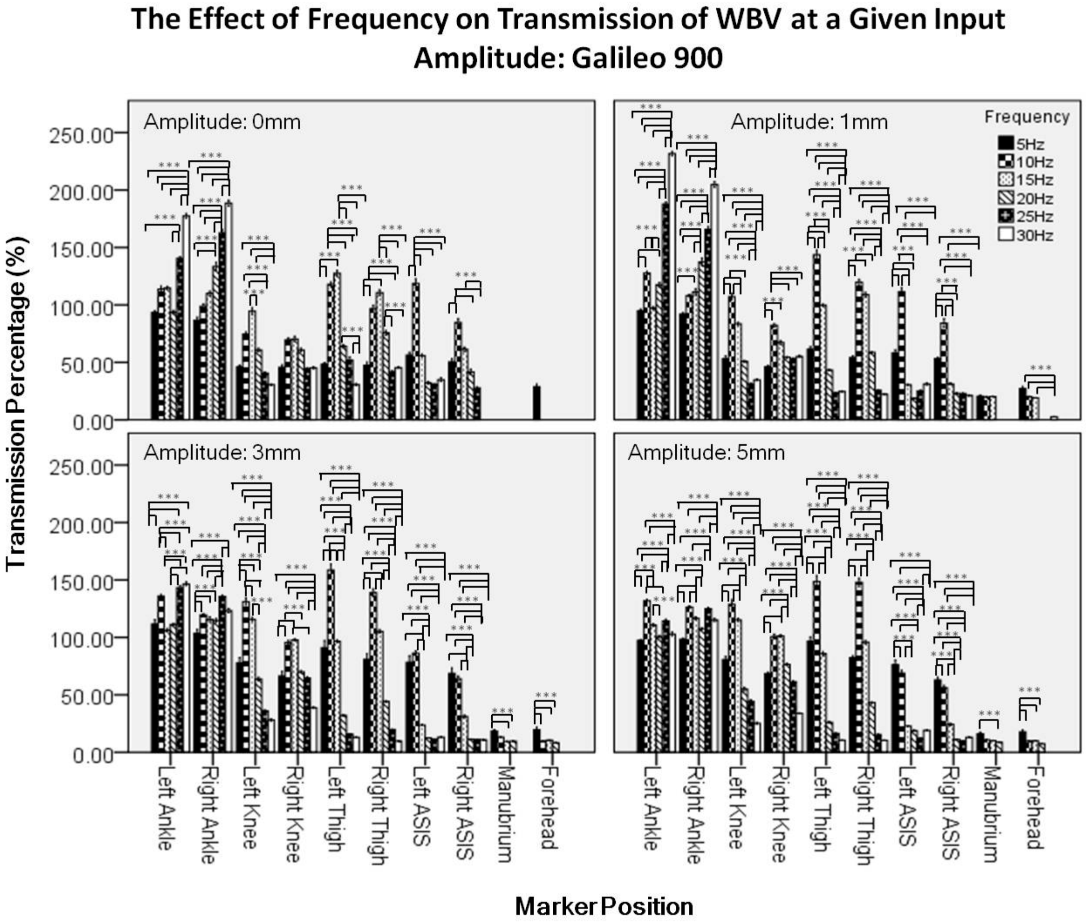

Figure 34: The effect of frequency on the transmission of whole body vibration (WBV) at delivered by the Galileo 900 platform.

Percentage of WBV transmitted to anatomical landmarks was calculated from peak to peak displacements measured using a Vicon motion capture system. Transmission of WBV was found to be dependent on the input frequency at most marker positions, with the exact relationship also dependent on the input amplitude. L & R refer to the left and right respectively. ASIS = anterior superior iliac spine. Differences in transmission between 5Hz, 10Hz, 15Hz, 20Hz, 25Hz and 30Hz stimuli were analysed for a given amplitude (0mm, 1mm, 3mm and 5mm) of WBV using a one-way ANOVA with Dunnett's T3 post-hoc test. All outcomes significant at $p<0.001$ unless indicated. NS=Not Significant, *$p<0.05$, ** $p<0.01$.

At the Ankle, transmission of vibration shows a clear frequency dependency at 0mm and 1mm amplitudes however this is lost at higher amplitudes.

At input amplitudes of 0mm and 1mm, a greater percentage of the input is transmitted to the ankle at higher frequencies (Figure 34). This difference in the amount of vibration transmitted to the ankle at an input amplitude of 0mm shows significant increase with frequency ($P<0.001$) interrupted by a plateau in the percent transmitted to the ankle between 10Hz and 15Hz and by a decrease in transmission from 15Hz to 20Hz (Figure 34, Amplitude: 0mm).

A similar significant (P<0.001) trend is shown at 1mm input amplitude, with a decrease or plateau in the percent of the input transmitted to ankle between 10Hz and 15Hz for the left and right ankles respectively. This results in no significant difference in the vibration transmitted to the left ankle at 5Hz compared to 15Hz and the right ankle at 10Hz compared to both 5Hz and 15Hz (Figure 34, Amplitude: 1mm). At 3mm and 5mm amplitudes this frequency dependence is lost at the ankle.

5.3.5.2 Amplitude Dependency of Whole Body Vibration Transmission

When observing the trend of WBV transmission with the inputs grouped by amplitude it also appears that the input amplitude has a bearing on the transmission percentage at a given marker, however the trend is less clear than for frequency.

In the lower limb, at 5Hz and 10Hz input frequency, the trend associated with input amplitude is an increase with increased input amplitude. At 20Hz, 25Hz and 30Hz, the effect of amplitude on transmission is less marked as a clear trend is seen at fewer markers as the input frequency increases.

At 5Hz input frequency, the trend associated with the input amplitude is clearly defined at each marker. In general, the transmission of WBV increases with input amplitude from 0mm to 3mm at the markers from the ankle up to the ASIS (P<0.001 with the exception of left ankle 0mm - 1mm, right knee 0mm - 1mm and left and right ASIS 0mm - 1mm NS) (Figure 35 Frequency: 5Hz). As the frequency of input is increased, this relationship is observed at fewer markers, with an increase of WBV transmission with increased input amplitude from 0mm to 5mm at the ankle to the thigh at 10Hz input frequency (P<0.001 with the exception of left ankle, right knee and right thigh 3mm - 5mm P<0.01, left knee 3mm - 5mm and left thigh 3mm- 5mm NS) and the ankle to the knee at 15Hz input frequency (P<0.001 with the exception of right ankle, left knee 3mm - 5mm and right knee 0mm -1mm NS (Figure 35 Frequency: 10Hz, Figure 35 Frequency: 15Hz). At 20Hz and 25Hz the only increase of transmission with increased input amplitude is between 0mm and 1mm at the left ankle (P<0.001) and 0mm to 3mm and 1mm to 5mm at the right knee respectively (P<0.001) whilst at 30Hz the only increase in WBV transmission with input amplitude was between 0mm and 1mm at the left ankle (P<0.001) (Figure 35: Frequency: 20Hz, Figure 35 Frequency: 25Hz, Figure 35 Frequency: 30Hz). However at 20-30Hz, the transmission to the ankle shows a decrease with increased input amplitude, in contrast to the increase seen at 5Hz and 10Hz. Above the ankle, a clear relationship appears harder to define at 20-30Hz (Figure 31).

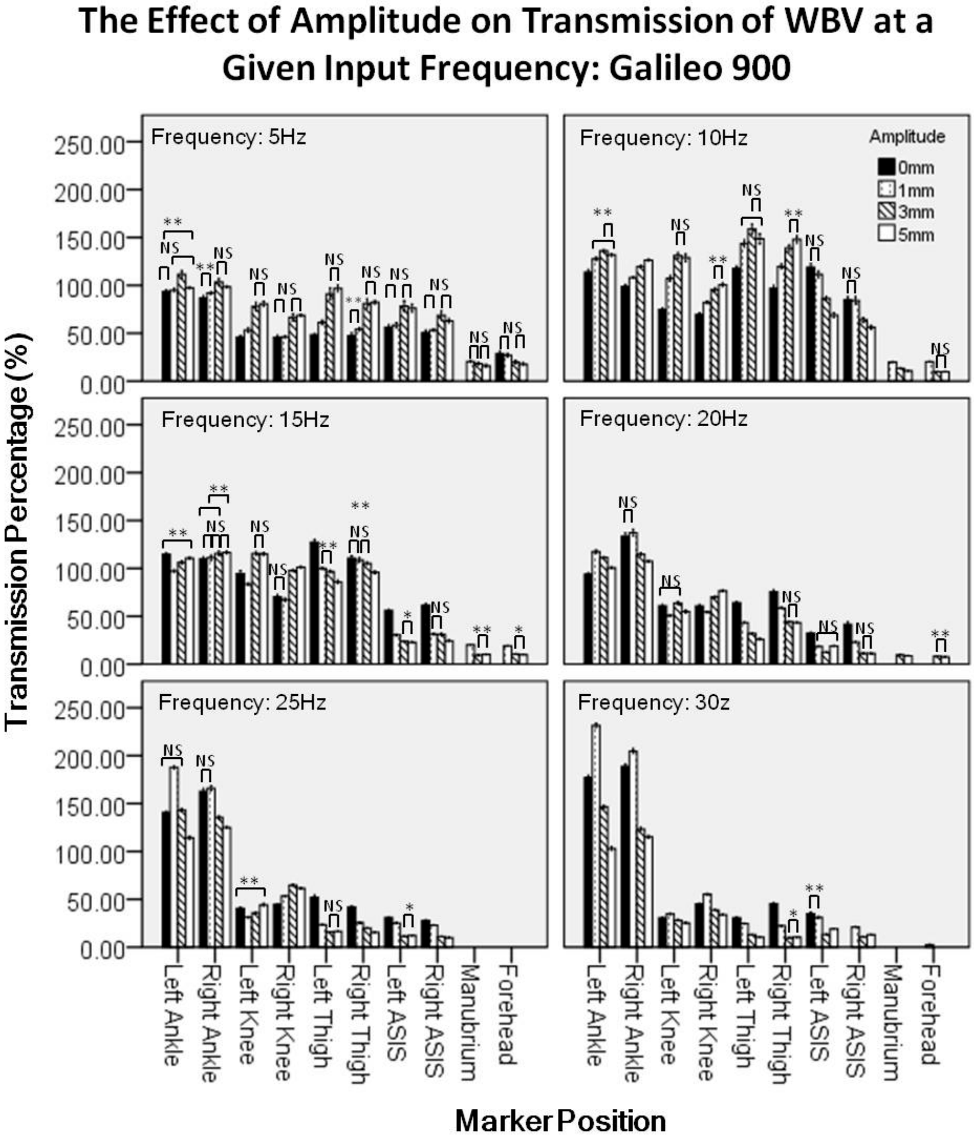

Figure 35: The effect of amplitude on the transmission of whole body vibration at different frequencies delivered by the Galileo 900 platform.

Percentage of WBV transmitted to anatomical landmarks was calculated from peak to peak displacements measured using a Vicon motion capture system. Mean transmission percentage with 95% confidence intervals are presented. Transmission of WBV was found to be dependent on the input amplitude at most marker positions, with the exact relationship also dependent on the input frequency. L & R refer to the left and right respectively. ASIS = anterior superior iliac spine. Differences in transmission between 5Hz, 10Hz, 15Hz, 20Hz, 25Hz and 30Hz stimuli were analysed for a given frequency (5Hz, 10Hz, 15Hz, 20Hz, 25Hz, 30Hz) of WBV using a one-way ANOVA with Dunnett's T3 post-hoc test. All outcomes significant at p<0.001 unless indicated. NS=Not Significant, *p<0.05, ** p<0.01.

Whilst at 5Hz to 15Hz input frequencies the trend is for an increase in WBV transmission with increased input amplitude, at 20Hz to 30Hz this trend shifts to a decrease in WBV transmission with increased input amplitude (Figure 35).

5.3.5.3 Transmission of Whole Body Vibration: Powerplate Pro 5

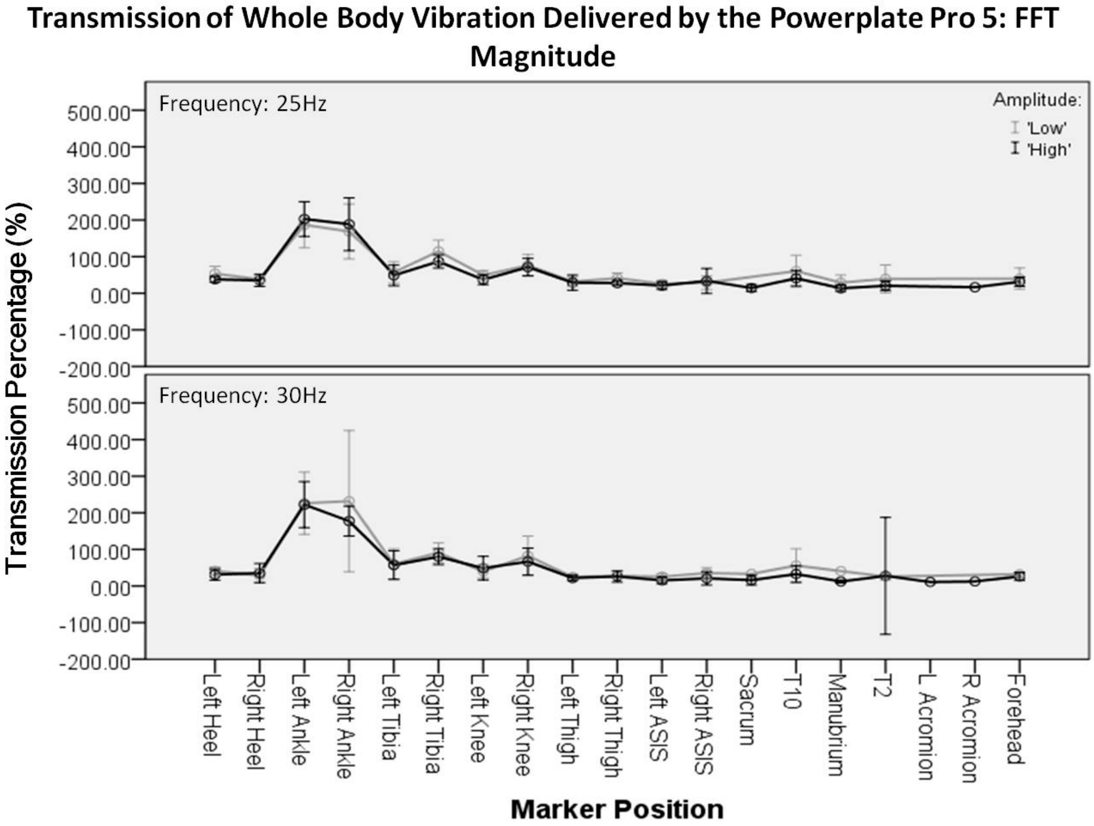

Figure 36: Transmission of whole body vibration (WBV) delivered by the Powerplate Pro 5 platform at frequencies of 25Hz and 30Hz and amplitude settings of 'Low' and 'High'.
A fast Fourier transform (FFT) of the displacements measured using a Vicon motion capture system was performed and the magnitude at the input frequency was recorded for each marker. Transmission was calculated as the FFT magnitude at a marker as a percentage of the FFT magnitude of the input. Mean transmission percentage with 95% confidence intervals are presented. Transmission shows a decreasing trend from the heel to the forehead, with slightly different transmission in the left and right leg. The percent of the input FFT magnitude transmitted to a given landmark does not appear to vary greatly with frequency or amplitude. L & R refer to the left and right respectively. ASIS = anterior

The Powerplate Pro 5 shows a similar trend in the transmission of vibration to that observed using the Galileo 900 platform at the same frequency input (Galileo 900: 25Hz 0mm & 30Hz 0mm similar to Powerplate Pro 5: 25Hz 'High' and 30Hz 'High' respectively). The greatest transmission percentage is observed at the ankle, above which transmission percentage decreases in a gradient from the tibia through to the forehead (Figure 36). In contrast to the Galileo 900, frequency and amplitude of input do not seem to have much bearing on the transmission of the whole body vibration. The transmission percentage for a given amplitude is slightly greater at 25Hz than at 30Hz, the relationship between frequency and transmission is less clear than that seen with the Galileo (Figure 36, Figure 32 Frequency:25Hz & Frequency: 30Hz).

At 25Hz Powerplate Pro 5 input frequency, there is a greater transmission percentage at all markers above the ankle at 'Low' compared to 'High' input amplitude (Figure 36). At 30Hz Powerplate Pro 5 input frequency, with the exception of the left knee there is also greater transmission percentage at all markers above the ankle at 'Low' compared to 'High' input amplitude (Figure 36). This is the same trend as is seen in the left leg data from the Galileo 900 at 0mm input amplitude, where an increase from 25Hz to 30Hz results in a significant decrease in transmission at markers above the ankle (Figure 34 Amplitude: 0mm).

As reflected by the RMS accelerations recorded at the ankle, the transmission percentage on the Powerplate Pro 5 at 25Hz 'High' and 30Hz 'High' is similar but slightly higher than that seen on the Galileo 900 at 25Hz0mm and 30Hz0mm respectively (Figure 36, Figure 31 Amplitude: 0mm & Amplitude:1mm, Figure 33, Frequency: 25 & Frequency: 30Hz). At the ASIS and spine, transmission of between 11.2% and 21% is observed on the Galileo 900 platform at 25Hz0mm and 30Hz0mm (Figure 33). On the Powerplate Pro 5 at 25Hz 'High' and 30Hz 'High', the transmission at the ASIS and spine ranges between 12.3% and 40.8% (Figure 36).

At the forehead, the greatest transmission percentage observed on the Galileo is 18.7% at 10Hz0mm input (actual input 9.7Hz 1.01mm, Table 12), whereas on the Powerplate Pro 5, the smallest transmission percentage observed is 26.3% at 30Hz 'High' (actual input 29.1Hz 1.12mm, Table 12) and the greatest is 40.0% at 25Hz 'Low' (actual input 27.5Hz 0.54mm, Table 12)(Figure 33, Figure 36). At 25Hz0mm and 30Hz0mm, the Galileo 900 transmits 14.1% and 12% of the input vibration to the forehead respectively (Figure 33).

Given the input amplitudes of the platforms that generate the greatest transmission to the forehead, the Powerplate Pro 5 and Galileo 900 platforms result in vibrations with a theoretical amplitude of 0.21mm and 0.18mm respectively at the forehead (calculated from the values in Table 12). However, the frequency of the input signal resulting in these comparable amplitudes at the forehead differ, resulting in greater RMS accelerations being transmitted to the forehead with the Powerplate Pro 5 (1.0g) (Figure 23) than with the Galileo 900 (0.07g) (Figure 24). Based on the measured input amplitude and frequency (Table 12) the theoretical RMS acceleration transmitted to the forehead at the above settings by the Powerplate Pro 5 is 1.8g and the Galileo 900 is 0.3g, both slightly greater than the measured values. For comparable inputs, the transmission by the Galileo 900 at 25Hz0mm and 30Hz0mm results in RMS accelerations of 0.34g and 0.41g at the forehead respectively, whereas the transmission of WBV by the Powerplate Pro 5 at 25Hz 'High' and 30Hz 'High' results in RMS accelerations of 1.0g and 0.9g at the forehead respectively (Figure 23). Thus the transmission of WBV by the Powerplate Pro 5 translates to greater RMS accelerations to the forehead.

5.3.5.4 Transmission of Whole Body Vibration: Juvent 1000

On the Juvent 1000 platform, transmission percentage increases from the heel to the ankle before decreasing to the sacrum (Figure 37). Above the sacrum, the transmission percentage increases to the forehead, however no transmission is observed at the right ASIS, the manubrium or the acromion processes (Figure 37). The transmission percentage at the right ankle is greater on the Juvent 1000 than on the Powerplate Pro 5 or the Galileo 900 at 30Hz input frequencies (Figure 33, Figure 36 and Figure 37).

At the left ankle, the Juvent 1000 has a lower transmission percentage than that seen on the Powerplate Pro 5 and Galileo 900 at 30Hz, with the exception of the Galileo 900 at 30Hz3mm and 30Hz5mm (Figure 33, Figure 36 and Figure 37). Through the use of the FFT to establish the transmission percentage for the Juvent 1000, the amplitude (which is below the detection level of the motion capture system) equating to a given transmission percentage can be estimated based on the input amplitude. Whilst the difference in transmission percentage between the left and right leg appears most pronounced on the Juvent 1000 platform, when considering the amplitude this represents based on the input amplitudes and the transmission percentage, the calculated difference in amplitude between the left and right leg is smaller on the Juvent 1000 platform (0.017mm) than on the Galileo 900 30Hz0mm & 30Hz1mm (0.11mm and 0.66m respectively) or Powerplate Pro 5 at 30Hz ‘Low’ and ‘High’ (0.03mm and 0.50mm respectively) (Table 12).

Again, at the ASIS and spine with the exception of the right ASIS, transmission percentage is greater on the Juvent 1000 than the Galileo 900 or Powerplate Pro 5 (Figure 33, Figure 36 and Figure 37). However, considering the differing input amplitudes of the three platforms, RMS accelerations at the ASIS and spine as a result of the transmitted WBV on the Juvent 1000 (01.g-0.7g) are less than those transmitted by the Powerplate Pro 5 (0.82g-1.77g) and Galileo 900 (0.4g-1.17g) at the same input frequency. Based on the input amplitude and percent transmission, the estimated amplitude of the vibration delivered to the ASIS and spine is less on the Juvent 1000 than on the Galileo 900 or Powerplate Pro 5 at 30Hz input frequency, with a calculated range of 0.009mm to 0.012mm at the ASIS and spine on the Juvent 1000, 0.10mm to 0.42mm on the Galileo 900 at 30Hz and 0.14mm to 0.37mm on the Powerplate Pro 5 at 30Hz.

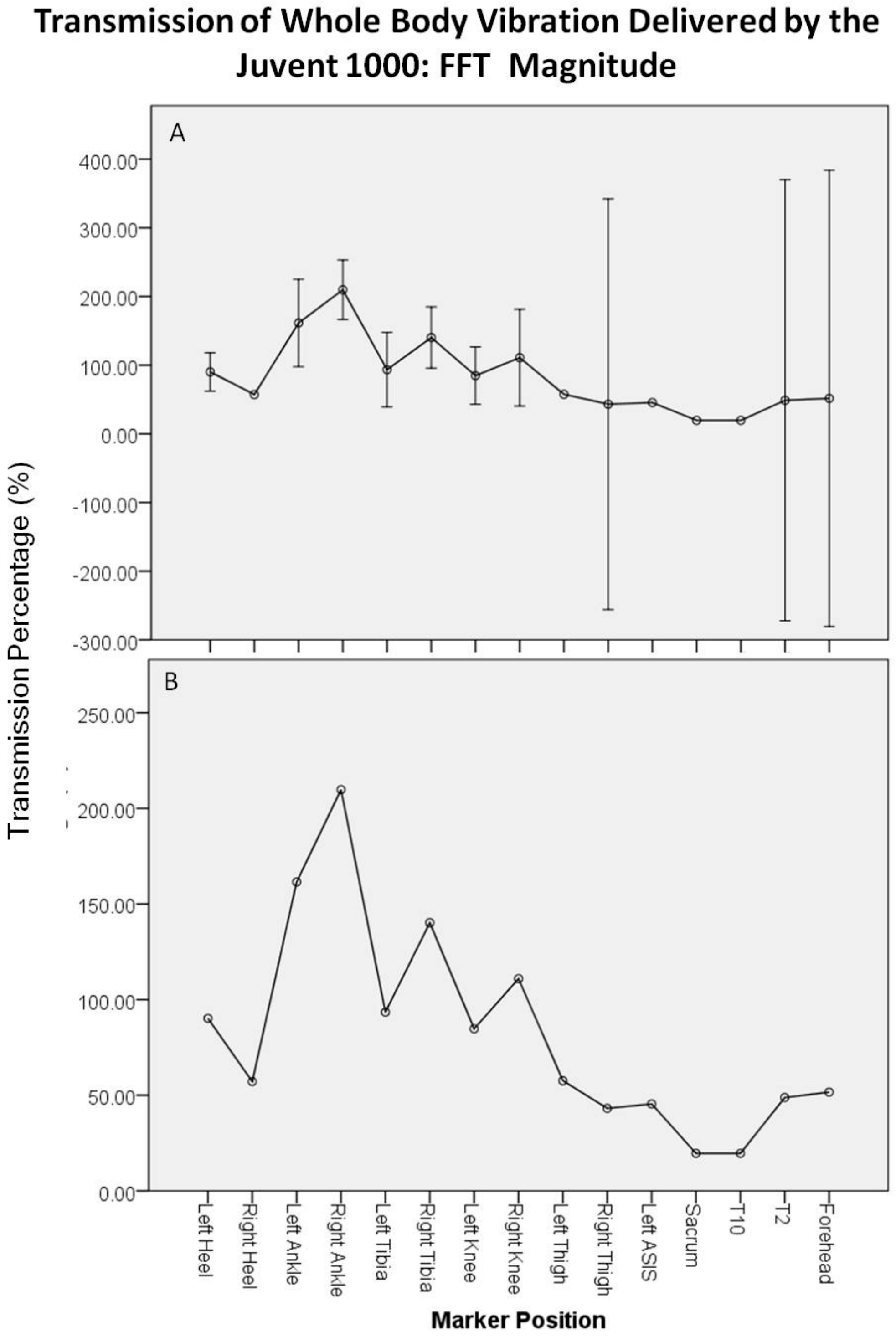

Figure 37: Transmission of whole body vibration (WBV) delivered by the Juvent 1000 platform at a frequency between 32-37Hz and input acceleration in the order of 0.3g.

A fast Fourier transform (FFT) of the displacements measured using a Vicon motion capture system was performed and the magnitude at the input frequency was recorded for each marker. Transmission was calculated by taking the FFT magnitude at a marker as a percentage of the FFT magnitude of the input. Mean transmission percentage with 95% confidence intervals are presented. Transmission increases from the heel to the ankle before decreasing to the forehead with a discrepancy between the percent transmitted in the left and right leg. L & R refer to the left and right respectively. ASIS = anterior superior iliac spine.

5.4 Discussion

Data from six participants was analysed in the current study. This was due to the simultaneous recording of motion capture and strain data limiting the sample size as the strain data required an invasive procedure. As such, the observations presented here should be interpreted tentatively. Further work in a larger cohort is needed to fully establish the conclusions suggested by this data set, however the data provides an preliminary insight into the transmission of WBV in healthy adults.

5.4.1 Input frequency, amplitude and acceleration

Three different whole body vibration platforms were used in this study, two vertical vibration platforms (Powerplate Pro 5 and Juvent 1000) and one side alternating platform (Galileo 900). Each platform had different manufacturer specified input frequencies, amplitudes and accelerations and each showed a different degree of accuracy when comparing recorded variables with the expected manufacturer specified variables.

5.4.1.1 The Juvent 1000

When considering the Juvent 1000 platform, the RMS acceleration calculated in this study (Table 12) is greater than that reported by Kiiski et al, who reported a accelerations lower than expected for the Juvent 1000 (Table 12), using a platform which delivered WBV at 0.05mm amplitude and 30Hz or 35Hz [123]. Additionally, Muir et al also found peak to peak accelerations on a Marodyne Liv MD, an alternative ‘low magnitude’ WBV platform, to be close to the expected peak acceleration value, rendering peak acceleration much lower than expected and approximately half of the RMS acceleration reported here for the Juvent 1000 [163].

These discrepancies can be potentially be explained by the slight differences in input frequencies and amplitudes of the different platforms used across the studies. The amplitude and frequency reported by Kiiski et al would result in an expected RMS acceleration lower than the expected RMS for the Juvent 1000. However, for the recorded frequency and amplitude, the expected RMS acceleration is 5 fold lower than that recorded.

For the first five participants in the study, 10 seconds of recording was made. During this time the Juvent 1000 performed a four second self-test and a calibration procedure to determine the frequency and amplitude that delivered the optimum resonance for each individual[166] (Chapter 10.2.3). This resulted in input frequencies varying by up to 5Hz across participants making determination of the input frequency and amplitude from a Fast Fourier Transform (FFT) (Table 12) and taken as an average across participants, susceptible to error. As a result, the RMS acceleration, calculated for the Juvent 1000 from the displacement data, is around three times the theoretical peak acceleration for the input frequency and amplitude taken from the FFT (Table 12).

For the sixth participant, recording continued into the 'treatment' period of the Juvent's vibration, allowing comparison between pre and post calibration periods. Whilst a difference in the primary frequency and amplitude is observed between the periods during and post calibration, the RMS acceleration does not differ greatly between these periods (Figure 25). This suggests that, whilst each participant is likely to have different RMS accelerations, the period during calibration can give useful information on the transmission of whole body vibration through the body.

During calibration, the platform does a frequency and amplitude sweep which would be expected to generate a signal with multiple frequency components each of differing amplitude [166] (Chapter 10.2.3). The FFT reveals a peak which is greater than other frequency components of the signal; however the peaks tend to be rounded, spread over consecutive frequencies and in three cases smaller frequency components are visible. In this instance, the amplitude may be a sum of the fast Fourier transform magnitudes of different frequency components and may vary with time, resulting in an underestimation of the amplitude if taken as the magnitude of a single frequency component. This could, at least in part, account for the discrepancy between the determined input frequency and amplitude and the calculated RMS acceleration.
As there is little difference between the RMS acceleration during and post calibration this suggests that the signal during the 'treatment' period is also an amalgamation of multiple frequency inputs.

Another source of error in the determined input characteristics could be the method of determining acceleration. In previous studies, accelerometers have been used to directly measure accelerations (Kiiski, Muir), however in this study a calculation of the second derivative of the displacement data was used. If there was any noise within the signal, this would be amplified by the differentiation and could cause short but large magnitude accelerations to effect the calculated RMS acceleration. Inspection of the fast Fourier transform of the acceleration data supports this as a source of error in five out of the six participants.

Whilst the limitations mentioned influence the interpretation of the Juvent 1000 data, the 95% confidence intervals of the data below the thigh do not span zero or one and therefore it is likely the RMS acceleration is below 1g. In addition, by taking the FFT peak as a percentage of the input peak at the toe for each individual, normalisation of the data can be achieved, making it possible to analyse the transmission of vibration through the body.

5.4.1.2 The Powerplate Pro 5

The Powerplate Pro 5 has specified input frequencies of 25Hz and 30Hz and input amplitudes of 'Low' and 'High'. In previous studies amplitudes of 0.85mm [163] and 0.6mm [167] have been reported for the 'Low' setting and 1.65mm [163] and 1.1mm [167] for the 'High' setting. Whilst the 0.6mm and 1.1mm reported by Pel et al are in line with the findings of this study, the 0.85mm and 1.65mm reported by Muir et al are both higher than those in this study. One explanation for the discrepancy in amplitudes could be the trend whereby amplitude appears to increase slightly with higher input frequency (Table 12). Both the amplitudes reported in this study and those reported by Pel et al were at input frequencies of 25Hz and 30Hz whereas Muir et al used a higher input frequency of 34Hz [163, 167].

At 30Hz 'Low' and 'High', the RMS accelerations reported in this study would equate to peak to peak accelerations of 5.72g and 9.56g respectively [165]. These values are lower than the 8.16g and 15.09g peak to peak accelerations reported by Muir et al; however given the higher input frequency and reported amplitude this is expected. At an input frequency of 25Hz and at 30Hz 'Low', the RMS accelerations reported by Pel et al are 0.42- 0.62g smaller than those found in this study, whereas at 30Hz 'High' the RMS accelerations are in agreement. This could be due to the actual frequency being delivered by the platform. At 25Hz, the fast Fourier transform determined an actual frequency of 27.2-27.5Hz dependent upon amplitude. This is greater than that reported by Pel et al by 1.2-2.5Hz which would be expected to result in greater RMS accelerations.

At 30Hz, the fast Fourier transform determined an actual frequency of 29.1-29.5Hz dependent on amplitude. This is lower than the 31Hz reported by Pel et al; therefore RMS accelerations would be expected to be smaller (as for 30Hz ‘High’).

This still leaves the case of 30Hz ‘Low’ being greater than in the study by Pel et al. In addition to the differences in recorded frequency, calculating the expected RMS acceleration from the input frequency and amplitude (Equation 11, Equation 12) results in values smaller than those reported in Table 12. This discrepancy could be due to similar assumptions to those made when defining the input variables of the Juvent, however in general the stated frequency of the input for a given setting does not vary more than 0.3Hz (with the exception of 0.6Hz at 30Hz High) between participants suggesting better accuracy when taking a mean value for input frequency than with the Juvent. The signal appeared to have a single dominant peak many fold greater than anything else on the FFT plot suggesting that taking the magnitude from FFT is a valid method of estimating the amplitude. In agreement with this, a previous study showed accelerometer output from the surface of a Powerplate to fit a sinusoidal pattern with error of less than 0.5% [167]. However, it is still possible that other frequency components could have resulted in a non-sinusoidal waveform, as seen with the Juvent and previously seen for vertical whole body vibration with an amplitude greater than 0.5mm [123]. Whilst this may not have appeared obvious on the fast fourier transform of the recorded displacements, once the second derivative of these values is determined in order to define the RMS acceleration, any other frequency components may be amplified to such an extent to cause spurious large peak accelerations to be detected. As with the Juvent 1000 platform, this would result in greater RMS accelerations than those predicted from the input frequency and amplitude.

This could account for the RMS accelerations calculated in this study being 25-54% greater than the theoretical RMS accelerations. The 95% confidence intervals in the lower limb are generally small, with the exception of the ankle where the range of possible movement is greater than at locations away from the joints. This suggests little variation in the calculated RMS accelerations. The 95% confidence intervals are also improved once the data is normalised as a percentage of the input at the toe.

5.4.1.3 The Galileo 900

The input frequency recorded for the Galileo 900 platform is within 0.5Hz of that stated by the manufacturer for frequencies between 5Hz and 20Hz (Table 12) (with the exception of the 14.4Hz recorded at 15Hz 3mm). At 25Hz and 30Hz input frequencies, the recorded value is between 0.7Hz and 1Hz lower than expected (Table 12).

In a previous study using a Galileo-Fitness platform, Pel et al recorded frequencies which matched those specified by the manufacturer between 5Hz and 30Hz, however, at 35Hz and 40Hz, the recorded frequency was 1Hz and 2Hz lower than specified respectively [167]. Given the use of a different platform, it is feasible to suggest that at frequencies towards the higher end of the range delivered by the Galileo 900, the platform delivers WBV at a frequency below that specified by the manufacturer.

At input amplitudes of 0mm, 1mm and 3mm, the recorded amplitude is greater than that specified by the manufacturer, whereas for input amplitudes of 5mm, the recorded amplitude is lower than expected (Table 12).

For a given toe position, the amplitudes reported in this study show an increase of between 13% and 43% between 5Hz input frequency and 20Hz or 25Hz input frequency. At 0mm and 1mm amplitude and 30Hz frequency, the recorded amplitude decreases by around 15% from that at 25Hz (Table 12). At 3mm and 5mm amplitude and 30Hz frequency, the recorded amplitude decreases by 3% and 7% respectively from that at 20Hz (Table 12).

As the amplitude of the platform is determined by the distance of the foot from the centre of the platform, it is possible that the deviation from the manufacturer specified amplitude is due to the feet of the participant being placed imprecisely along the platform. In addition, it is likely that the exact position of the foot was not the same for all recordings and at higher frequencies it is likely to have been harder to keep the feet in a given spot during recording. Therefore it is probable that the deviation from the expected and the variation in recordings is due to foot movement.

The calculated RMS accelerations for the Galileo 900 platform are in general agreement with what would be expected for an input frequency and amplitude as recorded (Figure 23). The calculated values are slightly higher than expected, but in the majority of cases (16/24), the discrepancy is no more than 15% greater than the expected RMS acceleration. In 5 cases, the discrepancy is in excess of 20% greater than expected (5Hz0mm, 15Hz0mm, 30Hz0mm, 15Hz1mm, 5Hz3mm). Most of these cases are at 0mm input amplitudes, for which the feet were placed together in the centre of the platform. In this position balance is most difficult; therefore it is possible that the participants inadvertently adjusted their foot position to keep balance. It is also difficult to keep foot contact with the platform in this position therefore the feet may also have been occasionally lifting off the platform. Either of these movements may have resulted in a sharp acceleration which affected the peak and RMS accelerations determined.

5.4.2 The Effect of Weight on the Input Signal

It was determined that the weight of a participant standing on the Galileo 900 or Powerplate Pro 5 platform did not significantly influence the vibration delivered by the platform. In the case of the Galileo 900, the stimulus at input was shown to have a significantly lower peak to peak displacement than for the other participants. This could be due to a number of things. Firstly, it could be due to the weight of the participant; however, given that no other significant trend or relationship between weight and input was determined, this is unlikely. Secondly, it could reflect a difference in the calibration of the motion capture system used to record the data. If this was the case, the same would be expected when considering the Powerplate Pro 5 vibration input, however no significant difference between participants was seen in this case, suggesting the calibration procedure was robust across study visits. Finally, this discrepancy could be due to the positioning of the marker on the platform. As the magnitude of the difference is less than 1mm, this is the most likely cause as this magnitude of difference could easily be caused by a variation in the marker positioning between participants.

Whilst no significant difference between the input for a given weight was seen on the Powerplate Pro 5, the confidence intervals around the mean FFT peaks were much greater than those around the Peak to Peak (P2P) displacements of the Galileo. This is most likely due to the number of observations. For the Galileo 900, hundreds of peak to peak displacements across recordings at 5Hz, 10Hz, 15Hz, 20Hz, 25Hz and 30Hz made up the data set for each participant. This was due to assessment of the data in the time domain and measurement of peak to peak displacement over at least five seconds of recording. However, given a lower signal to noise ratio for the data collected on the Powerplate Pro 5, the P2P displacement could not be used as a measure and FFT peak was used instead. The FFT peak determined for each of the Powerplate Pro 5 settings was a single value, resulting in 4 values being recorded for each participant. The smaller sample size used to determine the mean for each weight would be expected to result in a greater confidence interval, explaining the difference between the data in Figure 21 and Figure 22.

The calibration of the Juvent 1000 (Chapter 5.4.3) suggests that the input will be dependent upon the body composition of the participant. As only a single recording per participant was made on the Juvent 1000, the effect of weight on the input stimulus could not be statistically assessed.

5.4.3 Calibration of the Juvent 1000 Platform

During the first 12 seconds of use, the Juvent 1000 platform performs a calibration to establish the optimum resonant frequency for a given user. This is achieved using a frequency sweep; therefore the input stimulus delivered by the platform during this time is not constant.

For the first five participants, recordings were made for twenty seconds, therefore a large proportion of the recordings were made during calibration and were not necessarily relevant to the stimulus delivered by the Juvent 1000 once a frequency was chosen and acceleration of 0.3g delivered.

However, when a period of WBV delivered by the Juvent 1000 platform after calibration was compared to that during calibration, very little difference was observed (Figure 25). This suggests that the data obtained for the first five participants will be informative about the transmission and accelerations of the whole body vibration delivered by the Juvent 1000 once calibrated.

5.4.4 Normalisation of the Data

In order to account for between participant variation in the input amplitudes and, in the case of the Juvent 1000, input frequency (Table 12), the transmission was analysed as a transmission percentage. Given the amplitude of the Galileo 900 is determined by the foot distance from centre line, it is susceptible to variations due to differences in foot position between recordings. Taking the transmission as a percentage of the amplitude at the toe was deemed to be more accurate than assuming foot position to be precise; resulting in the exact manufacturer specified input amplitude.

5.4.4.1 Contralateral Variation in Amplitude at the Toe

For a representative subset of Galileo 900 input settings, the mean P2P displacement delivered to markers on the left and right sides of the body were analysed (Figure 27). At several markers, small but significant differences were observed between the landmarks on the left and right limb. When transmission for markers on the left leg was taken as a percentage of the mean P2P displacement at the left toe and transmission for markers on the right leg was taken as a percentage of the mean P2P displacement at the right toe, the same small but significant differences were observed (Figure 28). This suggests that the normalisation allowed for between participant comparison without affecting the overall trend of the data. The observed contralateral differences are most likely due to side to side differences in weight distribution and associated subtle biomechanical differences in response to the WBV stimuli. This is reflected in the trend of the transmission as, when a greater P2P displacement or transmission percentage is seen for a given side of the body at the ankle, subsequent values at the tibia and knee tend to then be lower for that side of the body. This reflects the greater absorption of the stimulus at the level of the ankle (Figure 29 30Hz 1mm).

This approach is different to that used in previous studies, where either unilateral recordings were made [168] or left and right markers were pooled to determine transmission [157]. In the case of pooled left and right data, a synchronous vibration platform was used and therefore differences between the WBV delivered to the left and right side would not be expected.

For continuity, the same approach to normalisation was applied to the Powerplate Pro 5 and Juvent 1000 data.

In the case of the Powerplate Pro 5, far fewer significant contralateral differences are observed (Figure 30). The majority of the significant differences are at the tibia, where markers were placed at different levels along the tibia and therefore differences might be expected, however makers on the thigh were also at different locations and no significant differences were observed. In addition, differences at the knee and ASIS are observed but unexpected, therefore the differences are likely not due to positioning of the markers. Again, these differences are more likely due to small differences in weight distribution between the legs and the biomechanical response to the WBV stimulus.

In the case of the Juvent 1000, no significant contralateral differences were observed (Figure 29).

5.4.5 Use of the FFT in the measurement of Whole Body Vibration Transmission

When measuring the transmission of WBV, previous work has used directly measured acceleration or displacement to quantify transmission. The displacements measured using the Vicon motion capture system used in this study were clearly cyclical and easily measurable using our in house computer program (Chapter 10.1.2) for measurements made on the Galileo 900 side alternating platform. However, the displacements generated by the vertical motion of the Powerplate Pro 5 and Juvent 1000 were less clearly cyclical and had far worse signal to noise ratio than the recordings made for the Galileo 900. This made automatic definition of peak to peak displacement using the in house Tibial Marker program (10.1.2) impossible and required manual definition of peak to peak displacement which was open to user interpretation in order to quantify peak to peak displacement.

In order to prevent the influence of user interpretation from affecting the calculated transmission, an alternative approach to measuring WBV transmission was developed using the magnitude of the FFT at the input frequency (Table 12). For the Galileo 900, correlation was observed between the transmission established using the P2P displacement and that established using the magnitude of the FFT (Figure 33). This suggest that, although the magnitude of the FFT is not necessarily the exact amplitude of the signal given that multiple frequency components may contribute to the amplitude at any one time, it does compare sufficiently to examine the transmission of WBV. The limitation of this method is that the amplitudes or P2P displacements inferred from a FFT may be underestimations; however, normalising them to the magnitude of the FFT at input clearly makes for a comparable measure of transmission to that established using the directly measured P2P displacement.

This provides a method by which transmission at a given frequency can be determined in signals with poor signal to noise ratio, without the need for heavy filtering of the data prior to assessment of the data.

5.4.6 Transmission of Whole Body Vibration

Whole body vibration was transmitted to landmarks throughout the body, with detection of movements as far up as the forehead for all platforms. This is in line with previous observations of the transmission of whole body vibration through the body in children [114, 157]. Whilst movement is observed throughout the body, by the time the WBV reaches the torso, the WBV stimulus is greatly attenuated in all instances. Attenuation of the stimulus is greater on the side alternating Galileo 900 than the vertical Powerplate Pro 5 and Juvent 1000, delivering the greatest stimulus to the lower limb whilst minimising WBV being delivered to areas surrounding vital organs in the torso.

The transmission of the WBV stimulus is dependent upon the biomechanics of the participants. Body composition, changes in posture and different muscle activation patterns in response to the whole body vibration all influence the transmissibility of a WBV stimulus [125, 169-173]. The biomechanical response of participants to the WBV stimulus delivered by side alternating and vertical vibration differ resulting in the differences in transmission. It is also possible that there is variation in the biomechanical response between participants to a given WBV stimulus. The confidence intervals surrounding the transmission of WBV delivered by the Galileo 900 suggest that the pattern of transmission is similar between participants (Figure 31, Figure 32, Figure 33) however biomechanical response to vertical vibration appears more variable (Figure 36, Figure 37). Wide confidence intervals surrounding transmission at the ankle on the Powerplate Pro 5 at both frequencies and the second thoracic vertebrae at 30Hz, as well as those at the thigh, second thoracic vertebrae and forehead on the Juvent 1000 are indicative in differences in biomechanical response to the WBV stimuli. The confidence interval at each of these sites exceeds 100% transmissibility suggesting a resonance in some participants.

5.4.6.1 Attenuation of Whole Body Vibration

The attenuation of the WBV is dependent both upon the amplitude and the frequency of the input. At lower frequencies, the amplitude of the input has greater bearing on the attenuation than at higher frequencies, where the input frequency appears to be the primary determinant of signal attenuation.

Where amplitude influences attenuation, the greater the amplitude, the less attenuation of the signal is observed (Figure 35). In contrast, greater attenuation is observed at higher input frequencies (Figure 34).

The above observations could be explained by the biomechanical response of the participant to the WBV stimulus delivered by the platform. At lower frequencies (5Hz 10Hz & 15Hz), a greater degree of transmission is observed at the thigh and ASIS markers than at surrounding markers. However, at higher frequencies (20Hz, 25Hz & 30Hz), a greater degree of transmission is seen at the ankle compared with surrounding markers and the thigh and ASIS do not show greater transmission than at surrounding markers.

This suggests that up to 15Hz, the majority of the WBV stimulus attenuation occurs in the thigh and around the ASIS, whereas at higher frequencies, more absorption of the WBV occurs through ankle joint movement. The greater ankle joint movement would be indicative of a greater flexion angle being achieved which, as at the knee, would be expected to result in greater attenuation at the ankle[168].

5.4.6.2 Relative Accelerations generated by Whole Body Vibration

Whilst the greatest transmission of vibration occurs at lower frequencies, the relative RMS accelerations associated with the transmitted WBV stimulus tend to be greater at greater frequencies. Due to the attenuation of the Galileo 900 WBV stimulus in the torso, the accelerations delivered to the ASIS and the spine by the Galileo 900 are comparable to those delivered by the Juvent 1000. This observation may go some way to explaining why previous studies investigating the effects of WBV on hip and lumbar spine BMD in postmenopausal women have shown similar magnitude changes irrespective of the platform used [105, 107, 111]. Having said this, accelerations twice as great as those delivered by the Juvent 1000 and Galileo 900 are observed at the ASIS and spine when using the Powerplate Pro 5. This suggests that if the magnitude of the acceleration is the key determinant of the osteogenic response to WBV, the Powerplate pro 5 may have the greatest osteogenic potential at the level of the ASIS and spine.

When analysing the RMS accelerations delivered by the different platforms, it must be noted that whilst the confidence intervals surrounding the RMS accelerations at most markers are not large, some do appear to be wide. For instance, the T2 marker on the Juvent 1000 shows a much wider confidence interval than those at the other landmarks, suggesting variation in the RMS accelerations at this level between participants. With the small number of participants in this study, large confidence intervals may be expected as there is a high likelihood of differences between the biomechanical response of six people. The movement at T2 is linked to movements of the head. Whilst a period of time of when the platform was up to speed was selected for analysis from the toe marker displacements, the movement at the head may not have been consistent throughout this period. Participants were asked to remain looking straight ahead, however this was not maintained throughout the recordings. Quick head movements that are unrelated to the input WBV could translate into quick movements at T2 and thus large accelerations. This in turn could account for the variability and wide confidence intervals around the RMS accelerations at T2. Also, as already established when discussing the transmission of WBV, the signal to noise ratio on the Juvent did not allow the P2P displacement to be identified. Noise within the signal could be reflected as a quick movement, influencing the RMS acceleration calculated. This makes interpretation of the transmission data based on the fast fourier transform more reliable than the accelerations calculated for the Juvent 1000 and Powerplate Pro 5 platforms.

The data presented here takes into account the WBV transmitted in the vertical direction only. As the Juvent 1000 and Powerplate Pro 5 deliver vertical vibration it is expected that the greatest accelerations generated by the platforms will be in the vertical plane, however, the Galileo 900 has a reciprocal motion which may also result in substantial accelerations about the hips in a lateral plane perpendicular to the vertical accelerations reported here. Previously, it has been shown that the primary direction of the WBV stimulus delivered by the Galileo 900 is vertical[167], however at the level of the spine, the accelerations in the lateral direction are greater than those in the vertical direction[111]. To fully assess the impact of the Galileo 900, further analysis of the accelerations in the lateral plane is required.

6 Chapter Six: Unilateral Whole Body Vibration

6.1 Background

Investigations in to the effect of whole body vibration (WBV) on the human skeleton have used a variety of control groups, making comparison between studies difficult. Control groups in WBV studies have included participants doing no activity, following a program of resistance exercises and using placebo platforms [1, 105-111, 174].

Control groups doing no activity, whilst potentially providing the biggest difference between WBV and control, do not account for any differences between the group due to the participant in the intervention group knowing they are receiving an intervention and the control knowing they are not. The control group doing resistive exercises provides comparison between two interventions, however does not allow the full extent of changes in bone parameters due to WBV to be assessed, as changes in bone parameters would also be expected with resistive exercises [175, 176].

The use of a placebo platform as a control overcomes the shortfalls in the other types of control, however has been restricted to studies investigating low magnitude WBV such as that delivered by the Juvent 1000 platform. Low magnitude vibrations produce such small movements that it is possible to blind subjects to a placebo or active platform using audible sounds [105].

In the case of high magnitude vibrations such as those delivered by the Galileo 900 and Powerplate Pro 5 platforms, the movements generated by the platform are much larger making true blinding to an active or placebo platform impractical.

Another approach when considering control groups is a self-control. The unilateral loading of the dominant arm of tennis players has provided a self-controlled model for observing the localised effects of mechanical load on the skeleton. Within each participant, side to side differences between the dominant and non-dominant arm of tennis players have revealed geometrical changes in bone due to loading, reflected by greater bone mineral content (BMC) in the dominant arm[74, 76, 80, 82, 84].

The aim of this investigation is to assess the potential for a unilateral loading model (placing only one foot on the Galileo 900 platform) of WBV for use as self-control in future studies.

6.2 Methods

6.2.1 Participant Population

Six healthy volunteers aged between 18 and 50 who were physically able and willing to undertake the study procedures were recruited from Sheffield (South Yorkshire,UK) . Participants had a bone mineral density (measured by dual x-ray absorptiometry (DXA)) within +/- 2 SD of the young normal at the lumbar spine and hip and a body mass index (BMI) <30. The characteristics of the six participants included in the study are detailed in Chapter 3.1, Table 4.

6.2.2 Measurement of Transmission

Reflective markers, positioned on 21 anatomical landmarks, were used to analyse the movements experienced throughout the human body during WBV. The motion capture system used comprised 8 MX-F40 cameras positioned around the gait laboratory at the Northern General Hospital. Data acquisition was made using Vicon Nexus software recording at a rate of 300Hz with a minimum of three cameras required to start a trajectory and two to continue a trajectory.

6.2.3 Whole Body Vibration

Each participant stood on the Galileo 900 platform with their feet spaced such that the input reciprocal vibration had an amplitude of 3mm. Recordings were made with the frequency of the input vibration set to 5Hz, 10Hz, 15Hz, 20Hz, 25Hz and 30Hz.

Recordings were made with a bilateral stance and two unilateral stances, the first with only the left foot on the platform, the second with only the right foot on the platform at the 3mm amplitude position. When unilateral stances were adopted, the foot not on the platform was placed on a fixed platform of the same height as the Galileo 900.

6.2.4 Data processing

Raw trajectories were exported to an excel spreadsheet (Microsoft 2010). Data for each marker was then filtered in MATLAB 2007b using a band-pass filter, with cut-offs dependent upon frequency (Table 11) as defined in Chapter 4.3.2.

Filtered data was cropped to encompass only a period of recording at which the WBV was at a consistent frequency and amplitude.

The cropped data files were imported into Matlab 2007b and the maximum and minimum points of each vibration cycle were determined using the Tibial_Marker Matlab program (Chapter 10.1.2).

Peak to peak displacements for each vibration cycle were determined using the minimum and maximum points (Equation 14).

Equation 14: The Peak to Peak Displacement of a given vibration cycle:

$$P2P\ Displacement = Maximum\ point - minimum\ point$$

The input signal was defined from the toe markers as these were in closest contact with the platform. For bilateral recordings, the input signal was taken as the mean of the peak to peak displacements recorded at both the right and left toe. For unilateral recordings, the input signal was taken as the mean of peak to peak displacements at the toe that was placed on the Galileo 900 platform.

Transmission was calculated as the percentage of the input signal recorded at a given landmark (Equation 15).

Equation 15: Calculation of the transmission of whole body vibration to a given landmark

$$Transmission = \left(\frac{P2P\ Displacement\ (landmark\ x)}{Input}\right) x100$$

6.2.5 Statistical Analysis

Differences in the transmission delivered to each of the 21 anatomical landmarks when adopting a bilateral, unilateral (left leg) or unilateral (right leg) stance were analysed using a One-Way ANOVA. Post-hoc comparisons were made using a Dunnett's T3 test. Side to side differences in transmission to the landmarks on the left and right leg for a given input and stance were assessed using an independent T-test. Significance was assumed at a level of 0.05 or below.

All statistical tests were performed in IBM SPSS version 20.

6.3 Results

6.3.1 Transmission of whole body vibration with both feet, left foot or right foot on the Galileo 900 platform

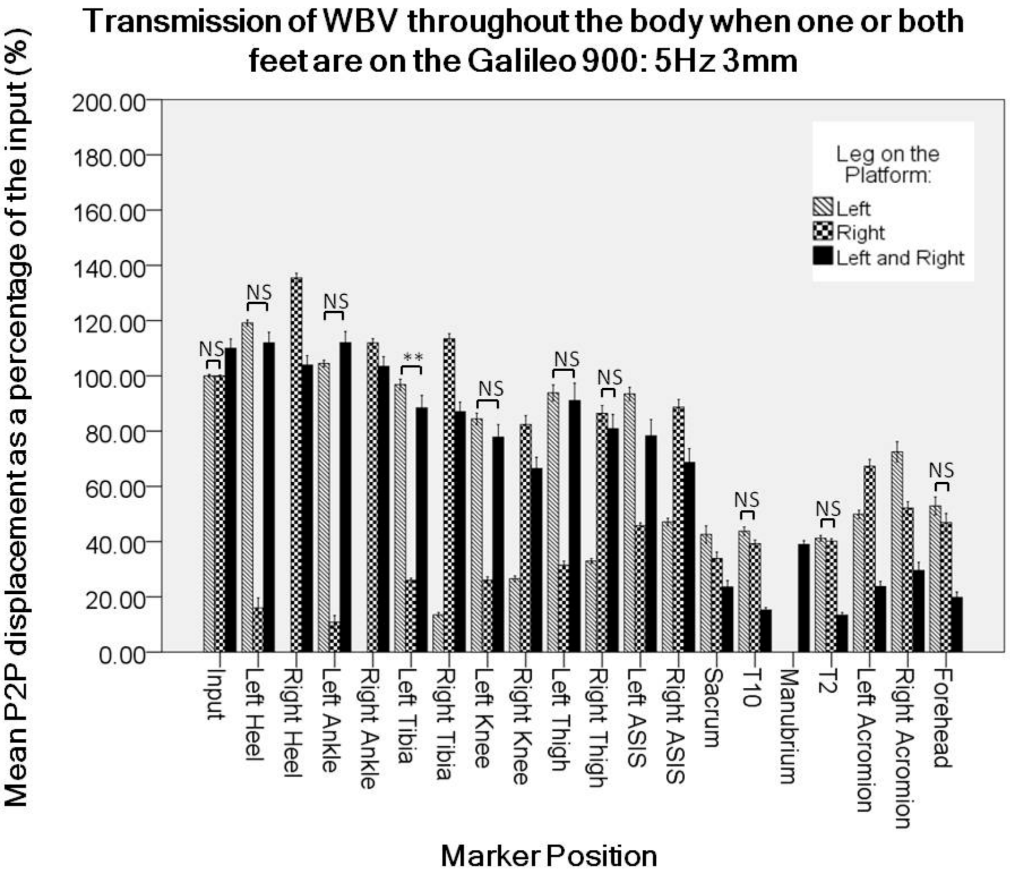

Figure 38: Transmission of 5Hz whole body vibration (WBV) with unilateral and bilateral stance.

WBV was delivered using the Galileo 900 platform at a frequency of 5Hz and amplitude of 3mm.In both unilateral and bilateral stances, transmission decreases from input to the forehead, however to different degrees dependent on whether there is one or both feet on the platform. Transmission in the torso is significantly greater in the unilateral stance than bilateral stance. Percentage of WBV transmitted to anatomical landmarks was calculated from peak to peak displacements measured using a Vicon motion capture system. Differences between vibration transmitted when both feet, the left foot and the right foot were on the platform were assessed using a one-way ANOVA with Dunnett's T3 post-hoc test. All outcomes are significant at $p<0.001$ unless indicated. NS=Not Significant, *$p<0.05$, ** $p<0.01$.

Irrespective of stance, percent of WBV input transmitted to a given landmark shows a decreasing trend from input to the forehead. At 5Hz (Figure 38), this trend begins from input, at 10Hz and 15Hz transmission peaks around the tibia (Figure 39) and above this frequency transmission peaks at the ankle before decreasing to the forehead (Figure 40) (Chapter 10.3.2).

Within this trend, a unilateral stance tends to result in greater transmission than a bilateral stance. When the left foot is on the platform, transmission at the heel, ankle, tibia, knee, thigh and ASIS on the left hand side is greater than when both feet are on the platform (Figure 38, Figure 39, Figure 40). The same is true for the right hand side when the right foot is on the platform. This difference in the vibration transmitted to landmarks in the lower limb, is greatest at 15Hz where transmission is 20-50% greater at the tibia and knee in a unilateral stance compared to a bilateral stance (Figure 39).

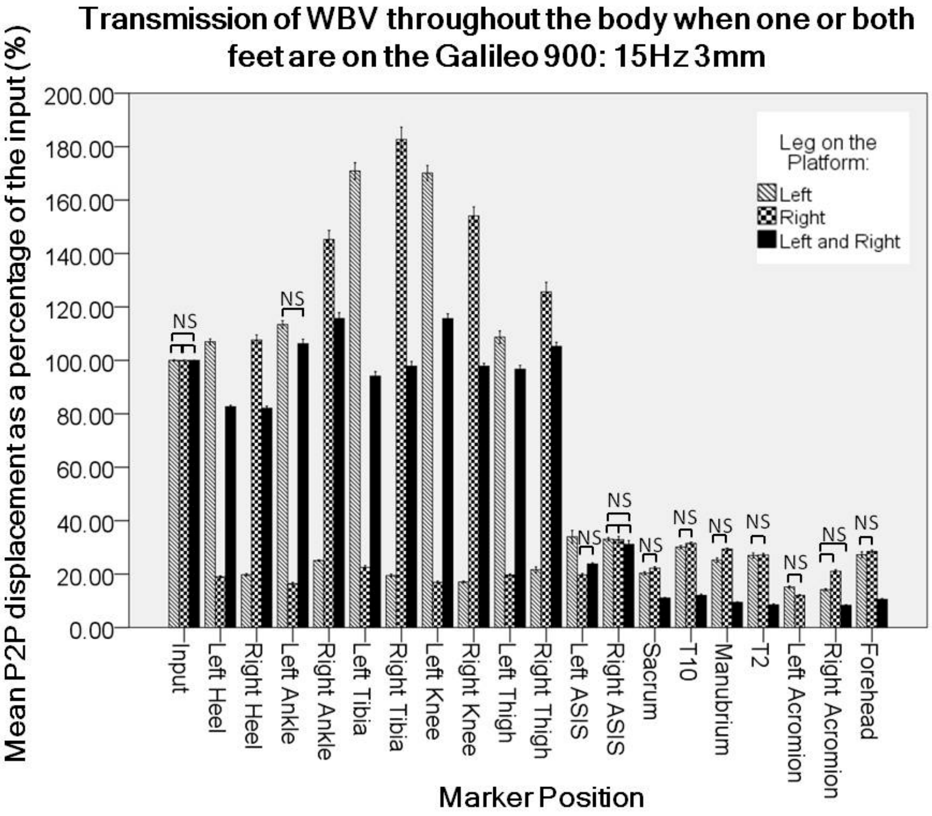

Figure 39: Transmission of 15Hz whole body vibration (WBV) with unilateral and bilateral stance.

WBV was delivered using the Galileo 900 platform at a frequency of 15Hz and amplitude of 3mm. In both unilateral and bilateral stances, transmission decreases from input to the forehead. The differences in transmission between unilateral and bilateral stances are greater than those seen at 5Hz input. Transmission in the torso is significantly greater in the unilateral stance than bilateral stance. Percentage of WBV transmitted to anatomical landmarks was calculated from peak to peak displacements measured using a Vicon motion capture system. Differences between vibration transmitted when both feet, the left foot and the right foot were on the platform were assessed using a one-way ANOVA with Dunnett's T3 post-hoc test. All outcomes are significant at $p<0.001$ unless indicated. NS=Not Significant, *$p<0.05$, ** $p<0.01$.

Similar differences are seen at 10Hz and 20Hz, however lower and higher input frequencies result in differences of <20% between bilateral and unilateral stances (on the side of input) (Chapter 10.3.2). There is no significant between stance differences in transmission to landmarks at the proximal end of the leg such as the left anterior superior iliac spine (ASIS) and left knee at 30Hz and both thighs at 5Hz (Figure 38, Figure 40).

In the Torso, again, transmission is greater when a unilateral rather than bilateral stance is adopted (Figure 38, Figure 39, Figure 40). At 5Hz, this difference is greatest with more than twice as much of the WBV signal transmitted to a given landmark in the torso with a unilateral stance compared to a bilateral stance (Figure 38). Transmission is observed at all landmarks in the torso up to a frequency of 15Hz, however above this frequency the whole body vibration signal is transmitted to few landmarks in the torso and at a frequency of 30Hz, a WBV signal is only observed at the forehead when the left foot is on the platform (Figure 40)(Chapter 10.3.2).

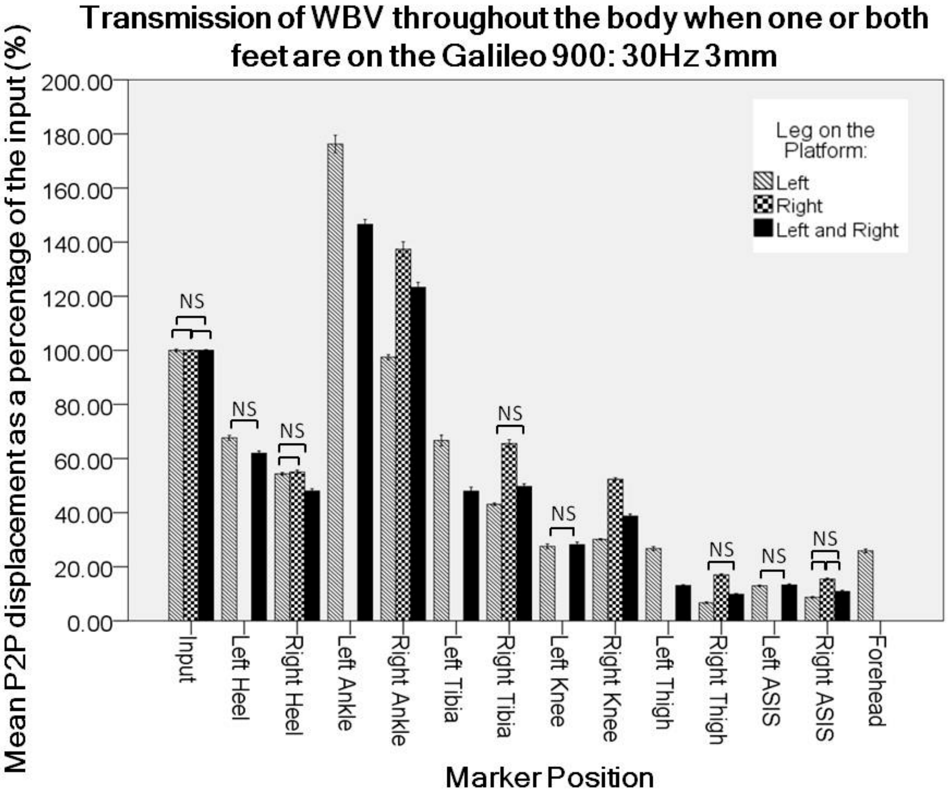

Figure 40: Transmission of 30Hz whole body vibration (WBV) with unilateral and bilateral stance.

WBV was delivered using the Galileo 900 platform at a frequency of 30Hz and amplitude of 3mm.In both unilateral and bilateral stances, transmission decreases from input to the forehead. The differences in transmission between unilateral and bilateral stances are greater than those seen at 5Hz but not as great as those at 15Hz input. Transmission in the torso is limited to the forehead. Percentage of WBV transmitted to anatomical landmarks was calculated from peak to peak displacements measured using a Vicon motion capture system. Differences between vibration transmitted when both feet, the left foot and the right foot were on the platform were assessed using a one-way ANOVA with Dunnett's T3 post-hoc test. All outcomes are significant at $p<0.001$ unless indicated. NS=Not Significant, *$p<0.05$, ** $p<0.01$.

6.3.2 Contralateral differences in the transmission of whole body vibration with both feet, left foot or right foot on the Galileo 900 platform

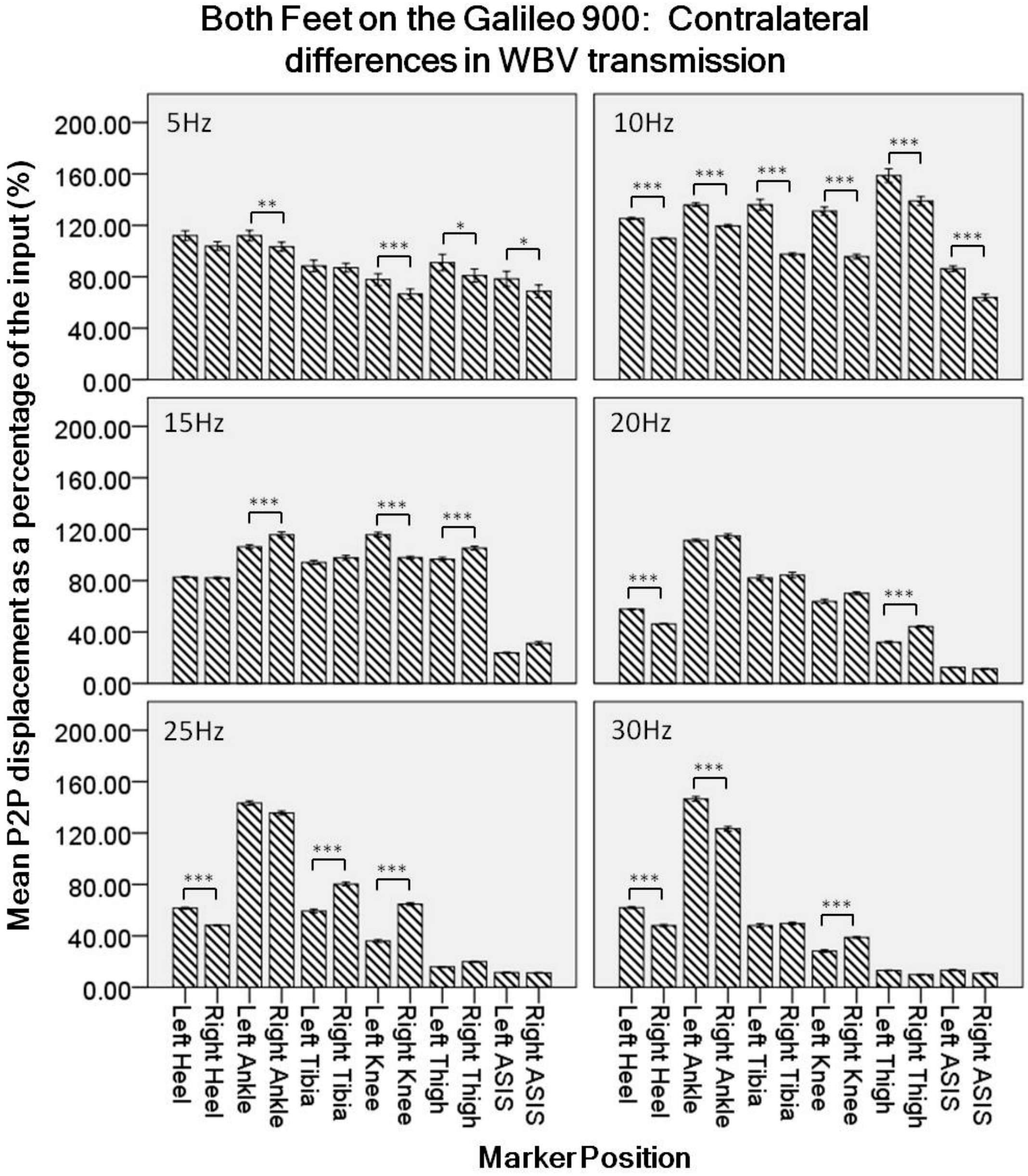

Figure 41: Contralateral difference in the transmission of whole body vibration (WBV) through the body when both feet are placed on the Galileo 900 Platform.

Recordings were made at frequencies between 5-30Hz and at 3mm amplitude. Greater transmission is seen at lower frequencies. Significant contralateral differences were seen at all frequencies. Percentage of WBV transmitted to anatomical landmarks was calculated from peak to peak displacements measured using a Vicon motion capture system. Differences between the transmission at the equivalent left and right maker were assessed using an independent students t-test, *p<0.05, **p<0.01, ***p<0.001.

With both bilateral and unilateral stances, contralateral differences in the transmission of WBV through the lower limb are present (Figure 40). With both feet on the platform, slightly more of the input signal is transmitted to the left hand side than the right at 5Hz and 10Hz (Figure 40: 5Hz & 10Hz). Above 10Hz, contralateral differences are still present however there is no clear dominance of a single side of the body (Figure 40: 15Hz, 20Hz, 25Hz, 30Hz). At all frequencies, contralateral differences in transmission lie between 0% and 25% of the greater value of transmission for a given landmark.

With only one foot on the platform, contralateral differences are much greater than when both feet were placed on the platform (Figure 41, Figure 42, Figure 43). When the left foot is on the platform, transmission to the right hand side landmarks between the heel and the thigh did not exceed 30% of that at the equivalent left hand marker (Figure 42). At most input frequencies, transmission to the right hand side did not exceed 15% of the equivalent left hand side transmission and at 20Hz and 25Hz, there was no transmission of the WBV to several right hand landmarks (Figure 42). The greatest contralateral differences are seen at 10Hz and 15Hz (Figure 42). The smallest contralateral differences are observed at 30Hz, with contralateral differences similar to those seen when both feet are on the platform (Figure 41, Figure 42). In the case of the ASIS, contralateral differences tend to be smaller, with transmission to the right hand landmark exceeding 50% of that at the left hand landmark in most cases.

The same trends are seen when the right foot is on the platform, but with the greater transmission to the right hand side as opposed to the left. In contrast to when the left foot is on the platform, at 20Hz, 25Hz and 30Hz, no transmission of WBV was observed to any of the left hand markers with the exception of the left ASIS at 20Hz (Figure 43).

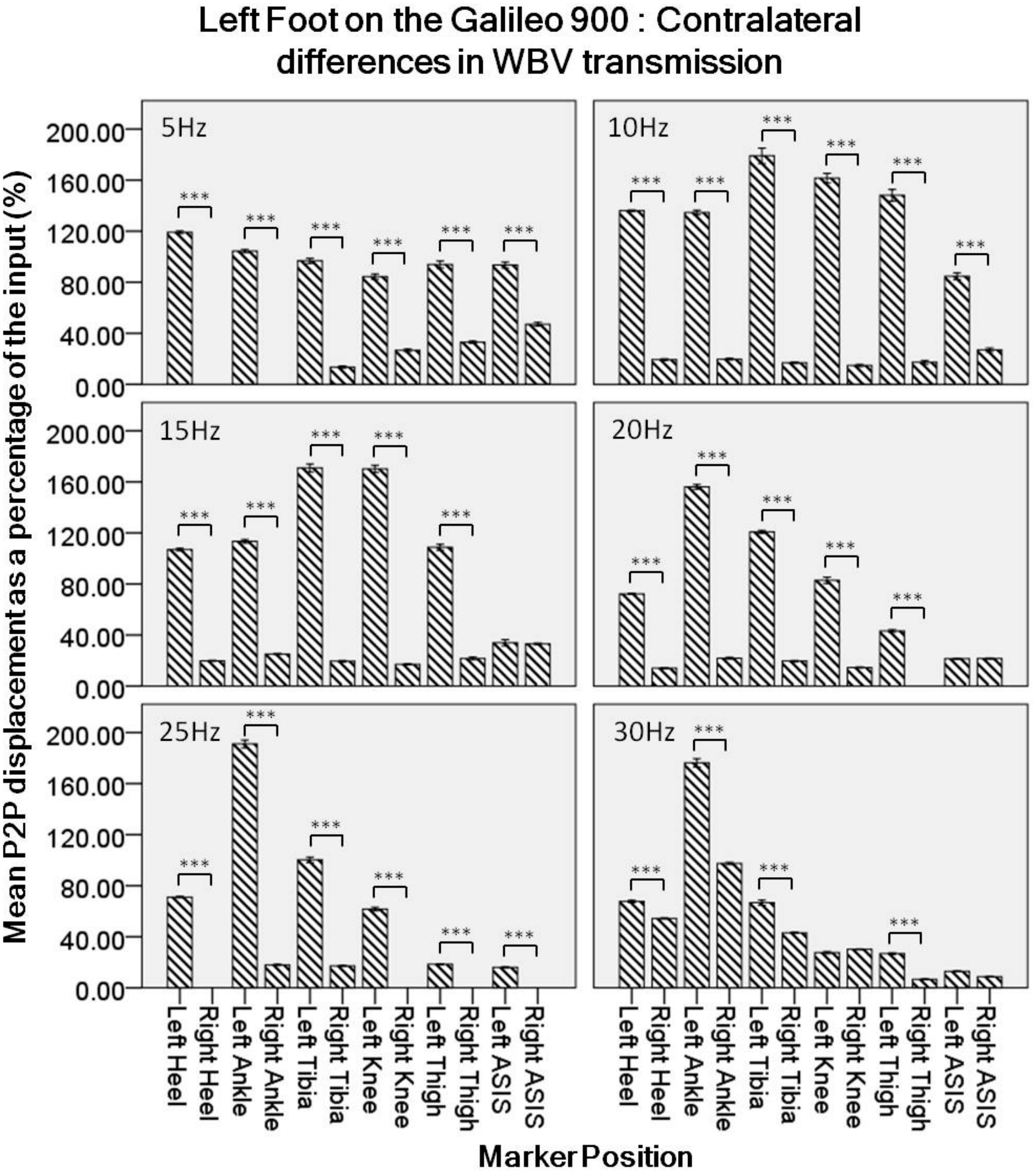

Figure 42: Contralateral differences in the transmission of whole body vibration (WBV) through the body when the left foot was placed on the Galileo 900 platform.

Recordings were made at frequencies between 5-30Hz and at 3mm amplitude. Greater transmission is seen at lower frequencies. Significant contralateral differences were seen at all frequencies with the greatest side to side differences at 10Hz & 15Hz input frequencies. Percentage of WBV transmitted to anatomical landmarks was calculated from peak to peak displacements measured using a Vicon motion capture system. Differences between the transmission at the equivalent left and right marker were assessed using an independent students t-test, *p<0.05, **p<0.01, ***p<0.001.

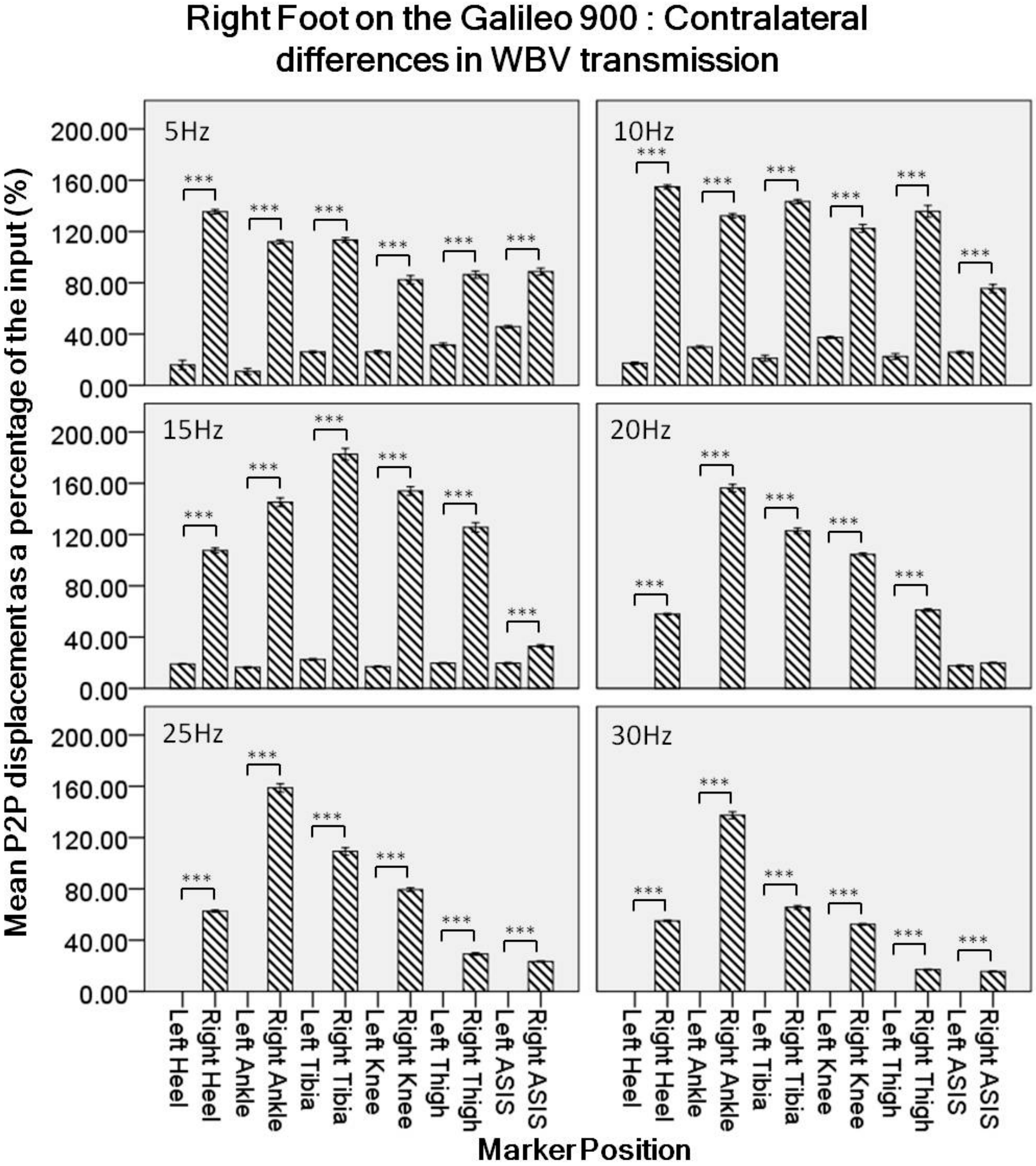

Figure 43: Contralateral differences in the transmission of whole body vibration through the body when the right foot was placed on the Galileo 900 platform.

Recordings were made at frequencies between 5-30Hz and at 3mm amplitude. Greater transmission is seen at lower frequencies. Significant contralateral differences were seen at all frequencies with the greatest side to side differences at 10&15Hz input frequencies. Percentage of WBV transmitted to anatomical landmarks was calculated from peak to peak displacements measured using a Vicon motion capture system. Differences between the transmission at the equivalent left and right marker were assessed using an independent students t-test, *p<0.05, ** p<0.01, ***p<0.001.

6.4 Discussion

With both a bilateral and unilateral stance, transmission of WBV through the body shows similar patterns in terms of peak transmission and decreasing trends from input to forehead (Figure 38, Figure 39, Figure 40). However, the magnitude of the transmission at a given landmark is greater with a unilateral stance than a bilateral stance in both the lower limb and torso (Figure 38, Figure 39, Figure 40).

This could be explained by the change in input stimulus from a side alternating mode of vibration to a mode more closely resembling vertical vibration. With the single foot on the platform, the loaded side of the body moves vertically whilst the non-loaded side of the body remains stationary as opposed to moving vertically in the opposite direction (as would occur with a bilateral stance).
As this generates a more vertical mode of vibration, transmission would be expected to be greater, especially to the torso, as this is seen when the Galileo 900 side alternating platform is compared to the Powerplate Pro 5 vertical vibration platform (Chapter 5). This means that a unilateral self-control at a given frequency would result in a greater stimulus at a given landmark than would be delivered in a bilateral stance. This should be taken into account when interpreting findings and advising on optimal WBV settings to be delivered through a bilateral stance aimed at enhancing bone parameters.

Contralateral differences in WBV transmission are seen in both bilateral and unilateral stances. In the case of the bilateral stance, there does not appear to be a clear dominance of one leg over the other, suggesting these differences could be due to spontaneous adjustment of foot positions on the platform, joint angles and weight distributions between the two legs in response to the WBV input. Given the inconsistency of which side shows greatest transmission and the small size of the contralateral differences generated with a bilateral stance (Figure 41), these differences are unlikely to be informative as a self-control for whole body vibration.

When a unilateral stance is adopted however, transmission is always greatest on the side of the body which has the foot on the WBV platform. The magnitude of the contralateral differences is also larger than that seen with the bilateral stance and together these characteristics show potential for a unilateral WBV self-control.

If the unilateral stance is to be used as a self-control in future studies, the conditions under which the greatest contralateral differences are observed could be suggested as the best candidate to generate significant differences in bone parameters due to WBV. In this instance, 10Hz or 15Hz input frequency should be used in future studies.

In addition, side to side differences are greatest at the distal end of the leg, with small or no significant difference in transmission to the ASIS at 15Hz. This could potentially mean traditional measures of aBMD at the hip and spine by DXA may not detect side to side differences due to unilateral WBV. A more suitable measure could be Xtreme computer tomography (CT), which measures vBMD at the distal end of the leg. Xtreme CT would also measure volumetric as opposed to areal BMD, allowing assessment of geometrical changes that would not be observed with aBMD.

Whilst the greatest contralateral differences were observed at these frequencies, a WBV stimulus is still detected on the side of the body which does not have the foot placed on the Galileo 900 platform. The amplitude of this stimulus is in the order of magnitude delivered by the Juvent 1000 platform, which has been shown to maintain bone mineral density (BMD) in postmenopausal women [105].
This may suggest that changes in aBMD would be expected in both legs, irrespective of the contralateral differences in the WBV transmission.

At 20Hz and 25Hz with the right leg on the platform, no transmission was observed at markers on the left hand side between the left heel and left thigh. Whilst contralateral differences are slightly less at these frequencies, the absence of transmission to the left hand side of the body may make a more complete control, with one leg experiencing no WBV stimulus. This may be advantageous if the small amount of WBV transmitted to the opposite ‘unloaded’ leg at 10Hz and 15Hz is considered to effect bone parameters.

Having said this, at 20Hz and 25Hz with the left foot on the platform there is still a small amount of transmission to the right leg (comparable to that seen at 10Hz and 15Hz).

Biomechanical differences between the left and right leg could be the cause of the differences in transmission of WBV to the contralateral leg when using a unilateral stance. A dominance of the right leg may result in this leg having stronger muscles which can withstand the WBV signal without need for support from the left leg. The ‘non-dominant’ left leg however may need support from the right leg in order to keep the body balanced when WBV is introduced.

The two legs certainly have different mechanisms for responding to the unbalancing WBV stimulus, when the left foot is placed on the platform (and a small amount of transmission to the right leg is observed), transmission values at the ankle and tibia are greater than when the right foot is placed on the platform. However, vibration is transmitted to a lesser extent at the knee and thigh when the left foot is on the platform as opposed to the right. The greater movement in the left lower leg may cause a greater unbalancing effect requiring a shift in weight to the right and transmission to the contralateral side of the body.

Whether this observation reflects the dominance of one leg will require further investigation, however another possible explanation for the discrepancies observed is that the right lower leg had undergone surgery during which local anaesthetic was administered around the site on the tibia that the strain gauge was attached. This may have caused an unusual biomechanical response to the WBV, potentially resulting in the smaller movements seen below the knee and a lack of transmission to the contralateral leg. To determine whether the differences observed are likely to be due to the dominance of one leg or due to the effects of the anaesthetic, similar recordings should be made in participants who have not undergone sugary.

Having said this, postural control in a unilateral stance and single leg squat strength have been shown not to differ between the dominant and non-dominant leg, suggesting the observations to be due to the anaesthetic rather than a lack of balance or strength [177, 178]

In this case, small amounts of transmission to the contralateral side of the body, as seen when the left leg is on the platform (Figure 42), must be expected in future studies using a unilateral loading model of WBV and as such, a 10-15Hz input frequency will generate the greatest side to side difference in WBV transmission.

Whilst both low and high magnitude WBV have been suggested to influence bone mineral density (BMD), the degree to which they maintain or increase BMD differs. In a postmenopausal population, a significant difference in hip bone mineral density (BMD) was observed compared to control when high magnitude WBV was delivered using a Powerplate platform [110] whereas only a reduction in bone loss at the hip was observed with a low magnitude WBV stimulus[105]. This suggests that even if the small amount of WBV transmitted to the contralateral side of the body is equivalent to the stimulus delivered by the Juvent 1000, side to side differences in BMD change from baseline should still be apparent and measurable.

In conclusion, there is potential for a self-controlled study of WBV using the Galileo 900 platform, however measurements of bone parameters at the distal end of the leg should be used as the side to side difference in WBV stimulus diminishes by the anterior superior iliac spine. This would make volumetric BMD (vBMD) by Xtreme CT a potential measurement tool, whereas standard DXA measurements of areal BMD (aBMD) at the hip and spine would be expected to show little if any side to side difference based on the data in this study. For the greatest difference between loaded and non-loaded leg, this data suggests that 10Hz or 15Hz input frequency should be used and the potential effects of the small amount of vibration transmitted to the contralateral leg should be acknowledged. The conclusions drawn here, whilst apparently based on clear trends, are from a small sample size, therefore further work in a larger cohort may expand on these observations.

7 Chapter Seven: Strain at the Tibia during Whole Body Vibration and Habitual Locomotor Activities

7.1 Background

Strain recorded at the tibia has been used to assess the impact of different activities on the skeleton. Previous studies documented strains generated during activities of daily living as well as during high impact activities thought to contribute to stress fracture development in army recruits[89, 97, 135, 138, 139, 143-145, 179].

Strain magnitude has been shown to increase with increasing impact of physical activity [89, 97, 138, 179]. However the strain magnitude alone does not full account for the osteogenic potential of an activity. Strain rate has also been shown to have a key role in determining the skeletal response to a given activity [180].

Strain is recorded at the tibia using strain gauges which can either be bonded directly to the tibial shaft or can be applied using pre prepared bone staples. When directly bonding the strain gauges to the surface of the bone, the cortex of the bone remains unaffected by the procedure, however de-bonding of the strain gauges is a potential problem [89]. The alternative bone staples result in small holes in the cortex caused by the insertion of the bone staples. Whilst de-bonding has not been reported as a problem using this technique, strain gauge failure was more common[138]. As neither process was without its limitations, in this study surface mounted strain gauges were used in order to avoid damage to the cortex of the bone.

The aim of this study is to compare tibial strain and associated strain rates during habitual locomotor activities and during whole body vibration (WBV).

7.2 Methods

7.2.1 Participant Population

Six healthy volunteers aged between 18 and 50 who were physically able and willing to undertake the study procedures were recruited from Sheffield (South Yorkshire, UK). Participants had a bone mineral density (measured by dual x-ray absorptiometry (DXA)) within +/- 2 SD of the young normal at the lumbar spine and hip and a body mass index (BMI) <30. Data reported here is for participant 3 and participant 4 as these are the only participants for which recordings from all three strain gauge elements are available. The characteristics of the six participants included in the study are detailed in Chapter 3.1, Table 4.

7.2.2 Strain Measurement

Strain was recorded directly from the anteromedial surface of the tibia at the midpoint between the medial aspect of the tibial plateau and the lower border of the medial malleolus using an FRA 2-11 rosette strain gauge (Vishay precision group, Basingstoke, UK). Details of the preparation and application of the gauge can be found in chapter 3.3.6. Data was recorded using a DLK 900 DataLINK system and DataLog software from Biometrics Ltd.

7.2.2.1 Calculating Principal Strain

Principal strain was calculated from the strain recordings made from the three individual strain gauge elements, each of which was spaced 45 degrees from the next. Calculations were made using the principal strain equation (Chapter 3.3.3, Equation 3).

7.2.2.2 Calculating Strain Rate

Strain rate was calculated from the principal strain using Equation 16.

Equation 16: Strain Rate Calculation

$$Strain\ Rate = \frac{\varepsilon_{n-\varepsilon_{n-1}}}{0.002}$$

ε_n= strain n, ε_{n-1}= strain recorded previous to $\varepsilon_{n,}$ 0.002 = number of seconds between recordings

7.2.3 Habitual Locomotor Activities

Strain recordings were made whilst the participants performed habitual locomotor activities of 1) Standing, 2) Walking, 3) Walking whilst carrying 15Kg weight in a rucksack 4)Hopping, 5) Jumping. These activities reflected those previously studied during in vivo strain gauge studies. The data presented here is for participant 4 only as one or more strain gauge elements had failed prior to these recordings for participant 3.

7.2.4 Whole Body Vibration

Strain recordings were made whilst participants stood on the Galileo 900, Powerplate Pro5 and Juvent 1000 whole body vibration platforms.

The Galileo 900 platform delivered reciprocal WBV at amplitudes of 0-5mm in 1mm increments and frequencies of 5-30Hz at increments of 5Hz. To achieve the different amplitudes the participant changed the spacing of their feet on the platform (Chapter 4.1.2: Figure 14).

The Powerplate Pro 5 platform delivered vertical WBV at amplitudes defined by the manufacturer as ‘Low’ and ‘High’ and frequencies of 25Hz and 30Hz. Both the amplitude and frequency were changed using the electronic platform settings.

The Juvent 1000 platform delivered vertical WBV at amplitudes 10 fold lower than either the Galileo 900 or Powerplate Pro 5 at a frequency between 32Hz and 37Hz. The outcome was an acceleration of 0.3g.

All recordings were made with participants maintaining a bilateral stance with knees slightly bent. Knee angle was at the discretion of the participant and the stance adopted was directed to be ‘comfortable’ for the participant.

7.2.4.1 Unilateral Whole Body Vibration

In addition to the bilateral stance, each participant stood in a unilateral stance on the Galileo 900 platform with their feet spaced such that the input reciprocal vibration had an amplitude of 3mm. Recordings were made with the frequency of the input vibration set to 5Hz, 10Hz, 15Hz, 20Hz, 25Hz and 30Hz.

Recordings were made with two unilateral stances, the first with only the left foot on the platform, the second with only the right foot on the platform at the 3mm amplitude position. When unilateral stances were adopted, the foot not on the platform was placed on a fixed platform of the same height as the Galileo 900.

7.3 Results

7.3.1 Strain and Strain Rate during Habitual Locomotor Activities

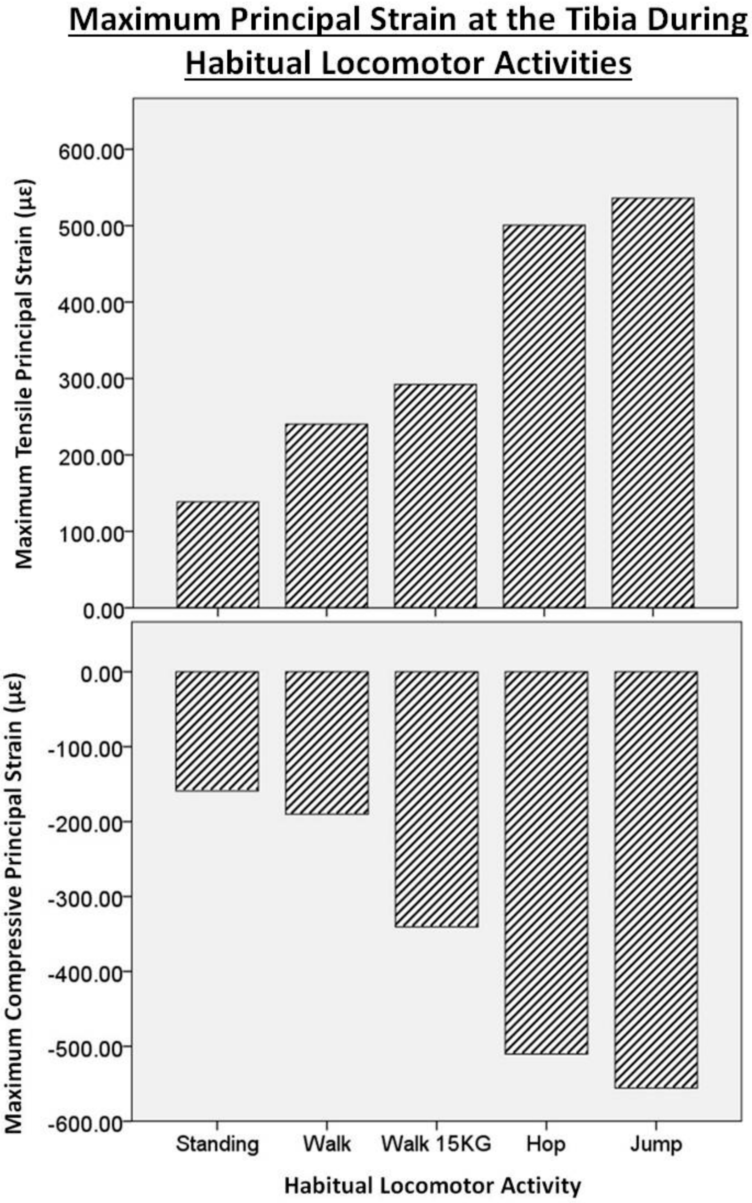

Figure 44: Principal Strain at the Tibia during Habitual Locomotor Activities.

Strain was recorded from the anteromedial surface of the tibia at the midpoint between the medial aspect of the tibial plateau and the lower border of the medial malleolus using an FRA-211 rosette strain gauge. Principal strain was calculated from the strain recorded at three strain gauge elements in a rectangular formation. Both maximum tensile and compressive principal strains increase with the increasing impact of the activity. Lowest strain is observed whilst standing whilst Jumping engenders the greatest tibial strains.

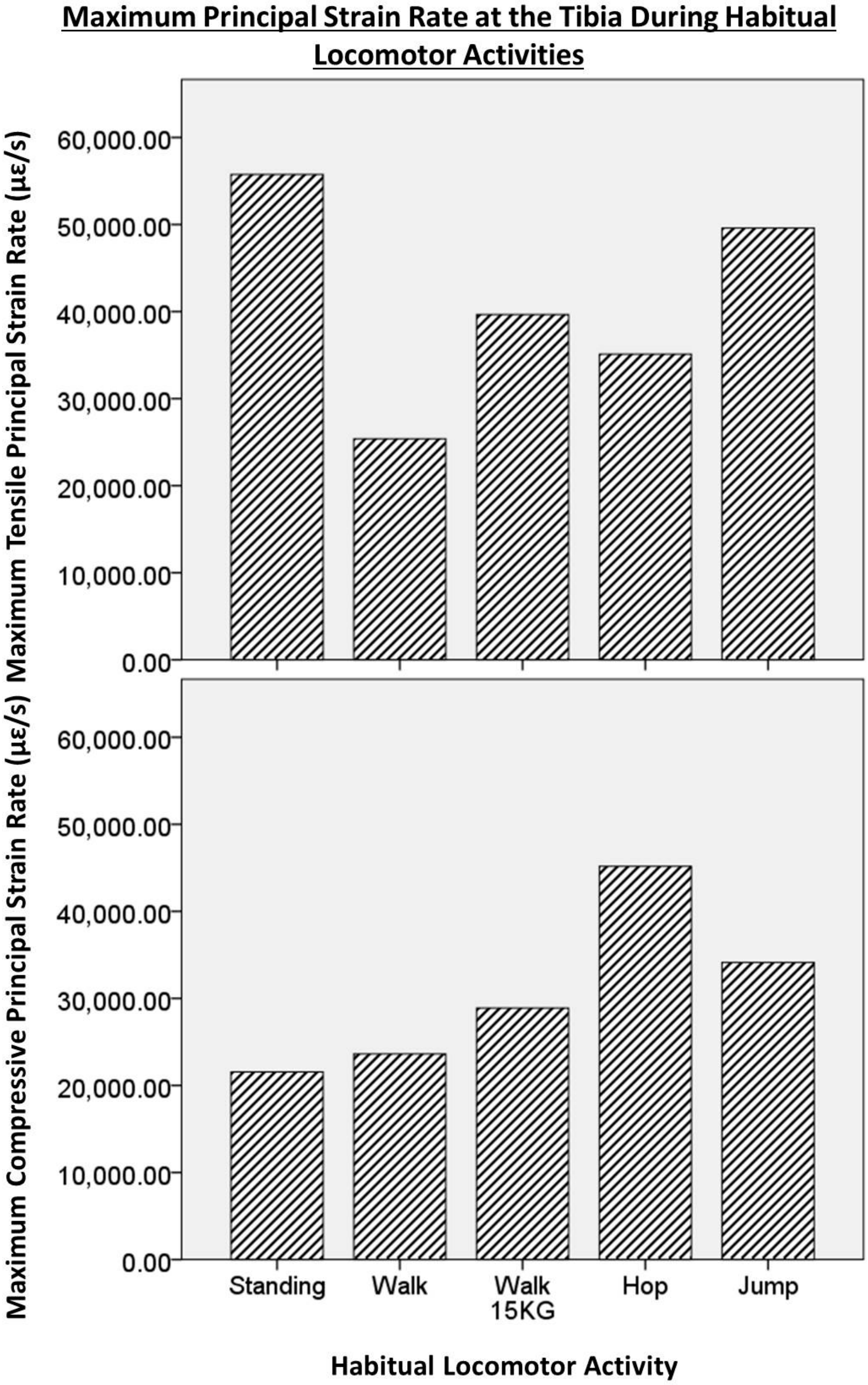

Figure 45: Strain Rate at the Tibia during Habitual Locomotor Activities.
Strain was recorded from the anteromedial surface of the tibia at the midpoint between the medial aspect of the tibial plateau and the lower border of the medial malleolus using an FRA-211 rosette strain gauge. Strain rate was calculated through differentiation of the principal strain. Tensile strain rate appears greatest whilst standing, however compressive strain rate is greater as the impact of activity increases, from smallest whilst standing to greatest whilst hopping. The compressive strain rate whilst jumping is greater than whilst walking however smaller than whilst hopping.

Principal strain at the tibia was greater with greater impact of the habitual locomotor activity studied, with standing engendering the smallest (~150µε) and jumping the greatest (~550µε) tensile and compressive principal strains (Figure 44). The strain rate followed a similar trend, with the exception of the tensile strain rate whilst standing which was much larger than the other strain rates observed (Figure 45). The greatest tensile strain rate other than during standing was observed whilst jumping and the greatest compressive strain rate was observed whilst hopping. Both were in the order of 45,000-50,000µε/s (Figure 45).

7.3.2 Strain and Strain Rate during Whole Body Vibration on the Galileo 900 Platform

On the Galileo 900 platform, principal strain generally increases with both input amplitude and frequency. With an input amplitude of 0mm, 1mm and 3mm, principal strain increases slightly with increasing input frequency (Figure 46, Figure 47). At 3mm input frequency, an increase is seen with increasing input frequency from 5-15Hz for participant 3 (P3) (Figure 46, Figure 47). At 5mm input amplitude, principal strain magnitude increases with input frequency up to 15Hz above which strain is similar or decreases with increasing input frequency (Figure 46, Figure 47). The greatest principal strains generated at the tibia during whole body vibration (WBV) on the Galileo 900 platform occur at 15Hz 5mm. The greatest tensile strains are in the order of 300µε (P3) and 600µε (P4) and the greatest compressive strains are in the order of -250µε (P3) and -400µε (P4) (Figure 46, Figure 47).

The strain rates generated at the tibia during WBV on the Galileo 900 increase both with increased input amplitude and frequency (Figure 48, Figure 49). In the case of participant 4, 0mm and 1mm amplitude inputs engender strain rates approximately one third of those at 3mm and 5mm input amplitudes. The maximum strain rates observed for participant 3 are in the order of 25,000µε, whereas those observed for participant 4 are in the order of 130,000µε, approximately 3 times greater than those generated during habitual locomotor activities (Figure 45, Figure 48, Figure 49).

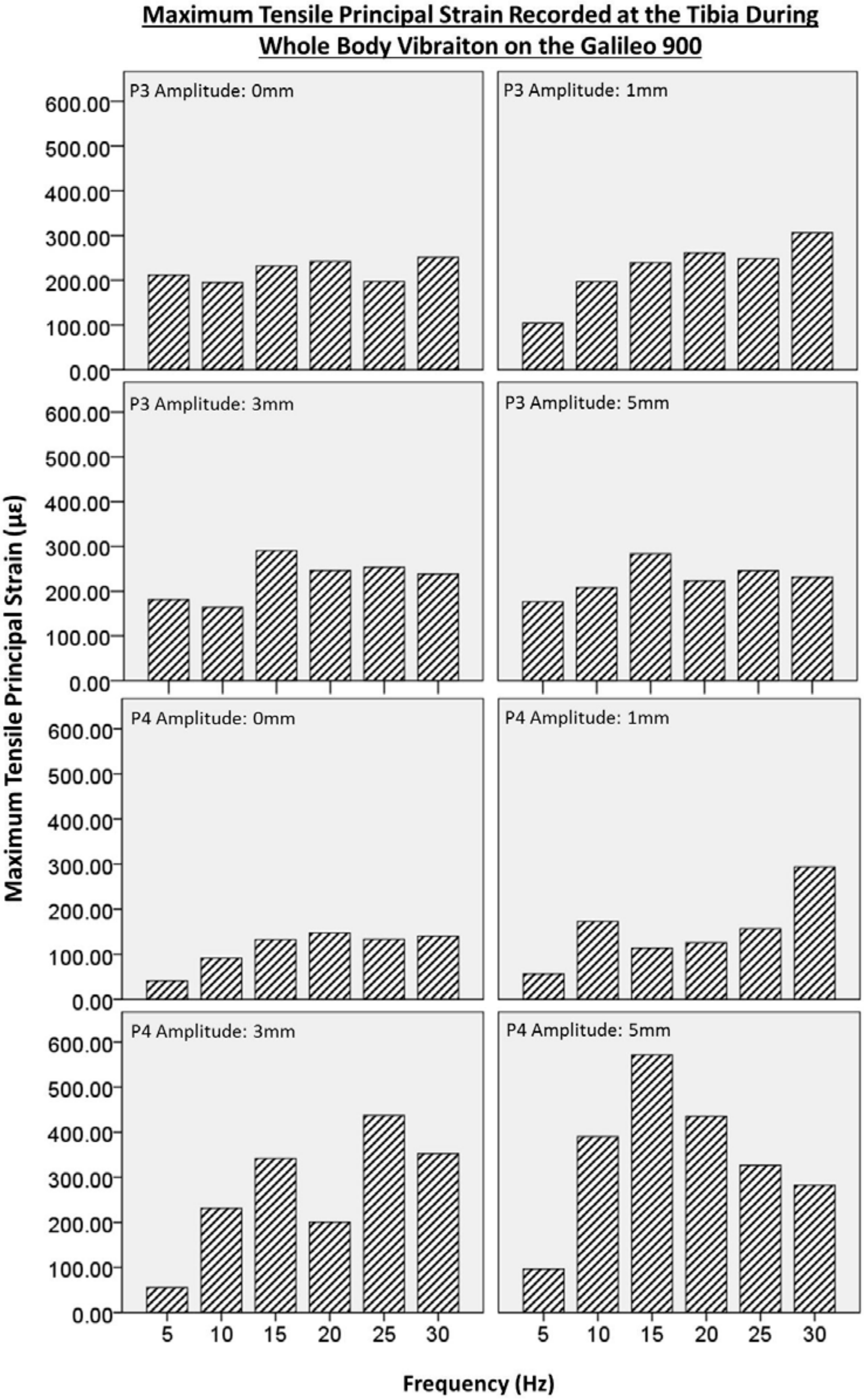

Figure 46: Tensile Principal Strain at the Tibia during Whole Body Vibration: Galileo 900. Strain was recorded from the anteromedial surface of the tibia at the midpoint between the medial aspect of the tibial plateau and the lower border of the medial malleolus using an FRA-211 rosette strain gauge. Principal strain was calculated from the strain recorded at three strain gauge elements in a rectangular formation. Tensile principal strain increases slightly with increased input frequency in participant 3 (P3). For Participant 4 (P4), tensile principal strain increases with input frequency and amplitude. At 5mm amplitude, the maximum tensile strain is observed at 15Hz above which the tensile strain decreases from 15-30Hz.

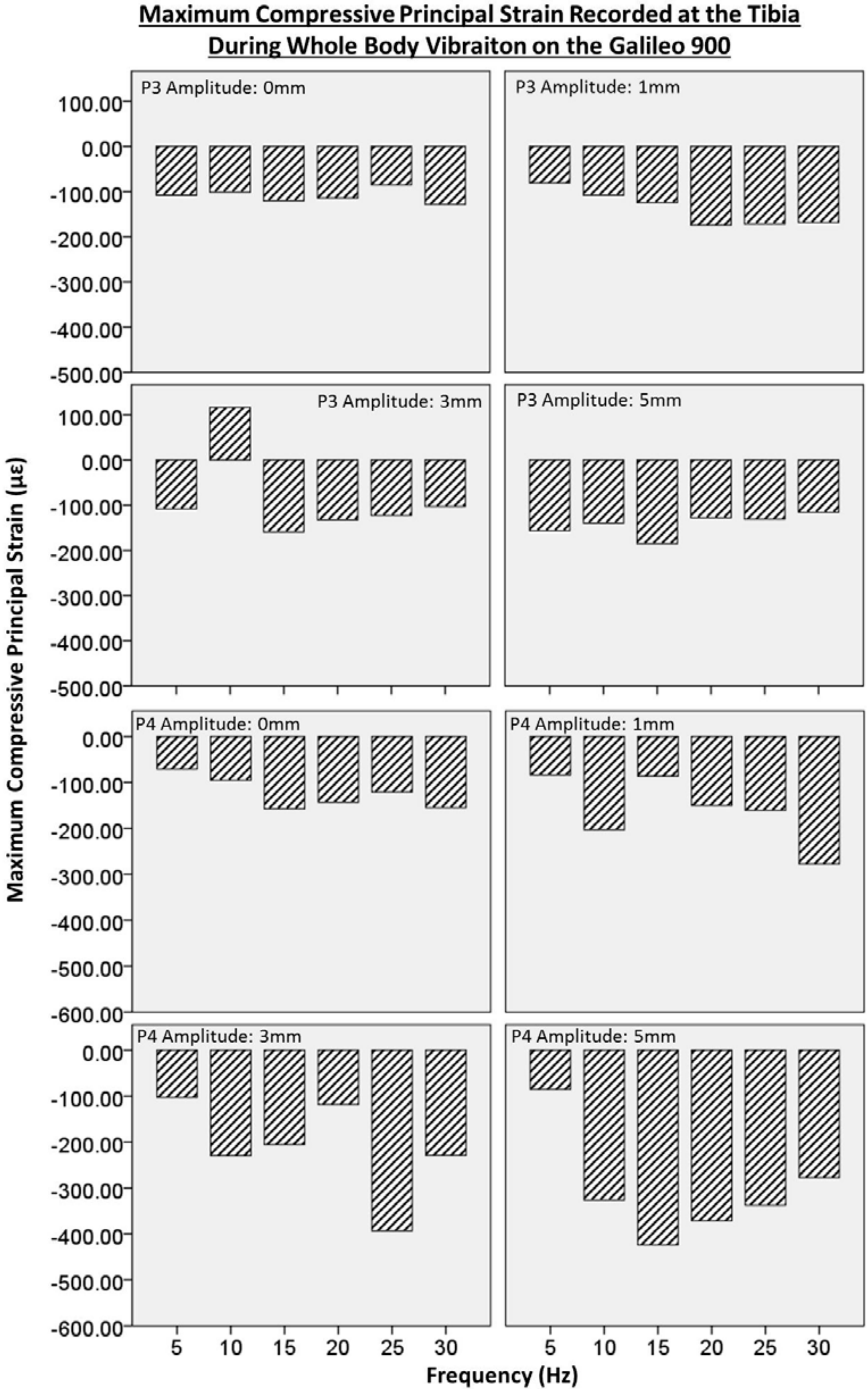

Figure 47: **Compressive Principal Strain at the tibia during Whole Body Vibration: Galileo 900.** Strain was recorded from the anteromedial surface of the tibia at the midpoint between the medial aspect of the tibial plateau and the lower border of the medial malleolus using an FRA-211 rosette strain gauge. Principal strain was calculated from the strain recorded at three strain gauge elements in a rectangular formation. Compressive principal strain increases slightly with increased input frequency in participant 3 (P3). For Participant 4 (P4), compressive principal strain increases with input frequency and amplitude. At 5mm amplitude, the maximum compressive strain is observed at 15Hz above which the tensile strain decreases from 15-30Hz.

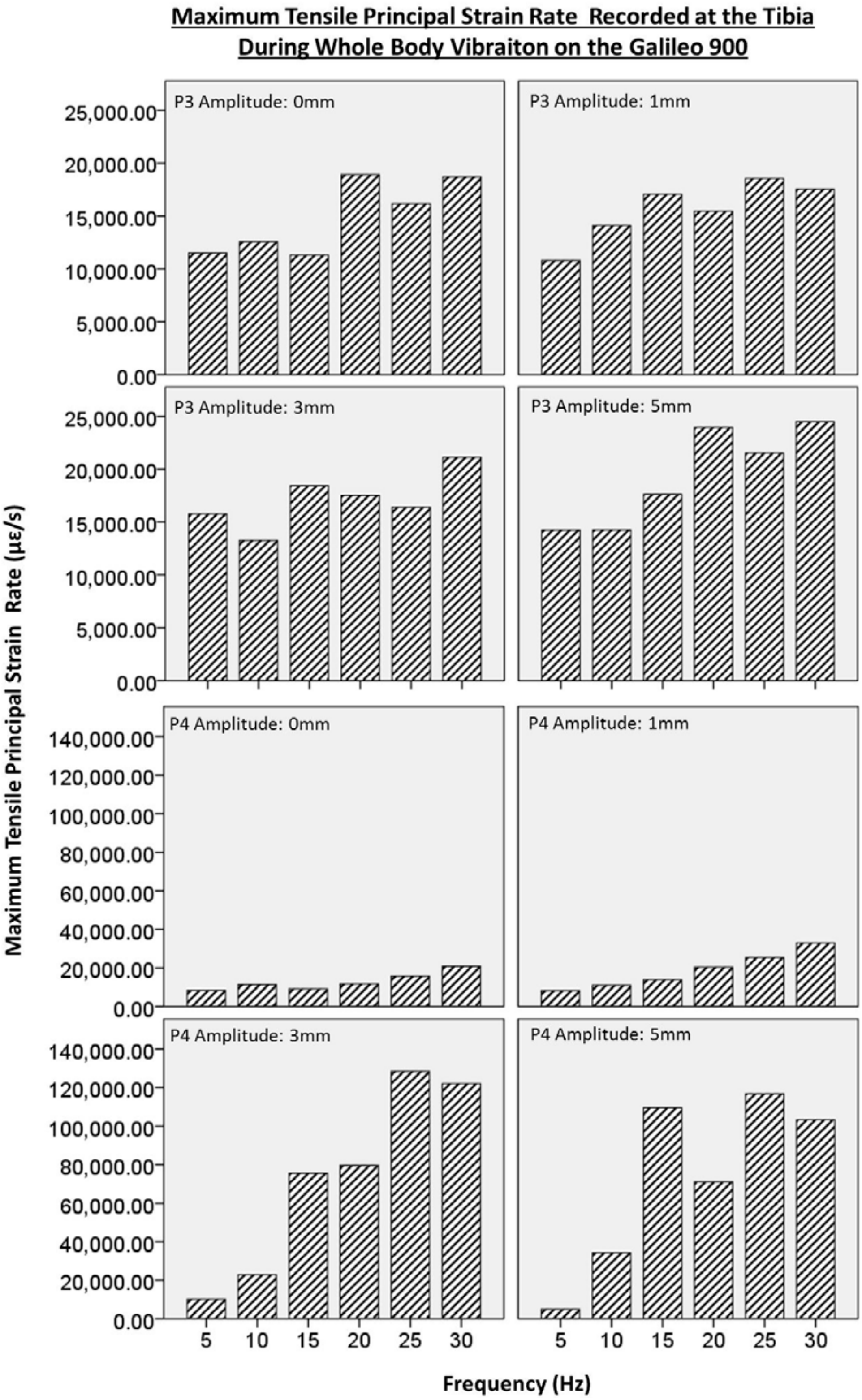

Figure 48: Tensile Strain Rate at the Tibia during Whole Body Vibration: Galileo 900
Strain was recorded from the anteromedial surface of the tibia at the midpoint between the medial aspect of the tibial plateau and the lower border of the medial malleolus using an FRA-211 rosette strain gauge. Strain rate was calculated through differentiation of the principal strain. Tensile strain rate generally increases with frequency and amplitude of input. This pattern is more clear for participant 4 (P4) than participant 3 (P3). For participant 4, at 5mm amplitude, there is a break in the trend, with greater tensile strain rate at 15Hz than at 20Hz.

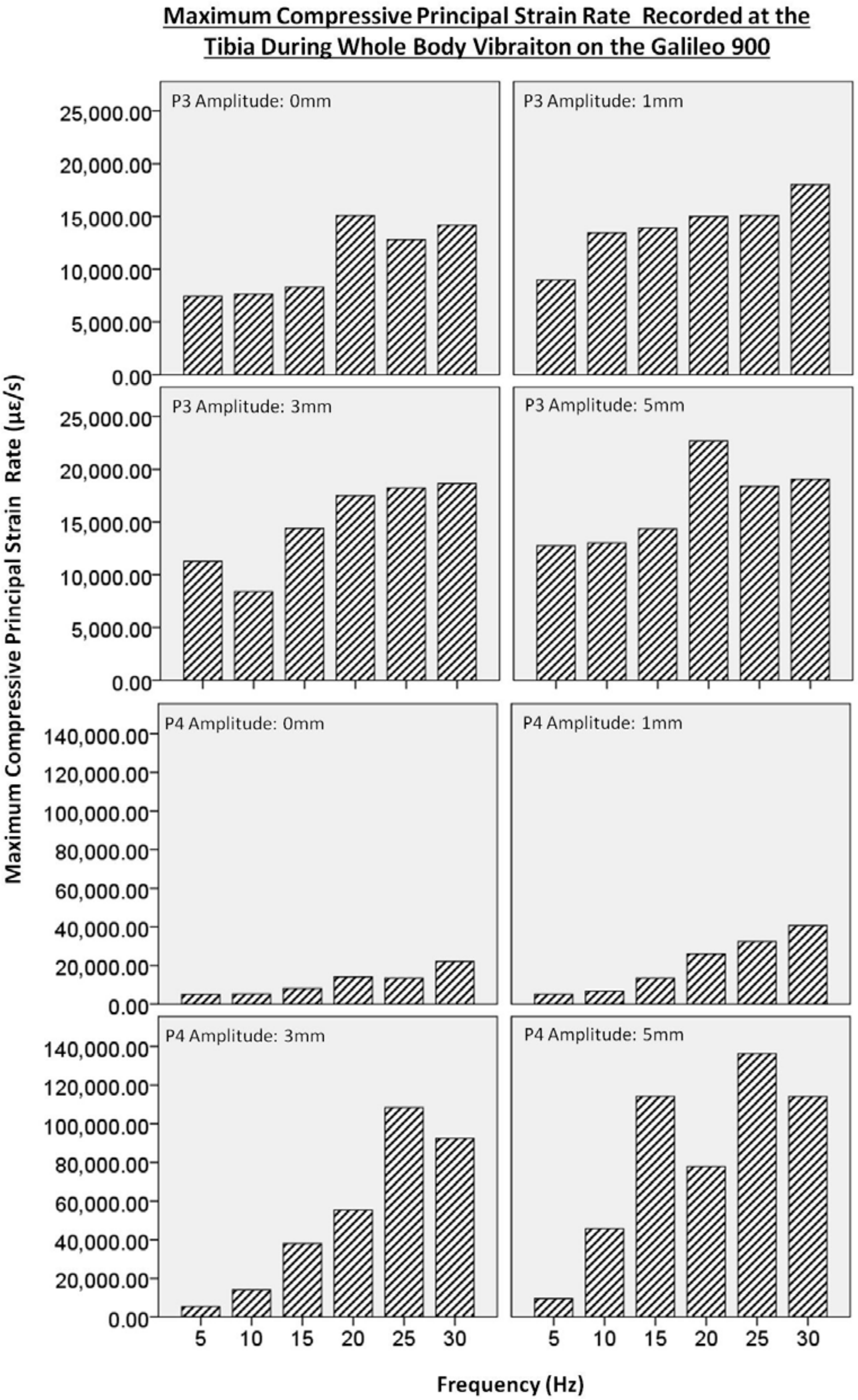

Figure 49: Compressive Strain Rate at the Tibia during Whole Body Vibration: Galileo 900

Strain was recorded from the anteromedial surface of the tibia at the midpoint between the medial aspect of the tibial plateau and the lower border of the medial malleolus using an FRA-211 rosette strain gauge. Strain rate was calculated through differentiation of the principal strain. Compressive strain rate generally increases with frequency and amplitude of input. This pattern is more clear for participant 4 (P4) than participant 3 (P3). For participant 4, at 5mm amplitude, there is a break in the trend, with greater tensile strain rate at 15Hz than at 20Hz.

7.3.3 Strain and Strain Rate during Whole Body Vibration on the Powerplate Pro 5

Principal strains generated at the tibia when participants were stood on the Powerplate Pro 5 increase with increasing input amplitude (from Low to High), however show little change with increasing input frequency (Figure 50). The greatest tensile and compressive strains are observed at 30Hz High and are in the order of (+/-) 150με for participant 3 and (+/-) 300με for participant 4 (Figure 50), approximately half of the greatest principal strains observed using the Galileo 900.

The strain rates generated using the Powerplate Pro 5 show little dependency on input amplitude or frequency for participant 3, however show a slight increase with increasing input amplitude and frequency in participant 4 (Figure 51). The greatest strain rates generated using the Powerplate Pro 5 occur at 30Hz High and are in the order of 10,000με/s for participant 3 and 25,000-30,000με/s for participant 4 (Figure 51).

7.3.4 Strain and Strain Rate during Whole Body Vibration on the Juvent 1000

Maximum tensile principal strains generated at the tibia when participants stood on the Juvent 1000 are in the order of 100-150με and maximum compressive principal strains are in the order of -70με (Figure 52). These are lower magnitude strains than those observed on the Galileo 900 (Figure 46, Figure 47) and Powerplate Pro 5 (Figure 50) and are comparable to those recorded whilst participants were standing (Figure 44).

The tensile strain rate generated at the tibia whilst participants were standing on the Juvent 1000 was in the order of 10,000με/s and the compressive strain rate in the order of 5,500με/s (Figure 53). Again, these values are lower than those generated by the Galileo 900 (Figure 48, Figure 49) and Powerplate Pro 5 (Figure 51) and are similar to those recorded whilst the participants were standing (Figure 45).

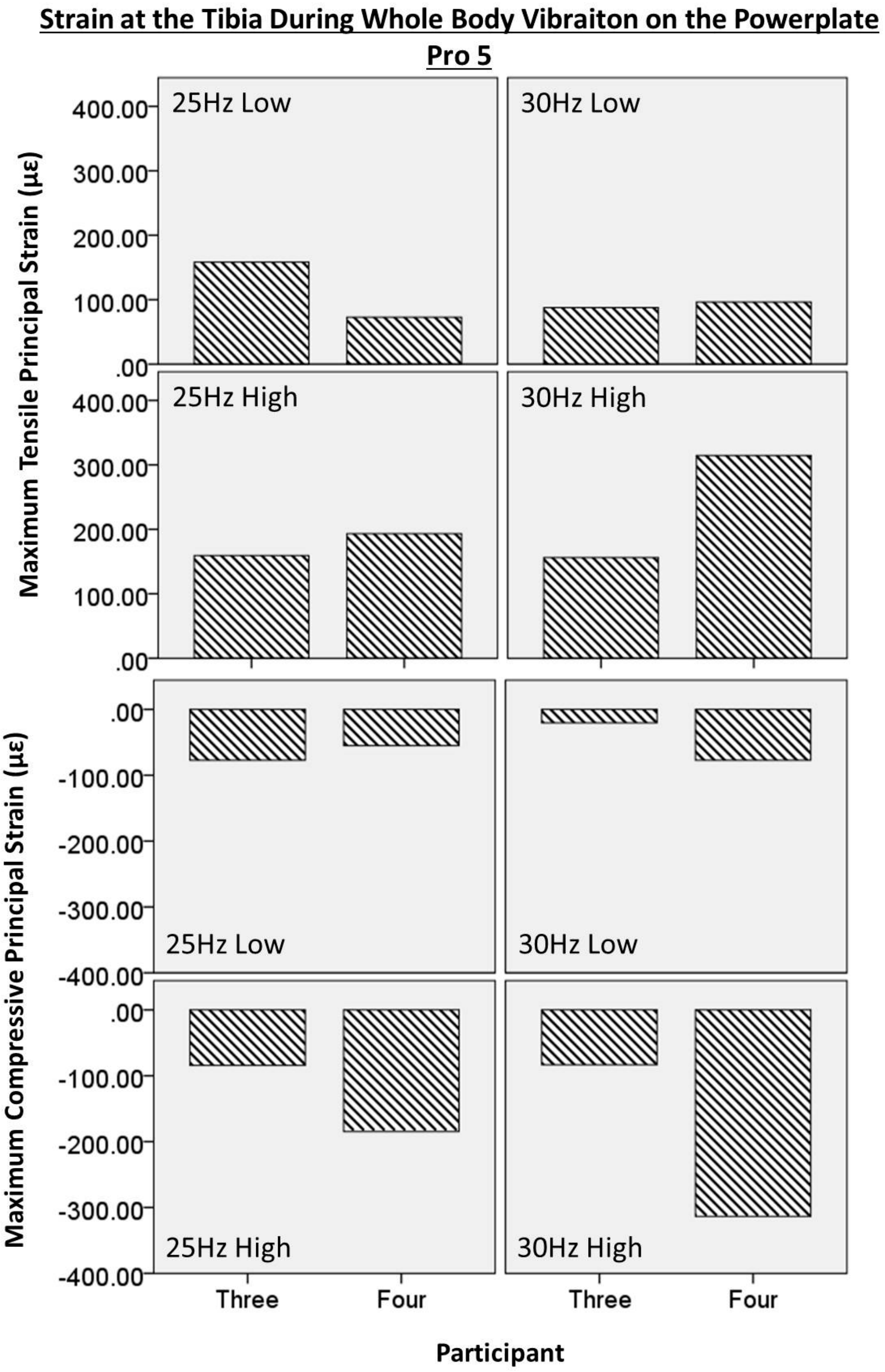

Figure 50: Strain at the Tibia during Whole Body Vibration: Powerplate Pro 5

Strain was recorded from the anteromedial surface of the tibia at the midpoint between the medial aspect of the tibial plateau and the lower border of the medial malleolus using an FRA-211 rosette strain gauge. Principal strain was calculated from the strain recorded at three strain gauge elements in a rectangular formation. Both tensile and compressive principal strain increased with greater amplitude. At Low amplitude, strain was similar across input frequencies, however at high amplitude, strain was slightly greater at 30Hz than 25Hz input frequency.

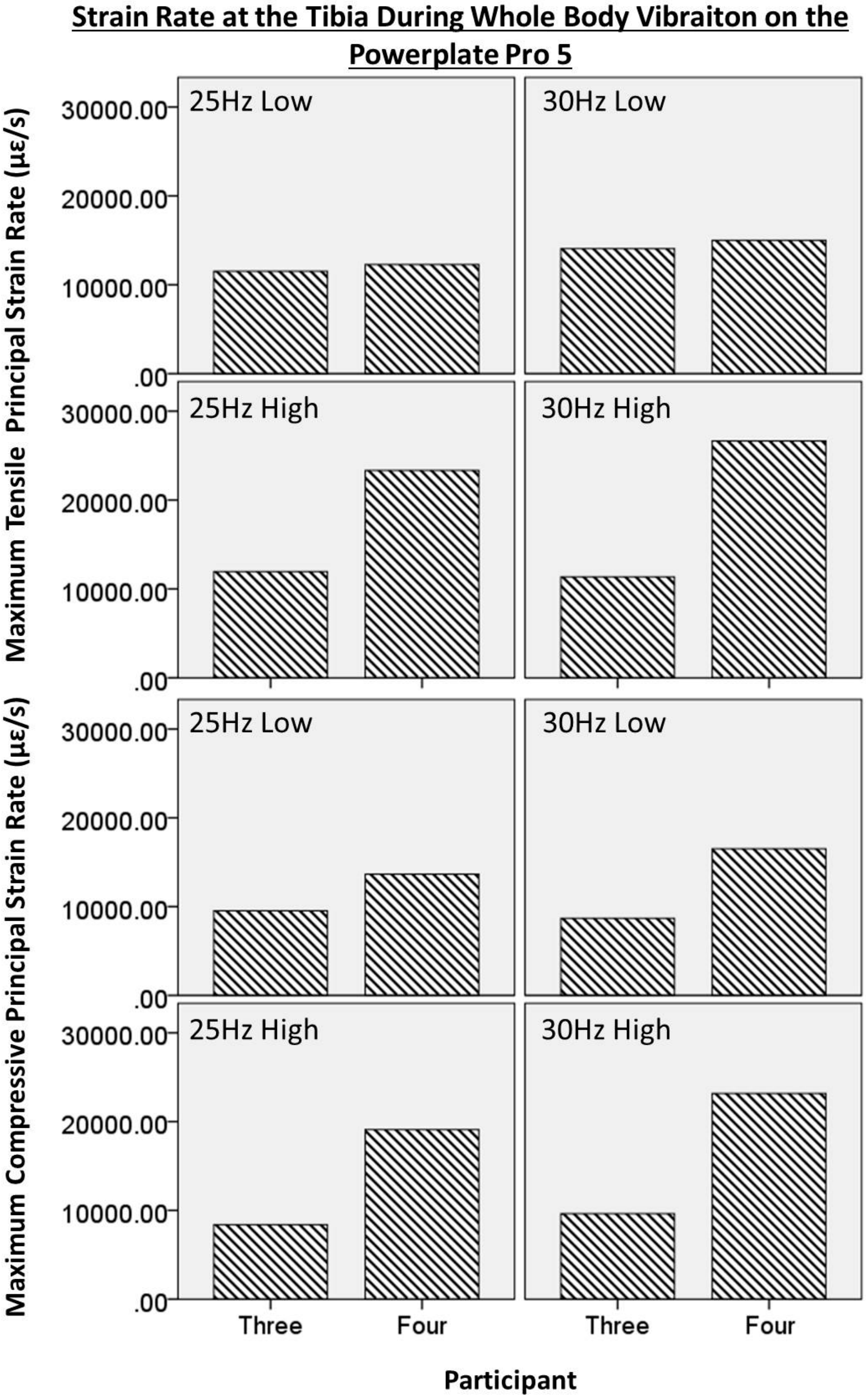

Figure 51: Strain Rate during Whole Body Vibration: Powerplate Pro 5

Strain was recorded from the anteromedial surface of the tibia at the midpoint between the medial aspect of the tibial plateau and the lower border of the medial malleolus using an FRA-211 rosette strain gauge. Strain rate was calculated through differentiation of the principal strain. Strain rate increases with input frequency. This is more apparent for participant 4 than participant 3.

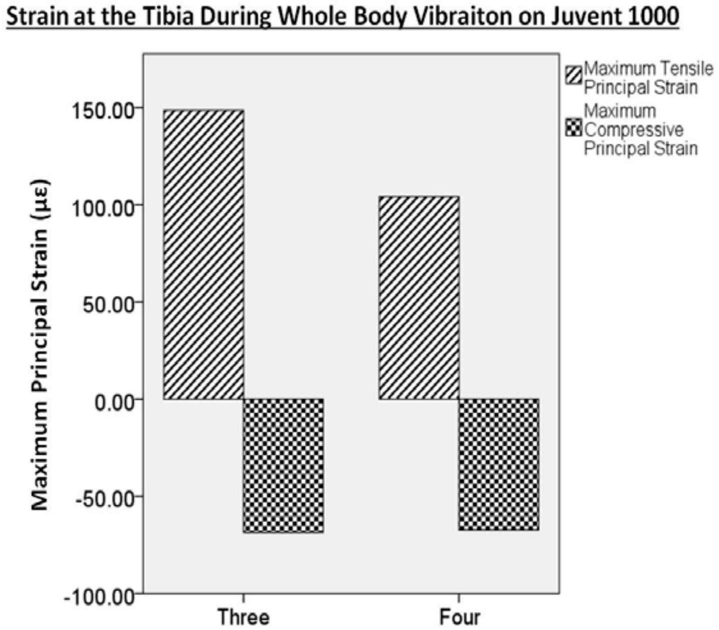

Figure 52: Strain at the Tibia during Whole Body Vibration: Juvent 1000
Strain was recorded from the anteromedial surface of the tibia at the midpoint between the medial aspect of the tibial plateau and the lower border of the medial malleolus using an FRA-211 rosette strain gauge. Principal strain was calculated from the strain recorded at three strain gauge elements in a rectangular formation. Tensile strains in the order of 150με and compressive strains in the order of -60με were observed.

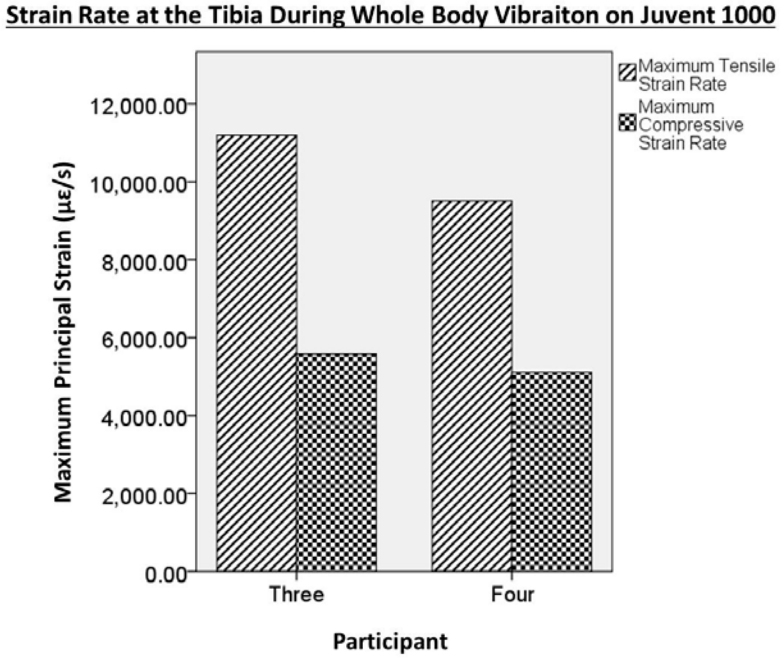

Figure 53: Strain Rate at the Tibia during Whole Body Vibration: Juvent 1000
Strain was recorded from the anteromedial surface of the tibia at the midpoint between the medial aspect of the tibial plateau and the lower border of the medial malleolus using an FRA-211 rosette strain gauge. Strain rate was calculated through differentiation of the principal strain. Tensile strain rates of up to 10000με/s and compressive strain rates of up to 5500με/s are observed.

7.3.5 Strain and Strain Rate during Unilateral Whole Body Vibration on the Galileo 900

The principal strain generated at the tibia is greater when the right leg (with the strain gauge attached) is on the Galileo 900 as opposed to off the platform on a stationary platform of the same height as the vibration platform (Figure 54, Figure 55). When the right leg is on the platform, tensile principal strains in the order of 200µε (P3) and 400µε (P4) (Figure 54) are observed and show a trend of increasing magnitude with increasing input frequency, as when both feet are on the Galileo 900 (Figure 46). The same is true for compressive principal strains, with magnitudes in the order of -100µε and -400µε observed (Figure 55). The magnitude of the principal strains at the tibia when only one foot is placed on the platform is comparable to that recorded when both feet are on the platform. When the right leg is placed at the same height as but not on the platform, tensile principal strains in the order of 100-150µε and compressive strains less than 100µε are generated for both participant 3 and participant 4. These strains are similar in magnitude to those generated when participants are standing (Figure 44). This results in greater tibial strain being generated when the right leg is on the platform as opposed to off the platform, with the difference being more marked in participant 4 than participant 3 (Figure 54, Figure 55).

Strain rate is also greater when the right leg is on the platform at frequencies between 20-30Hz for participant 3 and at frequencies between 10-30Hz for participant 4 (Figure 56, Figure 57). Strain rates generated when the right leg is on the platform are in the order of (+/-) 15,000µε/s for participant 3 and (+/-)100,000µε/s for participant 4 (Figure 56, Figure 57), similar to the magnitude of the strain rate generated when both feet are on the platform (Figure 48, Figure 49). Strain rates when the right leg is not on the platform are in the order of 10,000-15,000, again showing a difference (particularly clear in participant 4) between having the right leg on and off the platform at frequencies between 20-30Hz for participant 3 and 10-30Hz for participant 4 (Figure 56, Figure 57).

The greatest difference in principal strain and strain rate between having the right leg on or off the Galileo 900 is observed at an input frequency of 20Hz, with the exception of compressive strain rate for which the greatest difference is observed at 30Hz input frequency.

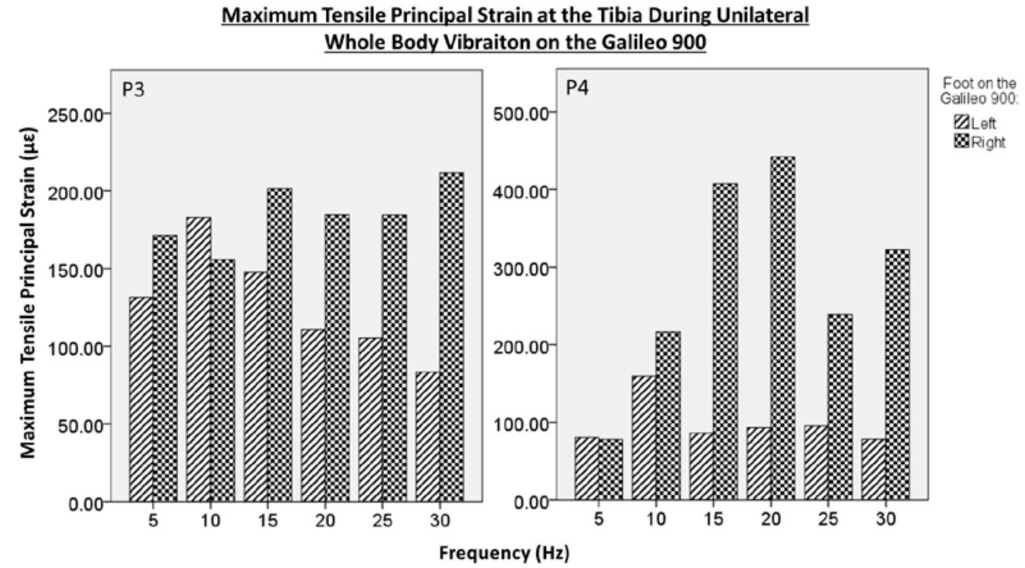

Figure 54: Tensile Strain at the Tibia during Unilateral Whole Body Vibration: Galileo 900

Strain was recorded from the anteromedial surface of the tibia at the midpoint between the medial aspect of the tibial plateau and the lower border of the medial malleolus using an FRA-211 rosette strain gauge. Principal strain was calculated from the strain recorded at three strain gauge elements in a rectangular formation. Tensile strain is greater when the strain gauges leg is on the Galileo 900 platform as opposed to off it. There is a clearer difference in participant 4 (P4) than participant 3 (P3), where tensile strains roughly double those of P3 are observed.

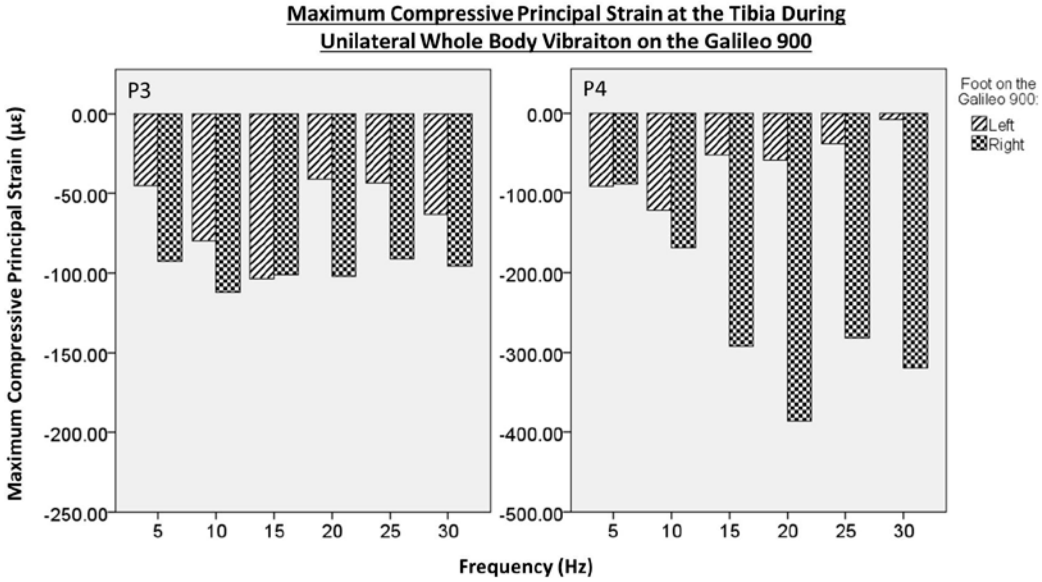

Figure 55: Compressive Strain at the Tibia during Unilateral Whole Body Vibration: Galileo 900

Strain was recorded from the anteromedial surface of the tibia at the midpoint between the medial aspect of the tibial plateau and the lower border of the medial malleolus using an FRA-211 rosette strain gauge. Principal strain was calculated from the strain recorded at three strain gauge elements in a rectangular formation. Compressive Strain is greater when the strain gauges leg is on the Galileo 900 platform as opposed to off it. There is a clearer difference in participant 4 (P4) than participant 3 (P3), where compressive strains roughly double those of P3 are observed.

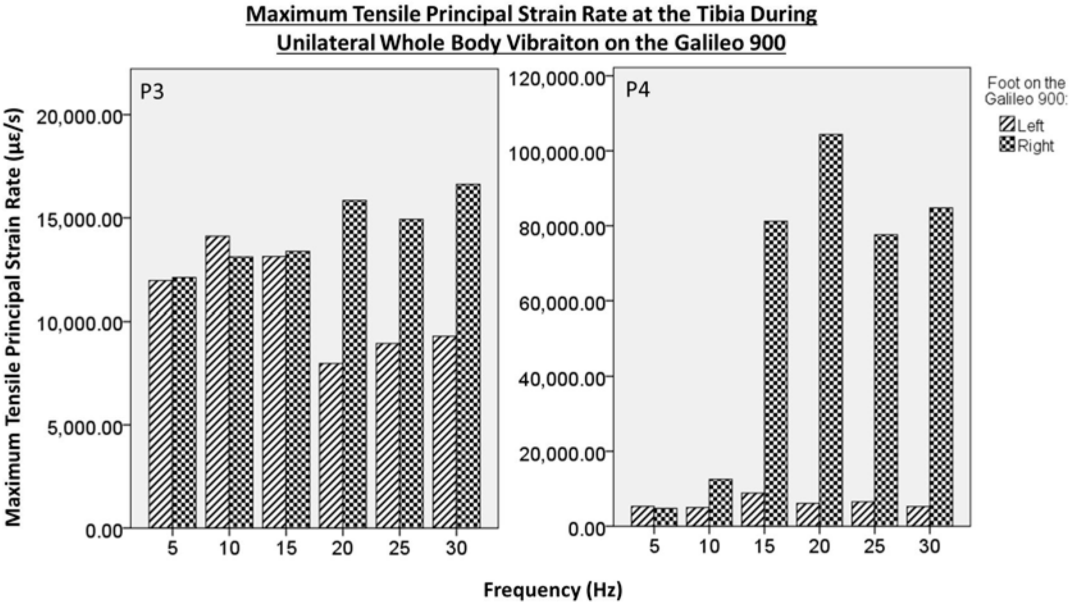

Figure 56: Tensile Strain Rate at the Tibia during Unilateral Whole Body Vibration: Galileo 900

Strain was recorded from the anteromedial surface of the tibia at the midpoint between the medial aspect of the tibial plateau and the lower border of the medial malleolus using an FRA-211 rosette strain gauge. Strain rate was calculated through differentiation of the principal strain. Tensile strain rate was greater when the strain gauged right leg was on the platform as opposed to off the platform at 20Hz, 25Hz and 30Hz in participant 3 and at input frequencies of 10Hz-30Hz in participant 4.

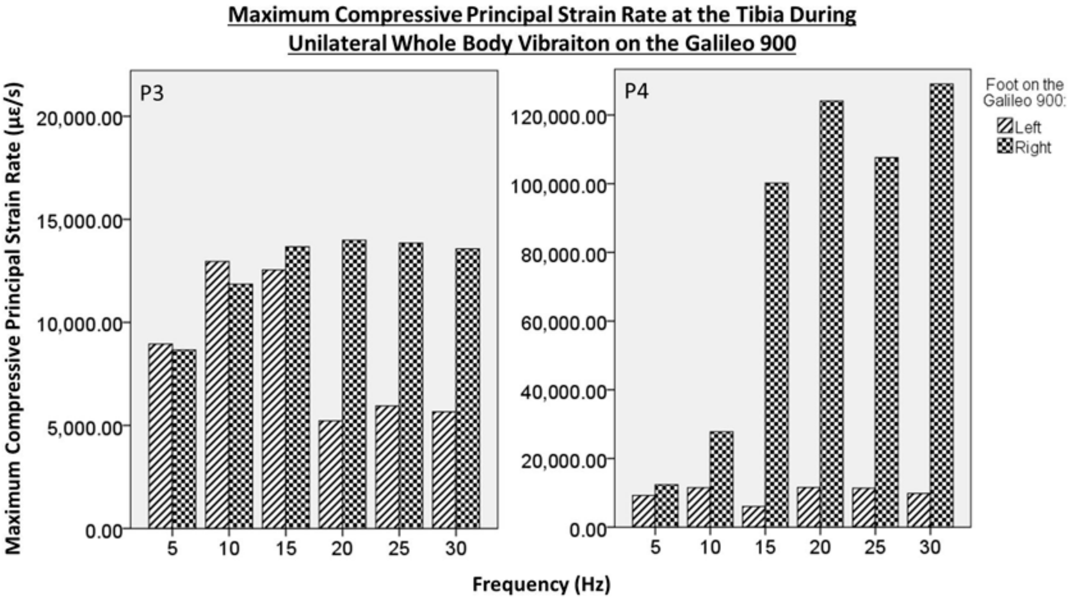

Figure 57: Compressive Strain Rate at the Tibia during Unilateral Whole Body Vibration: Galileo 900

Strain was recorded from the anteromedial surface of the tibia at the midpoint between the medial aspect of the tibial plateau and the lower border of the medial malleolus using an FRA-211 rosette strain gauge. Strain rate was calculated through differentiation of the principal strain. Compressive strain rate was greater when the strain gauged right leg was on the platform as opposed to off the platform at 20Hz, 25Hz and 30Hz in participant 3 and at input frequencies of 10Hz-30Hz in participant 4.

7.4 Discussion

The greatest strains generated at the tibia were observed during jumping (Figure 44) and are matched by the strains generated during WBV on the Galileo 900 platform at 15Hz 5mm (Figure 46, Figure 47).

Jumping has been shown to be sufficient activity to be protective with respect to bone loss [181, 182], therefore if we assume the magnitude of the strain to be the primary determinant of the osteogenic potential of an activity, then WBV on the Galileo 900 at 15Hz5mm would be the only WBV stimulus expected to be useful in preventing postmenopausal bone loss. However, previous studies have suggested that reciprocal WBV at settings other than 15Hz5mm and vertical vibration similar to that generated by the Powerplate Pro5 and the Juvent 1000 can be of benefit to the skeleton [105, 107, 108, 110, 111]. Therefore the strain rate associated with the WBV is potentially of greater importance than the magnitude of the strain generated in determining the skeletal response to WBV, as previously documented [180, 183].

When considering participant 4 (as this is the participant for which habitual locomotor activity data is available), whilst the strains during jumping and WBV on the Galileo 900 at 15Hz 5mm are comparable, the strain rates during jumping are approximately one third of those generated during WBV on the Galileo 900 at 15Hz5mm (Figure 45, Figure 48, Figure 49). At 3mm or 5mm amplitudes, strain rates comparable or greater than those generated during jumping are observed at all frequencies from 15Hz-30Hz. The Galileo 900 therefore presents the opportunity to match or exceed both the strain and strain rate generated during high impact skeletally protective activity, in a controlled setting.

The tibial strains and strain rates generated by the Powerplate pro 5 and Juvent 1000 are much lower than those generated by the Galileo 900 at 15Hz5mm, not exceeding the strains generated during walking. Whilst walking is a much lower impact activity, the benefits of walking for a postmenopausal population have been noted [184]. However, in this population the risks of fracture is increased by strenuous walking activity [90]. WBV on the Powerplate Pro 5 and Juvent 1000 may be expected to be of benefit in preventing bone loss in a postmenopausal osteoporotic population to a similar degree to walking activities, however with the ability for the activity to be delivered in lower impact, measured and controlled manner, potentially reducing the risk of fracture associated with this activity.

When considering a unilateral model of WBV, the strain and strain rate at the tibia are greater when the right leg (with the strain gauge attached) is placed on the platform as opposed to off the platform on a stationary platform of the same height. This is particularly evident for participant 4 at frequencies between 10Hz and 30Hz (Figure 54, Figure 55, Figure 56, Figure 57). A smaller difference is apparent for participant 3 at frequencies between 20Hz and 30Hz (Figure 54, Figure 55, Figure 56, Figure 57). The greatest difference is observed at 20Hz input frequency. At this setting, the strain and strain rate recorded when the right leg is not on the platform do not exceed those recorded during standing and therefore would not be expected to be osteogenic. Whereas when the right leg is on the platform, strains and strain rates comparable to those generated with both feet on the platform are observed (Figure 54, Figure 55, Figure 56, Figure 57). This suggests that unilateral WBV using the Galileo 900 at 20Hz 3mm holds potential as a loading model that engenders substantially different mechanical stimuli in each leg with only one expected to be an osteogenic stimulus.

The pattern of increasing strain magnitude and strain rate from standing to jumping has been previously reported. However, compared to previous studies investigating the strain generated at the tibia during habitual locomotor activities, the principal strains reported here are lower. In the case of walking, the principal strains reported are slightly lower than those reported previously, however the strain rates are 3-4 times higher[89, 97, 134, 135, 138, 139, 144, 145, 179]. The greatest compressive strains reported during jumping are not dissimilar to those previously reported, however the tensile strain is approximately 1/3 of that previously reported[145]. Again, the strain rate reported here is far greater than that previously documented.

There are several factors that may influence the recorded strain, most notably the positioning of the strain gauge. With such a small sample, the importance of this factor can be seen in the difference between the recordings made for participant 3 and participant 4. The strain gauge records strain at a very local site which experiences strain dependent upon the biomechanical loading of the tibia. Differences in bone geometry and composition would result in differences in the strain exerted at a particular point on the tibia and application of the strain gauge in even slightly differing locations between participants would also be expected to result in differing strain recordings. As there is a similar pattern of strain increase for both participants (albeit at lower magnitudes and of smaller increments for participant) and the differences in the magnitude of the strains previously reported are generally small, differing locations of strain gauge application may explain the differences in strain magnitude seen both between participants and with previous work.

Another consideration is the method of attaining strain measurements. Previously, both bone mounted and bone stapled strain gauges have been used to record strains at the tibia. The bone staples may result in greater strain magnitudes being documented, however, as strains previously recorded using bone mounted strain gauges are also higher than those we report, the method of gauge application is probably not a major determinant of the differences seen [89, 134].

Between participants, recordings may have been different due to the integrity or thickness of the glue bonding the strain gauge to the surface of the tibia. At the end of the experiment the strain gauges were removed and no sign of de-bonding of the gauge was noted, a problem which had occurred in previous work [89], suggesting this was not a contributing factor in the differing strain magnitudes between participants. This does not rule out differences in the thickness of the glue layer between the gauge and the bone influencing the observed recordings.

Finally, data for only two out of a possible six participants are reported due to strain gauge failure, similar to that previously reported for strain gauged bone staples [138]. Every effort was made to reduce the forces applied to the strain gauge wires due to their attachment through the skin and long output wires to try and prevent strain gauge damage or failure. As failure rate was so high, it is possible that the data reported here is from gauges that are not fully functioning, however the likelihood of this is small. When the gauges failed clear wire breaks were observed upon removal and during recording a clearly abnormal trace appeared for the failed strain gauge element. For the recordings reported here, no abnormal element recordings were observed and clear cyclical strains relating to the activity or WBV were apparent. Whilst both gauges went on to fail at a later time point, the failure was obvious during the recording in which it happened and a clear wire break only for the element that had failed was apparent at removal. Non the less, the failure of the majority of the strain gauges rendered a sample size of two, therefore the data presented here should be interpreted with care.

In terms of the large strain rates observed in this study, this is most likely a result of differing data processing. In previous studies, filters applied to the strain gauge data will have defined the limit of the strain rates it is possible to measure. Low pass filters with cut offs at 5Hz and 16Hz have previously been used to filter the strain gauge data prior to calculation of the principal strains and strain rates [89, 97, 138, 139, 144, 179]. In removing frequency components of the signal greater than 5Hz or 16Hz, the maximum possible detectable strain rate is limited. This can be demonstrated as the strain rates recorded when data is filtered at 5Hz are lower than those recorded when data is filtered at 16Hz [89, 97, 139, 144, 179] both of which are lower than the strain rates reported in this study where no filtering was applied to the data.

On inspection of the recorded data, cyclical strain recordings corresponding to the repetitive activity or WBV frequency are apparent (Chapter10.3.3, Chapter 10.3.4). It can also be seen that the strain rate cycles at the same frequency as the strain, with peaks in strain rate at the expected point in time (maximum gradient of strain curve)(Chapter 10.3.5). This indicates that the strain rates shown in Figure 44 to Figure 57 are due to real changes in recorded strain, rather than background noise.

The exception to this is during standing, where an unexpectedly high strain rate is observed. On inspection of the recorded data, the strain during standing appears to be cyclical, as though recorded during a dynamic activity or WBV. However, the cycles in strain and strain rate are at 50Hz, the frequency of UK mains voltage, suggesting this is due to electrical interference in the recording (Chapter 10.3.5). No 50Hz interference is observed in other recordings; therefore this is an isolated problem. Both the strain and strain rate during standing will have been influenced by this interference and as such, the data for standing should be discarded from analysis.

In this study, no filtering was applied to the data prior to calculation of the principal strain and strain rates. This approach leaves the strain rate susceptible to system noise.

In summary, in this small cohort, strains comparable to those generated by a high impact osteogenic activity were generated using the Galileo 900. Strain rates in excess of those generated during habitual locomotor activities were also observed using the Galileo 900, suggesting that this platform has potential to deliver mechanical stimuli that would be of benefit in a postmenopausal population. In comparison, the Powerplate Pro 5 and Juvent 1000 deliver lower strain and strain rates to the tibia, similar in magnitude to those generated during walking. Therefore these platforms appear to be of use in simulating walking load in a controlled environment. For future studies, this data suggests a unilateral loading model of WBV using the Galileo 900 at 20Hz3mm may prove useful in providing a self-controlled method to assess the impact of WBV on bone at the distal tibia as well as at the hip and spine. Work in a larger sample, whether examining strain at the tibia or WBV as an intervention, will expand on the observations of this study.

8 Chapter Eight: Discussion

8.1 Summary and Conclusions

In order to address the aims of this project, the accuracy of the system used to measure strain at the tibia has been validated and a suitable zeroing method established (Chapter 4.2). The feasibility of measuring movements due to whole body vibration (WBV) using motion capture has been assessed and the limits of this method established, along with the development of suitable filtering methods for data post processing (Chapter 4.14.2 & 4.3).

This has led to a strong data set which allowed the analysis of transmission of WBV throughout the body, especially transmission to the hip (anterior superior iliac spine) and spine (Sacrum, T2, T10), investigation of a unilateral loading model of WBV and assessment of the strain and strain rates delivered by habitual locomotor activities and WBV (Chapter 2.2).

There are several conclusions to be drawn from this project, however these should be treated tentatively given the small sample size within the study. With regards to the transmission of vibration through the body, greater transmission is seen at lower frequencies as opposed to higher frequencies. The transmission is greatly attenuated in the torso, particularly so with the Galileo 900 which shows less transmission to the torso than the Powerplate Pro 5 and Juvent 1000. Transmission to the hip and spine is greatest using the Powerplate Pro 5 and similar for the Galileo 900 and Juvent 1000. Whilst similar degrees of transmission are observed in the torso for the Galileo 900 and Juvent 1000, the accelerations at input are greater for several of the Galileo 900 settings therefore, within this small cohort, greater accelerations appear to be delivered to the torso using the Galileo 900.

When considering the unilateral loading model of WBV, there is a appears to be a difference in the stimulus transmitted to the leg that is positioned on the platform as opposed to the one not on the platform (Chapter 6). This is reinforced by corresponding differences in tibial strain observed when the right leg is positioned on the platform or off the platform (Chapter 7.2.4.1).

When examining the unilateral loading model in terms of transmission, the greatest difference in transmission is seen at 10Hz and 15Hz, whereas the greatest difference in strain at the tibia is observed at 20Hz. At 10Hz, the difference in strain when the right leg is on or off the platform is negligible and at 15Hz is not great in participant 3.Therefore, as the side to side difference in transmission at 20Hz is still significantly different and, in the case of placing the right foot on the platform there is zero transmission to the left leg in several instances, using a unilateral loading model at 20Hz3mm is potentially the most robust option for use in future studies. However, if strain had successfully been recorded in more subjects, the case for this may be strengthened or weakened. With a greater sample of data, the side to side differences in transmission and strain may be found to be in better agreement, or conversely, a strong difference between the two measures may be found.

The strains recorded in this study show an increase in magnitude with increasing impact of habitual locomotor activity and an increase with increasing frequency and amplitude of WBV on the Galileo 900. The strain and strain rates associated with the Powerplate Pro 5 and Juvent 1000 are similar to those generated during walking, whereas the Galileo 900 generates strains up to those comparable to high impact activities such as jumping whilst delivering much higher strain rates than those generated during habitual locomotor activities. Whilst the trend observed is in agreement with previous publications [89, 97, 179], the data presented in this study is for a single participant, therefore results should be interpreted with caution . From this case study of strain at the tibia, it could be suggested that in order to deliver the highest strains using the Galileo 900, a 15Hz 5mm setting should be used. However slightly higher strain rates may be achieved at 25Hz 5mm and 30Hz 5mm settings.

8.2 Limitations

There are several limitations to the work presented.

1) The data was only collected for 6 participants and in the case of the strain recordings, only two participants worth of data is reportable. The small sample number is due to the invasive nature of the strain gauge recordings. Strain gauge failure due to wires breaking meant only two participants had strain data with three elements of the gauge working. Once the failures became apparent, measures to minimise the risk of breakages were taken. Firstly, participant activity prior to arriving at the gait lab was limited. The tension in the wires was

relieved both using stiches during surgery and taping of wires outside of the body during recordings. Finally the type of gauge used was changed from an FRA 2-11 stacked rectangular rosette strain gauge (TML, Tokyo Sokki Kenkyujo Co., Ltd.) to a C2A-06-062LR-120 planar rectangular rosette strain gauge (Vishay – precision group, Basingstoke, UK). However the strain gauge failures remained an inherent part of the work.

2) We used skin mounted markers to assess the transmission of vibration to the underlying skeleton. Skin movement artefact is a well-documented problem associated with skin mounted motion capture markers and accelerometers which results in overestimation of movements or accelerations [113]. Whilst the accelerations documented may therefore be greater than those experienced at the skeletal level, the same pattern associated with frequency and amplitude is seen both for acceleration and strain/strain rate. As frequency increases, the accelerations at the tibia increase, as do the strain and strain rate generated at the tibia. This suggests that conclusions over the relationship between frequency/amplitude and motion capture data are likely to be accurate. Also, in reporting transmission, the skin movement artefact is essentially normalised as a percentage is reported. Whilst this may be affected by more or less skin movement at different locations, all landmarks studied were bony prominences, with the exception of the thigh. This should minimise the skin movement artefact and however in the case of the thigh, greater skin movement may be expected.

   To avoid skin movement artefact, reflective markers could have been mounted on bone pins and directly inserted into the bone. However this would have been an invasive procedure on top of the strain gauge procedure, therefore fewer locations could have been assessed. As it stands, we have a large amount of information for locations throughout the body, giving a thorough overview of the transmission of the WBV. The possible overestimation of accelerations, especially at the thigh, should be considered when reviewing this data.

3) Only the motion capture data recorded in the Z axis was analysed. The movements in the X and Y direction may show different relationships between

the frequency, amplitude and mode of vibration and the transmission achieved. This is perhaps particularly true for the Galileo 900 as this has a side alternating movement. Having said this, previous work has shown the primary direction of the whole body vibration delivered by the Galileo 900 to be in the vertical Z axis [167]. Whether there are differences in the movements generated between different platforms in the X and Y direction is still to be determined.

8.3 Future work

To build on this work, the joint angles generated about the ankle, knee and anterior superior iliac spine during whole body vibration could be analysed in order to fully identify distinct modes of WBV attenuation. As already mentioned, the movements in the X and Y direction should also be analysed.

During the study, a computer tomography (CT) scan was taken of the tibia of each participant. From this image, a finite element model can be developed and validated using the complete strain data recorded. This will provide an insight into the strain distribution across the entire surface of the tibia during habitual locomotor activities and WBV. It may also be possible to use the motion capture data to calculate the forces that would be acting on the tibia during the different activities and use the validated model to determine the direction of recorded strains or the strain that would be expected in the tibia for those recordings in which at least one strain gauge element had failed.

Ultimately this work aimed to form the basis of future research into the use of WBV in the treatment of an osteopenic or osteoporotic population. The work has proven the concept that WBV can be delivered to areas of interest in the prevention of osteoporotic fracture. The data suggest that the unilateral loading model using the Galileo 900 at 20Hz 3mm could provide a good platform to assess the effects of WBV in a postmenopausal osteoporotic population. As previous work has shown positive but small effects of WBV on the skeleton of postmenopausal osteoporotic women, an interesting question to explore would be whether WBV has any impact as a combination therapy. By combining Teriparatide treatment with WBV it may be possible to augment the response to either the Teriparatide or the WBV, ultimately reducing the need for high doses of expensive pharmaceuticals. By using the unilateral loading model and a combination of Xtreme CT and dual energy x-ray absorptiometry (DXA), the self-controlled and systemic effects of WBV in combination with Teriparatide can be assessed.

9 Chapter Nine: References

1. Gilsanz, V., et al., *Low-level, high-frequency mechanical signals enhance musculoskeletal development of young women with low BMD.* J Bone Miner Res, 2006. **21**(9): p. 1464-74.
2. Martin, R.B., *Bones: structure and mechanics: John D. Currey (Ed.), Princeton University Press or Amazon.com, Princeton, NJ, price $69.50 paperback, ISBN: 0-691-09096-3.* Journal of biomechanics, 2003. **36**(6): p. 893.
3. Currey, J.D., *The mechanical consequences of variation in the mineral content of bone.* Journal of Biomechanics, 1969. **2**(1): p. 1-11.
4. Currey, J.D., *Physical characteristics affecting the tensile failure properties of compact bone.* Journal of Biomechanics, 1990. **23**(8): p. 837-844.
5. Ermanno, B., *Basic Composition and Structure of Bone*, in *Mechanical Testing of Bone and the Bone-Implant Interface*. 1999, CRC Press. p. 3-21.
6. Clarke, B., *Normal bone anatomy and physiology.* Clin J Am Soc Nephrol, 2008. **3 Suppl 3**: p. S131-9.
7. Ashizawa, N., et al., *Tomographical description of tennis-loaded radius: reciprocal relation between bone size and volumetric BMD.* Journal of Applied Physiology, 1999. **86**(4): p. 1347-1351.
8. Pistoia, W., B. van Rietbergen, and P. Rüegsegger, *Mechanical consequences of different scenarios for simulated bone atrophy and recovery in the distal radius.* Bone, 2003. **33**(6): p. 937-945.
9. Haapasalo, H., et al., *Exercise-induced bone gain is due to enlargement in bone size without a change in volumetric bone density: a peripheral quantitative computed tomography study of the upper arms of male tennis players.* Bone, 2000. **27**(3): p. 351-357.
10. Frost, H.M., *Bone Biodynamics.* The American Journal of the Medical Sciences, 1965. **249**(5).
11. Robling, A.G., A.B. Castillo, and C.H. Turner, *Biomechanical and molecular regulation of bone remodeling.* Annu Rev Biomed Eng, 2006. **8**: p. 455-98.
12. Rosen, C.J.S.f.B.a.M.R., *Primer on the metabolic bone diseases and disorders of mineral metabolism.* 8th ed. ed. 2013: Ames, Iowa : Wiley-Blackwell.
13. Hodge, J.M., M.A. Kirkland, and G.C. Nicholson, *Multiple roles of M-CSF in human osteoclastogenesis.* J Cell Biochem, 2007. **102**(3): p. 759-68.
14. Burgess, T.L., et al., *The ligand for osteoprotegerin (OPGL) directly activates mature osteoclasts.* J Cell Biol, 1999. **145**(3): p. 527-38.
15. Lacey, D.L., et al., *Osteoprotegerin ligand is a cytokine that regulates osteoclast differentiation and activation.* Cell, 1998. **93**(2): p. 165-76.
16. Kurata, K., et al., *Bone marrow cell differentiation induced by mechanically damaged osteocytes in 3D gel-embedded culture.* J Bone Miner Res, 2006. **21**(4): p. 616-25.
17. Cardoso, L., et al., *Osteocyte apoptosis controls activation of intracortical resorption in response to bone fatigue.* J Bone Miner Res, 2009. **24**(4): p. 597-605.
18. Takahashi, N., N. Udagawa, and T. Suda, *Vitamin D endocrine system and osteoclasts.* Bonekey Rep, 2014. **3**: p. 495.
19. Baron, R. and M. Kneissel, *WNT signaling in bone homeostasis and disease: from human mutations to treatments.* Nat Med, 2013. **19**(2): p. 179-92.
20. Poole, K.E., et al., *Sclerostin is a delayed secreted product of osteocytes that inhibits bone formation.* FASEB J, 2005. **19**(13): p. 1842-4.
21. O'Brien, C.A., et al., *Control of bone mass and remodeling by PTH receptor signaling in osteocytes.* PLoS One, 2008. **3**(8): p. e2942.
22. Rhee, Y., et al., *PTH receptor signaling in osteocytes governs periosteal bone formation and intracortical remodeling.* J Bone Miner Res, 2011. **26**(5): p. 1035-46.
23. Bailey, D.A., et al., *A Six-Year Longitudinal Study of the Relationship of Physical Activity to Bone Mineral Accrual in Growing Children: The University of Saskatchewan Bone*

Mineral Accrual Study. Journal of Bone and Mineral Research, 1999. **14**(10): p. 1672-1679.

24. Warming, L., C. Hassager C Fau - Christiansen, and C. Christiansen, *Changes in bone mineral density with age in men and women: a longitudinal study.* Osteoporos Int, 2002. **13**(2): p. 105-112.
25. Nichols, J.F., et al., *Bone mineral density in female high school athletes: interactions of menstrual function and type of mechanical loading.* Bone, 2007. **41**(3): p. 371-7.
26. Srivastava, S., et al., *Estrogen blocks M-CSF gene expression and osteoclast formation by regulating phosphorylation of Egr-1 and its interaction with Sp-1.* J Clin Invest, 1998. **102**(10): p. 1850-9.
27. Chen, F., et al., *Estrogen inhibits RANKL-induced osteoclastic differentiation by increasing the expression of TRPV5 channel.* J Cell Biochem, 2014. **115**(4): p. 651-8.
28. Kameda, T., et al., *Estrogen inhibits bone resorption by directly inducing apoptosis of the bone-resorbing osteoclasts.* J Exp Med, 1997. **186**(4): p. 489-95.
29. Slemenda, C., et al., *Sex steroids, bone mass, and bone loss. A prospective study of pre-, peri-, and postmenopausal women.* J Clin Invest., 1996. **97**(1): p. 14-21.
30. Recker, R., et al., *Bone remodeling increases substantially in the years after menopause and remains increased in older osteoporosis patients.* J Bone Miner Res, 2004. **19**(10): p. 1628-33.
31. Recker, R., et al., *Characterization of Perimenopausal Bone Loss: A Prospective Study.* Journal of Bone and Mineral Research, 2000. **15**(10): p. 1965-1973.
32. Kanis, J., *WHO SCIENTIFIC GROUP ON THE ASSESSMENT OF OSTEOPOROSIS AT PRIMARY HEALTH CARE LEVEL*, in *WHO Osteoporosis Meeting, May 5-7, 2004*. 2007: Brussels, Belgium.
33. Marshall, D., O. Johnell, and H. Wedel, *Meta-analysis of how well measures of bone mineral density predict occurrence of osteoporotic fractures.* BMJ, 1996. **312**(7041): p. 1254-9.
34. Leeming, D.J., et al., *An update on biomarkers of bone turnover and their utility in biomedical research and clinical practice.* Eur J Clin Pharmacol, 2006. **62**(10): p. 781-92.
35. Kawate, H., et al., *Alendronate improves QOL of postmenopausal women with osteoporosis.* Clin Interv Aging, 2010. **5**: p. 123-31.
36. Beaupre, L.A., et al., *Oral bisphosphonates are associated with reduced mortality after hip fracture.* Osteoporos Int, 2011. **22**(3): p. 983-91.
37. Braga de Castro Machado, A., R. Hannon, and R. Eastell, *Monitoring alendronate therapy for osteoporosis.* J Bone Miner Res, 1999. **14**(4): p. 602-8.
38. Neviaser, A.S., et al., *Low-energy femoral shaft fractures associated with alendronate use.* J Orthop Trauma, 2008. **22**(5): p. 346-50.
39. Cermak, K., et al., *Case reports: subtrochanteric femoral stress fractures after prolonged alendronate therapy.* Clin Orthop Relat Res, 2010. **468**(7): p. 1991-6.
40. Abrahamsen, B., P. Eiken, and R. Eastell, *Subtrochanteric and diaphyseal femur fractures in patients treated with alendronate: a register-based national cohort study.* J Bone Miner Res, 2009. **24**(6): p. 1095-102.
41. Liberman, U.A., et al., *Effect of oral alendronate on bone mineral density and the incidence of fractures in postmenopausal osteoporosis. The Alendronate Phase III Osteoporosis Treatment Study Group.* N Engl J Med, 1995. **333**(22): p. 1437-43.
42. Neer, R.M., et al., *Effect of parathyroid hormone (1-34) on fractures and bone mineral density in postmenopausal women with osteoporosis.* N Engl J Med, 2001. **344**(19): p. 1434-41.
43. McClung, M.R., et al., *Opposite bone remodeling effects of teriparatide and alendronate in increasing bone mass.* Arch Intern Med, 2005. **165**(15): p. 1762-8.

44. Arlot, M., et al., *Differential effects of teriparatide and alendronate on bone remodeling in postmenopausal women assessed by histomorphometric parameters.* J Bone Miner Res, 2005. **20**(7): p. 1244-53.
45. Finkelstein, J.S., et al., *The effects of parathyroid hormone, alendronate, or both in men with osteoporosis.* N Engl J Med, 2003. **349**(13): p. 1216-26.
46. Black, D.M., et al., *The effects of parathyroid hormone and alendronate alone or in combination in postmenopausal osteoporosis.* N Engl J Med, 2003. **349**(13): p. 1207-15.
47. (NICE), N.I.f.H.a.C.E., *TA161 Osteoporosis - secondary prevention including strontium ranelate: guidance*. 2011: http://guidance.nice.org.uk/TA161/Guidance/pdf/English.
48. Frost, H.M., *Bone "mass" and the "mechanostat": A proposal.* The Anatomical Record, 1987. **219**(1): p. 1-9.
49. Belavy, D.L., et al., *Bone structure and density via HR-pQCT in 60d bed-rest, 2-years recovery with and without countermeasures.* J Musculoskelet Neuronal Interact, 2011. **11**(3): p. 215-26.
50. Rittweger, J. and D. Felsenberg, *Patterns of bone loss in bed-ridden healthy young male subjects: results from the Long Term Bed Rest Study in Toulouse.* J Musculoskelet Neuronal Interact, 2003. **3**(4): p. 290-1; discussion 292-4.
51. Rubin, C.T. and L.E. Lanyon, *Osteoregulatory nature of mechanical stimuli: Function as a determinant for adaptive remodeling in bone.* Journal of Orthopaedic Research, 1987. **5**(2): p. 300-310.
52. Srinivasan, S., et al., *Low-Magnitude Mechanical Loading Becomes Osteogenic When Rest Is Inserted Between Each Load Cycle.* Journal of Bone and Mineral Research, 2002. **17**(9): p. 1613-1620.
53. Rubin, C.T. and L.E. Lanyon, *Regulation of bone formation by applied dynamic loads.* J Bone Joint Surg Am, 1984. **66**(3): p. 397-402.
54. Cullen, D.M., R.T. Smith, and M.P. Akhter, *Bone-loading response varies with strain magnitude and cycle number.* Journal of Applied Physiology, 2001. **91**(5): p. 1971-1976.
55. Umemura, Y., et al., *Five Jumps per Day Increase Bone Mass and Breaking Force in Rats.* Journal of Bone and Mineral Research, 1997. **12**(9): p. 1480-1485.
56. Robling, A.G., et al., *Improved bone structure and strength after long-term mechanical loading is greatest if loading is separated into short bouts.* J Bone Miner Res, 2002. **17**(8): p. 1545-54.
57. Skerry, T.M., *One mechanostat or many? Modifications of the site-specific response of bone to mechanical loading by nature and nurture.* J Musculoskelet Neuronal Interact, 2006. **6**(2): p. 122-7.
58. Kular, J., et al., *An overview of the regulation of bone remodelling at the cellular level.* Clin Biochem, 2012. **45**(12): p. 863-73.
59. Bakker, A., J. Klein-Nulend, and E. Burger, *Shear stress inhibits while disuse promotes osteocyte apoptosis.* Biochemical and Biophysical Research Communications, 2004. **320**(4): p. 1163-1168.
60. Tan, S.D., et al., *Inhibition of osteocyte apoptosis by fluid flow is mediated by nitric oxide.* Biochemical and Biophysical Research Communications, 2008. **369**(4): p. 1150-1154.
61. Noble, B.S., et al., *Mechanical loading: biphasic osteocyte survival and targeting of osteoclasts for bone destruction in rat cortical bone.* American Journal of Physiology - Cell Physiology, 2003. **284**(4): p. C934-C943.
62. Bakker, A.D., et al., *The production of nitric oxide and prostaglandin E2 by primary bone cells is shear stress dependent.* Journal of biomechanics, 2001. **34**(5): p. 671-677.
63. Cherian, P.P., et al., *Mechanical strain opens connexin 43 hemichannels in osteocytes: a novel mechanism for the release of prostaglandin.* Mol Biol Cell, 2005. **16**(7): p. 3100-6.
64. Li, J., et al., *The P2X7 Nucleotide Receptor Mediates Skeletal Mechanotransduction.* Journal of Biological Chemistry, 2005. **280**(52): p. 42952-42959.

65. Mano, M., et al., *Prostaglandin E2 directly inhibits bone-resorbing activity of isolated mature osteoclasts mainly through the EP4 receptor.* Calcif Tissue Int, 2000. **67**(1): p. 85-92.
66. MacIntyre, I., et al., *Osteoclastic inhibition: an action of nitric oxide not mediated by cyclic GMP.* Proc Natl Acad Sci U S A, 1991. **88**(7): p. 2936-40.
67. Tan, S.D., et al., *Osteocytes subjected to fluid flow inhibit osteoclast formation and bone resorption.* Bone, 2007. **41**(5): p. 745-51.
68. Robling, A.G., et al., *Mechanical Stimulation of Bone in Vivo Reduces Osteocyte Expression of Sost/Sclerostin.* Journal of Biological Chemistry, 2008. **283**(9): p. 5866-5875.
69. Li, X., et al., *Sclerostin Binds to LRP5/6 and Antagonizes Canonical Wnt Signaling.* Journal of Biological Chemistry, 2005. **280**(20): p. 19883-19887.
70. Lin, C., et al., *Sclerostin Mediates Bone Response to Mechanical Unloading Through Antagonizing Wnt/β-Catenin Signaling.* Journal of Bone and Mineral Research, 2009. **24**(10): p. 1651-1661.
71. Knothe Tate, M.L., P. Niederer, and U. Knothe, *In Vivo Tracer Transport Through the Lacunocanalicular System of Rat Bone in an Environment Devoid of Mechanical Loading.* Bone, 1998. **22**(2): p. 107-117.
72. Knothe Tate, M.L., et al., *In vivo demonstration of load-induced fluid flow in the rat tibia and its potential implications for processes associated with functional adaptation.* J Exp Biol, 2000. **203**(Pt 18): p. 2737-45.
73. Nicolella, D.P., et al., *Measurement of microstructural strain in cortical bone.* Eur J Morphol, 2005. **42**(1-2): p. 23-9.
74. Calbet, J.A.L., et al., *Bone Mineral Content and Density in Professional Tennis Players.* Calcified Tissue International, 1998. **62**(6): p. 491-496.
75. Haapasalo, H., et al., *Effect of long-term unilateral activity on bone mineral density of female junior tennis players.* J Bone Miner Res, 1998. **13**(2): p. 310-9.
76. Sanchis-Moysi, J., et al., *Bone and lean mass inter-arm asymmetries in young male tennis players depend on training frequency.* Eur J Appl Physiol, 2010. **110**(1): p. 83-90.
77. Ermin, K., et al., *Bone mineral density of adolescent female tennis players and nontennis players.* J Osteoporos, 2012. **2012**: p. 423910.
78. Bass, S.L., et al., *The effect of mechanical loading on the size and shape of bone in pre-, peri-, and postpubertal girls: a study in tennis players.* J Bone Miner Res, 2002. **17**(12): p. 2274-80.
79. Ducher, G., et al., *Effects of repetitive loading on the growth-induced changes in bone mass and cortical bone geometry: a 12-month study in pre/peri- and postmenarcheal tennis players.* J Bone Miner Res, 2011. **26**(6): p. 1321-9.
80. Sanchis-Moysi, J., et al., *Inter-arm asymmetry in bone mineral content and bone area in postmenopausal recreational tennis players.* Maturitas, 2004. **48**(3): p. 289-98.
81. Schreuder, M.F., et al., *Volumetric measurements of bone mineral density of the lumbar spine: comparison of three geometrical approximations using dual-energy X-ray absorptiometry (DXA).* Nucl Med Commun, 1998. **19**(8): p. 727-33.
82. Ducher, G., et al., *Bone geometry in response to long-term tennis playing and its relationship with muscle volume: a quantitative magnetic resonance imaging study in tennis players.* Bone, 2005. **37**(4): p. 457-66.
83. Nara-Ashizawa, N., et al., *Paradoxical adaptation of mature radius to unilateral use in tennis playing.* Bone, 2002. **30**(4): p. 619-23.
84. Ireland, A., et al., *Effects of age and starting age upon side asymmetry in the arms of veteran tennis players: a cross-sectional study.* Osteoporos Int, 2014. **25**(4): p. 1389-400.

85. Karlsson, M.K., R. Hasserius, and K.J. Obrant, *Bone mineral density in athletes during and after career: a comparison between loaded and unloaded skeletal regions.* Calcif Tissue Int, 1996. **59**(4): p. 245-8.
86. Gustavsson, A., T. Olsson, and P. Nordström, *Rapid Loss of Bone Mineral Density of the Femoral Neck After Cessation of Ice Hockey Training: A 6-Year Longitudinal Study in Males.* Journal of Bone and Mineral Research, 2003. **18**(11): p. 1964-1969.
87. Pajamaki, I., et al., *The bone gain induced by exercise in puberty is not preserved through a virtually life-long deconditioning: a randomized controlled experimental study in male rats.* J Bone Miner Res, 2003. **18**(3): p. 544-52.
88. Nordstrom, A., et al., *Bone loss and fracture risk after reduced physical activity.* J Bone Miner Res, 2005. **20**(2): p. 202-7.
89. Burr, D.B., et al., *In vivo measurement of human tibial strains during vigorous activity.* Bone, 1996. **18**(5): p. 405-10.
90. Moon, M.S., et al., *Strenuous walking exercise and spontaneous fracture of the femoral neck in the elderly.* J Orthop Surg (Hong Kong), 2000. **8**(2): p. 39-43.
91. LeBlanc, A., et al., *Bone mineral and lean tissue loss after long duration space flight.* J Musculoskelet Neuronal Interact, 2000. **1**(2): p. 157-60.
92. Caillot-Augusseau, A., et al., *Bone formation and resorption biological markers in cosmonauts during and after a 180-day space flight (Euromir 95).* Clin Chem, 1998. **44**(3): p. 578-85.
93. Smith, S.M., et al., *Collagen cross-link excretion during space flight and bed rest.* J Clin Endocrinol Metab, 1998. **83**(10): p. 3584-91.
94. Lang, T., et al., *Cortical and trabecular bone mineral loss from the spine and hip in long-duration spaceflight.* J Bone Miner Res, 2004. **19**(6): p. 1006-12.
95. LeBlanc, A.D., et al., *Skeletal responses to space flight and the bed rest analog: a review.* J Musculoskelet Neuronal Interact, 2007. **7**(1): p. 33-47.
96. Rubin, C., G. Xu, and S. Judex, *The anabolic activity of bone tissue, suppressed by disuse, is normalized by brief exposure to extremely low-magnitude mechanical stimuli.* Faseb j, 2001. **15**(12): p. 2225-9.
97. Milgrom, C., et al., *In-vivo strain measurements to evaluate the strengthening potential of exercises on the tibial bone.* J Bone Joint Surg Br, 2000. **82**(4): p. 591-4.
98. Nichols, J.F., J.E. Palmer, and S.S. Levy, *Low bone mineral density in highly trained male master cyclists.* Osteoporos Int, 2003. **14**(8): p. 644-9.
99. Rubin, C., et al., *Quantity and quality of trabecular bone in the femur are enhanced by a strongly anabolic, noninvasive mechanical intervention.* J Bone Miner Res, 2002. **17**(2): p. 349-57.
100. Zange, J., et al., *20-Hz whole body vibration training fails to counteract the decrease in leg muscle volume caused by 14 days of 6 degrees head down tilt bed rest.* Eur J Appl Physiol, 2009. **105**(2): p. 271-7.
101. Baecker, N., et al., *Effects of vibration training on bone metabolism: results from a short-term bed rest study.* Eur J Appl Physiol, 2012. **112**(5): p. 1741-50.
102. Rittweger, J., et al., *Prevention of bone loss during 56 days of strict bed rest by side-alternating resistive vibration exercise.* Bone, 2010. **46**(1): p. 137-47.
103. Wang, H., et al., *Resistive vibration exercise retards bone loss in weight-bearing skeletons during 60 days bed rest.* Osteoporos Int, 2012. **23**(8): p. 2169-78.
104. Belavý, D.L., et al., *Evidence for an additional effect of whole-body vibration above resistive exercise alone in preventing bone loss during prolonged bed rest.* Osteoporos Int, 2011. **22**(5): p. 1581-91.
105. Rubin, C., et al., *Prevention of postmenopausal bone loss by a low-magnitude, high-frequency mechanical stimuli: a clinical trial assessing compliance, efficacy, and safety.* J Bone Miner Res, 2004. **19**(3): p. 343-51.

106. Ward, K., et al., *Low magnitude mechanical loading is osteogenic in children with disabling conditions.* J Bone Miner Res, 2004. **19**(3): p. 360-9.
107. Ruan, X.Y., et al., *Effects of vibration therapy on bone mineral density in postmenopausal women with osteoporosis.* Chin Med J (Engl), 2008. **121**(13): p. 1155-8.
108. Russo, C.R., et al., *High-frequency vibration training increases muscle power in postmenopausal women.* Arch Phys Med Rehabil, 2003. **84**(12): p. 1854-7.
109. Torvinen, S., et al., *Effect of 8-month vertical whole body vibration on bone, muscle performance, and body balance: a randomized controlled study.* J Bone Miner Res, 2003. **18**(5): p. 876-84.
110. Verschueren, S.M., et al., *Effect of 6-month whole body vibration training on hip density, muscle strength, and postural control in postmenopausal women: a randomized controlled pilot study.* J Bone Miner Res, 2004. **19**(3): p. 352-9.
111. Gusi, N., A. Raimundo, and A. Leal, *Low-frequency vibratory exercise reduces the risk of bone fracture more than walking: a randomized controlled trial.* BMC Musculoskelet Disord, 2006. **7**: p. 92.
112. Rubin, C.T. and L.E. Lanyon, *Regulation of bone mass by mechanical strain magnitude.* Calcif Tissue Int, 1985. **37**(4): p. 411-7.
113. Leardini, A., et al., *Human movement analysis using stereophotogrammetry. Part 3. Soft tissue artifact assessment and compensation.* Gait Posture, 2005. **21**(2): p. 212-25.
114. Bressel, E., G. Smith, and J. Branscomb, *Transmission of whole body vibration in children while standing.* Clin Biomech (Bristol, Avon), 2010. **25**(2): p. 181-6.
115. Andriacchi, T.P. and E.J. Alexander, *Studies of human locomotion: past, present and future.* J Biomech, 2000. **33**(10): p. 1217-24.
116. Godfrey, A., et al., *Direct measurement of human movement by accelerometry.* Med Eng Phys, 2008. **30**(10): p. 1364-86.
117. Chen, K.Y. and D.R. Bassett, *The technology of accelerometry-based activity monitors: current and future.* Med Sci Sports Exerc, 2005. **37**(11 Suppl): p. S490-500.
118. Mathie, M.J., et al., *Accelerometry: providing an integrated, practical method for long-term, ambulatory monitoring of human movement.* Physiol Meas, 2004. **25**(2): p. R1-20.
119. Jack, R. and T. Eger, *The effects of posture on seat-to-head Whole-body vibration transmission.* Journal of Low Frequency Noise, Vibration and Active Control, 2008. **27**(4): p. 309-325.
120. DiGiovine, C.P., et al., *Analysis of whole-body vibration during manual wheelchair propulsion: a comparison of seat cushions and back supports for individuals without a disability.* Assist Technol, 2003. **15**(2): p. 129-44.
121. DiGiovine, C.P., et al., *Whole-body vibration during manual wheelchair propulsion with selected seat cushions and back supports.* IEEE Trans Neural Syst Rehabil Eng, 2003. **11**(3): p. 311-22.
122. M-Pranesh, A., S. Rakheja, and R. Demont, *Influence of support conditions on vertical whole-body vibration of the seated human body.* Ind Health, 2010. **48**(5): p. 682-97.
123. Kiiski, J., et al., *Transmission of vertical whole body vibration to the human body.* J Bone Miner Res, 2008. **23**(8): p. 1318-25.
124. Asselin, P., et al., *Transmission of low-intensity vibration through the axial skeleton of persons with spinal cord injury as a potential intervention for preservation of bone quantity and quality.* J Spinal Cord Med, 2011. **34**(1): p. 52-9.
125. Rubin, C., et al., *Transmissibility of 15-hertz to 35-hertz vibrations to the human hip and lumbar spine: determining the physiologic feasibility of delivering low-level anabolic mechanical stimuli to skeletal regions at greatest risk of fracture because of osteoporosis.* Spine (Phila Pa 1976), 2003. **28**(23): p. 2621-7.

126. Allard, P., I.A.F. Stokes, and J.P. Blanchi, *Three-dimensional analysis of human movement*. 1995: Human Kinetics.
127. Adrian Woolard, V.W., *Vicon 512 User Manual*, N.B. Jonathan Attias, Warren Lester, Martin Lyster, Julian Morris, Brain Nilles, and P.T.a.J.D. Paul Smyth, Editors. 1999, www.vicon.com.
128. *Plug In Gait User Manual*. http://wweb.uta.edu/faculty/ricard/Classes/KINE-5350/PIGManualver1.pdf.
129. Inc, M.L.S., *Knee Alignment Device User Manual*. 1998, Motion Lab Systems Inc., 1998.
130. Pratt, E., *Personal Communication - Gaps*. 26.10.2011.
131. Benham, P.P., R.J. Crawford, and C.G. Armstrong, *Mechanics of Engineering Materials*. 1996: Longman.
132. Ammann, P. and R. Rizzoli, *Bone strength and its determinants.* Osteoporos Int, 2003. **14 Suppl 3**: p. S13-8.
133. PLC, V.M.G., *Strain Gage Rosette: Selection, Application and Data Reduction*. 12 September 2010.
134. Milgrom, C., et al., *The effect of shoe gear on human tibial strains recorded during dynamic loading: a pilot study.* Foot Ankle Int, 1996. **17**(11): p. 667-71.
135. Lanyon, L.E., et al., *Bone deformation recorded in vivo from strain gauges attached to the human tibial shaft.* Acta Orthop Scand, 1975. **46**(2): p. 256-68.
136. Lanyon, L.E. and R.N. Smith, *Bone strain in the tibia during normal quadrupedal locomotion.* Acta Orthop Scand, 1970. **41**(3): p. 238-48.
137. Davies, H.M., *Ex vivo calibration and validation of in vivo equine bone strain measures.* Equine Vet J, 2009. **41**(3): p. 225-8.
138. Milgrom, C., et al., *Do high impact exercises produce higher tibial strains than running?* Br J Sports Med, 2000. **34**(3): p. 195-9.
139. Milgrom, C., et al., *The effect of shoe sole composition on in vivo tibial strains during walking.* Foot Ankle Int, 2001. **22**(7): p. 598-602.
140. Milgrom, C., et al., *A home exercise program for tibial bone strengthening based on in vivo strain measurements.* Am J Phys Med Rehabil, 2001. **80**(6): p. 433-8.
141. Ekenman, I., et al., *The role of biomechanical shoe orthoses in tibial stress fracture prevention.* Am J Sports Med, 2002. **30**(6): p. 866-70.
142. Arndt, A., et al., *Effects of fatigue and load variation on metatarsal deformation measured in vivo during barefoot walking.* J Biomech, 2002. **35**(5): p. 621-8.
143. Milgrom, C., et al., *Are overground or treadmill runners more likely to sustain tibial stress fracture?* Br J Sports Med, 2003. **37**(2): p. 160-3.
144. Milgrom, C., et al., *The effect of muscle fatigue on in vivo tibial strains.* J Biomech, 2007. **40**(4): p. 845-50.
145. Milgrom, C., et al., *Metatarsal strains are sufficient to cause fatigue fracture during cyclic overloading.* Foot Ankle Int, 2002. **23**(3): p. 230-5.
146. Porat, B., *A course in digital signal processing*. 1997: John Wiley.
147. Cooley, J.W. and J.W. Tukey, *An algorithm for the machine calculation of complex Fourier series.* Mathematics of computation, 1965. **19**(90): p. 297-301.
148. Instruments, N., *The Fundamentals of FFT-Based Signal Analysis and Measurement in LabVIEW and Lab Windows/CVI*. 2009, National Instruments: http://www.ni.com/white-paper/4278/en/.
149. Instruments, N., *Windowing: Optimizing FFTs using Windowing Functions*. 2014: http://www.ni.com/white-paper/4844/en/.
150. Simon, S.R., *Quantification of human motion: gait analysis-benefits and limitations to its application to clinical problems.* J Biomech, 2004. **37**(12): p. 1869-80.
151. Ounpuu, S., *The biomechanics of walking and running.* Clin Sports Med, 1994. **13**(4): p. 843-63.

152. *Biomechanical Research Applications.* 2013 09 July 2013]; Available from: http://www.vicon.com/applications/biomechanical.html.
153. Chiari, L., et al., *Human movement analysis using stereophotogrammetry. Part 2: instrumental errors.* Gait Posture, 2005. **21**(2): p. 197-211.
154. Della Croce, U. and A. Cappozzo, *A spot check for estimating stereophotogrammetric errors.* Med Biol Eng Comput, 2000. **38**(3): p. 260-6.
155. Ehara, Y., et al., *Comparison of the performance of 3D camera systems.* Gait & Posture, 1995. **3**(3): p. 166-169.
156. Ehara, Y., et al., *Comparison of the performance of 3D camera systems II.* Gait & Posture, 1997. **5**(3): p. 251-255.
157. Bressel E, S.G., Branscomb J, *Transmission of Whole Body Vibration in Children Whilst Standing*, in *American Society of Biomechanics*. 2009: Pennsylvania State University.
158. Yang, P.F., et al., *Evaluation of the performance of a motion capture system for small displacement recording and a discussion for its application potential in bone deformation in vivo measurements.* Proc Inst Mech Eng H, 2012. **226**(11): p. 838-47.
159. Drake Richard, V.W., Mitchell Adam, *Gray's Anatomy for students*. 2nd Edition ed. 2009: Churchill Livingstone Elsevier.
160. Davies, H.M.S., *The relationship between surface strain and measurements of bone quality, quantity and shape*, in *Proceedings of the 4th International Workshop on Animal Locomotion (IWAL2000)*. 2001, **Equine Vet. J.**: Vienna. p. 16-20.
161. Eadric Bressel, G.S., *Personal Communication*. 02 Feb 2012.
162. Smith, S.W., *The Scientist & Engineer's Guide to Digital Signal Processing*. 1997: California Technical Pub.
163. Muir, J., D.P. Kiel, and C.T. Rubin, *Safety and severity of accelerations delivered from whole body vibration exercise devices to standing adults.* J Sci Med Sport, 2013. **16**(6): p. 526-31.
164. Zumbahlen, H., *Linear Circuit Design Handbook*. 1 ed, ed. H. Zumbahlen. 2008: *Newnes*.
165. M, G., *The Handbook of Human Vibration*. 1996: Academic Press.
166. Simonson, P., *Personal Communication - Juvent Technical Description*. 08.08.2014.
167. Pel, J.J., et al., *Platform accelerations of three different whole-body vibration devices and the transmission of vertical vibrations to the lower limbs.* Med Eng Phys, 2009. **31**(8): p. 937-44.
168. Furness Trentham, J.C., Share Bianca, Naughton Geraldine, Maschette Wayne, Lorenzen Christian, *Transmission of Vibration About the Knee*, in *The XXVI International Conference on Biomechanics in Sports*. 2010.
169. Yue, Z. and J. Mester, *A model analysis of internal loads, energetics, and effects of wobbling mass during the whole-body vibration.* J Biomech, 2002. **35**(5): p. 639-47.
170. Abercromby, A.F., et al., *Vibration exposure and biodynamic responses during whole-body vibration training.* Med Sci Sports Exerc, 2007. **39**(10): p. 1794-800.
171. Fritz, M., *Simulating the response of a standing operator to vibration stress by means of a biomechanical model.* J Biomech, 2000. **33**(7): p. 795-802.
172. Guo, L.X., et al., *Vibration characteristics of the human spine under axial cyclic loads: effect of frequency and damping.* Spine (Phila Pa 1976), 2005. **30**(6): p. 631-7.
173. Wakeling, J.M., B.M. Nigg, and A.I. Rozitis, *Muscle activity damps the soft tissue resonance that occurs in response to pulsed and continuous vibrations.* J Appl Physiol (1985), 2002. **93**(3): p. 1093-103.
174. Iwamoto, J., et al., *Effect of whole-body vibration exercise on lumbar bone mineral density, bone turnover, and chronic back pain in post-menopausal osteoporotic women treated with alendronate.* Aging Clin Exp Res, 2005. **17**(2): p. 157-63.
175. Kerr, D., et al., *Resistance training over 2 years increases bone mass in calcium-replete postmenopausal women.* J Bone Miner Res, 2001. **16**(1): p. 175-81.

176. Kelley, G.A., K.S. Kelley, and Z.V. Tran, *Resistance training and bone mineral density in women: a meta-analysis of controlled trials.* Am J Phys Med Rehabil, 2001. **80**(1): p. 65-77.
177. Hoffman, M., et al., *Unilateral postural control of the functionally dominant and nondominant extremities of healthy subjects.* J Athl Train, 1998. **33**(4): p. 319-22.
178. McCurdy, K. and G. Langford, *Comparison of unilateral squat strength between the dominant and non-dominant leg in men and women.* J Sports Sci Med, 2005. **4**(2): p. 153-9.
179. Milgrom, C., et al., *Using bone's adaptation ability to lower the incidence of stress fractures.* Am J Sports Med, 2000. **28**(2): p. 245-51.
180. Turner, C.H., I. Owan, and Y. Takano, *Mechanotransduction in bone: role of strain rate.* Am J Physiol, 1995. **269**(3 Pt 1): p. E438-42.
181. Heinonen, A., et al., *Randomised controlled trial of effect of high-impact exercise on selected risk factors for osteoporotic fractures.* Lancet, 1996. **348**(9038): p. 1343-7.
182. Umemura, Y., et al., *Five jumps per day increase bone mass and breaking force in rats.* J Bone Miner Res, 1997. **12**(9): p. 1480-5.
183. Qin, Y.X., C.T. Rubin, and K.J. McLeod, *Nonlinear dependence of loading intensity and cycle number in the maintenance of bone mass and morphology.* J Orthop Res, 1998. **16**(4): p. 482-9.
184. Howe, T.E., et al., *Exercise for preventing and treating osteoporosis in postmenopausal women.* Cochrane Database Syst Rev, 2011(7): p. CD000333.

10 Chapter Ten: Appendix

10.1 Computer Program Descriptions

10.1.1 Order of WBV delivery

	SG01	SG02	SG03	SG04	SG06	SG07
Galileo 900						
5Hz0mm	6	1	1	5	5	2
10Hz0mm	7	2	2	6	6	3
15Hz0mm	8	3	3	7	7	4
20Hz0mm	9	4	4	8	8	5
25Hz0mm	10	5	5	9	9	6
30Hz0mm	11	6	6	10	10	7
5Hz1mm	17	12	16	16	16	8
10Hz1mm	16	11	15	15	15	9
15Hz1mm	15	10	14	14	14	10
20Hz1mm	14	9	13	13	13	11
25Hz1mm	13	8	12	12	12	12
30Hz1mm	12	7	7	11	11	13
5Hz3mm	18	13	17	17	17	14
10Hz3mm	19	14	18	18	18	15
15Hz3mm	20	15	19	19	19	16
20Hz3mm	21	16	20	20	20	17
25Hz3mm	22	17	21	21	21	18
30Hz3mm	23	18	22	22	22	19
5Hz3mmLF	30	24	40	29	28	20
10Hz3mmLF	31	23	39	30	27	21
15Hz3mmLF	32	22	38	31	26	22
20Hz3mmLF	33	21	37	32	25	23
25Hz3mmLF	34	20	36	33	24	24
30Hz3mmLF	35	19	35	34	23	25
5Hz3mmRF	29	25	29	40	29	26
10Hz3mmRF	28	26	30	39	30	27
15Hz3mmRF	27	27	31	38	31	28
20Hz3mmRF	26	28	32	37	32	29
25Hz3mmRF	25	29	33	36	33	30
30Hz3mmRF	24	30	34	35	34	31
5Hz5mm	41	36	28	28	41	32
10Hz5mm	40	35	27	27	40	33
15Hz5mm	39	34	26	26	39	34
20Hz5mm	38	33	25	25	38	35
25Hz5mm	37	32	24	24	37	36
30Hz5mm	36	31	23	23	36	37
Powerplate Pro 5						
25Hz Low	2	39	11	1	1	40
25Hz High	3	38	8	2	2	38
30Hz Low	1	40	10	4	3	41
30Hz High	4	41	9	3	4	39
Juvent 1000	5	37	41	41	35	1

S 1: The order of WBV delivery. The order in which the WBV on different platforms and of different frequencies and amplitudes were delivered to each participant. The first setting is indicated by 1 and the last by 41 with the order in between indicated by increasing values. The ‘Hz’ value indicates the frequency and the ‘mm, ‘Low’ and ‘High’ values indicate the amplitude. LF and RF refer to only one (left and right foot respectively) foot on the platform.

10.1.2 Fast Fourier Transform

Program used to run a windowed fast fourier transform using do_FFT function written by Prof Keith Wardon, Sheffield University.

```
Fs = 300;          % Sampling frequency
nfft = 1024;                 % FFT length


l=input('lower limit')
h=input('upper limit')
FOHE=FOHE(l:h)
RACR=RACR(l:h)
LACR=LACR(l:h)
T2=T2(l:h)
MANU=MANU(l:h)
T10=T10(l:h)
SACR=SACR(l:h)
RASI=RASI(l:h)
LASI=LASI(l:h)
RTHI=RTHI(l:h)
LTHI=LTHI(l:h)
RKNE=RKNE(l:h)
LKNE=LKNE(l:h)
RTIB=RTIB(l:h)
LTIB=LTIB(l:h)
RANK=RANK(l:h)
LANK=LANK(l:h)
RHEE=RHEE(l:h)
LHEE=LHEE(l:h)
```

```
RTOE=RTOE(l:h)

LTOE=LTOE(l:h)

PLAT=PLAT(l:h)


x=FOHE;

[f,Gxy]=do_FFT(x,nfft,Fs)

A=figure

plot(f,squeeze(Gxy(1,1,:)))

saveas(A,'FOHEfft')

FOHEGxy=Gxy

FOHEf=f

FOHEpeak=max(Gxy)


x=RACR;

[f,Gxy]=do_FFT(x,nfft,Fs)

A=figure

plot(f,squeeze(Gxy(1,1,:)))

saveas(A,'RACRfft')

RACRGxy=Gxy

RACRf=f

RACRpeak=max(Gxy)


x=LACR;

[f,Gxy]=do_FFT(x,nfft,Fs)

A=figure

plot(f,squeeze(Gxy(1,1,:)))

saveas(A,'LACRfft')
```

```
LACRGxy=Gxy

LACRf=f

LACRpeak=max(Gxy)


x=T2;

[f,Gxy]=do_FFT(x,nfft,Fs)

A=figure

plot(f,squeeze(Gxy(1,1,:)))

saveas(A,'T2fft')

T2Gxy=Gxy

T2f=f

T2peak=max(Gxy)


x=MANU;

[f,Gxy]=do_FFT(x,nfft,Fs)

A=figure

plot(f,squeeze(Gxy(1,1,:)))

saveas(A,'MANUfft')

MANUGxy=Gxy

MANUf=f

MANUpeak=max(Gxy)


x=T10;

[f,Gxy]=do_FFT(x,nfft,Fs)

A=figure

plot(f,squeeze(Gxy(1,1,:)))

saveas(A,'T10fft')
```

```
T10Gxy=Gxy

T10f=f

T10peak=max(Gxy)



x=SACR;

[f,Gxy]=do_FFT(x,nfft,Fs)

A=figure

plot(f,squeeze(Gxy(1,1,:)))

saveas(A,'SACRfft')

SACRGxy=Gxy

SACRf=f

SACRpeak=max(Gxy)


x=RASI;

[f,Gxy]=do_FFT(x,nfft,Fs)

A=figure

plot(f,squeeze(Gxy(1,1,:)))

saveas(A,'RASIfft')

RASIGxy=Gxy

RASIf=f

RASIpeak=max(Gxy)


x=LASI;

[f,Gxy]=do_FFT(x,nfft,Fs)

A=figure

plot(f,squeeze(Gxy(1,1,:)))
```

```
saveas(A,'LASIfft')

LASIGxy=Gxy

LASIf=f

LASIpeak=max(Gxy)


x=RTHI;

[f,Gxy]=do_FFT(x,nfft,Fs)

A=figure

plot(f,squeeze(Gxy(1,1,:)))

saveas(A,'RTHIfft')

RTHIGxy=Gxy

RTHIf=f

RTHIpeak=max(Gxy)


x=LTHI;

[f,Gxy]=do_FFT(x,nfft,Fs)

A=figure

plot(f,squeeze(Gxy(1,1,:)))

saveas(A,'LTHIfft')

LTHIGxy=Gxy

LTHIf=f

LTHIpeak=max(Gxy)


x=RKNE;

[f,Gxy]=do_FFT(x,nfft,Fs)

A=figure

plot(f,squeeze(Gxy(1,1,:)))
```

```
saveas(A,'RKNEfft')

RKNEGxy=Gxy

RKNEf=f

RKNEpeak=max(Gxy)


x=LKNE;

[f,Gxy]=do_FFT(x,nfft,Fs)

A=figure

plot(f,squeeze(Gxy(1,1,:)))

saveas(A,'LKNEfft')

LKNEGxy=Gxy

LKNEf=f

LKNEpeak=max(Gxy)


x=RTIB;

[f,Gxy]=do_FFT(x,nfft,Fs)

A=figure

plot(f,squeeze(Gxy(1,1,:)))

saveas(A,'RTIBfft')

RTIBGxy=Gxy

RTIBf=f

RTIBpeak=max(Gxy)


x=LTIB;

[f,Gxy]=do_FFT(x,nfft,Fs)

A=figure

plot(f,squeeze(Gxy(1,1,:)))
```

```
saveas(A,'LTIBfft')

LTIBGxy=Gxy

LTIBf=f

LTIBpeak=max(Gxy)


x=RANK;

[f,Gxy]=do_FFT(x,nfft,Fs)

A=figure

plot(f,squeeze(Gxy(1,1,:)))

saveas(A,'RANKfft')

RANKGxy=Gxy

RANKf=f

RANKpeak=max(Gxy)


x=LANK;

[f,Gxy]=do_FFT(x,nfft,Fs)

A=figure

plot(f,squeeze(Gxy(1,1,:)))

saveas(A,'LANKfft')

LANKGxy=Gxy

LANKf=f

LANKpeak=max(Gxy)


x=RHEE;

[f,Gxy]=do_FFT(x,nfft,Fs)

A=figure

plot(f,squeeze(Gxy(1,1,:)))
```

```
saveas(A,'RHEEfft')

RHEEGxy=Gxy

RHEEf=f

RHEEpeak=max(Gxy)


x=LHEE;

[f,Gxy]=do_FFT(x,nfft,Fs)

A=figure

plot(f,squeeze(Gxy(1,1,:)))

saveas(A,'LHEEfft')

LHEEGxy=Gxy

LHEEf=f

LHEEpeak=max(Gxy)


x=RTOE;

[f,Gxy]=do_FFT(x,nfft,Fs)

A=figure

plot(f,squeeze(Gxy(1,1,:)))

saveas(A,'RTOEfft')

RTOEGxy=Gxy

RTOEf=f

RTOEpeak=max(Gxy)


x=LTOE;

[f,Gxy]=do_FFT(x,nfft,Fs)

A=figure

plot(f,squeeze(Gxy(1,1,:)))
```

```
saveas(A,'LTOEfft')
LTOEGxy=Gxy
LTOEf=f
LTOEpeak=max(Gxy)

x=PLAT;
[f,Gxy]=do_FFT(x,nfft,Fs)
A=figure
plot(f,squeeze(Gxy(1,1,:)))
saveas(A,'PLATfft')
PLATGxy=Gxy
PLATf=f
PLATpeak=max(Gxy)

close all

outputGxy=[FOHEGxy RACRGxy LACRGxy T2Gxy MANUGxy T10Gxy SACRGxy RASIGxy LASIGxy RTHIGxy LTHIGxy RKNEGxy LKNEGxy RTIBGxy LTIBGxy RANKGxy LANKGxy RTOEGxy LTOEGxy RHEEGxy LHEEGxy PLATGxy]
outputf=[FOHEf RACRf LACRf T2f MANUf T10f SACRf RASIf LASIf RTHIf LTHIf RKNEf LKNEf RTIBf LTIBf RANKf LANKf RTOEf LTOEf RHEEf LHEEf PLATf]
outputpeak=[FOHEpeak RACRpeak LACRpeak T2peak MANUpeak T10peak SACRpeak RASIpeak LASIpeak RTHIpeak LTHIpeak RKNEpeak LKNEpeak RTIBpeak LTIBpeak RANKpeak LANKpeak RTOEpeak LTOEpeak RHEEpeak LHEEpeak PLATpeak]
```

10.1.3 Peak to Peak Displacements

Peak to peak displacements were determined using the Tibial_marker program written by Dr Lang Yang, University of Sheffield.

10.1.4 Filter Design and Implementation

Butterworth bandpass filters were designed and implemented using filter_design and filter_apply matlab programs written by Prof Keith Wardon, University of Sheffield.

10.2 Personal Communications

10.2.1 Emma Pratt – Sheffield Teaching Hospitals

26/10/11

Hi Lucy,

Clinicallly anything under 10 fill without looking! 10-40 have a good look at the pattern fill options to check happy with. Above this I wouldn't be happy filling. However, you could try changing some of your reconstruction parameters if you think they are not real obstructions, namely the ray intersection factor but there are a few more to have a play with. The speed may also need increasing, as movement is much faster than gait. HAve a play and see if it gets any better!

Emma

10.2.2 Gerald Smith – Colorado Mesa University

06/02/12

Hello Lucy,

The detrending was to get rid of the small, low frequency shifts of position that occur with balance on the vibrating plate. It was accomplished by subtracting a moving average (over .04 s) from each position data point. This in effect removed the low frequency changes of position and left the high frequency vibration in place. See the attached figure to show how this worked over a one second time period.

The accelerations were calculated directly from the detrended position data using a central difference formula for acceleration:

a(i) = [X(i-1) - 2*X(i) + X(i+1)] / [(delta t)^2]

where the i indices indicate the sample numbers and delta t is the time interval between samples.

Good luck with your project,
GS

10.2.3 Peter Simonson – Juvent

11/08/14

Hello Lucy,

I understand you needed a concise decryption of the Juvent's 'magic'

Pete

The Juvent 1000N uses an accelerometer/micro-processor combined with patented algorithms to optimise safe, effective, and convenient micro-impact for each user, each time.

For the first 12 seconds, this patented algorithm running on the onboard microprocessor analyses the acceleration/force response from the user's body within a sweep (32Hz – 37Hz, at 0.3g. It uses this data to calculates the user's optimal resonant frequency; resulting in the the most efficient, safe, and effective frequency.

In real-time throughout the session, the patented algorithm monitors data and makes real-time adjustments to the force output to maintain a .3g force/acceleration at the optimum frequency for that user.

At the end, the system records the chosen frequency was during a 20 minute treatment.

10.3 Supporting Data and Documents

10.3.1 Area of the Gait Laboratory

Data and figures provided by Mark Reeves, Sheffield Teaching Hospitals.

Area and Volume Estimations

Area at 0.1m = 38m^2
Area at 2.0m = 32m^2
Average Area = 35m^2
If height = 2.2m
Volume = 35 x 2.2 = 77m^3

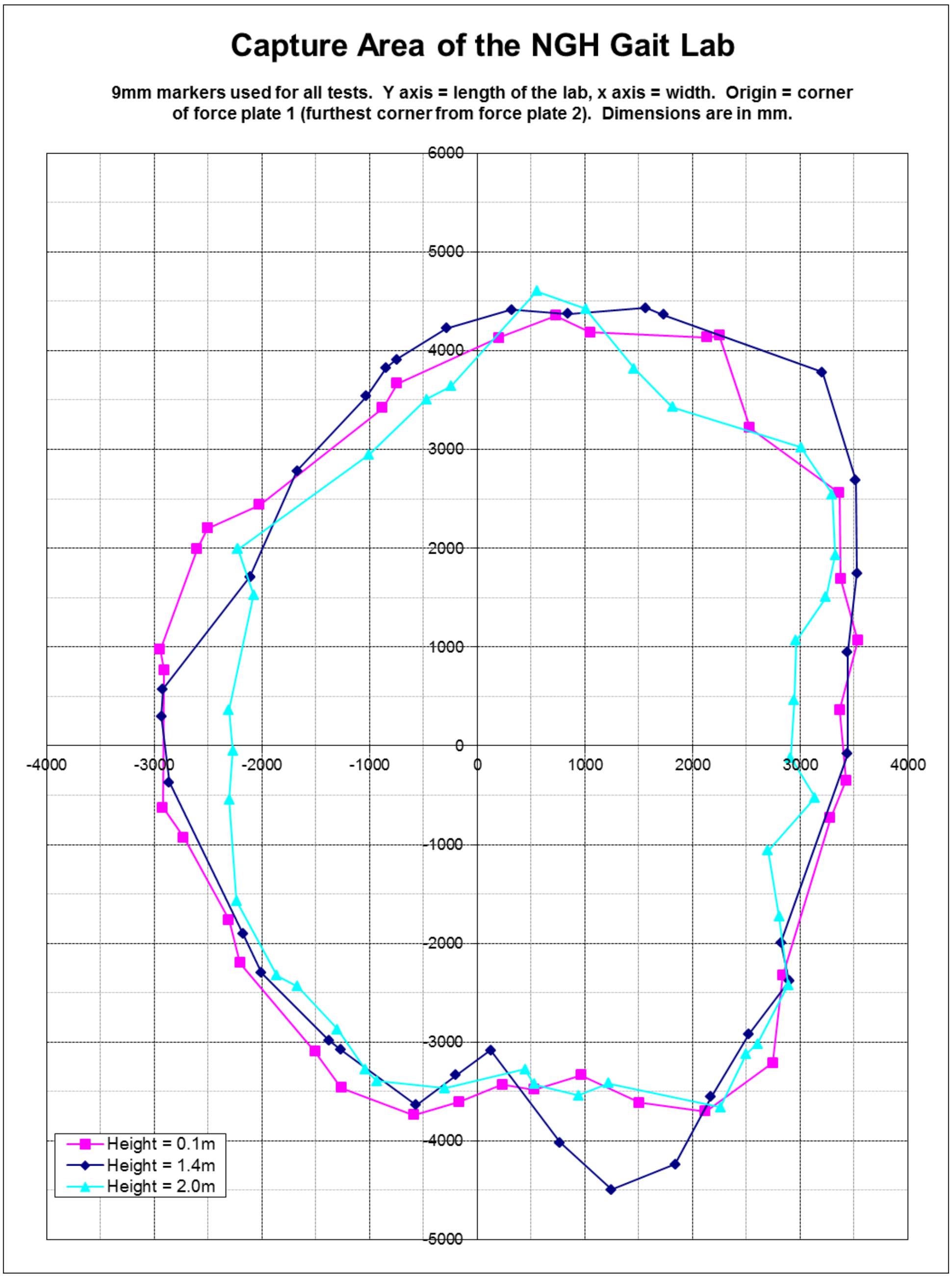

S 2: Capture Volume of the Gait Lab at the Northern General Hospital, Sheffield. Marker coordinates of a single reflective marker at the boundaries of view were established at heights of 0.1m, 1.4m and 2.0m. The area of the gait lab was calculated from these boundaries. An average area of 35m^2 was recorded which equates to a 3D volume of 77m^3 as the capture volume has a height of 2.2m.

10.3.2 Transmission with One or Both Feet on the Galileo 900

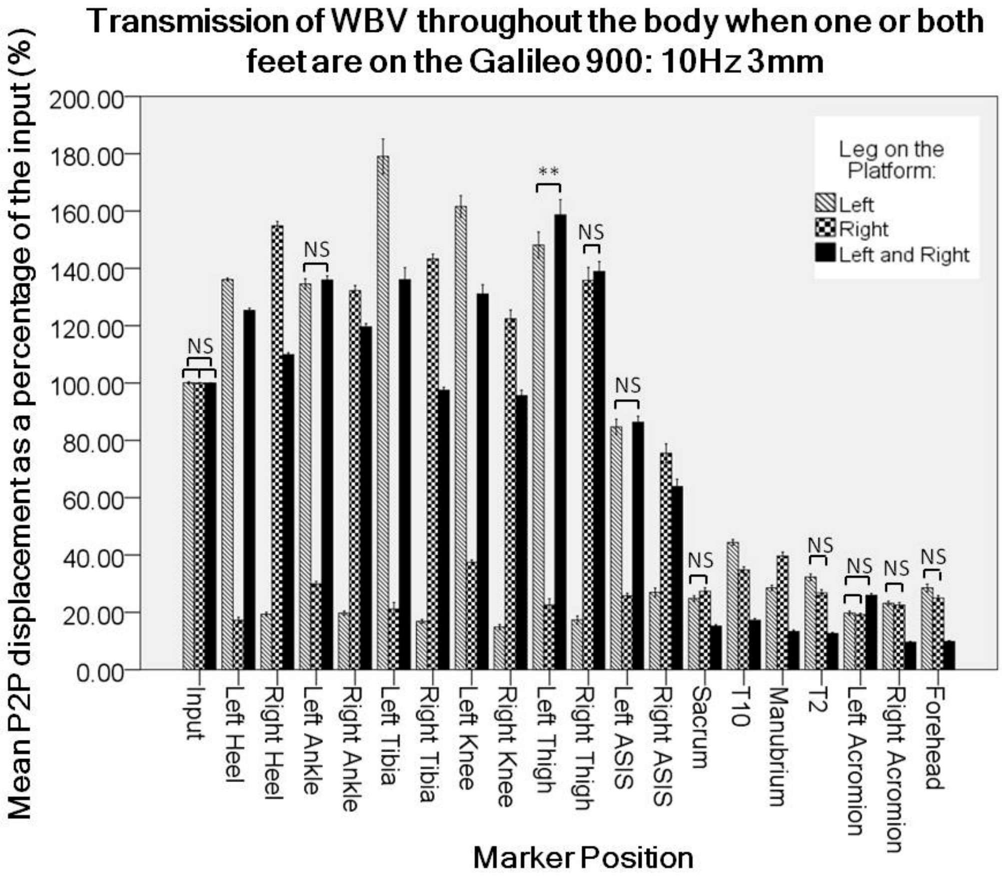

S 3: Transmission of 10Hz whole body vibration (WBV) with unilateral and bilateral stance.

WBV was delivered using the Galileo 900 platform at a frequency of 10Hz and amplitude of 3mm.In both unilateral and bilateral stances, transmission decreases from input to the forehead, however to different degrees dependent on whether there is one or both feet on the platform. Transmission in the torso is significantly greater in the unilateral stance than bilateral stance. Percentage of WBV transmitted to anatomical landmarks was calculated from peak to peak displacements measured using a Vicon motion capture system. Differences between vibration transmitted when both feet, the left foot and the right foot were on the platform were assessed using a one-way ANOVA with Dunnett's T3 post-hoc test. All outcomes are significant at $p<0.001$ unless indicated. NS=Not Significant, *$p<0.05$, ** $p<0.01$.

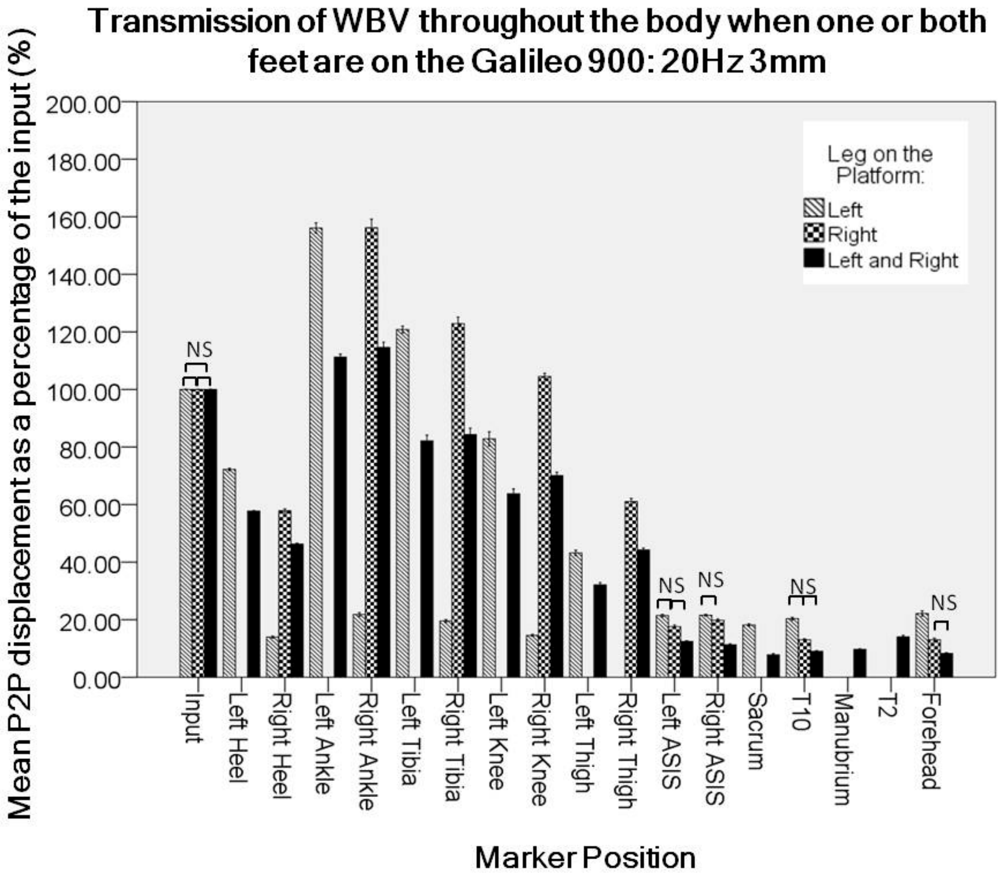

S 4: Transmission of 20Hz whole body vibration (WBV) with unilateral and bilateral stance. WBV was delivered using the Galileo 900 platform at a frequency of 20Hz and amplitude of 3mm.In both unilateral and bilateral stances, transmission decreases from input to the forehead, however to different degrees dependent on whether there is one or both feet on the platform. Transmission in the torso is significantly greater in the unilateral stance than bilateral stance. Percentage of WBV transmitted to anatomical landmarks was calculated from peak to peak displacements measured using a Vicon motion capture system. Differences between vibration transmitted when both feet, the left foot and the right foot were on the platform were assessed using a one-way ANOVA with Dunnett's T3 post-hoc test. All outcomes are significant at $p<0.001$ unless indicated. NS=Not Significant, *$p<0.05$, ** $p<0.01$.

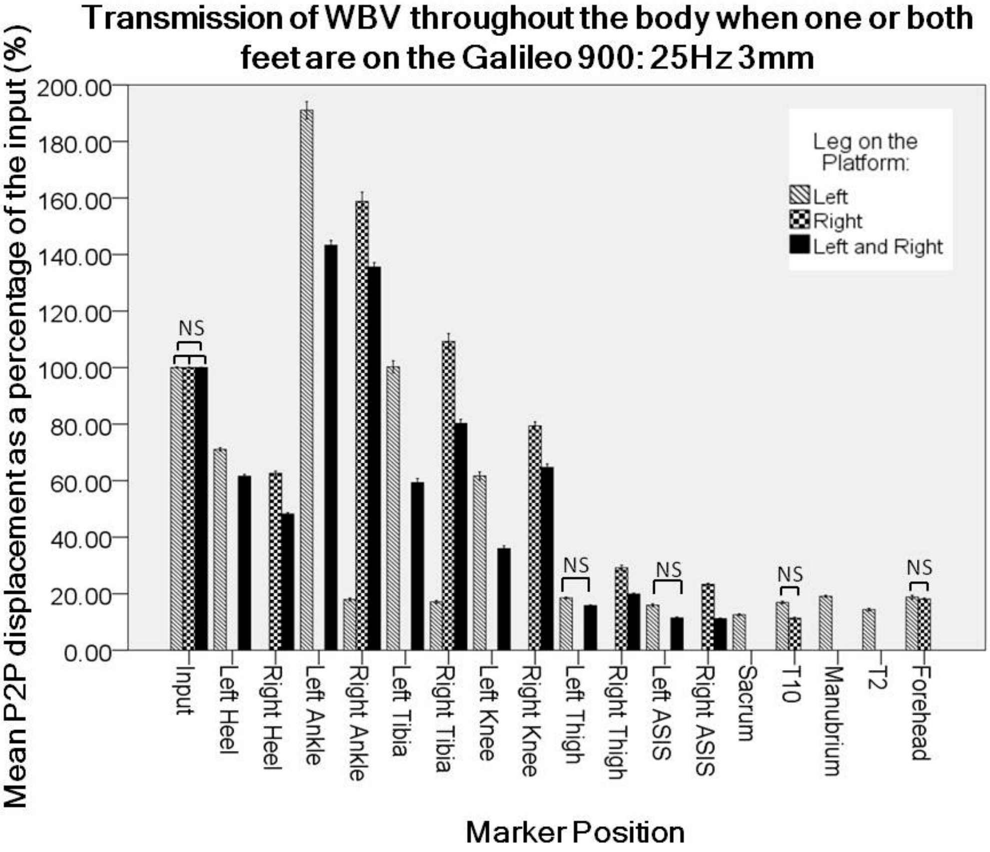

S 5: Transmission of 25Hz whole body vibration (WBV) with unilateral and bilateral stance. WBV was delivered using the Galileo 900 platform at a frequency of 25Hz and amplitude of 3mm.In both unilateral and bilateral stances, transmission decreases from input to the forehead, however to different degrees dependent on whether there is one or both feet on the platform. Transmission in the torso is significantly greater in the unilateral stance than bilateral stance. Percentage of WBV transmitted to anatomical landmarks was calculated from peak to peak displacements measured using a Vicon motion capture system. Differences between vibration transmitted when both feet, the left foot and the right foot were on the platform were assessed using a one-way ANOVA with Dunnett's T3 post-hoc test. All outcomes are significant at $p<0.001$ unless indicated. NS=Not Significant, *$p<0.05$, ** $p<0.01$.

10.3.3 Strain and Corresponding Strain Rate during Walking

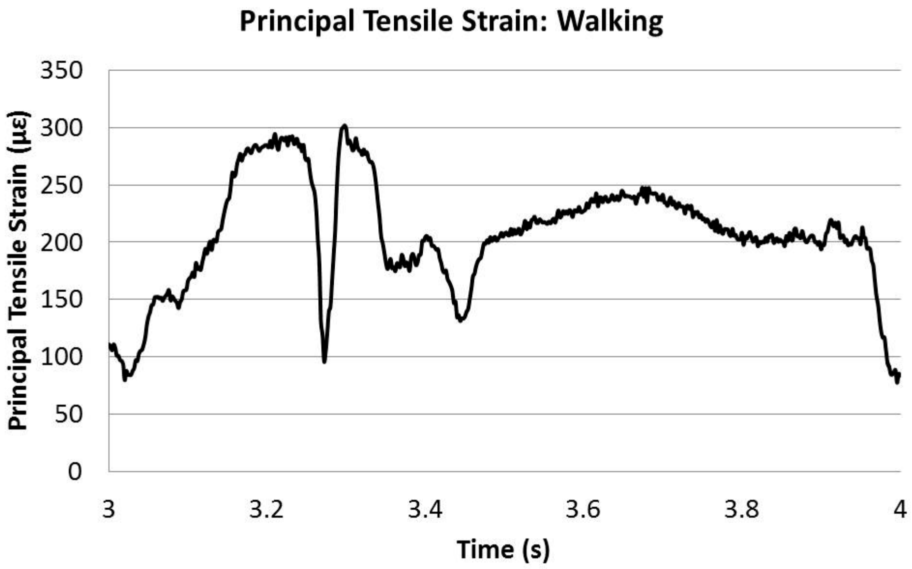

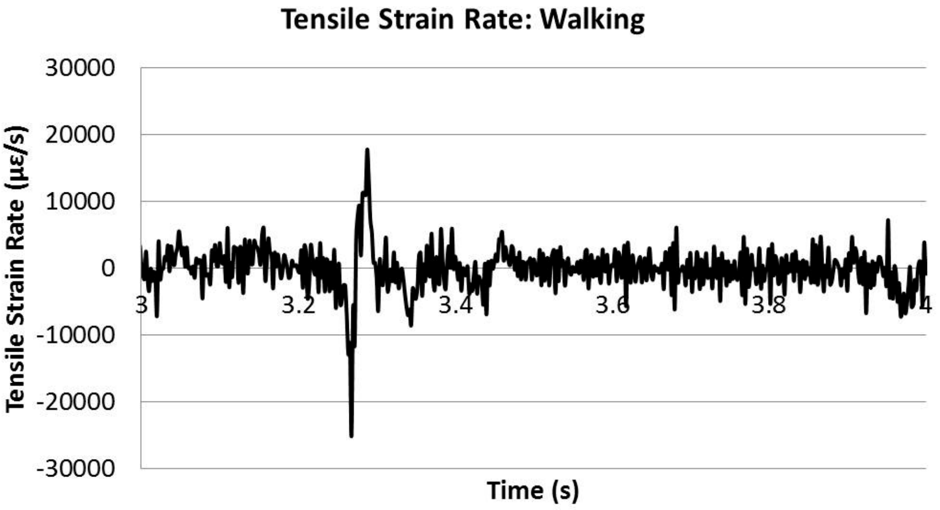

S 6: Strain and Strain Rate Recorded during Walking

The principal tensile strain during a single gait cycle is shown. The tensile strain rate shows a corresponding pattern, with the highest strain rates observed at the periods of greatest change in strain.

10.3.4 Strain and Corresponding Strain Rate during Whole Body Vibration

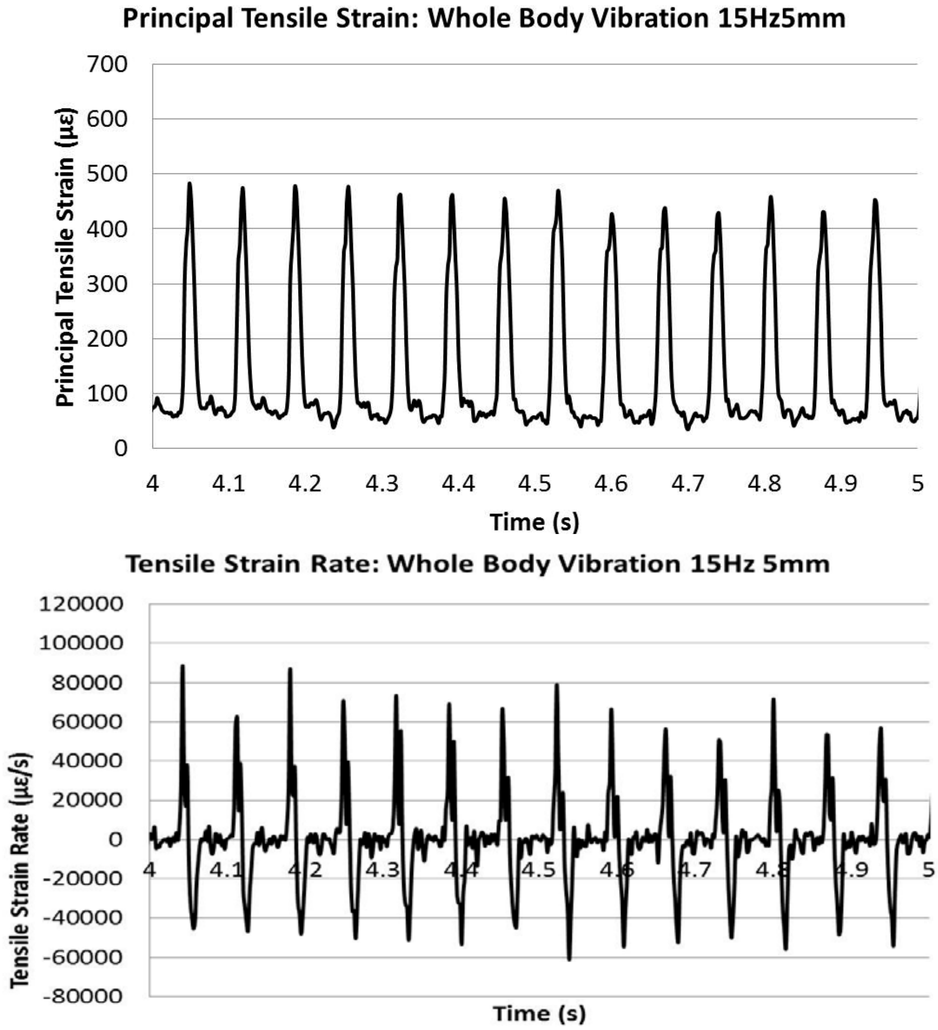

S 7: Strain and Strain Rate Recorded during Whole Body Vibration on the Galileo 900 at 15Hz5mm.

Principal tensile strain shows a cyclical pattern at 15Hz when participants are stood on the Galileo 900 at a frequency of 15Hz and amplitude of 5mm. The tensile strain rate shows a corresponding pattern, with the highest strain rates observed at the periods of greatest change in strain.

10.3.5 Electrical Interference During Strain Recordings during Standing

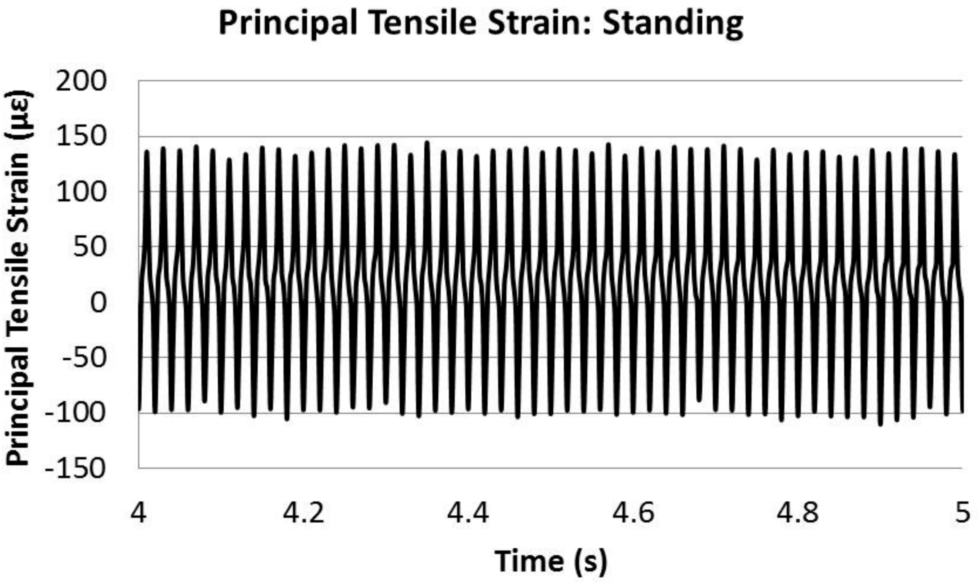

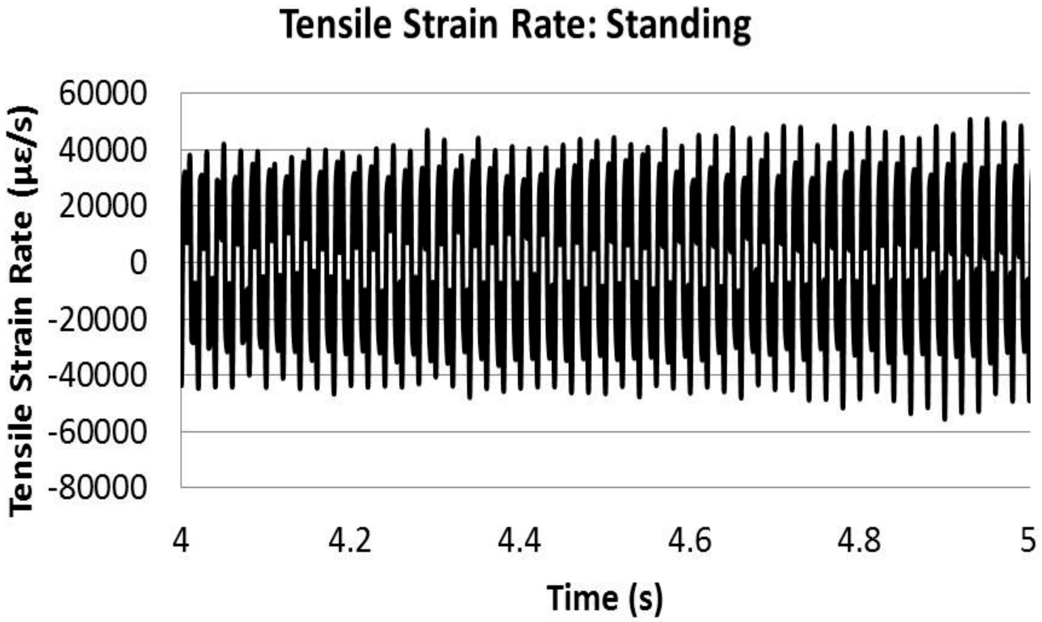

S 8: Strain and Strain Rate Recorded during Standing

Principal tensile strain and strain rate recorded during standing show a 50Hz cyclical pattern. This is unexpected during standing, however is the frequency of UK mains voltage, suggesting electrical interference during this recording. This interference does not appear to influence other strain recordings made during habitual locomotor activities or during whole body vibration.